Development of novel titanium dioxide based solid phase extraction for the selective isolation and identification of siderophores

Dissertation

Zur Erlangung des akademischen Doktorgrades der Naturwissenschaften

Doctor rerum naturalium

- Dr. rer. nat. -

an der

Universität Bremen

im Fachbereich Biologie/ Chemie

im Fach Chemie

vorgelegt von

Philipp Hans Egbers

M.Sc. Chemie

2022

Kolloquium: 20.01.2023

1. Gutachter: Prof. Dr. Boris Koch

2. Gutachterin: Prof. Dr. Rachel Codd

Gutachter *(Evaluators)*

Gutachter *(Evaluator)* 1: **Prof. Dr. Boris Koch**

Alfred-Wegener-Institut, Helmholtz-zentrum für Polar- und Meeresforschung

Hochschule Bremerhaven, Fachbereich 1

Gutachter (*Evaluator*) 2: **Prof. Dr. Rachel Codd**

University of Sidney, Faculty of Medicine and Health

Mitglieder des Prüfungsausschusses *(Examiners)*

1. Vorsitzender (*Chair*): **Prof. Dr. Tilmann Harder**

Universität Bremen, Fachbereich 2

Alfred-Wegener-Institut, Helmholtz-Zentrum für Polar- und Meeresforschung

2. Prüfer (*Examiner*): **Prof Dr. Peter Spiteller**

Universität Bremen, Fachbereich 2

3. Prüfer (*Examiner*): **Prof Dr. Boris Koch**

Alfred-Wegener-Institut, Helmholtz-Zentrum für Polar- und Meeresforschung

Hochschule Bremerhaven, Fachbereich 1

4. Prüfer (*Examiner*): **Dr. Jan Tebben**

Alfred-Wegener-Institut, Helmholtz-Zentrum für Polar- und Meeresforschung

Versicherung an Eides Statt

Ich, Philipp Hans Egbers (Vorname, Name)

versichere an Eides Statt durch meine Unterschrift, dass ich die vorstehende Arbeit selbständig und ohne fremde Hilfe angefertigt und alle Stellen, die ich wörtlich dem Sinne nach aus Veröffentlichungen entnommen habe, als solche kenntlich gemacht habe, mich auch keiner anderen als der angegebenen Literatur oder sonstiger Hilfsmittel bedient habe.

Ich versichere an Eides Statt, dass ich die vorgenannten Angaben nach bestem Wissen und Gewissen gemacht habe und dass die Angaben der Wahrheit entsprechen und ich nichts verschwiegen habe.

Die Strafbarkeit einer falschen eidesstattlichen Versicherung ist mir bekannt, namentlich die Strafandrohung gemäß § 156 StGB bis zu drei Jahren Freiheitsstrafe oder Geldstrafe bei vorsätzlicher Begehung der Tat bzw. gemäß § 161 Abs. 1 StGB bis zu einem Jahr Freiheitsstrafe oder Geldstrafe bei fahrlässiger Begehung.

Hamburg, 28.10.2022

Ort, Datum / Unterschrift

Erklärung zur elektronischen Version und zur Überprüfung einer Dissertation

Hiermit bestätige ich gemäß §7, Abs. 7, Punkt 4, dass die zu Prüfungszwecken beigelegte elektronische Version meiner Dissertation identisch ist mit der abgegebenen gedruckten Version.

Ich bin mit der Überprüfung meiner Dissertation gemäß §6 Abs. 2, Punkt 5 mit qualifizierter Software im Rahmen der Untersuchung von Plagiatsvorwürfen einverstanden.

Hamburg, 28.10.2022

Ort, Datum / Unterschrift

Danksagung

Ich möchte mich ganz herzlich bei Prof. Dr. Tilmann Harder für das Angebot bedanken in seiner Arbeitsgruppe meine Dissertation anzufertigen. Zudem möchte ich mich bei Ihm für die immer offene Tür und die verlässliche Unterstützung bedanken.

Außerdem bin ich Dr. Jan Tebben für den fachlichen Austausch und die immer vorhandene Hilfsbereitschaft sehr dankbar.

Jennifer Bergemann gilt ein besonderer Dank für die Unterstützung im Labor und die Einführung in die Kultivierung von Bakterien.

Bei Christian Zurhelle und Fabian Moye möchte ich mich für die lehrreichen Gespräche und den kollegialen Zusammenhalt bedanken.

Außerdem möchte ich mich bei allen ehemaligen wie aktuellen Mitgliedern für gesammelten Erfahrungen, wissenschaftlich wie sozial, bedanken.

Bei meiner Familie, meinen Freunden und speziell Krystina möchte ich mich besonders bedanken. Ohne den starken Rückhalt und die niemals endende Zuversicht wären die letzten Jahre eine viel größere Herausforderung gewesen.

Table of Content

List of Publications

The manuscripts that are part of this doctoral thesis are listed below. Chapter 2 is a reprint of an already published paper in an international peer-review journal. The content of Chapter 2 as well as the labeling of figures and tables is unchanged compared to the published version. Chapter 3 is the most recent version of a resubmitted manuscript (under review), with formatting and labeling adapted to the general format of the dissertation. Chapters 4 and 5 are in preparation to be submitted as a combined manuscript.

Chapter 2: Siderophore purification with titanium dioxide nanoparticle solid phase extraction

Philipp H. Egbers, Tilmann Harder, Boris P. Koch, Jan Tebben

This manuscript was published in Analyst 2020, 145(22), 7303-7311 (DOI: 10.1039/D0AN00949K)

Chapter 3: Selective purification of catecholate, hydroxamate and α-hydroxycarboxylate siderophores with Titanium Dioxide Affinity Chromatography

Philipp H. Egbers, Christian Zurhelle, Tilmann Harder, Boris P. Koch, Jan Tebben

This manuscript has already been submitted to Separation and Purification and has been reviewed. The version now listed here address all of the reviewers' criticisms and a similar version has been resubmitted to this journal. At the time of dissertation submission, the submitted manuscript is still under review.

Chapter 4: Extraction of siderophores from seawater by means of TDAC

Philipp H. Egbers, Tilmann Harder, Jan Tebben

This manuscript is not intended for a standalone submission, but rather can be viewed as a key preliminary study for Chapter 5.

Chapter 5: Siderophore identification in complex seawater extracts

Philipp H. Egbers, Tilmann Harder, Jan Tebben

This manuscript is in preparation for submission with key aspects of Chapter 4.

Declaration on the contribution of the candidate to a multi-author article/manuscript which is included as a chapter in the submitted doctoral thesis

Chapter 2:

Contribution of the candidate in % of the total work load (up to 100% for each of the following categories):

Experimental concept and design:	ca. 80%
Experimental work and/or acquisition of (experimental) data:	ca. 90%
Data analysis and interpretation:	ca. 90%
Preparation of Figures and Tables:	ca. 100%
Drafting of the manuscript:	ca. 75%

Chapter 3:

Contribution of the candidate in % of the total work load (up to 100% for each of the following categories):

Experimental concept and design:	ca. 75%
Experimental work and/or acquisition of (experimental) data:	ca. 90%
Data analysis and interpretation:	ca. 90%
Preparation of Figures and Tables:	ca. 100%
Drafting of the manuscript:	ca. 75%

Chapter 4:

Contribution of the candidate in % of the total work load (up to 100% for each of the following categories):

Experimental concept and design:	ca. 90%
Experimental work and/or acquisition of (experimental) data:	ca. 100%
Data analysis and interpretation:	ca. 100%
Preparation of Figures and Tables:	ca. 100%
Drafting of the manuscript:	ca. 95%

Chapter 5:

Contribution of the candidate in % of the total work load (up to 100% for each of the following categories):

Experimental concept and design:	ca. 85%
Experimental work and/or acquisition of (experimental) data:	ca. 90%
Data analysis and interpretation:	ca. 100%
Preparation of Figures and Tables:	ca. 100%
Drafting of the manuscript:	ca. 95%

Date: 28.10.2022

Signatures:

List of Figures

List of Tables

List of Abbreviations

μM	micromolar concentration
1D	one-dimensional
BPC	base peak chromatogram
CAS	chrome azurol S
Da	Dalton
DSSC	dye sensitized solar cells
DFOB	desferrioxamine B
DFOE	desferrioxamine E
DHBA	dihydroxybenzoic acid
DNA	deoxyribonucleic acid
DOC	dissolved organic carbon
DOM	dissolved organic matter
EDTA	ethylenediaminetetraacetic acid
EIC	extracted ion chromatogram
ESI	electron spray ionization
$E_T(30)$	solvent polarity parameter
FA	formic acid
FT-ICR	Fourier-transform ion cyclotron
Fur	ferric uptake regulator
Gt	gigatons
HDTMA	hexadecyltrimethylammonium bromide
His-tag	histidine-tagged
HNLC	high nutrient low chlorophyll
HPLC	high-pressure liquid chromatography
HRMS	high-resolution mass spectrometry
ICP	inductively coupled plasma
IMAC	immobilized metal affinity chromatography
LC	liquid chromatography
M	molar concentration
m/z	mass to charge ratio
mM	millimolar concentration
MS	mass spectrometry
MS/MS	tandem mass spectrometry
MS^2	tandem mass spectrometry
MSPE	magnetic solid-phase extraction

NIS	NRPS-independent
NMR	nuclear magnetic resonance
NRPS	non-ribosomal peptide synthetase
PB	petrobactin
pK_a	negative common logarithm of acid dissociation constant
pM	picomolar concentration
ppm	parts per million
PTFE	polytetrafluoroethylene
SPE	solid-phase extraction
SPME	solid-phase microextraction
TDAC	titanium dioxide affinity chromatography
TIC	total ion chromatogram
UV	ultraviolet
VF	vibrioferrin
WBA	woodybactin A
XRF	X-ray fluorescence spectroscopy

Abstract

This thesis focused on simplifying the identification of organic Fe(III)-ligands, so-called siderophores, by means of a new affinity chromatography approach using titanium dioxide (TiO_2). Siderophores are generally produced by microorganisms as a response to iron limiting growth conditions. The biological need for iron is based on the fact that this element is an essential micronutrient since a variety of enzymatic processes relay on its unique redox potential. This class of metabolites is known to occur in a variety of habitats and is expected to be one of the key factors to microbial iron uptake processes as well as to pathogenic and mutualistic relationships involving micro- and multicellular organisms. Siderophores are characterized by their specific and inherent affinity for Fe(III) caused by the typical functional groups present in siderophore structures: Hydroxamates, catecholates and α-hydroxycarboxylates. Since siderophores are paramount to the general iron bioavailability, independent of the habitat, the identification and characterization of such compounds is of special interest. However, their detection in natural samples like soil and seawater poses several difficulties and is often limited by low concentrations and high sample complexity.

Therefore, this thesis aimed to develop a new approach on how to facilitate the detection of siderophores in crude natural samples to mirror the natural iron ligand composition and therefore shed light on the iron speciation in habitats like the world's oceans. TiO_2 was investigated as a possible affinity chromatography sorbent since strong adsorption of siderophore characteristic functional groups on this particular metal oxide are well documented and even employed in applications like solar panels or photocatalysts.

This thesis describes for the first time a TiO_2 based extraction approach for the targeted isolation of siderophores from apolar as well as polar and highly complex sample matrices. The proof of concept was provided using commercially available TiO_2 nanoparticles and performed as disperse solid phase extraction showing remarkably high recoveries of the hydroxamate-type siderophore desferrioxamine B (DFOB). To allow faster processing and large volume extraction this approach was evolved to the commonly used solid phase extraction (SPE) cartridge setup employing self-prepared TiO_2 micron powder (Figure 1). By means of this developed TiO_2 affinity chromatography (TDAC) it was possible to extract and purify all siderophore types independent of their functional group from bacteria culture supernatants as well as from marine water extracts, posing one of the most complex types of sample. However, it was shown that depending on the functional group of the siderophores, the maximum recoveries were obtained at different elution conditions. In addition, it was also described that the adjustment of solution conditions prior to extraction via TDAC resulted in suppressed adsorption of dissolved organic matter (DOM) while siderophore adsorption remained unchanged. These adjustments in pH, anion

concentration and type of anion led to depleted sample complexity in TDAC eluates and thus to a simplified identification of siderophores. The potential of TDAC to unravel natural siderophore compositions was highlighted since by means of TDAC two putative siderophores were identified in DOM extracts from cruise HE533 to the arctic fjords of Norway.

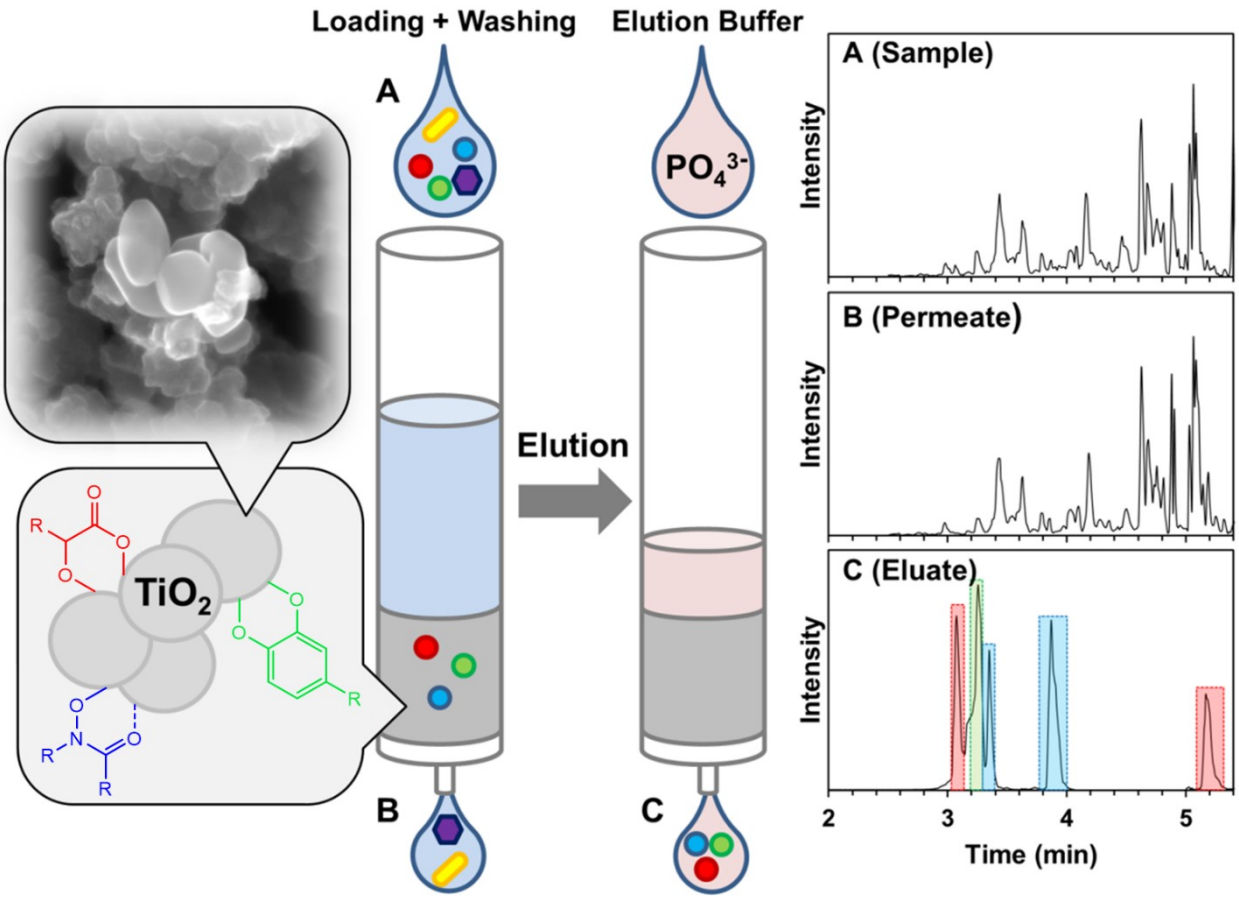

Figure 1. Schematic representation of TiO_2 affinity chromatography (TDAC) for the targeted isolation of siderophores, characterized by the presence of functional groups like hydroxamates (blue), catecholates (green) and α-hydroxycarboxylates (red). Total ion chromatograms of the crude sample (A), TDAC permeate (B) and TDAC eluate (C) are displayed to highlight the depletion in sample complexity by TDAC.

Zusammenfassung

Im Mittelpunkt dieser Arbeit stand die Vereinfachung der Identifizierung organischer Fe(III)-Liganden, so genannter Siderophore, durch einen neuen affinitätschromatographischen Ansatz mit Titandioxid (TiO_2). Siderophore werden im Allgemeinen von Mikroorganismen als Reaktion auf eisenlimitierende Wachstumsbedingungen gebildet. Der biologische Bedarf an Eisen beruht auf der Tatsache, dass dieses Element ein essentieller Mikronährstoff ist, da eine Vielzahl von enzymatischen Prozessen auf sein einzigartiges Redoxpotential angewiesen sind. Es ist bekannt, dass diese Klasse von Metaboliten in einer Vielzahl von Lebensräumen vorkommt, und es wird erwartet, dass sie einer der Schlüsselfaktoren für mikrobielle Eisenaufnahmeprozesse sowie für pathogene und mutualistische Beziehungen zwischen mikro- und multizellulären Organismen sind. Siderophore zeichnen sich durch ihre spezifische und inhärente Affinität für Fe(III) aus, die durch die typischen funktionellen Gruppen in deren Strukturen verursacht wird: Hydroxamate, Catecholate und α-Hydroxycarboxylate. Da Siderophore unabhängig vom Lebensraum an der allgemeinen Bioverfügbarkeit von Eisen beteiligt sind, ist die Identifizierung und Charakterisierung solcher Verbindungen von besonderem Interesse. Ihr Nachweis in natürlichen Proben wie Boden und Meerwasser ist jedoch mit einigen Schwierigkeiten verbunden und wird oft durch niedrige Konzentrationen und hohe Komplexität der Proben eingeschränkt.

Ziel dieser Arbeit war es daher, einen neuen Ansatz zu entwickeln, der den Nachweis von Siderophoren in natürlichen Rohproben erleichtert, um die natürliche Eisenligandenzusammensetzung widerzuspiegeln und somit Licht in die Eisenspeziation in Lebensräumen wie den Weltmeeren zu bringen. TiO_2 wurde als mögliches Sorptionsmittel für die Affinitätschromatographie untersucht, da die starke Adsorption von für Siderophore charakteristischen funktionellen Gruppen an dieses spezielle Metalloxid gut dokumentiert ist und sogar in Anwendungen wie Solarzellen oder Photokatalysatoren eingesetzt wird.

In dieser Arbeit wurde erstmals ein TiO_2-basierter Extraktionsansatz für die gezielte Isolierung von Siderophoren aus apolaren sowie polaren und hochkomplexen Probenmatrices beschrieben. Der Nachweis des Konzepts wurde mit kommerziell erhältlichen TiO_2-Nanopartikeln erbracht und als disperse Festphasenextraktion durchgeführt, die bemerkenswert hohe Wiederfindungsraten des Siderophors Desferrioxamin B (DFOB) zeigte, welches zu den Hydroxamat-Typ Siderophoren gehört. Um eine schnellere Verarbeitung und eine großvolumige Extraktion zu ermöglichen, wurde dieser Ansatz zu der üblicherweise verwendeten Festphasenextraktion (SPE) mit selbst hergestelltem TiO_2-Mikronpulver weiterentwickelt (Abbildung 1). Mit Hilfe dieser entwickelten TiO_2-Affinitätschromatographie (TDAC) war es möglich, alle Siderophor-Typen unabhängig von ihrer funktionellen Gruppe aus Überständen von Bakterienkulturen sowie aus Meerwasserextrakten, was eine der komplexesten Probenarten darstellt, zu extrahieren. Es

wurde jedoch gezeigt, dass je nach funktioneller Gruppe der Siderophore die maximalen Wiederfindungen bei unterschiedlichen Elutionsbedingungen erzielt wurden. Darüber hinaus wurde beschrieben, dass die Anpassung der Lösungsbedingungen vor der Extraktion mittels TDAC zu einer unterdrückten Adsorption von gelöster organischer Materie (dissolved organic matter = DOM) führte, während die Siderophor-Adsorption unverändert blieb. Diese Anpassungen des pH-Werts, der Anionen Konzentration und des Anionentyps führten zu einer verringerten Komplexität der Proben in den TDAC-Eluaten und damit zu einer vereinfachten Identifizierung der Siderophore. Das Potenzial von TDAC zur Entschlüsselung der Zusammensetzung natürlicher Siderophore wurde hervorgehoben, da mit Hilfe von TDAC zwei mutmaßliche Siderophore in DOM-Extrakten von der Kreuzfahrt HE533 in den arktischen Fjorden Norwegens identifiziert wurden.

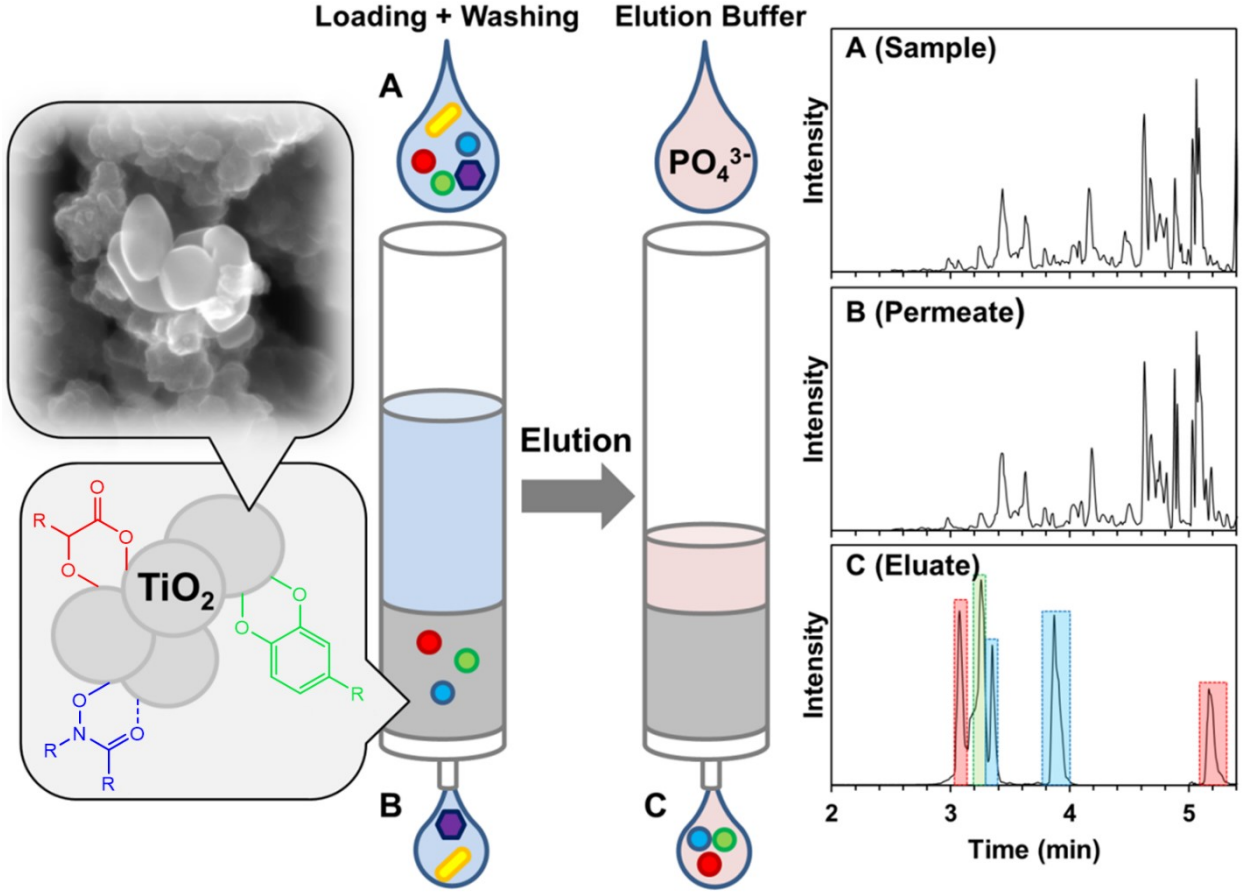

Abbildung 1. Schematische Darstellung der TiO_2-Affinitätschromatographie (TDAC) für die gezielte Isolierung von Siderophoren, die durch das Vorhandensein von funktionellen Gruppen wie Hydroxamaten (blau), Catecholaten (grün) und α-Hydroxycarboxylaten (rot) gekennzeichnet sind. Die Gesamtionenstromchromatogramme der ursprünglichen Probe (A), des TDAC-Permeats (B) und des TDAC-Eluats (C) zeigen die Verarmung der Komplexität der Probe durch TDAC.

1. General Introduction

1.1 Importance of iron in the environment

Iron is an essential nutrient to almost all life on earth (Johnson 2008). The biological importance of iron lies in its ability to cycle between the two oxidation states Fe(II) and Fe(III) via an one-electron oxidation-reduction reaction (Hentze et al. 2004). The standard potential of this redox reaction is E° = +0.77 V at 25 °C (Hoffmann 2005). Iron is functioning as an indispensable co-factor or redox catalyst for a variety of cellular processes such as oxygen transport, respiration, tricarboxylic acid cycle, lipid metabolism, gene regulation and DNA synthesis (Cairo et al. 2006). Furthermore, phototrophic organisms require iron for the synthesis of chlorophyll and the reduction of nitrate as well as sulphate during the photosynthetic production of organic compounds (Glover 1977; Rueler and Ades. 1987). Therefore, iron scarcity has dramatic effects on virtually all organisms. For example, iron deficiency is the primary nutritional disorder in the world, affecting roughly two billion people (2006) (Cairo et al. 2006). Contrary, an excess of free iron is also resulting in severe biological damage caused by the exact same redox chemistry making it so valuable for all life (Winterbourn 1995). Under cytoplasm conditions its redox activity leads to the generation of hydroxyl or lipid radicals (Fenton reaction) which in turn are responsible for the destruction of proteins or membrane lipids. It is assumed that the majority of reactive oxygen species causing oxidative stress are a result of Fenton-like reactions. Since both - cellular iron overload and iron deficiency - lead to cell death, reactive iron levels must be carefully controlled. Iron is often the limiting growth factor in various habitats (Rue and Bruland 1995), even though it is the fourth most abundant element and the most abundant transition metal in the Earth's crust (Taylor 1964; Rout and Sahoo 2015). Therefore in most environments iron deficiency is not caused by low total iron concentrations but by low iron bioavailability (Kraemer 2004). The bioavailability of iron is mainly determined by its aqueous chemistry and the slow dissolution kinetics of iron-bearing minerals like hematite (Fe_2O_3), limonite (FeO(OH)) and siderite ($FeCO_3$) (Kraemer 2004; Hoffmann 2005). In general, Fe(II) salts are more soluble than Fe(III) salts and it has also been shown that dissolved Fe(II) is usually more bioavailable than Fe(III) (Hoffmann 2005). However, under aerobic and not strongly acidic conditions Fe(III) is the thermodynamically most stable oxidation state of iron (Boukhalfa and Crumbliss 2002; Sandy and Butler 2009), resulting in the oxidation of Fe(II) to Fe(III) (Butler et al. 2021). Therefore, the bioavailability of iron is largely characterized by the solubility of its Fe(III) species. The speciation of Fe(III) in aqueous solutions can be described as a function of pH. Increasing pH (pH > 6) leads to the formation of highly insoluble oxohydroxides at neutral pH conditions. The formation of such oxohydroxides like $Fe(OH)_3$ leads to precipitation and consequently to a decrease in dissolved Fe(III) (Figure 2).

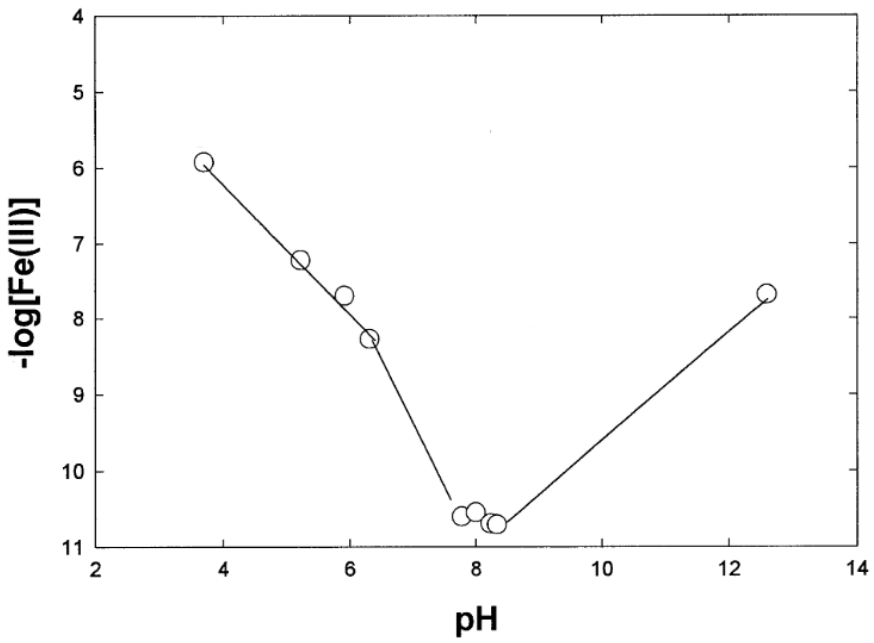

Figure 2. Effect of pH on solubility of Fe(III) in 0.7 M NaCl at 25°C. Figure is adapted from (Liu and Millero 1999).

With further increasing pH, $[Fe(OH)_4]^-$ is formed and the solubility of Fe(III) increases again (Liu and Millero 1999; Millero 2001), but this increase in solubility is irrelevant to most natural habitats such as the oceans and soils. This decrease in solubility leads ultimately to a reduced bioavailability of iron at neutral or slightly alkaline pH conditions (Boukhalfa and Crumbliss 2002; Sandy and Butler 2009). Such reduced iron bioavailability is well documented for marine waters as well as for agriculturally used soils (Römheld and Marschner 1986; Martin and Fitzwater 1988). To satisfy their iron demands despite the low bioavailability of iron, microorganisms have evolved sophisticated strategies to scavenge, adsorb or dissolve iron from the surrounding environment, depending on the molecular constraints of the iron pool (Hider and Kong 2010). The central role in microbial ferric iron uptake strategies is played by high-affinity Fe(III)-specific binding compounds, so called siderophores.

1.2 Siderophores

Siderophores are low-molecular weight, secondary metabolites that are often produced by microorganisms and plants as a response to iron deficiency (Hider and Kong 2010; Kramer et al. 2020). Since almost all known bacterial phyla produce siderophores, this iron accumulation pathway is the most prevalent mechanism in the bacterial world (Guerinot 1994; Ratledge and Dover 2000; Kramer et al. 2020).

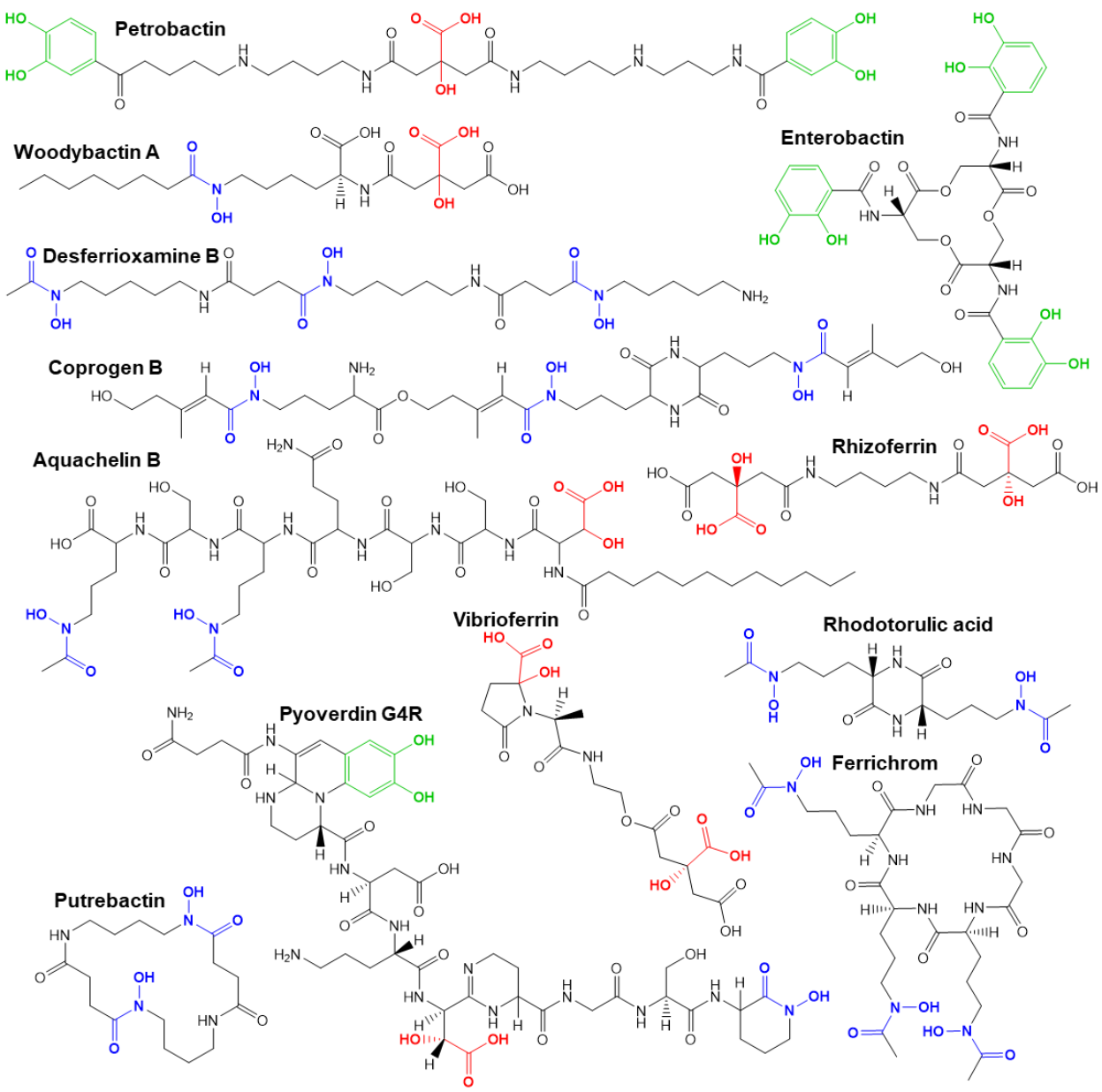

Figure 3. Overview of prominent siderophores and their characteristic Fe(III)-binding groups. To illustrate that siderophores with only one type of functional group and mixed siderophores exist, catechols (green), hydroxamic acids (blue) and α-hydroxycarboxylic acids (red) are highlighted in color.

Different fungi are also known for their ability to synthesize siderophores, whereas graminaceous plants like grasses and related cereals secrete phytosiderophores into the rhizosphere. The fact that plants can suffer from iron deficiency, which causes the production of siderophores as a strategic response, is counterintuitive since most soil types are composed of iron-rich minerals, but can be attributed to the poor solubility of iron under neutral/basic conditions. Phytosiderophores differ in the type and composition of iron binding groups from microbial siderophores by the presence of two α-aminocarboxylate binding centers together with a single α-hydroxycarboxylate unit (Hider and Kong 2010). Taking all known siderophores together, regardless of their microbial or plant origin, more than 500 siderophores have been identified in the last 60 years. (Hider and Kong 2010). The first siderophore that has been isolated and de-

scribed for its high affinity towards iron was mycobactin, making it the first representative of this substance class (Francis et al. 1949). The most predominant metal cation binding groups found among those hundreds of molecules are hydroxamates, catecholates and α-hydroxycarboxylates, resulting in four different classes of microbial siderophores namely: Tris-hydroxamates, tris-catecholates, tris-α-hydroxycarboxylates and mixed type siderophores (Figure 3). An exception to this general description of the functional groups of siderophores is the recently discovered gramibactin, which has a diazeniumdiolate ligand (Hermenau et al. 2018, 2019).

1.2.1 Metal cation affinity and classification of siderophores

Although the term siderophore is derived from Greek and translates to 'iron carrier', siderophores do not exhibit the same behavior towards all oxidation states of iron. Without any known exception, siderophores show a higher affinity towards Fe(III) than to oxidation states like Fe(0), Fe(II) or Fe(IV) (Hider and Kong 2010). The reason for the different affinities lies in the number of donor atoms and favored geometry of siderophores. In general siderophores have three functional groups with two donor atoms per group, adding up to a total of six donor atoms per siderophore molecule.

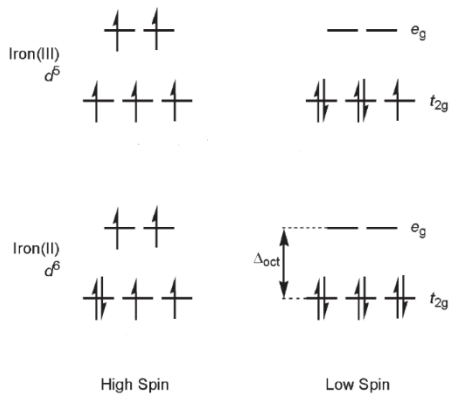

Figure 4. Representation of d-orbital occupancies of high- and low spin Fe(III) and Fe(II) complexes. In the high-spin state, all five d-electrons of Fe(III) are unpaired and since the energy required to overcome the electrostatic repulsion between pairs of electrons in the same d-orbital is greater than the energy difference between the e_g and t_{2g} d-orbitals in the octahedral field (Δ_{oct}), this geometry is preferred for Fe(III) complexes. Figure is adapted from (Halcrow 2008).

Six donor atoms are most easily arranged around one central atom in an octahedral geometry, leading to minimal electrostatic repulsion between the donor atoms. Those donor atoms, able to form coordinative bonds with the central metal cation, are described as ligands. Such an octahedral field thermodynamically favors in turn the complex formation with the high-spin Fe(III) (Halcrow 2008; Hider and Kong 2010) (Figure 4). The most common donor atom in siderophores is negatively charged oxygen, but nitrogen and sulfur are also known to function as donor atoms in siderophores. The affinity towards Fe(III) tends to be reduced if such donor atoms

are incorporated instead of oxygen, since negatively charged oxygen is the hardest Lewis base among those donor atoms and interacts the strongest with the hard Lewis acid Fe(III). This change in affinity is in accordance with the Pearson concept, which essentially describes that soft acids react faster and form stronger bonds with soft bases, whereas hard acids react faster and form stronger bonds with hard bases if all other factors being equal. In general, the affinity of siderophores towards any cation is determined by the charge-to-ion radius ratio. Metal cations like Al(III), Ga(III) and Th(IV) are also known to form complexes with siderophores, but which do not meet the stability of the corresponding Fe(III) complex (Keith-Roach et al. 2005; Jain et al. 2017) (Figure 5).

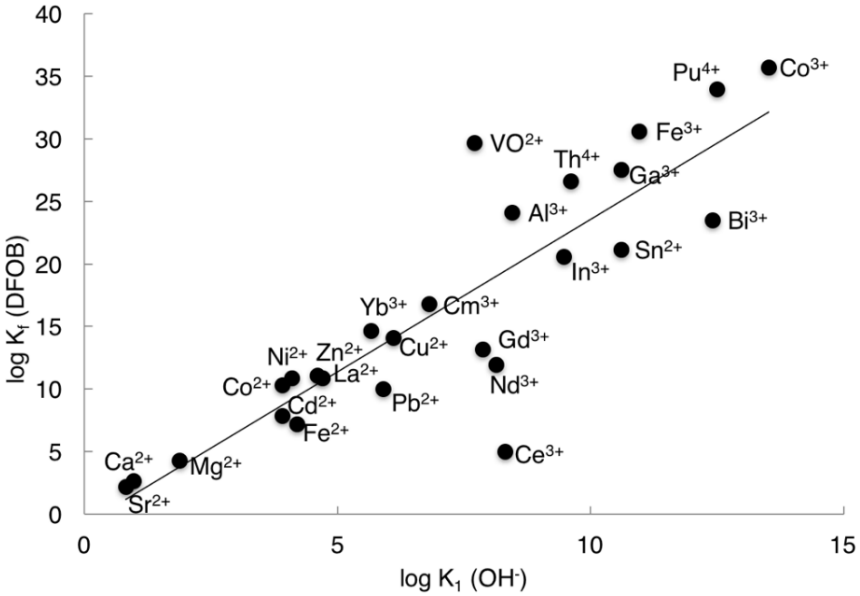

Figure 5. Correlation of the affinity constants (log K) of desferrioxamine B (DFOB) and hydroxide ions (log K) with various metal ions. Figure is taken from (Jones 2017).

Siderophore complexes with Ti(IV) or Pu(IV) were found to be even more stable (Jones et al. 2017). However, it is assumed that other environmental metal siderophore complexes than iron complexes do not play an important role. As stated in Chapter 1.2, siderophores can be classified by the bidentate functional group incorporated into their molecular structure, namely hydroxamates, catecholates and α-hydroxycarboxylates. Hydroxamates can be defined as *N*-hydroxy amides with two mesomeric forms, one of which produces a high charge density at the carbonyl oxygen (Table 1).

Table 1. Most prominent functional groups in siderophores with typical corresponding values of the acid dissociation constant pK_a.

Name	Structure	pK_a
Catecholate	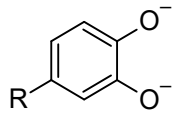	9.2 and 13
α-Hydroxycarboxylate	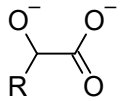	3.0 and 14.5
Hydroxamate	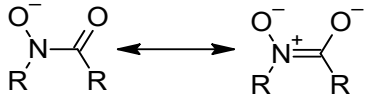	9.0

pK_a values taken from (Hider and Kong 2010).

Desferrioxamines are a well-known group of tris-hydroxamate siderophores, including linear and cyclic ligands like desferrioxamine B (DFOB) and desferrioxamine E (DFOE). The most prominent representative of the tris-catecholate siderophores is enterobactin, due to the highest documented affinity constant, K_f, of any known Fe(III)-siderophore complex (logK_f = 49.0 (Loomis and Raymond 1991)). The affinity constant K_f is defined by the following equation (i) (Hider and Kong 2010):

(i) $$Fe + L \rightleftharpoons FeL \qquad K_f = [FeL]/ [Fe][L]$$

Enterobactin is a trilactone of 2,3-dihydroxybenzoyl-L-serine (Raymond et al. 2003) and therefore belongs to the predominant type of catechol siderophores, containing the 2,3-dihydroxybenzoic acid (2,3-DHBA) group (Maier and Butler 2017). In addition to this group, 3,4-DHBA as well as the sulfonated derivatives of 3,4-DHBA have also been observed in the mixed type siderophore petrobactin (Hickford et al. 2004; Pfleger et al. 2007). Both 2,3- and 3,4-DBHA groups are labile to oxidation into orthoquinones in aqueous solutions. The oxidation kinetics are positively correlated to pH, which means that catechols tend to oxidize under neutral or alkaline conditions (Danner et al. 2012). The loss of the catecholate functionality results in decreased affinity towards metal cations. Siderophores containing the α-hydroxycarboxylate group are also subdivided into the following three minor classes: central α-hydroxycarboxylates, terminal α-hydroxycarboxylates and α-hydroxycarboxylates present as β-hydroxyaspartates (Butler et al. 2021). All α-hydroxycarboxylate siderophores share the characteristic property that the corresponding Fe(III) complexes exhibit photoactivity. This photoactivity is usually accompanied by photooxidation of the siderophore ligand with simultaneous reduction of Fe(III) to Fe(II) (Butler et al. 2021).Tris-α-hydroxycarboxylates, such as achromobactin (Franza et al. 2005), or bis-α-hydroxycarboxylates, like vibrioferrin and rhizoferrin, belong to the minority of α-

hydroxycarboxylates siderophores compared to the plethora of mixed siderophores, which contain at least one α-hydroxycarboxylate group and one of the other two functional groups, like the catecholate containing petrobactin. Remarkably, siderophores produced by marine microbes often exhibit the α-hydroxycarboxylate group and therefore the associated photoactivity of the Fe(III) complex. In addition to this seemingly characteristic trait, marine siderophores also show a certain degree of amphiphilicity. These two structural features dominate the majority of discovered marine siderophores (Butler 2005; Vraspir and Butler 2009). The differences in amphiphilicity arise from the molecular composition of the Fe(III)-binding head group relative to the length of the fatty acid chain. With an increasing fatty acid chain length or number of fatty acid chains those siderophore become more cell-associated. In addition to the property of cell association, the investigation of marinobactins also showed that these amphiphilic molecules tend to self-assemble and form micelles or other vesicles (Martinez et al. 2000). Above the critical micelle concentration of about 50 µM and 75 µM, respectively, both the free siderophore and the corresponding Fe(III) complex form micelles (Martinez et al. 2000).

1.2.2 Stability and photochemistry of Fe(III)-siderophore complexes

The stability of Fe(III)-siderophore complexes is mainly determined by the interaction of the binding group with Fe(III). However, the denticity of the siderophore has also a considerable impact on the stability of the formed complex. As stated in Chapter 1.2.1, most siderophores are hexadentate ligands, meaning that one siderophore displaces six coordinated water molecules during the complex formation. This substitution increases the number of freely moving molecules during the reaction, leading to an increase in entropy. Consequently, the higher the denticity of the siderophore, the higher the stability of the complex when bidentate ligands are compared with the corresponding hexadentate ligands containing the same functional group.

In addition, the lower the denticity of the ligand, the more kinetically labile the ligand, which means that the replacement of the ligand by protons is increasing (Liu and Hider 2002). The proton induced dissociation of hexadentate siderophore complexes is therefore much lower compared to the corresponding bi- or tridentate ligands. At neutral pH hexadentate Fe(III)-siderophore complexes are very stable and show almost no dissociation, resulting in a hindered exchange of Fe(III) between two siderophores. However, the dissociation rate of siderophore complexes increases with decreasing pH, due to the stronger competition by protons. But depending on the functional group, different pH sensitivities of the Fe(III)-siderophore complexes are observed. Catecholate and α-hydroxycarboxylate complexes are more labile under acidic conditions than hydroxamate complexes, due to the higher acid dissociation constant (pK_a) values of the two *o*-phenolate oxygens or alkoxide oxygen compared to the hydroxamate oxygen (Table 1). The second reason for the higher stability of hydroxamate complexes at low pH values is the smaller number of protons substituted during complex formation. In terms of cate-

cholates and α-hydroxycarboxylate two protons compete with one functional group whereas only one proton competes with the coordinated hydroxamate group (Hider and Kong 2010), lowering therefore the proton concentration dependency of hydroxamate complexes.

Fe(III)-siderophore complexes are mainly characterized by their high complex stability but a unique subset of complexes poses another specific feature – photoactivity. All known photoactive Fe(III)-siderophore complexes have the presence of an α-hydroxy acid group in common. Photoactive complexes can be further subdivided into α-hydroxycarboxylates, terminal citrates and β-hydroxyaspartates (Butler et al. 2021). The photoactivity of such complexes relies on the light induced electron transfer from the α-hydroxy acid ligand to the Fe(III), resulting in the reduction of Fe(III) to Fe(II) and the formation of a carboxylic radical complex. The formed radical reacts further to a C-centered radical by releasing CO_2, which in turn undergoes a variety of reactions. Depending on the structure of the intact siderophore, stereochemistry and pH during light exposure, different ketones and hydroxyl photoproducts can be observed (Abrahamson et al. 1994; Butler and Theisen 2010; Glebov et al. 2011; Pozdnyakov et al. 2013).

1.2.3 Biosynthesis and uptake mechanisms of siderophores

Siderophores are produced by different organisms in a vast structural variety but their biosynthesis can be divided into just two major pathways: The non-ribosomal peptide synthetase (NRPS) or the NRPS-independent (NIS) pathway (Barry and Challis 2009; Hider and Kong 2010). Peptide-based siderophores are synthesized by the NRPS-dependent pathway involving the formation of thioester intermediates (Frueh et al. 2008). In contrast to peptide-based siderophores, the biosynthesis of many citrate-containing siderophores and all known phytosiderophores is following the NIS pathway (Schmelz et al. 2009; Hider and Kong 2010).

Not only the biosynthesis and release of siderophores is activated under iron deficiency but also the uptake mechanisms. The most common transcriptional repressor in bacteria is the ferric uptake regulator (Fur) protein (Kramer et al. 2020). Fur limits the expression of genes involved in the iron acquisition by blocking their promoter regions as a function of the iron concentration in the cytosol. The protein itself cannot bind to the promoter regions, but by forming a complex with Fe(II) its conformation changes allowing docking to these specific DNA sequences (Troxell and Hassan 2013). Similar to Fur proteins in bacteria, there are also such transcription factors in fungi and graminaceous plants, typical examples being the group of GATA (Scazzocchio 2000) and bHLH-type factors (Giehl et al. 2009). Several different iron uptake strategies involving siderophores are known. Bacteria use specific receptor proteins to either strip the iron from the siderophore complex or import in the intact complex into the cell where the Fe(III) is released upon reduction. The uptake mechanisms differ drastically between Gram-negative and Gram-positive, since Gram-positive bacteria have no outer membrane. It was also observed

that some siderophores release Fe(III) in the external surface of the cell involving reduction of Fe(III) to Fe(II). Fungi uptake mechanisms of siderophore complexes relay on the presence of membrane potentials and ion gradients, plasma membrane transporters or the release of the iron in the external of the cell membrane (Hider and Kong 2010). The Fe(III)-siderophore uptake strategy in plants is governed by a proton symport mechanism, transporting the phytosiderophore complex across the cytoplasmic membrane where it is reduced and the released Fe(II) is captured by the nicotianamine.

1.2.4 Siderophore ecology

Fe(III)-siderophore complexes can only be taken up if they are located in the direct vicinity of the cell. Therefore, from an evolutionary point of view, it is surprising that the majority of all known siderophores are highly diffusible which could result in the siderophore solubilizing iron but not diffusing back to the producer.. Hence, siderophores could make iron available not only to the producer but also to other individuals with matching receptors (Figure 6).

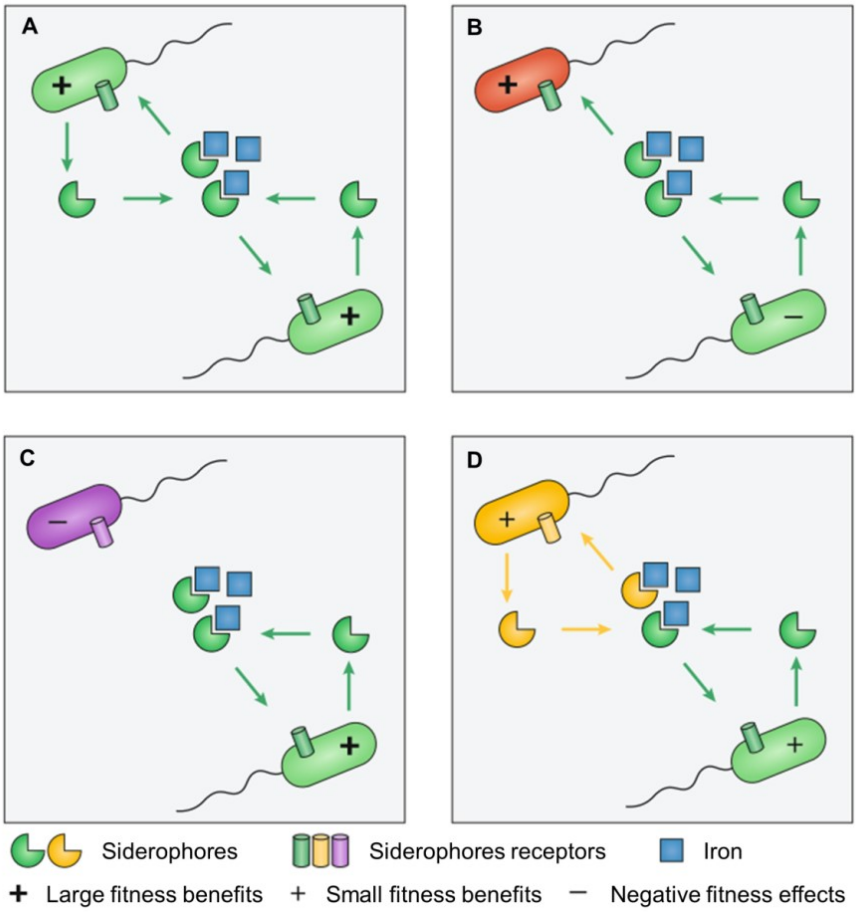

Figure 6. Siderophore-mediated bacterial interaction: (A) Uptake among clonal cells, (B) Cheating, (C) Competition by locking iron away from opponents that lack the matching siderophore receptors and (D) Competition by the segregation of specific siderophores. Figure is adapted from (Kramer et al. 2020).

Alternatively, the binding of iron to siderophores may lead to iron deficiency in microorganisms that lack the appropriate receptor for uptake. In addition, there is the possibility that cheaters, who cannot produce siderophores themselves, gain an evolutionary advantage by ensuring iron uptake and conserving energy through the possession of suitable receptors. Accordingly, siderophores play not only an important role in the composition of microbial communities but also in the interaction of such microbial communities with multicellular organisms. In general it is expected that the environmental concentrations of siderophores increase with increasing cell densities under iron limiting conditions (Völker and Wolf-Gladrow 1999). This positive correlation is underlined by the determined siderophore concentrations in biofilms and rhizospheres (>1 mM), in bulk soil (<10 µM) and in marine waters (<2 nM) (Gledhill and van den Berg 1994; Rue and Bruland 1995; Gledhill et al. 1998; Kraemer 2004; Essén et al. 2006).

1.2.4.1 Habitat: Soil

That the composition and siderophore activity of microbial communities could have an influence on higher organisms became clear when iron deficiency in plants and the counteracting processes in the rhizospheres were studied (Römheld and Marschner 1986; Loper and Buyer 1991). It was shown that microbial siderophores can not only increase the iron bioavailability to plants through mineral dissolution (Kraemer 2004), but can also inhibit the iron supply to plant pathogens and thus provide additional support to the plant (Raaijmakers et al. 1995). This relationship is of global importance and particularly relevant for plants that do not produce siderophores, since one third of the world's farmland is characterized as calcareous soil in which the pH is buffered in the neutral, slightly alkaline range, thus reducing the dissolution of iron-bearing minerals and therefore decreasing its bioavailability (Guerinot and Yi 1994). Soil pH is also thought to influence microbial community composition, as different siderophore classes show different pH stabilities of the corresponding Fe(III) complexes (Hider and Kong 2010). Thus, it has been postulated that catecholate siderophore-producing and metabolizing microorganisms are restricted to neutral or alkaline soils, whereas hydroxamate-producing bacteria or fungi can also thrive under acidic conditions, since such Fe(III)-complexes exhibit higher stabilities under acidic conditions compared to catecholates (Chapter 1.2.2). Regardless of the functional groups, siderophore-based mineral dissolution can be divided into the following three steps: surface complex formation, detachment of the surface metal center and regeneration of the mineral surface (Holmén and Casey 1996; Kraemer 2004). It is assumed that the formation of the oxo-bonds during surface complexation increases the electron density and thus destabilizes the surface metal center (Wehrli et al. 1990). However, the nature and stability of the formed surface complex depends on the functional groups and the denticity of the siderophore as well as on the elemental composition, structural defects and lattice energy of the mineral (Kraemer 2004; Akafia et al. 2014).

1.2.4.2 Habitat: Host

Another example of interaction between microorganisms and multicellular organisms influenced by siderophores are infection processes. Since iron is bound and transported within the host by molecules like nicotianamine and citrate in case of plants (Von Wirén et al. 1999) or proteins like transferrin or ferritin in case of animals (Crichton 2001), pathogens have evolved the biosynthesis of strong-binding siderophores like enterobactin to scavenge iron from host tissues. In the course of evolution, mammals have developed infection-fighting mechanisms in addition to the aforementioned protein classes that reduce the availability of iron to pathogens in the first place (Ratledge and Dover 2000). For example, mammals produce the protein siderochelin, which is able to bind various Fe(III)-complexes of tris-catechols, as an infection response to prevent iron supply to the parasite (Flower et al. 2000).

1.2.4.3 Habitat: Seawater

The largest habitats where iron deficiency is prevalent, and therefore iron complexation with organic ligands like siderophores is of particular importance, are the world's oceans (Vraspir and Butler 2009). In particular, the subarctic Pacific, the equatorial Pacific and the Southern Ocean are characterized by high nutrient concentration but low levels of chlorophyll or phytoplankton growth, presumably caused by low iron concentration (de Baar et al. 1995; Behrenfeld et al. 1996). The evidence for this conclusion and the ultimate confirmation of the so-called iron hypothesis was provided by ten large-scale fertilization experiments in which Fe(II) solutions were introduced into the three major high nutrient low chlorophyll (HNLC) regions on a hundred kilogram scale (Martin et al. 1994; Coale et al. 1996, 2004; Boyd et al. 2000, 2004; Gervais and Riebesell 2002; Tsuda et al. 2003; Hoffmann et al. 2006; Roy et al. 2008). Subsequently to the addition of iron, chlorophyll concentration increased in all experiments. As chlorophyll concentration increased, an increase in weak and strong ligand concentrations was also observed (Rue and Bruland 1997; Hogle et al. 2016). Those strong Fe(III)-ligands showed a similar affinity to Fe(III) compared to siderophores (Rue and Bruland 1995). The increase in siderophore-like ligands seemed to be counterintuitive since microbial siderophore production is expected to be downregulated under iron-replete conditions. However, Rue and Bruland emphasized that this observation could be interpreted as a conditioned response of the ambient iron-deficient microbial population to an iron input and therefore as a link between ligands and phytoplankton growth. But since eukaryotic phytoplankton is not thought to be able to produce siderophores themselves or to take up Fe(III)-siderophore complexes, but show genomic evidence for ferrireductases and associated Fe(II) transporters (Maldonado and Price 2001; Morel and Price 2003; Kustka et al. 2007; Kazamia et al. 2018; Coale et al. 2019), the relationship between phytoplankton and siderophore-producing bacteria has become the focus of ecological chemistry in recent years.

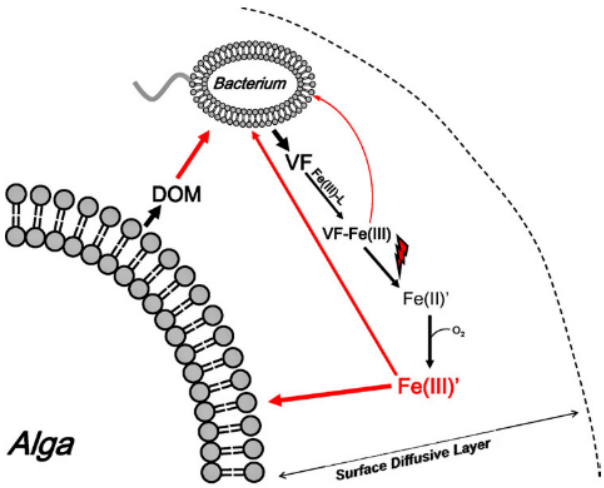

Figure 7. Schematic display of bacterial-algae mutualism based on the siderophore vibrioferrin and its photolabile Fe(III)-complexes. Figure is taken from (Amin et al. 2009a).

A particular example of the postulated mutualism between phytoplankton and siderophore-producing bacteria is the vibrioferrin system (Figure 7). Vibrioferrin is an α-hydroxycarboxylate siderophore (Yamamoto et al. 1992, 1994) and therefore forms photolabile Fe(III)-complexes (Amin et al. 2009b). This property suggests that vibrioferrin in the dark only supports iron uptake by microorganisms that have a specific and light-independent uptake mechanism (Amin et al. 2012). However, when the complex is exposed to sunlight, photolysis of the vibrioferrin-iron complex occurs within minutes, releasing inorganic soluble iron. This labile form of iron is then rapidly taken up by the bacteria and also the phytoplankton host, which releases dissolved organic carbon (DOC) to support bacterial growth (Amin et al. 2009a; Seymour et al. 2017). This mutualistic coexistence of bacteria and phytoplankton can be summarized as the carbon-for-iron hypothesis.

1.2.5 Alternative functions of siderophores and their applications

In addition to their best-known role in iron uptake processes, siderophores also play a central role in other mechanisms such as toxic metal sequestration, signaling or antibiotic activity (Kramer et al. 2020). Siderophores bind a wide variety of toxic heavy metals in addition to iron. However, the resulting complexes are sterically very distinct from Fe(III) compounds that they are not transported into the cells (Braud et al. 2010; Schalk et al. 2011). This complexation thus reduces the toxicity of such metals, not only for the siderophore producers, but also in general and can be described as a cooperative behavior (O'Brien et al. 2014). Siderophores can not only directly help with iron uptake, but also indirectly by acting as a signal and regulating further siderophore production as well as influencing other processes that are also involved in iron uptake (Lamont et al. 2002). This signaling effect of siderophores can be observed not only within a species but also across species (Guan et al. 2001; Grandcham et al. 2017).

As already listed at the beginning of this chapter, there are also siderophores, namely sideromycins, which are characterized by their antibiotic activity. These compounds consist of siderophore backbones and a bactericidal unit, which act as a “Trojan Horse” (Budzikiewicz 2005). The specificity and efficiency of this class of antibiotics is largely determined by the presence of the corresponding siderophore receptor (Braun et al. 2009; Sassone-Corsi et al. 2016). Based on the properties of those naturally occurring siderophore antibiotics, a number of pharmaceuticals have been developed. In particular, some progress has been made in the fields of “Trojan Horse” antibiotics, metal chelate therapy, cancer therapy, diagnostics and vaccine systems based on siderophores and their metal compounds (Swayambhu et al. 2021). The “Trojan Horse” antibiotics and some cancer therapy drugs either relay on the insertion of metal ions similar to Fe(III) like Al(III) and Ga(III) via siderophore uptake mechanism (Gokarn and Pal 2017; Telfer et al. 2017) or on a structural feature added to the siderophore backbone, similar to the naturally occurring sideromycins (Liu et al. 2016).

1.3 Chemical detection, characterization and identification of siderophores

1.3.1 Assays

The most common and ‘universal’ functional assay for the detection of siderophores in crude liquid samples is the CAS assay. This assay was developed by Schwyn and Neilands in 1987 and is based on the high affinity of siderophores for Fe(III) (Schwyn and Neilands 1987). The dye used for this test is a ternary complex composed of the components chrome azurol S, Fe(III) and the surfactant hexadecyltrimethylammonium bromide (HDTMA). If a strong complexing agent is added to this dye, Fe(III) is removed from the ternary complex, leading to a change in color from blue to orange. This test has the advantage that the net chelating activity can be determined independently of the structure or number of different ligands in a sample. The color change thus provides general information about the activity of strong Fe(III) complexing agents. With this assay Fe(III) ligand activity can be monitored at concentrations down to 2 µM by using a conventional 1 cm path length spectrometric cell. However, this test also has several disadvantages that affect the application or require prior sample preparation. First, the test only works in a narrow pH range of about pH 5.6 - 6.8 (Schwyn and Neilands 1987). If the pH is outside this range, the ternary complex decomposes, resulting in a color change from blue to purple or yellow. Second, this test is also susceptible to weak ligands, such as phosphate or citrate, which are regularly used in growth media. The CAS assay is only capable of tolerating phosphate concentrations below 20 mM. To avoid such drawbacks, samples have to be buffered and chelating agents in growth media have to be substituted. As stated, the CAS assay is the most common and universal assay applicable to siderophores. However, this test does not allow any further information except for the net chelating activity of the sample. To distinguish which type of siderophore is present in the sample different specific assays need to be performed. To de-

tect siderophores containing hydroxamate groups as Fe(III) binding sides, the Atkins and Csaky assay is used. The Atkins assay relies, similar to the CAS assay, on the strong affinity of siderophores towards Fe(III). But in contrast to the CAS assay, the Atkins assay detects the red color of the formed Fe(III)-hydroxamate complexes. To achieve the formation of Fe(III) complexes the crude sample is mixed with $Fe(ClO_4)_3$ in $HClO_4$. If hydroxamates are present in the sample the change in color is immediate. The detected color of the Fe(III) complex formed depends on the hydroxamate-type siderophore present. This means that the wavelength of maximum absorption changes from siderophore to siderophore. Furthermore, it has to be taken into account, that the added assay solution interacts with remaining growth medium components leading to a yellow coloration in the blanks, suppressing the overall sensitivity of this assay (Atkin et al. 1970). The second hydroxamate specific colorimetric assay, the Csaky assay, does not target the Fe(III) binding ability of siderophores. In contrast to the Atkins assay, the Csaky assay involves hydrolysis of the hydroxamate containing siderophore, followed by oxidation of hydroxylamine and formation of nitrite. The occurring nitrite is detected using sulfanilamide and *N*-(1-naphthyl)ethylendiamine, leading to the formation of a strongly colored azo-complex (Csaky 1948; Glllam et al. 1981; Velasquez et al. 2011).

Colorimetric assays, namely the Arnow and Rioux Assay, are performed to detect catecholates (Arnow 1937; Rioux et al. 1983). The Arnow test, like the hydroxamate assays, is not based on the ligand property of this functional group. The assay is conducted by adding HCl and nitrite-molybdate reagent to the sample solution, followed by the addition of NaOH after 5 min. The observed color change from colorless over yellow to red or pink is based on the nitration of the aromatic ring, present in catecholates, and the deprotonation under alkaline conditions. The Rioux assay is based on the reducing capabilities of the catecholate group. Under acidic conditions and excess of Fe(III), catecholates are oxidized to *o*-benzoquinone and Fe(III) is reduced to Fe(II). The Fe(II) produced is detected by complexation with 1,10-phenanthroline or specific Fe(II) ligands.

1.3.2 Siderophore identification and structural elucidation

After the presence of siderophores in a sample solution is confirmed via liquid assays, further experiments are carried out to verify the Fe(III)-complexing properties as well as to elucidate the structure of the possible ligand. Using a mass spectrometer, equipped with a soft ionization source like the electron spray ionization source (ESI), allows the detection of the free as well as the corresponding metal complexes of the siderophore. Depending on the resolution of the used mass spectrometer, exact masses of the different ions can be measured and matching molecular formulas are suggested. In addition to the measured masses, isotopic patterns are also observed. Especially the isotopic pattern of iron facilitates the detection of siderophores (Baars et al. 2014; Baumeister et al. 2018; Aron et al. 2022). Iron occurs naturally as four different stable

isotopes with the following abundance: ^{54}Fe (5.845%), ^{56}Fe (91.754%), ^{57}Fe (2.119%) and ^{58}Fe (0.282%) (Hoffmann 2005). Due to the low abundance of ^{57}Fe and ^{58}Fe, the *Δm/z* of 1.9954 between ^{54}Fe and ^{56}Fe in combination with an intensity ratio of 6.37/100 (De Hoffmann and Stroobant 1991; Taylor et al. 1992) is the characteristic feature for the presence of an iron containing molecule. Mass spectrometry in combination with liquid chromatography (LC-MS), is capable of detecting different siderophores simultaneously since interfering compounds are separated and signal suppression decreased (Gledhill 2001; Boiteau et al. 2019a). In addition, LC-MS measurements allow additional verification of Fe(III)-complexes via retention time comparison (Figure 8).

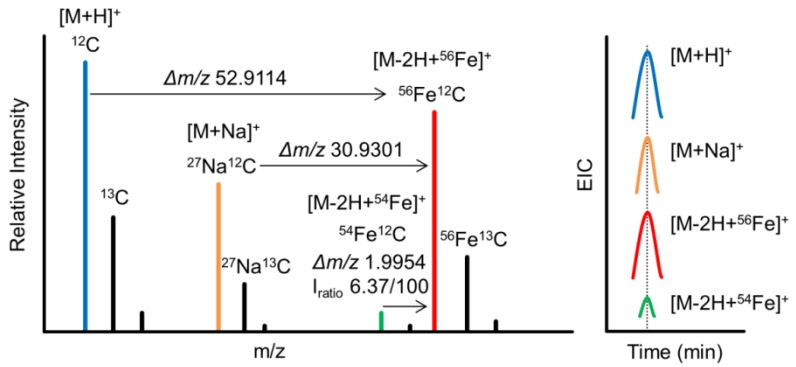

Figure 8. Schematic representation of the mass spectrum of an iron complex and the corresponding coherence in the chromatographic behavior of the different species. Figure is adapted from (Baars et al. 2014; Aron et al. 2022).

False positives showing the characteristic *Δm/z* and intensity ratio can be detected and excluded via the missing coherence between chromatographic and isotopic features (Baars et al. 2014; Aron et al. 2022), meaning that the extracted ion chromatograms (EICs) of both iron complexes, ^{54}Fe and ^{56}Fe, have to show chromatographic peaks at the same retention time with the same peak shape. In addition, the corresponding free ligand is detected at the same retention time than the iron complexes, either since the free ligand is present in the sample and partly complex formation occurs after separation on the LC or already present complexes dissociated in the source during ionization. Novel computational tools like the ion identity molecular networking approach (Schmid et al. 2021), similar to CAMERA (Kuhl et al. 2012) and RAMClust (Broeckling et al. 2014), are not only capable of linking the iron-bound ions to the free ligands or to adducts that occur during ionization but also to check for fragmentation similarity (Aron et al. 2022). Information about structural similarity is gained using mass spectrometers with collision cells that are able to perform collision induced fragmentation experiments (MS^2). These experiments provide not only information about the structure of the precursor ion but also additional confirmation about the presence of iron complexes, since the iron isotope pattern is still observable after fragmentation. Masses that fulfill all chromatographic and isotopic requirements are compared with available siderophore data bases in terms of exact masses of the precursor ions, fragments and neutral losses (Lehner et al. 2013; Baars et al. 2014; Bundy et al. 2018).

Iron binding capabilities can also be investigated using methods such as inductively coupled plasma-mass spectrometry (ICP-MS) (Boiteau et al. 2013; Boiteau and Repeta 2022), X-ray fluorescence spectroscopy (XRF) (Aschner et al. 2017), UV-visible absorption spectroscopy and nuclear magnetic resonance (NMR) spectroscopy (Neilands 1995). NMR is also a powerful tool for further structural elucidation, especially if no matches for any fragments or neutral losses were obtained. However, NMR requires large quantities of analyte and additional purification prior to analysis to meet the instruments threshold and to overcome signal overlapping. In addition, the analysis of Fe(III)-siderophore complexes is not possible due to the paramagnetic properties of iron (Hoffmann 2005), which is therefore often replaced by Ga(III) (Stephan et al. 1993).

1.3.3 Extraction and detection of siderophores in natural samples

The detection of siderophores as well as the investigation of their distribution in natural habitats like ocean waters is often complicated due to their low concentrations in such complex samples. Seawater as a sample matrix is defined by high salt concentration and a plethora of dissolved organic compounds in concentrations ranging from fM up to mM levels. To meet thresholds for instrumental analysis or even siderophore assays like CAS, a concentration and desalting step must be performed from large volumes. The most common techniques to achieve concentration of siderophores from aqueous saline matrices are solid phase extraction (SPE) approaches using different types of sorbent materials. However, the salinity of seawater and complexity of dissolved organic matter often lead to reduced recoveries of the analytes and highly complex extracts hampering easy identification of single compounds. Nonpolar sorbents like polystyrene-divinylbenzene polymers or bonded silica are one class of sorbents regularly used for the extraction of siderophores from complex aqueous samples (Mills et al. 1982; Donat et al. 1986; Elbaz-Poulichet et al. 1994; Macrellis et al. 2001; Mawji et al. 2011; Velasquez et al. 2011; Waska et al. 2015). Especially, the non-ionic polystyrene adsorbent XAD-16 has become the standard sorbent for the isolation of siderophores from laboratory cultures (Trick 1989; Reid et al. 1993). The hydroxylated polystyrene-divinylbenzene polymer ENV+ is regularly used for the extraction of siderophores from natural waters (McCormack et al. 2003; Mawji et al. 2008; Boiteau et al. 2013; Manck et al. 2021). Although both of these sorbent types, polystyrene-divinylbenzene polymers and bonded silica, are hydrophobic, their extraction mechanisms differ. Extraction with bonded silica sorbents, especially C18, relies mainly on the retention via van der Waals forces and hydrogen bonding. Retention on polystyrene polymers, such as XAD-16, ENV+ or PPL, occurs not only via van der Waals forces but also via π-π interactions between the aromatic structures of the analytes and the sorbents. This leads to a better retention of aromatic and often more polar compounds on those crosslinked polystyrene polymers, compared to bonded silica sorbents (Ferrer and Barceloè 1999). The extraction efficiency of siderophores with hydrophobic sorbents depends also on the siderophore speciation, meaning if the sidero-

phore is present as the free ligand or as the corresponding metal complex. The polarity of the free ligand compared to its Fe(III)-complex often differ causing different chromatographic retention behaviors. In general, siderophores are retained best on hydrophobic resins at acidic conditions, due to the protonation of the functional groups present in the siderophores structure. Ion exchange resins have also been investigated as a sorbent type for the extraction of siderophores. In case of the two model siderophores rhodotorulic acid and DFOB only poor retention effectiveness from UV-treated seawater were observed (Macrellis et al. 2001). However, purification of the catecholate type siderophore corynebactin from bacterial culture supernatants was achieved by sequential anion-exchange chromatography (Zajdowicz et al. 2012). All of these techniques, reversed-phase as well as ion exchange approaches, often show poor recoveries as well as no specific enrichment of siderophores, leading to concentrated yet very complex extracts, since the extraction is based on rather general properties like polarity or charge. Furthermore, it is assumed that by using nonpolar resins for the extraction of siderophores from aqueous natural samples, the extraction efficiency for nonpolar siderophores is higher than for polar ones – creating a possible bias in the distribution of siderophores in natural habitats with a possible overrepresentation of nonpolar ligands. Nonetheless, with the currently available methodologies, known siderophores are detected in complex environmental samples like seawater extracts (Boiteau et al. 2016, 2019b; Bundy et al. 2018; Manck et al. 2021). The identification of siderophores in such extracts remains difficult despite the use of ultra-high-resolution mass spectrometry (Boiteau et al. 2019a). In some cases, it was possible to detect unknown ligands (Velasquez et al. 2011; Boiteau et al. 2019b) by examining the characteristic Fe isotope fingerprint and associated chromatographic behavior (Baars et al. 2014), but this approach is limited only to those siderophores whose Fe(III)-complexes are stable under the chromatographic conditions used and do not dissociate during ionization. Non-targeted reversed-phase LC-ESI-MS analysis of small molecules like siderophores usually involve low pH, high percentages of organic solvent and low iron concentrations, which lowers complex formation (Waska et al. 2016; Aron et al. 2022). Especially catecholate type Fe(III)-siderophore complexes undergo hydrolysis at low pH and are thus undetectable (Loomis and Raymond 1991), as confirmed for petrobactin, whose Fe(III)-complexes were not detected in natural extracts while the apo-form (apo = unbound ligand) of petrobactin was (Manck et al. 2021). Therefore, siderophore analysis in environmental extracts is often based on database-driven targeted analysis using high-resolution soft-ionization mass spectrometry, excluding possible new siderophores whose corresponding complexes were not detected under applied conditions or which show no MS/MS similarity to already known ligands. One solution to the problem of dissociating Fe(III)-complexes during soft ionization is using split-flow LC approaches which offer innovative strategies for simultaneously analyzing metal content (ICP-MS) and structures (ESI-MS) (Boiteau et al. 2016). However, this approach requires expensive and specialized equipment as well as customized set-ups. Another possible solution approach to overcome insufficient complex for-

mation is the recently published native ESI-MS method with post-column pH adjustment and metal infusion (Aron et al. 2022).

1.3.3.1 Untargeted identification of siderophores

Thus, an untargeted approach to detected and quantify siderophores in natural samples is still lacking that does not rely solely on the identification of the iron isotope pattern in complex chromatograms, but minimizes the overall sample complexity, and thus automatically the number of false positives, in other ways, allowing the simplified identification of unknown siderophores in environmental extracts.

To reduce the sample complexity of natural extracts, additional purification steps need to be performed prior to analysis. However, subsequent reduction of complexity of such extracts may not be possible because siderophore concentrations are below the detection limit of the CAS assay and thus no fractionation by ligand activity can be performed. The purification of seawater extracts is a special case. The extracted dissolved organic matter (DOM) can no longer be separated chromatographically using established techniques (Sandron et al. 2015), which leads to an “unresolved hump” in LC-MS analyses (Sandron et al. 2018). This problem demonstrates the need to adjust the SPE step to keep sample complexity as low as possible from sampling to analysis, while still ensuring high recoveries of the targeted analyte class.

Immobilized metal affinity chromatography (IMAC) is one technique for a selective extraction, targeting the functional groups present in chelating molecules. IMAC was developed as a purification technique for recombinant histidine-tagged (His-tag) proteins (Porath et al. 1975) but it was shown that the underlying affinity principle can be transferred to the extraction of a variety of different ligands even from marine waters (Ross et al. 2003; Gu and Codd 2012; Nixon and Ross 2016). The retention of ligands on IMAC resins is caused by the interaction of the chelating groups with free binding sites of the immobilized metal cation. In case of siderophores, this purification approach seems to be limited to hydroxamate-type siderophores or to siderophores not exceeding a certain affinity towards the immobilized cation (Ni(II) or Fe(III)) (Braich and Codd 2008; Ejje et al. 2013; Gu and Codd 2015), since the catecholate-type siderophore bacillibactin and the mixed-type siderophore pyoverdine were not concentrated using IMAC (Heine et al. 2017; Li et al. 2018). In case of bacillibactin it was observed that only the corresponding monomer, containing only one catecholate group, was retained and eluted. Another drawback of the IMAC approach is the need to adjust the pH prior to adsorption, limiting its potential to mirror the actual conditions since any addition could render the natural ratio of complexed to free ligands in the sample. Due to these disadvantages, IMAC is not suitable for the targeted

extraction of all siderophore species from environmental samples and the representation of the natural state without bias.

However, since the affinity chromatography approach holds promising advantages for analyzing complexed samples by reducing the amount of interfering compounds prior to analysis, there continues to be great interest in a less sensitive affinity chromatography method. Such a method should, above all, be able to exploit the characteristic high affinity of siderophores for metal cations, but be sufficiently robust that the affinity binding sites are even more tightly bound to the sorbent, thus ensuring siderophore retention. A possible candidate for such a siderophore-compatible affinity chromatography sorbent could be titanium dioxide (TiO_2), since this material forms very stable surface complexes with a number of functional groups including the typical siderophore metal binding groups. TiO_2 is also characterized by its chemical stability and insolubility under a variety of harsh conditions. Since TiO_2 appears to combine both necessary properties, formation of stable surface complexes and resistance to dissolution, it can be hypothesized that this material is suitable for the targeted extraction of siderophores.

1.4 Titanium dioxide

The transition metal titanium is the ninth most abundant element in the Earth's crust (Emsley 1989). Most of the titanium occurs naturally in the Ti(IV) oxidation state in three different oxide forms, namely rutile, anatase and brookite (Jones 2001; Chen and Mao 2007; Kabata-Pendias and Mukherjee 2007) or in mixed oxides like ilmenite ($FeTiO_3$) (Correns 1969). Rutile, anatase and brookite (Figure 9) can all be described as titanium dioxides (TiO_2) but differ in parameters like crystal structure and density (Samsonov 1982; Esch et al. 2014). TiO_2 is a white, chemically and biologically inert solid with a variety of technically interesting properties (Sundgren et al. 1986; Jones 2001; Kang et al. 2019).

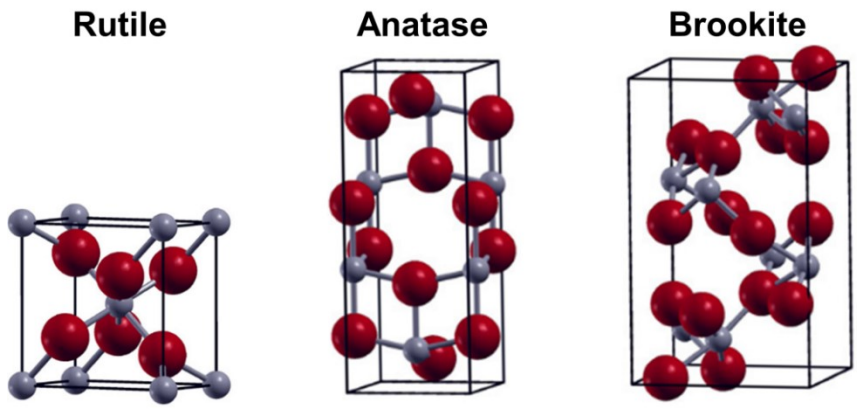

Figure 9. The primitive cells of the three naturally occurring TiO_2 modifications rutile, anatase and brookite (Ti^{4+}in grey, O^{2-}in red). Figure is adapted from (Esch et al. 2014).

1.4.1 Applications of TiO_2

Due to its brilliant color and outstanding opacity, nano-TiO_2 is commonly used as a pigment in a variety of different products ranging from paints and lacquer to cosmetics and food products (Dunford et al. 1997; Phillips and Barbano 1997; Diebold 2003; Yuan et al. 2005). Due to the wide field of pigment application and high demand of such products, the annual production of TiO_2 pigments is estimated to be 8.4 million tons worldwide (2021) (U.S. Geological Survey 2022). But in the last two years laws were changed leading to stricter regularities concerning the use of TiO_2 as the food additive E171. After France and Switzerland banned E171 from all food products, the EU adapted these regulations in May 2021, changing the status of E171 to unsafe (Younes et al. 2021). In contrast, the use of TiO_2 in pharmaceuticals is still permitted.

Besides the widespread use as a color agent, TiO_2 is also used in heterogeneous catalysis. In addition to vanadate, mixed metal oxide catalysts for selective oxidation reactions often contain TiO_2 (Sambi et al. 1996; Biener et al. 1999; Guo et al. 1999). TiO_2 also has applications in electrical engineering as polycrystalline TiO_2 or as a ceramics component because of its high non-linearity between current density and electric field. This characteristic allows it to be used as a varistor to suppress large transient voltages (Sambrano et al. 1997). Furthermore, TiO_2 plays an important role in medical technology. Bone implants are regularly manufactured out of titanium since the thin surface oxide layer provides corrosion resistance and enhances the biocompatibility (Sittig et al. 1999; Curtin et al. 2018).

However, the properties of TiO_2 that caused most attention are its photochemical characteristics. Since the discovery of photocatalytic splitting of water on a TiO_2 electrode (Fujishima and Honda 1972) extensive research was conducted in this field, which has led to many applications in different areas ranging from photocatalytics and photovoltaics to photo-/electrochromics and sensors (Hagfeldt and Grätzel 1995; Linsebigler et al. 1995; Grätzel 2001; Diebold 2003). Photocatalytic oxidation or photo-assisted degradation of organic molecules is based on the formation of radical oxygen species upon the irradiation of TiO_2 with UV light. These reactive species attack any adsorbed molecule and lead to the complete decomposition. This mechanism is used in areas like wastewater treatment, disinfection or self-cleaning coatings (Mills et al. 1993; Choi et al. 2010; Banerjee et al. 2015; Laxma Reddy et al. 2017). In general, TiO_2 shows a low quantum yield in the photochemical conversion of solar energy. But by surface functionalization of TiO_2 with photosensitive dye molecules the efficiency of TiO_2-based photovoltaic or water-splitting photoelectrochemical cells is significantly increased (O'Regan and Grätzel 1991; Zhang and Cole 2015; Materna et al. 2017). To ensure high endurance and long-lasting efficiency of such dye-sensitized cells the immobilization of dye molecules on the semiconducting metal oxide surface is crucial.

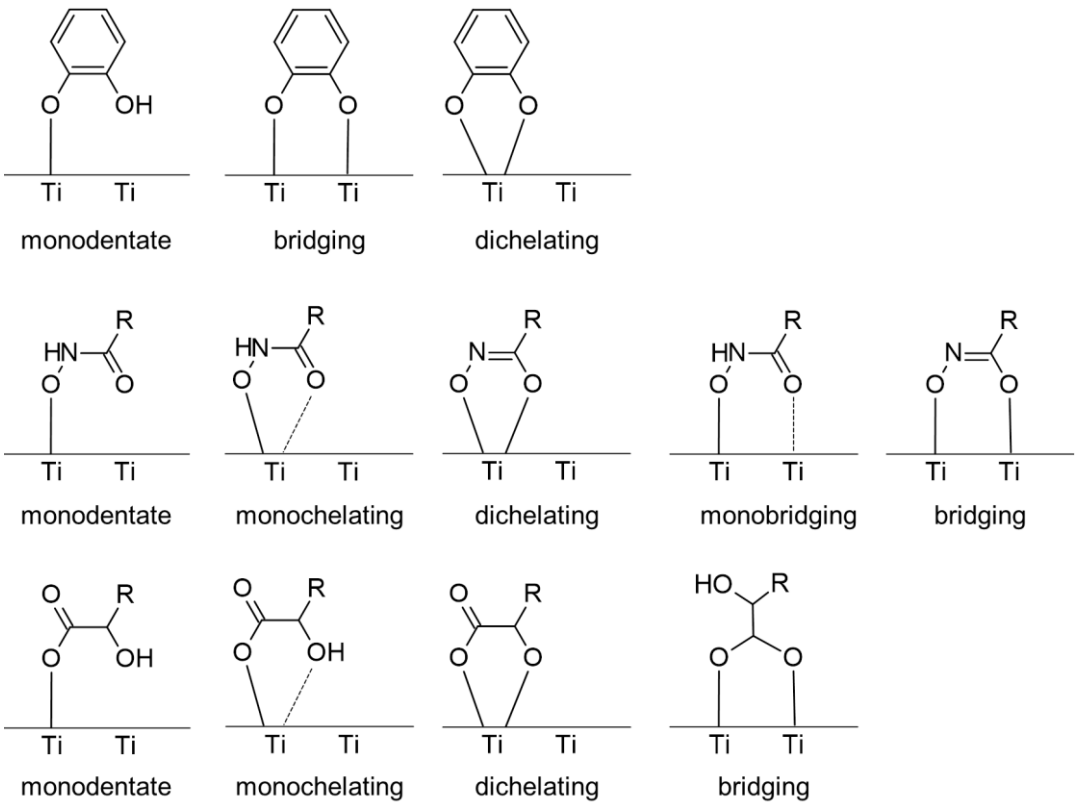

Figure 10. Possible binding modes of anchoring groups like catechols, α-hydroxycarboxylic acids and hydroxamic acids on TiO_2. Figure partly adapted from (Finkelstein-Shapiro et al. 2016; Materna et al. 2017; Christ et al. 2022)

The immobilization of dye molecules is achieved by the addition of an anchoring group to the photoactive dye molecule. In the last years a variety of different anchoring groups were investigated, ranging from cyanoacrylic and phosphonic acids to siderophore typical functional groups like carboxylic acids, hydroxamic acids and catechols (Tulevski et al. 2004; McNamara et al. 2010; Brennan et al. 2013; Koenigsmann et al. 2014; Zhang and Cole 2015; Materna et al. 2017). The binding modes of how such anchoring groups are bound to TiO_2 have been investigated extensively (Figure 10). Although surface functionalization is facilitated via different mechanisms like electrostatic interactions, hydrogen bonding, hydrophobic interactions, van der Waals forces or physical entrapment (Kalyanasundaram and Grätzel 1998), most of the anchoring groups used for the preparation of dye sensitized solar cells (DSSC) are covalently bound to the metal oxide layer (Zhang and Cole 2015). It was shown that the immobilization of dye molecules with carboxylic acid anchoring groups is only stable under acidic aqueous conditions (pH < 4) (McNamara et al. 2009, 2010; Martini et al. 2013). The water-stability of carboxylic anchoring groups is decreasing at higher pH leading to rapid hydrolysis and the desorption of the dye molecule from the metal oxide surface (Brennan et al. 2013). In contrast, hydroxamic acids are classified as one of the most robust anchoring groups under aqueous conditions and almost independent of pH (pH range 2-11 investigated) (McNamara et al. 2009, 2010; Materna et al. 2015). Catechol containing dendrimers were used for the functionalization of TiO_2 nanoparticles and the formed covalent bonds between these functional groups and Ti surface ions were so

stable that by the presence of three catechol groups per dendrimer the observed adsorption was irreversible (Gillich et al. 2011). Over the past three decades, the surface chemistry of TiO_2 has been studied not only in terms of its unique photochemical and catalytic capabilities, but also in terms of its remarkable chromatographic properties. In particular, the affinity chromatography approach for the purification of phosphocompounds has achieved special attention and is a promising indication for the targeted extraction of other analytes with oxygen-rich functional groups, such as those present in siderophores.

1.4.2 Usage as solid phase material

TiO_2 can act as both an anion exchanger at low pH and a cation exchanger at high pH. Ion exchange properties of TiO_2 originate from the presents of hydroxyl groups and their protonation state according to the pH of the surrounding solution (Nawrocki et al. 2004). The pH at which these ion exchange properties change is the isoelectric point. At this pH, the total surface charge is neutral or in the case of nanoparticles, the ζ-potential is approximately 0 eV. The isoelectric point depends on the type of synthesis and morphology of the TiO_2 and is usually between pH 5 and 6 (Dobson et al. 1997; Suttiponparnit et al. 2011; Nduwa-Mushidi and Anderson 2017). TiO_2 also shows ligand exchange properties, caused by the affinity for electron pair donating compounds of the unsaturated Lewis acid sites on its surface (Xu et al. 2016). The strength of the affinity of a Lewis bases or ligands towards the TiO_2 surface depends on the electron density and polarizability of the base. The lower the polarizability and the higher the electron density, the stronger the interaction between TiO_2 and Lewis base (Nawrocki et al. 2004; Xu et al. 2016). TiO_2-based materials have been used in analytical chemistry using various strategies and techniques, including high-performance liquid chromatography (HPLC), solid-phase extraction (SPE), magnetic solid-phase extraction (MSPE), and solid-phase microextraction (SPME) (Matsuda et al. 1990; Larsen et al. 2005; Calvano et al. 2009; Ma et al. 2012). With the first description of the selectivity of phosphate groups for TiO_2 a lot of interest was drawn to this research topic (Kawahara et al. 1989; Matsuda et al. 1990; Ikeguchi and Nakamura 1997, 2000). But especially with the work of Pinkse et al. in 2004 the interest in TiO_2 based chromatographic techniques grew exponentially. They showed that by using TiO_2 as a solid phase material selective isolation of femtomolar amounts of phosphopeptides from proteolytic digests can be achieved. Following studies have investigated the potential of TiO_2 as an applicable solid-phase material for a variety of different substances ranging from other phosphocompounds, glycopeptides, pesticides, flavonoids and hormones to polycyclic aromatic hydrocarbons and heavy metal ions like Cr(III, IV) and As(III, V) (Kim et al. 2004; Liang et al. 2006; Liang and Liu 2007; Calvano et al. 2009; Yan et al. 2010; Kurepa et al. 2014; Zhou and Fang 2015; Qiao et al. 2015; Zhang et al. 2016; Khan et al. 2017; Mancera-Arteu et al. 2020). In comparison to other metal oxides like ZrO_2, CeO_2 and Al_2O_3, TiO_2 poses a pH independent adsorption chemistry for some analytes like cis-diols (Wang et al. 2013, 2014b), suggesting the

formation of covalent bonds similar to the anchoring groups used in surface functionalization of TiO_2. Another feature of TiO_2 is the hampered dissolution by organic ligands in comparison to other metal oxides or minerals. The example of the siderophore pyoverdine is underlining that although adsorption on TiO_2 is occurring (McWhirter et al. 2003), no dissolution of Ti nor the presence of Ti(IV)-pyoverdine complexes were observed in solution (Jones 2017). In contrast to these findings it is well known that pyoverdines promote the weathering of iron bearing minerals (Ferret et al. 2014). The chromatographic applications listed above are all aimed at isolation from concentrated samples with small volumes, which is possible with commercially available TiO_2 microspheres and HPLC columns. However, pure TiO_2 ready to use sorbent materials for the processing of large sample volumes are not available.

1.5 Aims and objectives of this thesis

The overall aim of this thesis was to simplify the identification of siderophores as well as to overcome different drawbacks in terms of their detection and the interpretation of their natural distributions. Siderophore identification is mainly based on the recognition of the iron isotope pattern in combination with chromatographic coherence or data base driven search algorithms. Therefore, their identification in natural samples is generally limited to those siderophores whose iron complexes are detectable, or to siderophores already identified and included in data bases. To overcome these limitations and to reduce interferences by coeluting substances, it is necessary to develop a new method that does not rely solely on the detection of the iron isotope pattern and that reduces the sample complexity prior to analysis. This new method must target the characteristic functional groups of siderophores to ensure their specific purification. Since TiO_2 is known to form stable bonds with such functional groups, causing the adsorption of siderophores, this work investigated if this material is suitable for the specific separation of siderophores from different complex matrices.

As a first step of this thesis, Chapter 2 investigated if siderophores are extractable from bacterial cultures using commercially available TiO_2 nanoparticles. Although much information is already available on the adsorption of characteristic functional groups of siderophores on TiO_2, the conditions leading to their quantitative elution have not yet been studied in detail. The main object of this chapter was therefore to investigate the necessary elution conditions and to provide the proof of concept that TiO_2 is suitable for the targeted extraction of hydroxamate-type siderophores.

After demonstrating that by means of disperse solid phase extraction, using TiO_2 nanoparticles, hydroxamate siderophores are extractable from bacterial cultures, the challenge in Chapter 3 was to transfer this approach to the column format to allow extraction of larger volumes and

faster processing. Thus, the first objective of this chapter was to obtain a novel TiO_2 sorbent, with the particle size distribution required for SPE cartridges. The second objective was to investigate whether this new affinity chromatography approach is suitable for all types of siderophores and what adjustments are required to ensure targeted extraction and elution depending on the functional group. In summary, this chapter aimed to present a TiO_2 affinity chromatography (TDAC) protocol with manually packed SPE cartridges for the targeted purification of all siderophores independent of their functional groups from complex saline sample matrices.

With the general method development of TDAC completed, Chapter 4 investigated if this method is capable of extracting siderophores from seawater. As a part of the marine ligand pool, siderophores occur in pM-nM concentrations in the oceans and it is known that their extraction and concentration with conventional sorbents only reflects their natural distribution to a limited extent. However, since deciphering the composition of the marine iron ligand pool is central to understanding the iron cycle and thus the global carbon cycle, there is an ongoing need for new methods that can mirror the natural ligand occurrence. To overcome extraction biases and to provide high recoveries, the main objective of Chapter 4 was to investigate how certain extraction parameters and matrix compositions affect the performance of TDAC and if it is applicable for the needed large volume extraction of siderophores from crude filtered seawater.

To conclude this thesis, Chapter 5 investigated if siderophores can be specifically separated from marine DOM using TDAC. DOM extracts present a particular analytical challenge, as they are among the most complex samples and no chromatographic method alone allows sufficient separation of such samples, resulting in co-elution and signal suppression. Since certain DOM constituents may interact with TiO_2, the first objective of this chapter was to determine adsorption conditions that would allow depletion of DOM relative to siderophores and thus facilitate identification of these analytes in the TDAC eluate. The second objective of this chapter was to use the adapted TDAC protocol to reprocess DOM extracts from cruise HE533 to the Arctic fjords of Norway to gain new insights into the composition of the ligand pool and the distribution in the fjord systems.

2. Siderophore purification with titanium dioxide nanoparticle solid phase extraction

In this chapter, I reported the proof-of-concept of a novel TiO_2 based extraction method for the purification of hydroxamate siderophores. The developed method was published describing the key elements of adsorption and especially desorption, underlining the unique separation approach which this technique offers. With this method we were not only able to purify the model siderophore desferrioxamine B from complex samples but also to identify novel ferrioxamine-type siderophores from crude bacterial culture supernatants. In this publication, I was responsible for the development of the extraction method, the execution and evaluation of LC-HRMS measurements, isolation and cultivation of bacteria cultures, as well as visualization and writing of the original draft.

Siderophore purification with titanium dioxide nanoparticle solid phase extraction

Philipp H. Egbers,[a] Tilmann Harder,[a,b] Boris P. Koch,[b,c] Jan Tebben[b]

a. University of Bremen, Faculty of Biology and Chemistry, Leobener Straße 6, 28359 Bremen, Germany.

b. Department of Ecological Chemistry, Alfred Wegener Institute, Helmholtz Centre for Polar and Marine Research, Am Handelshafen 12, 27570 Bremerhaven, Germany.

c. University of Applied Sciences, An der Karlstadt 8, 27568 Bremerhaven, Germany.

Analyst **2020**, *145*(22), 7303-7311 (DOI: 10.1039/D0AN00949K)

Analyst

ROYAL SOCIETY OF CHEMISTRY

PAPER

View Article Online
View Journal

Open Access Article. Published on 09 September 2020. Downloaded on 9/23/2020 1:11:15 PM.
This article is licensed under a Creative Commons Attribution-NonCommercial 3.0 Unported Licence.

Check for updates

Cite this: DOI: 10.1039/d0an00949k

Siderophore purification with titanium dioxide nanoparticle solid phase extraction†

Philipp H. Egbers,[a] Tilmann Harder,[a,b] Boris P. Koch[b,c] and Jan Tebben *[b]

Siderophores are metal chelators produced by microorganisms to facilitate binding and uptake of iron. The isolation and characterization of siderophores are impeded by typically low siderophore yields and the complexity of siderophore-containing extracts generated with traditional purification methods. We investigated titanium dioxide nanoparticle solid-phase extraction (TiO_2 NP SPE) as a technique to selectively concentrate and purify siderophores from complex matrices for subsequent LC-MS detection and identification. TiO_2 NP SPE showed a high binding capacity (15.7 ± 0.2 μmol mg^{-1} TiO_2) for the model siderophore desferrioxamine B (DFOB) and proved robust to pH changes and the presence of EDTA. These are significant advances in comparison to immobilized metal affinity chromatography (IMAC). The TiO_2 NP SPE was highly selective and recovered 77.6 ± 6.2% of DFOB spiked to a compositionally complex bacterial culture supernatant. The simple clean-up procedure removed the majority of contaminants and allowed direct detection of siderophores from the LC-MS base peak chromatogram. The 'untargeted' purification and analysis of an untreated supernatant of iron-deprived bacterial culture allowed for the direct identification of two known and three novel ferrioxamines. Thus, TiO_2 NP SPE in combination with LC-MS offers great potential as a discovery platform for the purification and subsequent quantification or identification of novel siderophores of microbial origin.

Received 11th May 2020,
Accepted 16th August 2020

DOI: 10.1039/d0an00949k

rsc.li/analyst

Introduction

Iron is an essential micronutrient required by terrestrial and marine microorganisms for many metabolic processes.[1] To acquire iron and to cope with iron limitation, many bacteria and fungi produce organic ligands with high binding affinities for iron (Fe).[2] These molecules, so-called siderophores, play a key role in the interaction of bacteria with higher organisms (*e.g.* pathogenicity) and competition between bacteria for Fe.[3]

While the ecological, geochemical and medical importance of siderophores has long been realized,[4] the analysis of these ligands is complicated due to their low natural concentrations (femto- to micromolar). Therefore, the analysis of siderophores often requires their concentration from large volumes of polar and highly complex sample-matrices (*e.g.* blood plasma, soil, bacterial culture supernatants or saline water) to reach instrumental detection thresholds. Several chromatographic strategies have been employed to separate and concentrate siderophores prior to analysis such as reversed-phase, size-exclusion and ion exchange chromatography and solid-phase extraction (SPE).[5–7] These techniques often have poor chromatographic recoveries for siderophores and are non-selective, resulting in concentrated yet complex samples. Recent advances in liquid chromatography-mass spectrometry (LC-MS) have facilitated the identification of siderophores in these complex extracts.[8–12] However, these techniques produce many false positives, due to complex mass signatures or have reduced intensities and detection thresholds due to ion suppression by co-eluting substances. Further, these analyses also have an analytical bias against molecules that do not retain the metal ion after ionization.

To overcome these disadvantages and reduce the complexity of siderophore extracts, chromatographic techniques can target the selective binding of functional groups common to siderophores, namely catecholates, hydroxamates, and α-hydroxycarboxylates.[2] Immobilized metal affinity chromatography (IMAC), for example, relies on the inherent metal affinity of siderophores to bind to the free coordination sites of immobilized metal complexes and is routinely utilized for the selective extraction of siderophores from liquid media.[13,14] IMAC, however, has a few limitations that reduce its range of methodological applications. For example, IMAC shows the best siderophore (hydroxamate) adsorption for samples

[a]University of Bremen, Faculty of Biology and Chemistry, Leobener Straße 6, 28359 Bremen, Germany
[b]Department of Ecological Chemistry, Alfred Wegener Institute, Helmholtz Centre for Polar and Marine Research, Am Handelshafen 12, 27570 Bremerhaven, Germany. E-mail: jtebben@awi.de
[c]University of Applied Sciences, An der Karlstadt 8, D-27568 Bremerhaven, Germany
†Electronic supplementary information (ESI) available: Working protocol TiO_2 NP SPE, LC-HRMS data, calibration curves. See DOI: 10.1039/d0an00949k

Open Access Article. Published on 09 September 2020. Downloaded on 9/23/2020 1:11:15 PM.
This article is licensed under a Creative Commons Attribution-NonCommercial 3.0 Unported Licence.

around pH 9[13,14] which requires that the spent medium or sample is adjusted to pH 9 prior to adsorption. It would be advantageous to develop a pH independent chromatographic method to both ensure minimal processing and limit changes to the natural ratio of complexed *vs.* free ligands in the sample. Furthermore, some ligands have higher complex stability constants for the immobilized cations (*e.g.* Fe or Ni) than the IMAC resin itself and may remove these cations from the IMAC resin. This can either lead to the elution of the complexed ligand or decrease the number of available binding sites.[13,15] As IMAC only binds free ligands,[13,14,16] consequently, samples with a high proportion of complexed ligands require a decomplexation step. Decomplexation can be achieved with agents such as EDTA, however, these ligands then need to be chromatographically removed from the sample because they may strip metal cations from IMAC and thereby reduce available binding sites.[13]

In this study, we investigated metal oxide chromatography, specifically titanium dioxide (TiO_2) nanoparticle SPE, as a technique to selectively concentrate and purify metal ligands. TiO_2 is routinely used in catalysis and for the production of ceramics, paints and solar cells[17] and for the adsorption of molecules such as phosphopeptides and phospholipids with functional groups of high electron density.[18,19] Dziomba *et al.* showed that this adsorption capacity could also be used for extraction of smaller hydrophilic phosphocompounds, like thiamine phosphates.[20] Catecholates, hydroxamates and mixed ligands also adsorb on TiO_2 surfaces,[21–23] suggesting that TiO_2 may be suitable as solid phase for siderophores. Elution of these compound classes from TiO_2, however, was not reported. In general, TiO_2 binds anions at low pH and cations at high pH due to the unsaturated Lewis acid site on the TiO_2 surface.[24] The strength and bond type between target compound and TiO_2 depends on the respective functional group and corresponding affinity of the analyte, TiO_2 crystal-structure, pH and ionic strength of the surrounding medium.[25–27]

We developed a reliable and selective SPE method for the chromatographic purification of siderophores from aqueous media. We then tested this method by spiking and extracting a siderophore standard from a highly complex bacterial culture supernatants because these are the main target for the discovery of novel siderophores and pose analytic challenges due to a plethora of compounds that interfere with chromatographic purification and detection.[8] Our method successfully reduced the amount of interfering compounds and enabled the untargeted analysis and identification of both complexed and free ligands by LC-MS.

Experimental

Chemicals and stock solutions

All glassware and vessels were acid washed unless noted otherwise. Chemicals used for the preparation of the saline aqueous matrix and bacterial growth medium (see ESI†) were all reagent grade (Roth, Sigma-Aldrich or VWR). Both media were treated with Chelex 100 (Bio-Rad, USA) prior to use. The Chelex resin was regenerated as described by the manufactures protocol. Methanol (MeOH) and formic acid (FA) were HPLC grade (Roth, VWR). TiO_2 nanopowder with 21 nm primary particle size (Sigma-Aldrich) and Chromabond C_{18} Hydra 1 mL per 100 mg SPE cartridges (Macherey-Nagel) were used as sorbent materials. NaH_2PO_4, NaOH and NH_3 (all VWR) were used for the eluents. Desferrioxamine B (DFOB) was prepared from desferrioxamine mesylate (Sigma-Aldrich) dissolved to the final concentration of 74.4 ± 0.8 μM in iron free saline aqueous matrix and 86.5 μM bacterial supernatants, respectively. The high concentrations of DFOB (in comparison to realistic environmental concentrations) were used to reduce the complexation of DFOB with background contaminants (Fe, Al, Ti) in order to accurately calculate binding capacities as well as recoveries and to compare the data to similar concentrations used in the literature.[13,14] The Fe complex ferrioxamine B (FOB) was prepared saturating 95 mL of a 114 μM DFOB solution with 5 mL of 44 mM $FeCl_3$ ($FeCl_3{\cdot}6H_2O$, Sigma-Aldrich) in ultrapure water. Seven eluents were tested: MeOH 100% (E1), $FeCl_3$ 200 μM, pH 3.3 (E2), NH_3 10%, pH 12.6 (E3), NaH_2PO_4 2.5 M, pH 8 (E4), NaH_2PO_4 100 mM, pH 8 (E5), NaH_2PO_4 100 mM, pH 11 (E6) and NaH_2PO_4 100 mM, pH 12.6 (E7). For the FOB calibration, dilution series were prepared in triplicate in ultrapure water (Fig. S4†).

Instrumental

For extraction experiments, a vortex mixer (Genius 3, IKA) and centrifuge (Eppendorf) were used. A cryomill (Retsch) was used without grinding balls to shake screw cap micro tubes (Sarstedt) in order to re-suspend TiO_2 pellets in the eluents. LC-HRMS analysis was performed with a Vanquish UPLC system coupled to a Q-Exactive Plus mass spectrometer, using a heated electrospray ionization source (both Thermo Fisher Scientific). Separation was performed on a C_{18} column (C18 BEH, 100 × 2 mm, 1.7 μm particle size, ACQUITY Waters, equipped with guard-column). Positive Ion Calibration Solution (Pierce, Thermo Fisher Scientific) was used for the calibration of the instrument. 1.5 mL short threat brown glass vials (Thermo Fisher Scientific) were used for all LC-HRMS measurements. Following solvent compositions and gradient settings were used: Solvent A = 0.1% formic acid in ultrapure water, solvent B = 0.1% formic acid in methanol; $T_{0\ min}$: B = 1%, $T_{0.2\ min}$ B = 1%, $T_{4\ min}$: B = 100%, $T_{4.9\ min}$: B = 100%; $T_{5\ min}$: B = 1% with a flow rate of 0.4 mL min^{-1}. The first 1.4 min of the LC method were kept at isocratic conditions and the flow diverted to avoid spaying nonvolatile salts into the mass spectrometer. MS measurements were performed using electrospray ionization in positive mode. Full MS mode with a resolution of 70 000 (*m*/*z* 200) and a scan range of 300 to 1500 *m*/*z* was used for analyte quantification.

Data dependent (Top 5) mode was used for the untargeted screening with a full scan at 70 000 (*m*/*z* 200) followed by five MS^2 experiments (Top *N*) at normalized collision energy (NCE) of 30, AGC target of 3×10^6 and 50 ms maximum injection

 This journal is © The Royal Society of Chemistry 2020

Open Access Article. Published on 09 September 2020. Downloaded on 9/23/2020 1:11:15 PM. This article is licensed under a Creative Commons Attribution-NonCommercial 3.0 Unported Licence.

time. For siderophore identification, an inclusion mass list was compiled and used for MS^2 experiments in data independent (DIA) mode with a resolution of 280 000 (*m/z* 200) and stepwise NCE 20, 30 and 40. The spray voltage for all experiments was 3 kV. Capillary temperature was set to 320 °C and the sheath gas was set to 5. Calibration was done using the Calmix standard (Thermo Fisher Scientific).

Standardized siderophore adsorption

1 mL DFOB (74.4 ± 0.8 μM in saline aqueous matrix) were extracted with 100 μL TiO_2 NP suspension (2, 4, 6, 8 and 10 g L^{-1}, each $n = 3$) in 2 mL screw cap micro tubes (Sarstedt) by vortexing for 20 min (Fig. 1). After centrifugation (14 000 rpm, 2 min), supernatants were collected by decantation and the TiO_2-NP was re-suspended by shaking (3 min at 30 Hz) in 1 mL ultrapure water followed by 5 min vortexing. This process was repeated twice. Desorption of DFOB was performed with 2 × 1 mL eluent (seven different eluents used, see chemicals and stock solutions) using the same procedure. Each eluent (1 mL) was neutralized to pH 7–8 immediately with formic acid in ultrapure water to limit potential analyte hydrolysis after elution (3 min shaking at 30 Hz, vortexing 10 min) and centrifugation (14 000 rpm, 2 min). After pH adjustment, all 1.5 mL micro tubes were centrifuged again (14 000 rpm, 20 min) to achieve particle free samples for analysis. A 10 μL aliquot was taken from each sample, filled into untreated LC-vials (La-Pha-Pack/Thermo Fisher Scientific), diluted 100-fold with ultrapure water and spiked with $FeCl_3$ (5 μM final concentration). Samples were stored at room temperature for 48 h before analysis to achieve complete complexation of iron by DFOB. The experiment was repeated three times to obtain independent replicates. Preliminary tests revealed that the DFOB complexes of Fe(III)-FOB and Al(III)-AlOB[28] occurred concurrently. A calibration experiment with FOB and AlOB prepared from DFOB with addition of Fe(III) or Al(III) in excess found equivalent peak areas for both species (Fig. S2†). Therefore, we used both AlOB and FOB individually as well as the sum of both peaks for the quantification with similar results. This quantification was not affected by differences in the salinity of the sample matrix (Fig. S3†).

DFOB-spiked complex siderophore samples

A *Pseudoalteromonas* sp. bacterium (originally isolated from surface seawater at 69°25.662′ N 019°01.458′ E on expedition HE533) was cultured in iron free saline growth medium (see ESI†) for 7 d at 18 °C with orbital shaking at 120 rpm in an acid washed glass flask. The cell free supernatant of was collected by centrifugation (14 000 rpm, 2 min). The cell free supernatant tested positive for siderophore production in the chrome-azurol assay (CAS) and Atkin's hydroxamate assay.[29,30] The supernatant was analyzed by LC-HRMS and showed no presence of DFOB or corresponding metal complexes. Therefore, this supernatant was suitable for (i) spiking experiments with DFOB to study siderophore recovery from a highly complex matrix and (ii) to test 'untargeted' extraction of other siderophores causative for the positive result of the CAS and Atkins assays. TiO_2 NP were used to directly adsorb siderophores from a complex sample matrix. For this, 1 mL of the CAS and Atkin's assay positive bacterial culture supernatant was spiked with DFOB (86.5 μM final concentration) and extracted as above, using 100 mg of TiO_2, adding a washing step with 1 mL 0.02% FA/MeOH (pH 2.5) to separate hydroxamate-containing siderophores from other non-specifically bound molecules before desorption with E7 (Fig. 2, for protocol see ESI†). The same spiked culture supernatant was extracted with a C_{18}-SPE cartridge for comparison. Before extraction, the C_{18}-SPE cartridge was conditioned with 2 mL MeOH and then with 4 mL ultrapure water. 1 mL of the supernatant was passed through the equilibrated C_{18}-SPE cartridge with a flow rate not exceeding one drop per second. The C_{18}-

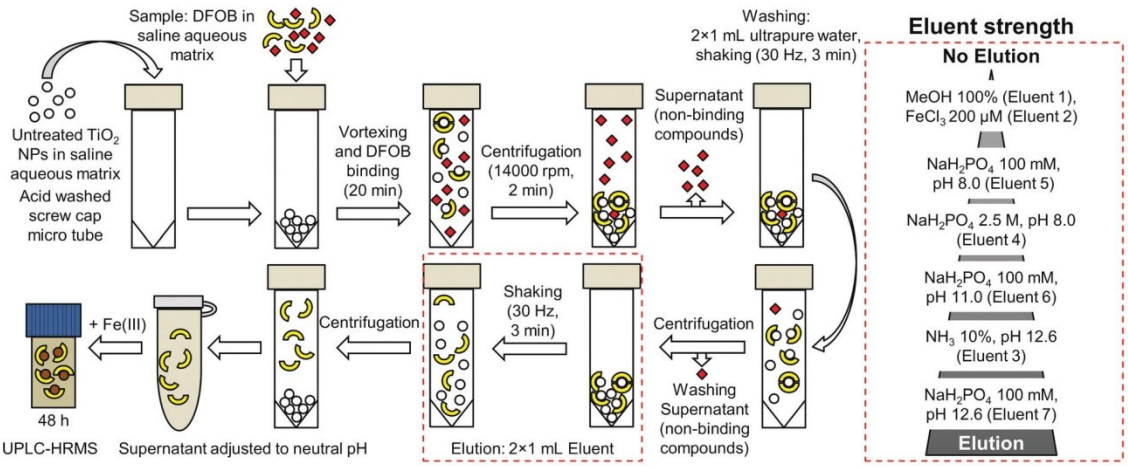

Fig. 1 Scheme for the TiO_2 NP phase extraction of hydroxamates from saline aqueous matrices.

Open Access Article. Published on 09 September 2020. Downloaded on 9/23/2020 1:11:15 PM.
This article is licensed under a Creative Commons Attribution-NonCommercial 3.0 Unported Licence.

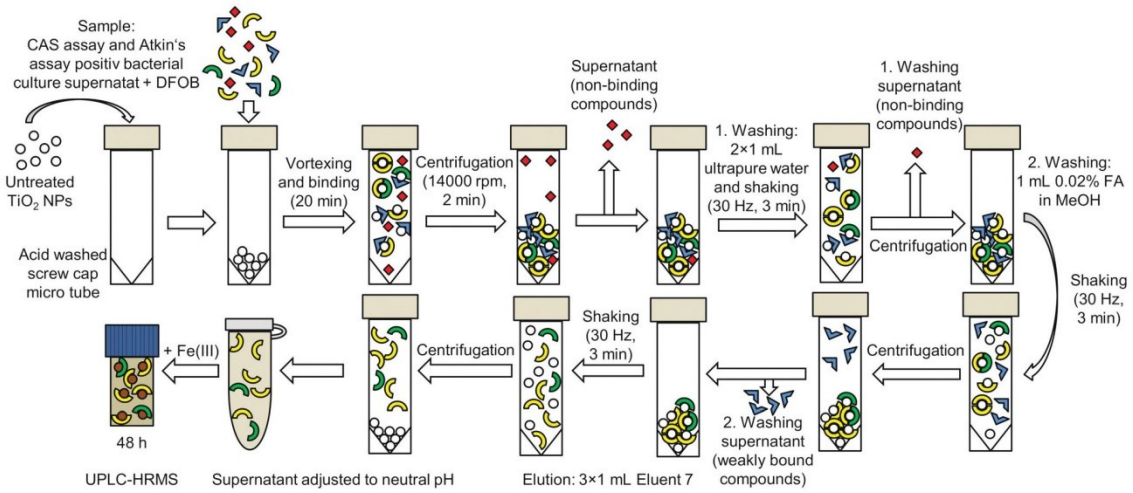

Fig. 2 Scheme for the TiO_2 NP phase extraction of hydroxamate containing siderophores from crude bacterial culture supernatants.

SPE cartridge was desalted with 4 mL ultrapure water, dried under vacuum and eluted with 1 mL MeOH. Samples from both SPE techniques were collected in untreated LC-vials and spiked with $FeCl_3$ (10 µM final concentration). The experiment was repeated three times to obtain independent replicates.

Decomplexation of metal complexes

FOB stock solution was prepared by adding 50 µL $FeCl_3$ (2 mM) to 4.95 mL of aqueous DFOB solution (60.6 µM). The prepared FOB stock solution was diluted 5 fold with aqueous EDTA solution (300 mM, pH 8) to a final volume of 1 mL, stored at room temperature for 24 h to achieve decomplexation of FOB and then extracted with 10 mg of TiO_2 as described above (Fig. 2). A control of the FOB stock solution was diluted with ultrapure water instead of EDTA and otherwise treated identically.

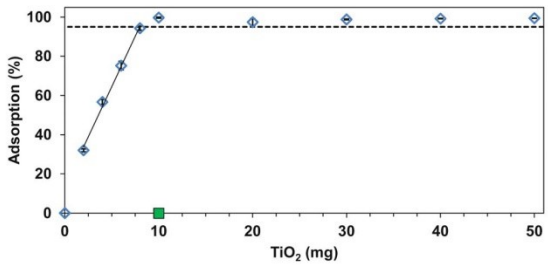

Fig. 3 Adsorption efficiency of DFOB (74.4 ± 0.8 µM) from 1 mL aqueous saline matrix depending on TiO_2 NP amount (blue diamonds). Error bars are standard deviation (n = 3). The linear range (2–8 mg) was used for binding capacity calculation according to Krenkova *et al.* (black solid line).[31] The binding capacity according to Gu *et al.*[14] defined as more than 95% DFOB bound is also shown (dotted line). Extraction of the Fe(III)-complex FOB (108.9 ± 1.2 µM) from saline aqueous matrix with 10 mg TiO_2 NPs is shown as a control (green square).

Results and discussion

TiO_2 NP binding capacity for the model siderophore DFOB

The binding of DFOB from 1 mL saline aqueous matrix onto TiO_2 NPs was tested with a fixed concentration of the standard (74.4 ± 0.8 µM) and variable amounts of sorbent (2–50 mg). We observed a linear increase of binding up to 8 mg TiO_2 NPs and close to 100% from 10 to 50 mg TiO_2 NPs (Fig. 3). This corresponded to a binding capacity of 15.7 ± 0.2 µmol DFOB per mg of TiO_2 NPs calculated for the linear range between 2 and 8 mg according to Krenkova *et al.*[31] This revealed an approximately 1000 times higher binding capacity of TiO_2 for DFOB than for the phosphocompounds TMP or TPP (Table S8†). The alternative calculation method of Gu *et al.*[14] resulted in a binding capacity of 8.8 ± 0.1 µmol mg^{-1}.

Gu *et al.* calculated a DFOB binding capacity of 8 µmol mL^{-1} for the Yb(III)-COM-IMAC[14] and of 3.5 µmol mL^{-1} for Ni(II)-IDA-IMAC[13,14] (or 20% of all possible binding calculated as per manufacturer information), respectively (Table S8†). Therefore, 1 mg of TiO_2 NPs bound more DFOB than 1 mL of the IMAC resins under ideal conditions. The Fe complex corresponding to DFOB, ferrioxamine B (FOB), showed no adsorption onto TiO_2 NPs (Fig. 3, green square). This confirmed that only free ligands adsorbed on TiO_2 similar to the IMAC methods, suggesting that complexed ligands require a decomplexation step prior to the SPE.

The adsorption of DFOB from ultrapure water onto TiO_2 was the same as for saline aqueous matrix. Therefore, we chose the saline aqueous matrix as matrix for all further extrac-

 This journal is © The Royal Society of Chemistry 2020

Open Access Article. Published on 09 September 2020. Downloaded on 9/23/2020 1:11:15 PM.
This article is licensed under a Creative Commons Attribution-NonCommercial 3.0 Unported Licence.

tion experiments to ensure that singly- and doubly-charged ions did not impede adsorption.

Elution buffer optimization

Elution of analytes bound on TiO_2 is typically achieved by pH adjustments of the elution buffers. Phosphopeptides/-lipids and glycopeptides, for example, require alkaline conditions to elute from TiO_2.[18,32] Flavonoids and other catecholate-containing molecules, on the other hand, require apolar solvents and acidic conditions for elution (5% FA in 50% MeOH[33] or ethanolic citric acid[34]). Some compounds, however, do not elute by adjustment of pH alone.

Cis-diol-containing molecules, for example, still have a high affinity to TiO_2 even under a wide range of pH and salt concentration.[35,36]

To optimize desorption of hydroxamate type siderophores from TiO_2, we tested seven different eluents (each in triplicate). The adsorption efficiency for DFOB was above 99% among for all replicates prior to the elution (n = 21, RSD = 0.71%) (Table S1†). E1 (MeOH 100%) showed low desorption of DFOB (1.4 ± 0.1%, Fig. 4), confirming hydroxamic acid ligands do not adsorb on TiO_2 because of unspecific hydrophobic interactions.[21] E2 ($FeCl_3$ 200 μM, pH 3.3) also resulted in low recoveries (1.6 ± 0.2%), indicating that while the complexed FOB did not adsorb, DFOB did not form the complex with Fe(III) after adsorption on TiO_2. This result was consistent with previous studies that showed that DFOB forms more stable complexes with Ti(IV) even in presence of an excess of Fe(III).[37,38] Surprisingly, E3 (NH_3 10%, pH 12.6) still showed poor recovery of DFOB (18.7 ± 5.2%). Therefore, pH-adjustment alone did not suffice to desorb hydroxamate-containing ligands from TiO_2. In contrast, the pH of the ammonia E3 solution was sufficient for quantitative desorption of phosphate-containing analytes such as flavin mononucleotide, thiamine monophosphate or pyrophosphate (approximately 90% recovery).[20] E4 (NaH_2PO_4 100 mM, pH 8) also did not elute high proportions of DFOB (16.9 ± 0.4%), despite the well documented ability of inorganic phosphate to compete for TiO_2 binding sites.[20,39,40] The same was observed for E5 (3.5 ± 0.4%), that contained 25 times less phosphate at a higher pH. Only the combination of high pH and a high concentration of phosphate resulted in quantitative DFOB recoveries (91.9 ± 3.3%) from TiO_2 (E7, NaH_2PO_4 100 mM, pH 12.6). As indicated by low recoveries for E6 (16.8 ± 0.4%, NaH_2PO_4 100 mM, pH 11), elution only occurred at highly alkaline conditions. This apparent connection between phosphate concentration, alkaline pH and recovery was seemingly in contradiction with the literature, showing no adsorption of phosphate on TiO_2 at pH ≥ 11.[40] Our results suggest that phosphate can destabilize the inner-sphere bidentate interaction[21] between hydroxamate groups and the TiO_2 surface at alkaline conditions. However, the exact mechanism of this destabilization is unclear and requires further investigation.

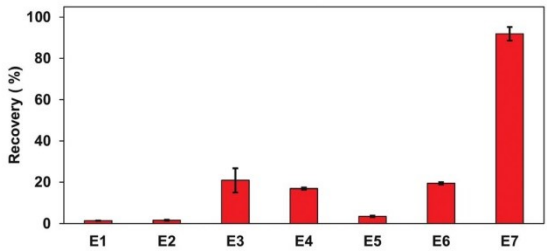

Fig. 4 Comparison of DFOB recoveries using different eluents: 1 mL of DFOB solution (74.4 ± 0.8 μM) was extracted with 10 mg TiO_2 NP and eluted with: MeOH 100% (E1), $FeCl_3$ 200 μM, pH 3.3 (E2), NH_3 10%, pH 12.6 (E3), NaH_2PO_4 2.5 M, pH 8 (E4), NaH_2PO_4 100 mM, pH 8 (E5), NaH_2PO_4 100 mM, pH 11 (E6) and NaH_2PO_4 100 mM or pH 12.6 (E7).

Siderophore concentration from complex matrices

To test the TiO_2 NP SPE method to enrich siderophores from complex biological samples, a siderophore-containing bacterial culture supernatant was spiked with DFOB and then extracted as above. The same supernatant was concentrated by traditional reversed-phased chromatography for comparison. The total DFOB recovery (86.5 μM initial concentration) was 77.6 ± 6.2% with the TiO_2 NP SPE compared to less than 0.1% with C_{18}-SPE (Table 1). The low recovery of DFOB by C_{18}-SPE is consistent with literature values for recoveries from pH neutral aqueous media.[41] Results showed that a far greater proportion of siderophores were directly extracted from the same volume of the bacterial culture supernatant with TiO_2 NP-based SPE than with the C_{18}-SPE.

For comparison, Braich *et al.*[13] showed that approximately 230 nmol (65%) of CAS active species (mainly DFOB) were recovered from a pH adjusted bacterial culture supernatant (*Streptomyces pilosus*) with a 5 mL Ni(II)-IDA-IMAC column.[13]

The extraction of siderophores with TiO_2 NP was highly specific, indicated by a reduced complexity of the LC-MS base peak chromatogram (Fig. 5B) in comparison to that of the original supernatant (Fig. 5A) and non-specific C_{18} extract (Fig. 5C). The overlay of the base peak chromatograms with the extracted ion chromatograms of the Fe complex FOB ($[M + H]^+ = [^{56}Fe(III)\ C_{25}H_{46}N_6O_8]^+$, m/z 614.2724) and the corresponding Al complex AlOB ($[M + H]^+ = [^{27}Al(III)\ C_{25}H_{46}N_6O_8]^+$, m/z 585.3190), showed a clear double-peak in the base peak chromatogram of the TiO_2 E7 eluate at 2.37 min (Fig. 5D) but no peaks in the base peak chromatogram of the C_{18} MeOH eluate (Fig. 5E).

Table 1 Siderophore recovered amounts and recovery percentages extracted with C_{18} or TiO_2 NP from a complex bacterial culture supernatant

	Name	C_{18}	TiO_2 NP
Recovered amount (μmol)	DFOB	0.04 ± 0.01	67.1 ± 5.4
	DFOG1	1.0 ± 0.4[a]	2.3 ± 1.5[a]
Recovery (%)	DFOB	0.03 ± 0.02	77.6 ± 6.2
	DFOG1	9.9 ± 3.4	22.2 ± 14.6

[a] Approximated with FOB calibration.

Open Access Article. Published on 09 September 2020. Downloaded on 9/23/2020 1:11:15 PM.
This article is licensed under a Creative Commons Attribution-NonCommercial 3.0 Unported Licence.

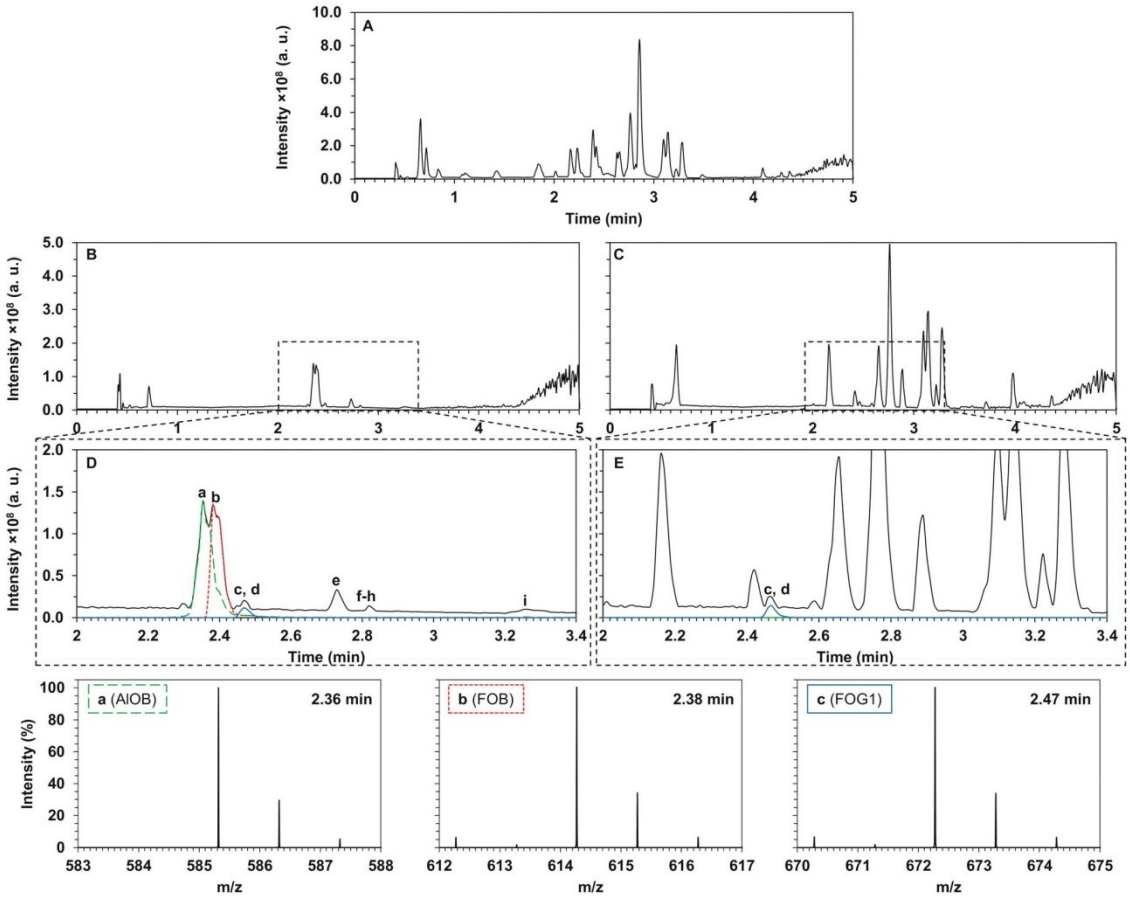

Fig. 5 Comparison of UPLC-HRMS chromatograms: (A) base peak chromatogram (solid black line) of crude bacterial culture spiked with DFOB; (B) base peak chromatogram of the first TiO_2 E7 eluate (NaH_2PO_4 100 mM, pH 12.6); (C) base peak chromatogram of C_{18} MeOH eluate; (D) enlarged area of (B) with extracted ion chromatogram of *m/z* 614.2724 analogous FOB ($[^{56}Fe(III)\ C_{25}H_{46}N_6O_8]^+$) (red dotted line), *m/z* 585.3190 analogous to AlOB ($[^{27}Al(III)\ C_{25}H_{46}N_6O_8]^+$) (green dashed line) and 672.2778 analogous to FOG1 ($[^{56}Fe(III)\ C_{27}H_{48}N_6O_{10}]^+$) (blue solid line); (E) enlarged area of (C) with the same extracted ion chromatograms. (a–i) Peaks showing a ferrioxamine-type fragmentation pattern: (a) AlOB, (b) FOB, (c) FOG1, (d) AlOG1, (e) **3**, (f) Fe(III)-**1**, (g) Al(III)-**1**, (h) **2**, (i) **1**.

The investigated bacterial supernatant was CAS and Atkin's assay positive before spiking with DFOB and therefore contained unknown hydroxamate-type siderophore(s). Therefore, we further investigated the remaining peaks in the base peak chromatogram of the TiO_2 E7 eluate (a-i in Fig. 5D). The signal at 2.47 min showed coeluting ions with *m/z* 672.2778 and *m/z* 670.2817. This characteristic difference ($\Delta m/z$ = 1.9954) and the signal intensity ratio of 100/6.35 ($^{56}Fe/^{54}Fe$)[42] suggested an Fe-containing complex (Fig. 5 FOG1). Mass fragmentation confirmed this complex as ferrioxamine G1[43] (FOG1, Fig. S5 and Table S2†). The Al complex of G1 (AlOG1: $[^{27}Al(III)\ C_{27}H_{48}N_6O_{10}]^+$, with *m/z* 643.3244) was also detected, but in low intensity.

Assuming similar ionization of FOG1 and FOB, C_{18}-SPE extracted 9.9 ± 3.4% of DFOG1 (approximately 1.0 ± 0.4 μmol) whereas 2.3 ± 1.5 μmol were extracted with the TiO_2 NP method (22.2 ± 14.6% (Table 1)). The low recovery of DFOG1 may be due to a large proportion of DFOG1 that was complexed before extraction with TiO_2.

The peak at 2.82 min showed an ion at (*m/z* 638.2722 with the ^{54}Fe ion (*m/z* 636.2763) and the Al complex also detected (*m/z* 609.3190) (Fig. S7†). The metal-free ligand was detected at 3.26 min (*m/z* 585.3610). The fragmentation (*e.g.* neutral loss of $C_9H_{16}O_3N_2$, 200 Da Fig. S9 and Table S4†) indicated an unknown desferrioxamine **1** ($C_{27}H_{49}O_8N_6$) analogous to the cyclic desferrioxamine E (Table S5†).[44,45] The peak at 2.82 min (*m/z* 603.3714) suggested a compound with the sum formula of $C_{27}H_{51}O_9N_6$ (**2**, Fig. S8†). MS^2 fragmentation experiments (*e.g.* neutral losses of $C_5H_4O_3$ (100 Da) and $C_5H_{14}N_2O$ (118 Da) (Fig. S10 and Table S6†)) suggested a un-complexed novel

Open Access Article. Published on 09 September 2020. Downloaded on 9/23/2020 1:11:15 PM.
This article is licensed under a Creative Commons Attribution-NonCommercial 3.0 Unported Licence.

Table 2 Summary of parent masses

Name	Exp. m/z $[M + H]^+$	Theo. m/z $[M + H]^+$	Δ_{ppm}	Sum formula $[M + H]^+$
DFOB	561.36078	561.36064	0.25	$C_{25}H_{49}N_6O_8$
FOB	614.27240	614.27211	0.48	$C_{25}H_{46}N_6O_8Fe$
AlOB	585.31897	585.31870	0.46	$C_{25}H_{46}N_6O_8Al$
DFOG1	619.36702	619.36612	0.34	$C_{27}H_{51}N_6O_{10}$
FOG1	672.27783	672.27759	0.36	$C_{27}H_{48}N_6O_{10}Fe$
AlOG1	643.32440	643.32418	0.34	$C_{27}H_{48}N_6O_{10}Al$
1 (un-complexed)	585.36096	585.36064	0.55	$C_{27}H_{49}N_6O_8$
1 (Fe(III)-complex)	638.27222	638.27211	0.17	$C_{27}H_{46}N_6O_8Fe$
1 (Al(III)-complex)	609.31903	609.31870	0.23	$C_{27}H_{46}N_6O_8Al$
2 (un-complexed)	603.37141	603.37120	0.34	$C_{27}H_{51}N_6O_9$
3 (un-complexed)	587.37659	587.37629	0.51	$C_{27}H_{51}N_6O_8$

hydroxamate analogous to DFOG1 (Fig. S6 and Table S3†).[45,46] MS^2 fragmentation experiments of the ion at 2.73 min (**3**, $C_{27}H_{51}O_8N_6$, m/z 587.3766 NL 100 Da, 118 Da, Fig. S11 and Table S7†) suggested a further novel un-complexed hydroxamate analogous to DFOG1.

Cumulatively, all peaks in the base chromatogram outside the injection peak and the column bleed could be assigned to siderophores or un-complexed hydroxamates (Fig. S8,† Table 2 and Table S9†). Only **1** (analogous to the cyclic DFOE) showed the corresponding Fe(III)- and Al(III)-complexed ions (m/z 638.2722 and m/z 609.3190) None of the novel linear hydroxamates (**2**, **3**) showed corresponding Fe(III)-complexed ions despite of excess Fe in the sample. MS^2 experiments suggested one (**1**, **2**) or two (**3**) fewer hydroxamate groups in comparison to DFOE or DFOG1.

Possibly, fewer hydroxamate groups in these compounds reduced complexation in the sample or changed the detection/ionization of the complexes but this requires further investigation. The results suggest that the TiO_2 NP SPE also concentrated molecules with one hydroxamate functional group. All analytes were also found in the C_{18} eluate and the untreated bacterial culture supernatant. The chromatograms and mass spectra of these samples were highly complex and contained 100s of ions with intensities higher than those of the siderophores (Fig. 5E). This result highlights the advantageous selectivity of the TiO_2 NP SPE for siderophore discovery and analysis.

Binding of decomplexed siderophores

By exposing FOB (12.0 nmol) to EDTA (2.5×10^5 nmol) at pH 8 for 24 h, it was possible to increase the total recovery of FOB from 0.07 nmol (0.6% recovery, Fig. 6B) to 1.3 nmol (10.8% recovery, Fig. 6A). This result proved that EDTA-de-complexed DFOB could at least partially be recovered from a sample containing a surplus of iron. This result was in contrast to the IDA-IMAC methods where EDTA concentrations exceeding 1 mM EDTA should be avoided. Small concentrations of FOB and AlOB detected in the non-EDTA treatment were likely due to incomplete complexation prior to extraction rather than adsorption of FOB on TiO_2. FOB/DFOB recovery may further be improved with a pH optimization because ferrioxamine decomplexation with EDTA increases to ≈100% at low pH.[47]

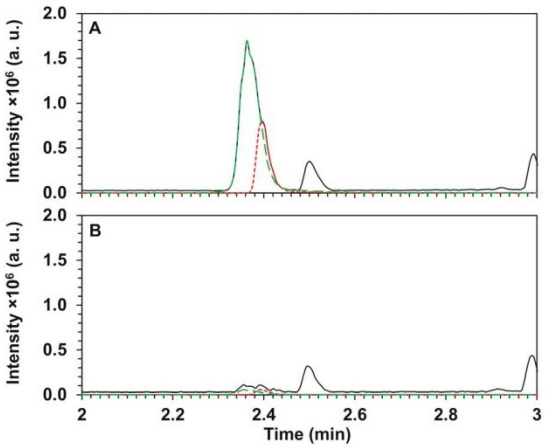

Fig. 6 Comparison of UPLC-HRMS chromatograms (A) with and (B) without EDTA decomplexation step: base peak chromatograms of TiO_2 E7 eluate (NaH_2PO_4 100 mM, pH 12.6) (black solid line) with extracted ion chromatogram of m/z 614.2724 analogous to FOB $[^{56}Fe(III)C_{25}H_{46}N_6O_8]^+$ (red dotted line), and m/z 585.3190 analogous to $[^{27}Al(III)C_{25}H_{46}N_6O_8]^+$ (green dashed line).

However, this study aimed at minimal manipulation of the source material and the role of de-complexation ratio or interference of EDTA with siderophore adsorption require further investigation.

Conclusion

In this study, we developed an efficient and highly specific enrichment of hydroxamate-type siderophores from complex polar protic matrices by TiO_2 NP-based SPE. We used the model siderophore DFOB to test the binding capacity of TiO_2 NPs for siderophore extraction. The TiO_2 NP SPE showed higher binding capacity than the IMAC methods (similar recovery for 1 mg of TiO_2 than for 1 mL of IMAC). A high recovery (77.6 ± 6.2%) of DFOB extracted from complex bacterial culture supernatants with TiO_2 NP was achieved with alkaline buffers containing phosphate. The TiO_2 NP SPE also served well as a simple clean-up procedure to selectively process complex samples containing an unknown mixture of siderophores. The TiO_2 NP SPE step removed most contaminants and therefore enabled the detection of siderophores or hydroxamates directly from LC-MS base peak chromatogram. We processed CAS assay and Atkin's assay positive bacterial culture supernatants and then easily identified ferrioxamine G1 and other novel ferrioxamines from the most abundant peaks in the base chromatogram due to the drastically reduced mass signatures of the TiO_2 extract in comparison to non-specific C_{18} extracts. All ferrioxamines were also detected in the untreated bacterial culture supernatant, suggesting that the conditions of the TiO_2 NP SPE did not alter the composition in the sample. The pH required for the elution of strong ligands from TiO_2, however,

Open Access Article. Published on 09 September 2020. Downloaded on 9/23/2020 1:11:15 PM.
This article is licensed under a Creative Commons Attribution-NonCommercial 3.0 Unported Licence.

may be a caveat for the isolation of siderophores susceptible to pH degradation. We also offered proof-of-principle that a decomplexation step (*e.g.* with EDTA) enables the adsorption of previously complexed siderophores in samples with high Fe background. Previous studies showed that phospho- or catechol-groups elute with basic or acidic buffer solutions respectively,[33,34,48] therefore, a future goal to further improve on this method will be to sequentially elute and separate different siderophore classes from complex extracts. The cost- and labour-efficient concentration and purification of siderophores highlighted in this study may find wide applications in both medical and environmental research to study the role of these molecules in *e.g.* iron cycling, bacterial competition, primary production and health.

Conflicts of interest

There are no conflicts to declare.

Acknowledgements

We thank Jennifer Bergemann for support with the bacterial cultures.

References

1 E. Ahmed and S. J. M. Holmström, *Microb. Biotechnol.*, 2014, **7**, 196–208.
2 R. C. Hider and X. Kong, *Nat. Prod. Rep.*, 2010, **27**, 637.
3 B. J. Gobin and M. A. Horwitz, *J. Exp. Med.*, 1996, **183**, 1527–1532.
4 J. B. Neilands, *J. Biol. Chem.*, 1995, **270**, 26723–26726.
5 C. Adler, N. S. Corbalán, M. R. Seyedsayamdost, M. F. Pomares, R. E. de Cristóbal, J. Clardy, R. Kolter and P. A. Vincent, *PLoS One*, 2012, **7**, 1–7.
6 A. T. Koppisch, C. C. Browder, A. L. Moe, J. T. Shelley, B. A. Kinkel, L. E. Hersman, S. Iyer and C. E. Ruggiero, *BioMetals*, 2005, **18**, 577–585.
7 R. Z. Sayyed and S. B. Chincholkar, *Bioresour. Technol.*, 2006, **97**, 1026–1029.
8 R. M. Boiteau, S. J. Fansler, Y. Farris, J. B. Shaw, D. W. Koppenaal, L. Pasa-Tolic and J. K. Jansson, *Metallomics*, 2019, **11**, 166–175.
9 R. M. Boiteau, J. N. Fitzsimmons, D. J. Repeta and E. A. Boyle, *Anal. Chem.*, 2013, **85**, 4357–4362.
10 O. Baars and D. H. Perlman, in *Application from Engineering with MATLAB Concepts*, 2016, p. 189.
11 O. Baars, F. M. M. Morel and D. H. Perlman, *Anal. Chem.*, 2014, **86**, 11298–11305.
12 M. Deicke, J. F. Mohr, J. P. Bellenger and T. Wichard, *Analyst*, 2014, **139**, 6096–6099.
13 N. Braich and R. Codd, *Analyst*, 2008, **133**, 877–880.
14 J. Gu and R. Codd, *RSC Adv.*, 2015, **5**, 3443–3453.
15 R. Codd, J. Gu, N. Ejje and T. Lifa, in *Inorganic chemical biology: Principles, techniques and applications*, John Wiley & Sons, Ltd, Chichester, 1st edn, 2014, pp. 1–35.
16 N. Ejje, C. Z. Soe, J. Gu and R. Codd, *Metallomics*, 2013, **5**, 1519.
17 U. Diebold, *Surf. Sci. Rep.*, 2003, **48**, 53–229.
18 M. W. H. Pinkse, P. M. Uitto, M. J. Hilhorst, B. Ooms and A. J. R. Heck, *Anal. Chem.*, 2004, **76**, 3935–3943.
19 M. R. Larsen, T. E. Thingholm, O. N. Jensen, P. Roepstorff and T. J. D. Jørgensen, *Mol. Cell. Proteomics*, 2005, **4**, 873–886.
20 S. Dziomba, A. Pawelec, K. Ciura, M. Dolegowska, A. Klimowska, W. Rodzaj, M. Guerrouache, B. Carbonnier and B. Wielgomas, *Microchem. J.*, 2019, **145**, 784–790.
21 Y. Jing, P. J. Bremer, I. L. Lamont and A. J. McQuillan, *Langmuir*, 2006, **22**, 10109–10117.
22 H. G. Upritchard, J. Yang, P. J. Bremer, I. L. Lamont and A. J. McQuillan, *Langmuir*, 2007, **23**, 7189–7195.
23 H. G. Upritchard, J. Yang, P. J. Bremer, I. L. Lamont and A. J. McQuillan, *Langmuir*, 2011, **27**, 10587–10596.
24 J. Xu, P. Wu, E. C. Ye, B. F. Yuan and Y. Q. Feng, *TrAC, Trends Anal. Chem.*, 2016, **80**, 41–56.
25 W. R. McNamara, R. L. Milot, H. E. Song, R. C. Snoeberger, V. S. Batista, C. A. Schmuttenmaer, G. W. Brudvig and R. H. Crabtree, *Energy Environ. Sci.*, 2010, **3**, 917–923.
26 B. J. Brennan, M. J. Llansola Portolés, P. A. Liddell, T. A. Moore, A. L. Moore and D. Gust, *Phys. Chem. Chem. Phys.*, 2013, **15**, 16605–16614.
27 H. Gulley-Stahl, P. A. Hogan, W. L. Schmidt, S. J. Wall, A. Buhrlage and H. A. Bullen, *Environ. Sci. Technol.*, 2010, **44**, 4116–4121.
28 M. Gledhill, P. McCormack, S. Ussher, E. P. Achterberg, R. F. C. Mantoura and P. J. Worsfold, *Mar. Chem.*, 2004, **88**, 75–83.
29 B. Schwyn and J. B. Neilands, *Anal. Biochem.*, 1987, **160**, 47–56.
30 C. L. Atkin, J. B. Neilands and H. J. Phaff, *J. Bacteriol.*, 1970, **103**, 722–733.
31 J. Krenkova, J. Moravkova, J. Buk and F. Foret, *J. Chromatogr. A*, 2016, **1427**, 8–15.
32 M. R. Larsen, S. S. Jensen, L. A. Jakobsen and N. H. H. Heegaard, *Mol. Cell. Proteomics*, 2007, **6**, 1778–1787.
33 J. Kurepa, R. Nakabayashi, T. Paunesku, M. Suzuki, K. Saito, G. E. Woloschak and J. A. Smalle, *Plant J.*, 2014, **77**, 443–453.
34 M. A. Khan, W. T. Wallace, S. Z. Islam, S. Nagpure, J. Strzalka, J. M. Littleton, S. E. Rankin and B. L. Knutson, *ACS Appl. Mater. Interfaces*, 2017, **9**, 32114–32125.
35 S. T. Wang, W. Huang, W. Lu, B. F. Yuan and Y. Q. Feng, *Anal. Chem.*, 2013, **85**, 10512–10518.
36 S. T. Wang, W. Huang, Y. F. Deng, Q. Gao, B. F. Yuan and Y. Q. Feng, *J. Chromatogr. A*, 2014, **1361**, 100–107.
37 K. E. Jones, K. L. Batchler, C. Zalouk and A. M. Valentine, *Inorg. Chem.*, 2017, **56**, 1264–1272.
38 S. Igarashi, K. Yoshida and T. Yotsuyanagi, *Bunseki Kagaku*, 1991, **40**, 571–573.

 This journal is © The Royal Society of Chemistry 2020

Open Access Article. Published on 09 September 2020. Downloaded on 9/23/2020 1:11:15 PM.
This article is licensed under a Creative Commons Attribution-NonCommercial 3.0 Unported Licence.

39 A. Leitner, *TrAC, Trends Anal. Chem.*, 2010, **29**, 177–185.
40 P. A. Connor and A. J. McQuillan, *Langmuir*, 1999, **15**, 2916–2921.
41 H. Waska, A. Koschinsky, M. J. Ruiz Chancho and T. Dittmar, *Mar. Chem.*, 2015, **173**, 78–92.
42 E. De Hoffmann and V. Stroobant, *Biol. Mass Spectrom.*, 1991, **20**, 142–152.
43 E. Mawji, M. Gledhill, P. J. Worsfold and E. P. Achterberg, *Rapid Commun. Mass Spectrom.*, 2008, **22**, 2195–2202.
44 C. H. R. Senges, A. Al-Dilaimi, D. H. Marchbank, D. Wibberg, A. Winkler, B. Haltli, M. Nowrousian, J. Kalinowski, R. G. Kerr and J. E. Bandow, *Proc. Natl. Acad. Sci. U. S. A.*, 2018, **115**, 2490–2495.
45 G. J. Feistner and L. L. Hsieh, *J. Am. Soc. Mass Spectrom.*, 1995, **6**, 836–846.
46 G. J. Feistner, D. C. Stahl and A. H. Gabrik, *Org. Mass Spectrom.*, 1993, **28**, 163–175.
47 R. Jain, S. Fan, P. Kaden, S. Tsushima, H. Foerstendorf, R. Barthen, F. Lehmann and K. Pollmann, *Water Res.*, 2019, **158**, 203–212.
48 Y. Kyono, N. Sugiyama, K. Imami, M. Tomita and Y. Ishihama, *J. Proteome Res.*, 2008, **7**, 4585–4593.

3. Selective purification of catecholate, hydroxamate and α-hydroxycarboxylate siderophores with Titanium Dioxide Affinity Chromatography

Building on the results of Chapter 2, I investigated in Chapter 3 whether the presented purification concept can be transferred to the solid phase extraction cartridge format to allow the extraction of larger volume samples. For this purpose, I first had to prepare a new TiO_2 sorbent that meets the requirements of solid phase extraction in terms of size distribution. Then, the extraction performance of this new sorbent was investigated, with a particular focus on how the elution of siderophores changes depending on the functional groups present in their structure. Our results showed that the developed TiO_2 chromatography (TDAC) is a powerful tool for the efficient purification of all types of siderophores. However, it was shown that dependent on the functional group of the siderophore different elution conditions result in optimal elution. In this study, I was responsible for the development of the TDAC method, the execution and evaluation of LC-HRMS measurements, as well as visualization and writing of the original draft. Cultivation of the bacterial strains for siderophore standard preparation was conducted by Jennifer Bergemann. NMR measurements and quantification of siderophore standards was performed by Christian Zurhelle. Crude TiO_2 and the particle size characterization of the washed and sieved TiO_2 sorbent was provided by Kronos Worldwide, Inc.

Selective purification of catecholate, hydroxamate and α-hydroxycarboxylate siderophores with Titanium Dioxide Affinity Chromatography

Philipp H. Egbers[a], Christian Zurhelle,[a] Tilmann Harder[a,b], Boris P. Koch[b,c], Jan Tebben[b]

a. University of Bremen, Faculty of Biology and Chemistry, Leobener Straße 6, 28359 Bremen, Germany.

b. Department of Ecological Chemistry, Alfred Wegener Institute, Helmholtz Centre for Polar and Marine Research, Am Handelshafen 12, 27570 Bremerhaven, Germany.

c. University of Applied Sciences, An der Karlstadt 8, 27568 Bremerhaven, Germany.

A former version of this manuscript has been re-submitted to Separation and Purification after all of the reviewers critic was addressed in the updated manuscript.

3.1 Introduction

Many bacteria, fungi and graminaceous plants produce organic ligands, termed siderophores, to scavenge the essential micronutrient iron (Fe). Siderophores are chemically diverse and considered 'keystone metabolites' that regulate various ecological roles ranging from niche adaptation to symbiosis and pathogenicity. The four most commonly occurring siderophores are classified into classes depending on their chelating group, namely catecholates, hydroxamates, α-hydroxy-carboxylates and mixed ligand siderophores (Figure 3) (Hider and Kong 2010). Natural siderophore concentrations in the environment are notoriously low and sample matrices (e.g. soil extracts, pore water, seawater, microbial culture media) are often too complex for their direct instrumental analysis (Boiteau et al. 2016). Therefore, both concentration and purification is prerequisite for reliable analyses. Reversed-phase or ion exchange chromatography is often used to concentrate and desalt samples, yet both methods show inconsistent recoveries across the polarity spectrum of siderophores and often result in siderophore fractions containing numerous other compounds in the same polarity spectrum. A selective purification of siderophores was first achieved with Immobilized Metal Affinity Chromatography (IMAC) based on the affinity of siderophores to free coordination sites of immobilized metal cations (Braich and Codd 2008). IMAC has been successfully applied to hydroxamate siderophores such as ferrioxamine and ferrichrome (Ejje et al. 2013; Heine et al. 2017). IMAC purification of the catechol bacillibactin only yielded a fragment with one catechol group while the intact siderophore with three catecholate groups was not recovered (Li et al. 2018). Similarly, the mixed ligand siderophore pyoverdine could not be detected in IMAC eluates (Heine et al. 2017), suggesting that siderophores with high complex stability constants are not retained. Thus, a different type of affinity chromatography that enables concurrent analyses of siderophores independent of polarity and complex stability constant is highly desirable. Metal Oxide Affinity Chromatography (MOAC), particularly using titanium dioxide (TiO_2), can circumvent some of the issues of IMAC due to its high lattice energy. Previous studies showed that catecholates and hydroxamates adsorb well on TiO_2 surfaces, therefore suggesting MOAC utilizing TiO_2 as a potential alternative for metal ligand extraction (Upritchard et al. 2007, 2011). TiO_2 acts as an anion or cation exchanger depending on whether the surface hydroxyl groups are protonated or dissociated. Additionally, unsaturated Lewis acid sites on the surface exhibit ligand-exchange functionality (Xu et al. 2016). We recently showed proof-of-concept that TiO_2 nanoparticle solid phase extraction (SPE) is well suited to extract and elute hydroxamate siderophores from complex matrices (Egbers et al. 2020). Hydroxamates form inner-sphere surface complexes on TiO_2 (Yang et al. 2006) and due to the unique conditions required to destabilize those complexes, hydroxamates can be largely separated from organic contaminants and inorganic salts. In contrast to outer-sphere surface complexes, whose formation is based on nonspecific interaction, like hydrogen bonding and electrostatic attraction (physisorption), inner-sphere surface complexes are not as susceptible to changes in solvent conditions (Gulley-Stahl et al. 2010). Catecholates and α-

hydroxycarboxylates are also known to form inner-sphere surface complexes with TiO_2 (Connor et al. 1995; Awatani et al. 1998; Tani and Ozawa 1999; Araujo et al. 2005; Petrone 2013). The elution of siderophores containing those functional groups from TiO_2 and, consequently, the application as chromatographic method is still unknown.

Here, we established a titanium dioxide affinity chromatography (TDAC) to concentrate and purify the three major siderophore classes, i.e. catecholates, α-hydroxycarboxylates and hydroxamates. The main aim was to concurrently analyze all siderophore types, yield high levels of purification and analyte recovery and to assess the scalability of this method. The project was divided into three objectives: (i) To develop and optimize a quantitative purification of four model siderophores with TiO_2 column chromatography, (ii) To separate those siderophores based on their functional groups and (iii) To achieve quantitative purification of siderophores from complex sample matrices.

3.2 Experimental

3.2.1 Materials and chemicals

All glassware and vessels were soaked in 10% hydrochloric acid for at least 48 h and washed generously with ultrapure water prior to use. Reagents used for the preparation of the elution solutions, e.g. sodium dihydrogen phosphate monohydrate (NaH_2PO_4) (Table 2), and bacterial growth media (see SI) were reagent grade (Roth, Sigma-Aldrich or VWR). All anions tested here were used with sodium as cation unless stated otherwise. Polypropylene solid phase extraction (SPE) cartridges (3 mL, 6 mL Chromabond) with fitting polyethylene filter elements were purchased from Macherey-Nagel. Desferrioxamine B (DFOB) was purchased as desferrioxamine mesylate (Sigma-Aldrich). Petrobactin (PB), vibrioferrin (VF) and woodybactin A (WBA) were prepared in our laboratories (see Siderophore Standard preparation). Titanium dioxide was obtained as oven clinker from rotary kilns (initial particle size > 1 mm, Kronos Worldwide, Inc., Nordenham Germany). The oven clinker was manually ground with mortar and pestle and wet sieved with nylon gauze filter units (50, 100 and 200 µm cut-off) until no turbidity of the wash water was recognizable. The 50 µm size fraction was collected and dried at 120 °C overnight and used for all SPE experiments. This TiO_2 had a surface area of 5.0 m²/g (BET) and the D_{50} mass-median-diameter of 54.092 µm (Figure SI 1). 200 or 500 mg of TiO_2 were weight in (± 5 mg) and filled into empty 3 or 6 mL SPE cartridges, respectively. To ensure reproducible extraction performances PE filter elements were used and the packed cartridges were compacted manually. We gladly make a limited amount of pre-packed TDAC SPE available upon request.

3.2.2 Instrumental

LC-HRMS analysis was performed with a Vanquish UPLC system coupled to a Q-Exactive Plus mass spectrometer, using a heated electrospray ionization source (both Thermo Fisher Scientific). The LC system was operated with a C18 column (C18 BEH, 100 × 2 mm, 1.7 µm, equipped with guard-column, Waters) using the following settings: Solvent A = 0.1% formic acid in ultrapure water, solvent B = 0.1% formic acid in methanol; $T_{0\ min}$: B = 1%, $T_{2\ min}$: B = 1%, $T_{5.0\ min}$: B = 99%, $T_{7.1\ min}$: B = 99%, $T_{7.2\ min}$: B = 1% with a flow rate of 0.35 mL min^{-1}. The effluent of the first 1.5 min was diverted to waste to limit salt deposits. The column oven was set to 32 °C. The mass spectrometer was calibrated using Positive Ion Calibration Solution (Pierce, Thermo Fisher Scientific), all MS measurements were done in positive mode. All sample solutions were prepared in 1.5 mL short threat brown glass vials (Agilent Technologies). Data independent mode with a full scan resolution of 70,000 (*m/z* 200) followed by MS^2 experiments (normalized collision energy of 30, automatic gain control target of 3×10^6 and 50 ms maximum injection time) was used for the identification and quantification of siderophore standards. All siderophores were quantified using the exact mass ± 5 ppm of the precursor ions as well as the main daughter ions. I.e. DFOB was quantified using the species: DFOB ($[M+H]^+$= $C_{25}H_{49}N_6O_8$, *m/z* 561.3606), FOB ($[M+H]^+$ = $C_{25}H_{46}N_6O_8Fe$, *m/z* 614.2721), AlOB ($[M+H]^+$ = $C_{25}H_{46}N_6O_8Al$, *m/z* 585.3287) as well as the *m/z* 201.12 daughter ion of *m/z* 561.3606. For the quantification of VF, apo-VF ($[M+H]^+$ = $C_{16}H_{23}N_2O_{12}$, *m/z* 435.1246), Fe-VF ($[M+H]^+$ = $C_{16}H_{20}N_2O_{12}Fe$, *m/z* 488.0360) and the daughter ion *m/z* 181.10 of *m/z* 435.1246 were used. Similar to VF, WBA was also quantified by using the single charged apo- ($[M+H]^+$ = $C_{20}H_{35}N_2O_{10}$, *m/z* 463.2286), Fe(III)-containing species ($[M+H]^+$ = $C_{20}H_{32}N_2O_{10}Fe$, *m/z* 516.1401) as well as the daughter ion *m/z* 145.10 of the free ligand precursor ion. Whereas PB was detected as the single ($[M+H]^+$ = $C_{34}H_{51}N_6O_{11}$, *m/z* 719.3610) or double protonated apo-PB ($[M+2H]^{2+}$ = $C_{34}H_{52}N_6O_{11}$, *m/z* 360.1842) with the corresponding daughter ion *m/z* 194.08. The corresponding calibration curves, chromatograms and mass spectra are listed in the supporting information of this chapter. NMR experiments were performed in 1.7 mm microtubes at 300 K with deuterated water (D_2O) or dimethyl sulfoxide (DMSO-d6) and at 292 K with deuterated methanol (MeOD) using an AVANCE II 600 MHz NMR spectrometer a CPTCI microcryoprobe (Bruker). Bruker standard pulse programs were used.

3.2.3 Bacterial cultures

The marine bacteria *Marinobacter sp.* DG870, *Paracoccus sp.* AR04 and *Marinomonas sp.* LOF59-2 were used for the production of vibrioferrin (VF), petrobactin (PB) and woodybactin A (WBA), respectively. All strains were cultivated at 18 °C in Fe-deficient bacterial growth medium, prepared with Chelex 100 (Bio-Rad, USA) using the column method described by the manufacturer. Autoclaved growth medium (1 L) was filled into acid-washed and sterilized 2-L flasks

and inoculated with bacteria. The production of siderophores was monitored regularly by the CAS assay (Schwyn and Neilands 1987).

3.2.4 Siderophore standard preparation

CAS-active bacterial cultures were centrifuged (14000 rpm) and the supernatants concentrated on a column packed with polystyrene/divinylbenzene resin (Diaion HP20) and desalted with ultrapure water. Retained material was eluted with methanol and dried under vacuum. The crude extracts were dissolved in minimal amounts of ultrapure water and fractionated by time on a C18 semipreparative HPLC. CAS-active fractions were combined and concentrated under vacuum. Aliquots of purified and dried extracts were dissolved in deuterated DMSO-d6 (WBA), MeOD (PB), or D_2O (VF), respectively. Each solvent contained an internal standard, namely tetramethylsilane (conc. 7.36×10^{-2} mol × L^{-1}) in DMSO-d6, dioxane (conc. 1.17×10^{-2} mol × L^{-1}) in MeOD, and dimethyl sulfoxide (conc. 1.88×10^{-3} mol × L^{-1}) in D_2O, respectively. Peak integration and quantification was done by multiplet analysis in MestreNova 11.0. Woodybactin B (Figure SI 11) was quantified with the integrals of C-7 (4.14 ppm, q, J = 8.0 Hz, 1 H), C-14 (2.33 ppm, t, J = 7.8 Hz, 1H) and C-20 (0.86 ppm, t, J = 6.8 Hz, 3H). Petrobactin (Figure SI 10) was quantified with the integrals of C-4/C-5 (6.92 – 6.78 ppm, 4 H), C-11 (2.97 ppm d, J = 8.7 Hz, 4 H), C-16 (2.78 – 2.51 ppm, 4 H) and C-13 (1.75 ppm, s, 4H). Vibrioferrin (Figure SI 12) was quantified using the integrals of C-3'' (1.47 ppm, d, J = 7.2 Hz, 3H). The presence of each siderophore in the purified fractions was confirmed by MS^2 experiments (Figure SI 7).

3.2.5 Elution conditions

3 mL SPE cartridges (Chromabond, Macherey-Nagel) were packed with 200 mg of TiO_2. Columns were conditioned prior to use with 6 mL of 0.25 M NaH_2PO_4 at pH 2.4, followed by 6 mL of ultrapure water, 6 mL of 20 mM NaOH and 18 mL of ultrapure water. Samples (0.5 M NaCl, pH 4, 2 mL) containing either 10 µM of one or 10 µM of all four model siderophores (DFOB, VF, PB and WBA) were processed with one column. The flow rate was adjusted to one drop per second. Subsequently, SPE cartridges were washed with 6 mL of ultrapure water before elution with 2 × 1 mL of elution solutions (ESs 1-32) or organic solvents (acetonitrile, acetone or methanol). Elution solutions were prepared by dissolving the corresponding salts in ultrapure water and pH adjustment was conducted with HCl or NaOH. To avoid any matrix or sample effects caused by the different elution solution compositions (Figure SI 4 and Figure SI 6), counter solutions (Table SI 2) have been prepared in advance to unify the matrix of all eluates prior to analysis. 50 µL of elution solution were diluted with 450 µL of the corresponding counter solution directly after elution. In addition, ^{13}C–labelled phenylalanine and hydroxybenzoic acid were added to the counter solution to verify the comparability of the adjusted elution solutions (Figure SI 5). All experiments were conducted at pH 4 since pre-experiments showed that the adsorption

of the α-hydroxycarboxylate siderophore (VF) onto TiO_2 is favoured at weakly acidic conditions, whereas the hydroxamate (DFOB), catecholate (PB) and mixed ligand (WBA) showed no such distinct pH dependence (Figure SI 2). Each experiment was performed in triplicates. The adsorption efficiencies (calculated as amount of analyte detected in the SPE permeate in comparison to the original sample) for all tested siderophores were higher than 93% for all treatments and replicates prior to elution. Desorption efficiencies (%) were determined relative to the amount of adsorbed analyte.

3.2.6 Elution profiles

To investigate the impact of elution solution composition on the elution profile and whether TDAC is applicable for the specific purification of siderophores in dependence of their functional group 2 mL of a siderophore mixture containing 10 µM DFOB, PB, VF and WBA in 0.5 M NaCl at pH 4 were passed over four different 3 mL cartridges, containing 200 mg TiO_2. Cartridges were rinsed with 12 mL of ultrapure water before either ES7 (0.1 M NaH_2PO_4, pH 2.4), ES14 (0.1 M Na_2SO_4, pH 12.6), ES15 (5.6 M NH_3, pH 12.6) or ES17 (1 mM NaH_2PO_4, pH 2.4) were used for elution. The choice of selected elution solutions used in this experiment is based on the results of the elution solution optimization experiment displayed in Table 2. Fractions of 8 × 1.0 mL were collected and elution solutions were diluted with the corresponding counter solution directly after elution.

3.2.7 Siderophore purification from bacterial culture media

50 mL of cell-free and CAS negative bacterial culture supernatant was adjusted to pH 4 using hydrochloric acid (32%) and spiked with DFOB (3.75 µM final concentration), PB, VF and WBA (75 µM final concentration each). We chose a bacterial culture supernatant as complex sample matrices because these contain a mixture of highly concentrated and chemically diverse compounds that often interfere with chromatographic purification and detection (e.g., salts, polysaccharides, lipids, proteins). The 6 mL, 500 mg TiO_2 SPE cartridge was conditioned as described above and the sample was applied at a flow rate of less than one drop per second. The column permeate (~50 mL) was collected and directly measured by LC-HRMS. The column was washed with 12 mL of ultrapure water, 6 mL of methanol and again 12 mL of ultrapure water. The column was eluted with 2 mL elution solution (ES3: 0.5 M NaH_2PO_4, pH 2.4). The added elution solution was kept on the column overnight to achieve maximum desorption (10 h). The eluate was measured via LC-HRMS without any further steps. Quantification of eluated siderophores was achieved with an external calibration line in the corresponding elution solution.

3.2.8 Untargeted siderophore screening

To screen for siderophores 3 mL of pH adjusted (pH 4), cell-free bacteria culture supernatant (*Pseudoalteromonas sp*. LOF198-2 and *Marinomonas sp.* LOF59-2) were extracted with 200 mg of fresh TiO_2 3 mL SPE cartridges. The supernatant of culture LOF198-2 showed strong CAS activity without any concentration prior to the assay whereas the supernatants of LOF59-2 and LODSC8-1 showed almost no CAS activity. Columns have been prepared similarly to the experiments already described. The first milliliter of permeate was collected and cartridges were washed with 6 mL ultrapure water, 6 ml 0.5 M NaCl pH 4 and had been eluated with either 1.5 mL of ES3 (0.5 M NaH_2PO_4, pH 2.4) or (ES14 0.1 M Na_2SO_4, pH 12.6). The alkaline elution solutions were neutralized with concentrated HCl directly after extraction and measured via LC-HRMS. Medium blank was also processed similarly. All samples were prepared in triplicates. To facilitate the untargeted siderophore screening approach, LC-MS data was analyzed using the open-access platform, XCMS Online (Tautenhahn et al. 2012). XCMS Online offers solutions for the entire untargeted metabolomics workflow ranging from feature detection, retention time correction calculations to statistical analysis and metabolite assignment using different types of comparing data-processing jobs (Forsberg et al. 2018). In XCMS Online, features are defined as an ion with a unique *m/z* value and retention time (Tautenhahn et al. 2012). The primary job type used in XCMS, the pairwise analysis, identifies features whose relative intensity varies between sample groups and calculates different parameters including *p*-values. We applied this analysis approach to compare growth medium TDAC eluates with CAS active bacterial culture TDAC eluates to identify upregulated features, possibly corresponding to putative siderophores. Furthermore, to illustrate the effect of TDAC on sample complexity, another pairwise analysis was performed between the corresponding bacterial crude culture supernatants and growth medium blanks. The pairwise analysis was performed with the standard XCMS Online parameters ‘’UPLC / Orbitrap’’ in positive ionization mode.

3.3 Results and discussion

3.3.1 Optimal elution strategy of TDAC

The elution of strongly adsorbing siderophores, such as hydroxamates, from TiO_2 is only achieved by simultaneous adjustment of the elution solution pH and ionic strength (Egbers et al. 2020). To determine optimal desorption conditions of α-hydroxycarboxylate, hydroxamate and catecholate siderophores from TiO_2, 15 different elution conditions were evaluated in a single siderophore experiment. It was also investigated if co-adsorbed siderophores are having an effect on the desorption behaviour of each other in a siderophore-mix experiment. In case of the siderophore mix experiment 32 elution solutions were evaluated. The number of elution solutions in the siderophore-mix experiment was increased to determine if a sequential or specific

elution protocol of the four different siderophores could be applied. Siderophores were not detected in organic solvent eluates (Table 2) suggesting that siderophores did not adsorb on TiO_2 due to unspecific hydrophobic interactions. *The best desorption efficiency of the hydroxamate siderophore* DFOB were achieved with the alkaline ESs 12-14, containing 0.1 M phosphate, chloride or sulphate at pH 12.6 (up to 79.9 ± 1.7%, Table 2). It was also shown that other adsorbed siderophores did not change the elution behavior of DFOB from TiO_2, resulting in desorption efficiencies of up to 82.4 ± 5.5%. The observed elution behavior of DFOB was in accordance with the optimized elution conditions of DFOB from TiO_2 nanoparticles.(Egbers et al. 2020) ES15 (NH_3, pH 12.6) showed poorer desorption efficiencies for the single DFOB sample (39.1 ± 1.2%) as well as for the siderophore mix sample (37.4 ± 2.9%) compared to the ESs 12-14, emphasizing that DFOB desorption required higher ionic strength. The anions used in the alkaline elution solution had almost no impact on the observed desorption efficiencies whereas under acidic conditions the presence of chloride and sulfate resulted in negligible elution of adsorbed DFOB. Only the addition of citrate and phosphate increased elution of DFOB under acidic conditions. Phosphate is the hardest Lewis base among the tested anions and may therefore compete most with adsorbed siderophores for Lewis acid binding sites on the TiO_2. This is supported by literature demonstrating that phosphate anions form strong bidentate inner-sphere surface complexes under acidic conditions with different metal oxide surfaces (Connor and McQuillan 1999). Surprisingly, increased phosphate concentrations in ES1 (5 M NaH_2PO_4, pH 2.4) did not lead to higher desorption efficiencies of adsorbed DFOB (29.3 ± 3.9%) than ES3 (28.9 ± 2.2%), containing only a tenth of the phosphate compared to ES1. Whereas ES3 showed better desorption efficiency than ES7 (0.1 M NaH_2PO_4, pH 2.4) (20.7 ± 2.1%). This may be explained with phosphate being a kosmotrope, therefore the elution solution viscosity increases with phosphate concentration (Collins 1997). We interpret the lower desorption efficiencies at near-saturated phosphate concentrations as a consequence of increased viscosity and the resulting poorer exchange between stationary and liquid phases. The addition of Ca^{2+} (ES6, 0.5 M $NaH_2PO_4/CaCl_2$, pH 2.4) did not alter the desorption of DFOB from TiO_2 in contrast to the desorption of DFOB from natural soil samples (Rai et al. 2020). This result underlined that the positively charged terminal amine group was not involved in the DFOB TiO_2 interaction. *The best desorption efficiencies of the α-hydroxycarboxylate siderophore* VF in the single siderophore experiment was obtained with the acidic phosphate eluents ES1 (56.5 ± 5.2%), ES3 (58.2 ± 4.4%) and ES7 (49.4 ± 1.3%). Surprisingly, the use of citric acid (ES10) as a competing agent did not result in increased displacement of VF (21.8 ± 3.2%) compared to phosphate, although it was expected that the α-hydroxycarboxylate groups of VF should be labile to substitution with the same functional group if present in high concentrations. Besides citric acid, the addition of sulfate under acidic conditions resulted in a similar desorption efficiency of VF (20.3 ± 1.7%). Only chloride did not enhance the elution VF. This may be explained with the fact that sulphate ions form mono- or bidentate inner-sphere surface complexes with TiO_2 under acidic conditions

similar to phosphate, whereas chloride anions are likely to form only monodentate inner-spherical or weaker outer-spherical complexes. Comparing the results of the single siderophore experiment with the data of the siderophore-mix experiment, the interpretation is that co-adsorbed siderophores affect the desorption behavior of VF. In general, the observed desorption efficiencies are reduced, especially in case of the citrate containing elution solution ES10 (down to 2.7 ± 0.4%). This difference highlights that further studies are needed to understand what effects are involved in the desorption of VF from TiO_2. *The best desorption of the catechol-type siderophore* PB in the single siderophore as well as in the siderophore-mix experiment was achieved with the alkaline ammonia elution solution ES15 (73.1 ± 6.1% and 69.6 ± 11.4%, respectively). These findings did not fit the expectations since catecholates are labile to oxidation under alkaline conditions (Herlinger et al. 1995). The second best desorption efficiencies (69.3 ± 2.5% and 45.6 ± 8.6%, respectively) were observed for the acidic phosphate elution solution ES1 (5 M NaH_2PO_4, pH 2.4). In comparison to the other siderophores, it is noticeable that only in the case of PB better desorption efficiencies were observed for ES1 than for ES3 or ES7. However, this confirmed previous findings of catechol desorption from TiO_2 under acidic conditions (Kurepa et al. 2014; Liang et al. 2014; Khan et al. 2017). ES10 (citric acid 20%), previously tested for flavonoid desorption from TiO_2 (Khan et al. 2017), resulted only in a desorption efficiency of less than 20%, similar to the observed desorption efficiencies for the other siderophores. As expected, ES5 (0.5 M Na_2SO_4, pH 2.4) did not increase the desorption of PB (< 5%), because sulphate anions show lower affinities for TiO_2 than catecholates under acidic conditions (Petrone 2013). PB desorption efficiencies with ES1, ES3, ES4 (0.5 M NaCl, pH 2.4), ES7 and ES11 (0.5 M NaH_2PO_4, pH 7) supported the effect of phosphate concentration and pH on catechol desorption from TiO_2: A low pH alone (ES4, < 2%) as well as phosphate at neutral conditions did not recover PB (ES11, < 5%), while the combination of both factors with increasing phosphate concentrations leads to increased desorption efficiencies. Contrary to our expectations, PB was detected in all alkaline elution solutions even with the highest desorption efficiency observed for ES15. Gulley-Stahl *et al.* showed that the catechol surface complex formed on TiO_2 depends on the pH during adsorption (Gulley-Stahl et al. 2010). Acidic conditions (pH 3) led to the binding via two hydrogen bonds or to the monodentate binding, whereas neutral-alkaline conditions lead to mono- or binuclear bidentate binding (Gulley-Stahl et al. 2010). Because the bidentate complexation exhibits higher binding strength to the TiO_2 surface (Yu et al. 2013) these findings suggest that at pH 4, PB forms mono- and bidentate catecholate TiO_2 complexes simultaneously, possibly leading to different conditions necessary for their desorption. This in turn may be the reason for PB detected in the acidic phosphate and the alkaline elution solutions. Why the composition of the alkaline elution soluions had an effect on the desorption efficiency of PB needs further investigation. *The best desorption efficiencies of the mixed hydroxamate- α-hydroxycarboxylate-type siderophore* WBA was achieved with alkaline elution solutions ES12 and ES14 (> 70%). The desorption behaviour and observed efficiencies

of WBA were similar to the hydroxamate-type DFOB but differed from the α-hydroxycarboxylate-type VF. This observation suggests that the hydroxamate group in WBA (Figure 3) had a greater influence on the interaction with the TiO_2 surface than the α-hydroxycarboxylate group. The composition of the alkaline elution solutions (ESs 12-15) changed the elution of WBA in contrast to DFOB. Although phosphate, sulphate and chloride have no affinity to TiO_2 under alkaline conditions due to electrostatic repulsion (Kazarinov et al. 1981; Connor and McQuillan 1999; Horányi 2003), we observed increased elution of the mixed-type siderophore WBA with alkaline phosphate and sulphate elution solutions. This result may be attributed to differences in the ionic strength and Lewis base hardness of the ions and requires further investigation. WBA showed the worst desorption efficiencies for the acidic phosphate elution solution compared to the three different model siderophores raising the question if the desorption of WBA is rendered by increasing viscosity.

Table 2. Desorption efficiencies of desferrioxamine B, vibrioferrin, petrobactin and woodybactin A from 3 mL, 200 mg TDAC depending on solution composition and pH.

Elution solution	Composition	Desorption efficiency (%)							
		DFOB		VF		PB		WBA	
		Single	Mix	Single	Mix	Single	Mix	Single	Mix
ES1	5 M NaH_2PO_4, pH 2.4	29.3 ± 3.9	25.3 ± 1.6	56.5 ± 5.2	35.3 ± 1.5	69.3 ± 2.5	45.6 ± 8.6	3.2 ± 0.5	ND
ES2	5 M NaCl, pH 2.4	1.7 ± 0.4	2.6 ± 0.6	ND	ND	ND	ND	ND	1.2 ± 0.8
ES3	0.5 M NaH_2PO_4, pH 2.4	30.4 ± 1.6	28.9 ± 2.2	58.2 ± 4.4	49.2 ± 1.8	30.2 ± 3.5	23.3 ± 7.4	18.2 ± 8.0	12.8 ± 1.5
ES4	0.5 M NaCl, pH 2.4	2.0 ± 0.2	3.9 ± 1.2	ND	ND	1.2 ± 0.4	ND	ND	1.5 ± 0.5
ES5	0.5 M Na_2SO_4, pH 2.4	7.5 ± 0.2	9.9 ± 1.4	20.3 ± 1.7	10.8 ± 1.0	1.3 ± 0.1	2.7 ± 1.9	ND	1.8 ± 0.6
ES6	0.5 M $NaH_2PO_4/CaCl_2$, pH 2.4	13.1 ± 0.7	14.0 ± 2.0	20.3 ± 2.3	19.2 ± 2,4	23.1 ± 1.1	14.8 ± 1.9	17.3 ± 9.1	12.9 ± 3.1
ES7	0.1 M NaH_2PO_4, pH 2.4	18.5 ± 1.5	20.7 ± 2.1	49.4 ± 1.3	29.8 ± 1.9	6.8 ± 2.4	3.5 ± 1.2	20.8 ± 6.4	7.6 ± 2.1
ES8	0.1 M NaCl, pH 2.4	1.0 ± 0.2	1.2 ± 0.2	ND	2.5 ± 0.3	1.3 ± 0.4	ND	ND	ND
ES9	0.1 M Na_2SO_4, pH 2.4	3.6 ± 1.0	5.1 ± 0.5	3.5 ± 0.7	3.5 ± 0.4	1.1 ± 0.4	ND	ND	ND
ES10	Citric acid 20%	21.4 ± 5.8	19.5 ± 4.0	21.8 ± 3.2	2.7 ± 0.4	18.8 ± 1.5	15.4 ± 2.2	16.9 ± 3.3	8.1 ± 3.8
ES11	0.5 M NaH_2PO_4, pH 7	30.5 ± 2.7	29.4 ± 3.9	24.5 ± 6.8	22.5 ± 0.6	2.9 ± 1.2	3.5 ± 1.4	20.9 ± 4.2	16.8 ± 4.7
ES12	0.1 M NaH_2PO_4, pH 12.6	79.9 ± 1.7	82.4 ± 5.5	ND	ND	43.3 ± 0.2	31.6 ± 7.8	78.7 ± 11.1	68.4 ± 5.0
ES13	0.1 M NaCl, pH 12.6	68.6 ± 1.8	68.0 ± 0.4	5.7 ± 2.5	10.7 ± 1.6	32.1 ± 0.4	20.2 ± 6.2	59.1 ± 9.2	49.4 ± 3.4
ES14	0.1 M Na_2SO_4, pH 12.6	73.9 ± 1.8	73.8 ± 2.4	ND	ND	22.5 ± 0.4	19.1 ± 4.1	71.6 ± 7.7	66.3 ± 4.6
ES15	5.6 M NH_3, pH 12.6	39.1 ± 1.2	37.4 ± 2.9	ND	ND	73.1 ± 6.1	69.6 ± 11.4	32.6 ± 4.4	11.9 ± 5.8
ES16	10 mM NaH_2PO_4, pH 2.4	/	6.8 ± 2.1	/	8.7 ± 0.6	/	ND	/	4.9 ± 1.4
ES17	1 mM NaH_2PO_4, pH 2.4	/	ND	/	13.5 ± 1.0	/	ND	/	2.8 ± 1.4
ES18	0.1 mM NaH_2PO_4, pH 2.4	/	ND	/	1.8 ± 0.3	/	ND	/	1.8 ± 1.7
ES19	0.1 M NaH_2PO_4, pH 7.0	/	13.6 ± 1.4	/	25.4 ± 2.0	/	ND	/	10.1 ± 0.9
ES20	0.1 M NaH_2PO_4, pH 9.0	/	15.7 ± 2.5	/	11.0 ± 0.3	/	ND	/	20.7 ± 2.0
ES21	0.1 M NaH_2PO_4, pH 10.0	/	25.2 ± 5.2	/	5.0 ± 0.4	/	1.4 ± 1.3	/	10.0 ± 0.3
ES22	0.1 M NaH_2PO_4, pH 11.0	/	39.3 ± 4.1	/	10.4 ± 0.3	/	3.1 ± 2.0	/	18.1 ± 7.4
ES23	5.6 M NH_3, pH 11.0	/	43.7 ± 6.3	/	ND	/	15.2 ± 5.1	/	9.1 ± 1.1
ES24	5.6 M NH_3, pH 10.0	/	35.6 ± 3.4	/	ND	/	7.8 ± 2.0	/	16.4 ± 1.1
ES25	10 mM NaH_2PO_4, pH 4.0	/	5.0 ± 1.0	/	ND	/	ND	/	1.5 ± 1.3
ES26	10 mM NaH_2PO_4, pH 7.0	/	ND	/	7.7 ± 0.2	/	ND	/	3.4 ± 1.8
ES27	10 mM NaH_2PO_4, pH 9.0	/	3.2 ± 0.8	/	6.5 ± 0.5	/	ND	/	6.8 ± 1.0
ES28	10 mM NaH_2PO_4, pH 10.0	/	5.5 ± 1.3	/	4.8 ± 0.6	/	ND	/	6.3 ± 1.8
ES29	1 mM NaH_2PO_4, pH 4.0	/	ND	/	ND	/	ND	/	ND
ES30	1 mM NaH_2PO_4, pH 7.0	/	ND	/	ND	/	ND	/	ND
ES31	1 mM NaH_2PO_4, pH 9.0	/	ND	/	2.1 ± 0.3	/	ND	/	ND
ES32	1 mM NaH_2PO_4, pH 10.0	/	ND	/	2.2 ± 0.3	/	ND	/	4.0 ± 1.7
ES33	Acetonitrile	/	ND	/	ND	/	ND	/	1.2 ± 0.5
ES34	Acetone	/	ND	/	ND	/	ND	/	2.1 ± 1.1
ES35	Methanol	/	ND	/	ND	/	ND	/	1.2 ± 1.1

ND = not detected, DFOB = Desferrioxamine B, VF = Vibrioferrin, PB = Petrobactin, WBA = Woodybactin A. More intense green coloration shows better desorption efficiency.

3.3.2 Elution profiles of siderophores from TiO_2

We tested if the different elution behaviour of hydroxamates, catecholates and α-hydroxycarboxylates from TiO_2 allowed the selective purification of a sample with multiple siderophore types. For the selective purification of the four different siderophores, the elution solutions ES7, ES14, ES15 and ES17 were investigated. These four elution solutions were chosen because the desorption efficiencies for the siderophore-mix experiment (Table 2) suggested that these elution solutions could lead to the enrichment of one of the siderophores at a time. The elution profile obtained for ES7 (Figure 11A) displays that under these conditions (0.1 M NaH_2PO_4, pH 2.4) VF and DFOB showed a similar elution behaviour, with the majority of the desorbed siderophore detected in the second millilitre of eluate.

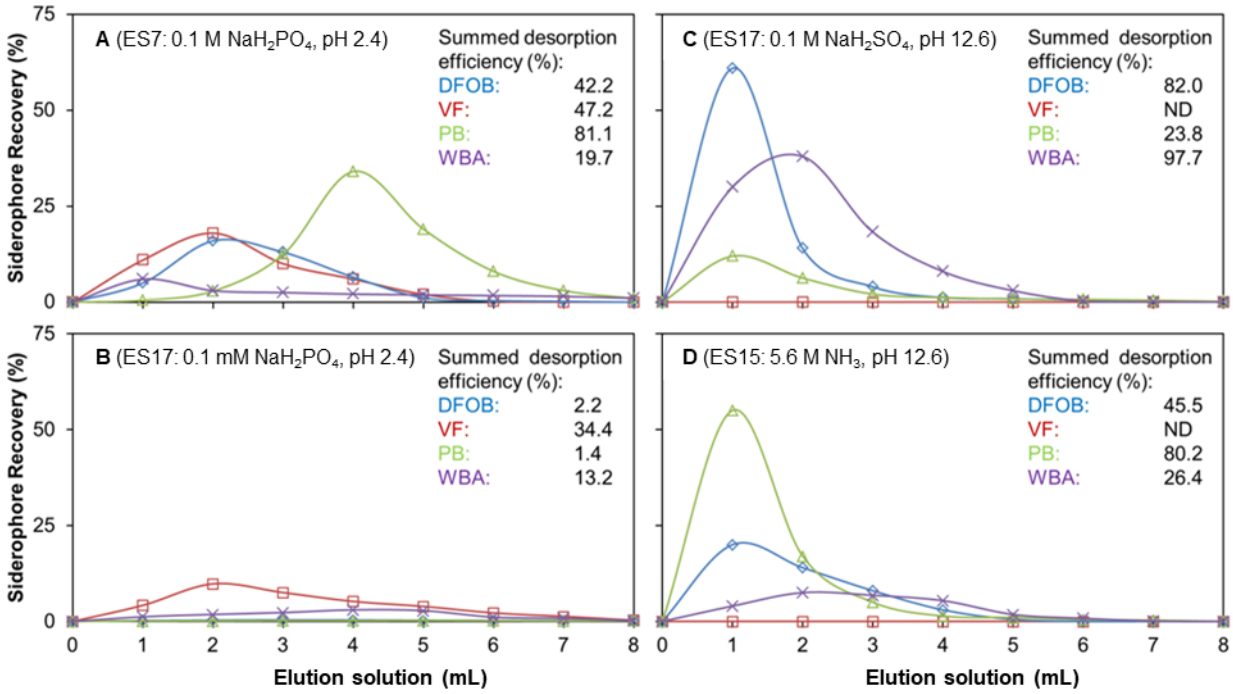

Figure 11. Elution profiles of an equimolar solution (10 µM) of DFOB (blue diamonds), VF (red squares), PB (green triangles) and WBA (purple crosses) in 2 mL of 0.5 M NaCl (pH 4) , using a 3 mL, 200 mg TiO_2 column in 1 mL fractions. Columns were washed with 12 mL ultrapure water before elution. Elution was conducted with four different elution solutions (A-D). The summed recoveries of the four model siderophores for all fractions are also displayed in each chromatogram.

The overall desorption efficiency for VF and DFOB were determined as 47.2% and 42.2%, respectively. However, particularly remarkable about this profile is the elution behaviour of PB. The desorption efficiency of ES7 was not considered to be particularly high for PB, as only a desorption efficiency of 3.5 ± 1.2% was detected at an elution volume of 2 mL. It appears that by quadrupling the volume, the desorption efficiency was increased up to 81.1%. In contrast to the other siderophores, the eluated PB was not concentrated at an elution volume of 2 mL but at 4 mL. Whereas the desorption efficiency for WBA could not be increased by increasing the

volume. Using ES17 (1 mM NaH_2PO_4, pH 2.4) as the elution solution led to a drastic change in the elution profiles compared to ES7 (Figure 11B). The decreased phosphate concentration caused the collapse of DFOB and PB desorption efficiencies (2.2% and 1.4%, respectively), whereas the desorption efficiency of VF remained above 34%. WBA also did not show such distinct changes in desorption efficiency. The elution profiles obtained for ES14 show a more rapid elution of DFOB and PB compared to the ones observed for ES7 (Figure 11C). Especially, in case of DFOB, roughly 75% of the eluated siderophore (summed desorption efficiency 82%) was detected in the first fraction. The highest desorption efficiency for ES14 was detected for WBA with 97.7%.In addition, WBA showed a less distinct elution profile than DFOB. VF, on the other hand, was not detected in any of the eight fractions, which is consistent with the results in Table 2. Despite the same pH value, the elution profiles of ES14 and ES15 differ considerably (Figure 11D). DFOB and WBA showed a broader elution profile whereas the elution of PB was enhanced, resulting in 80.2% desorption efficiency with the majority of eluted PB detected in the first fraction. Similar to the results for ES14, VF was also not detected in any of the elution fractions of ES15. Our results suggested that a single-step elution with acidic phosphate elution solution (> 0.1 M phosphate) is most suited for the untargeted concurrent screening of all siderophore classes. If, on the other hand, a specific siderophore class is targeted, the elution profiles obtained recommend tailoring the extraction protocol to the composition of the sample.

3.3.3 Siderophore extraction from complex sample matrices

The performance of TDAC for purification of siderophores from complex sample matrices was tested using a bacterial culture supernatant spiked with four model siderophores DFOB, VF, PB, and WBA. The total recoveries were determined as 62%, 45%, 82% and 25% respectively. These recoveries were similar to the summed desorption efficiencies observed under clean sample conditions with no organic background using 8 mL of the less concentrated phosphate elution solution ES7 for elution (Figure 11A). Therefore TDAC is robust against high concentrations of contaminants present in bacterial growth media which typically contain a plethora of possible co-eluting and interfering compounds. The recovery of DFOB out of the bacterial culture supernatant sample was higher than in the clean sample when only 2 mL of elution solution were used for elution (Table 2). This observation probably resulted from the fact that we extended the exposure time of the TDAC SPE column to the acidic phosphate elution solution ES3 (10 h). The chromatograms and mass spectra of the crude bacterial culture supernatant sample and the TDAC eluate, confirmed the high specificity of TDAC for siderophore purification from complex sample matrix (Figure 12), since the background-subtracted base peak chromatogram of the crude bacterial culture supernatant sample revealed more peaks than the chromatogram of the TiO_2 eluate. Peak **1** correlates to apo-VF ($[M+H]^+$ = $C_{16}H_{23}N_2O_{12}$, *m/z* 435.1246), as shown by the corresponding mass spectrum (Figure 12B1).

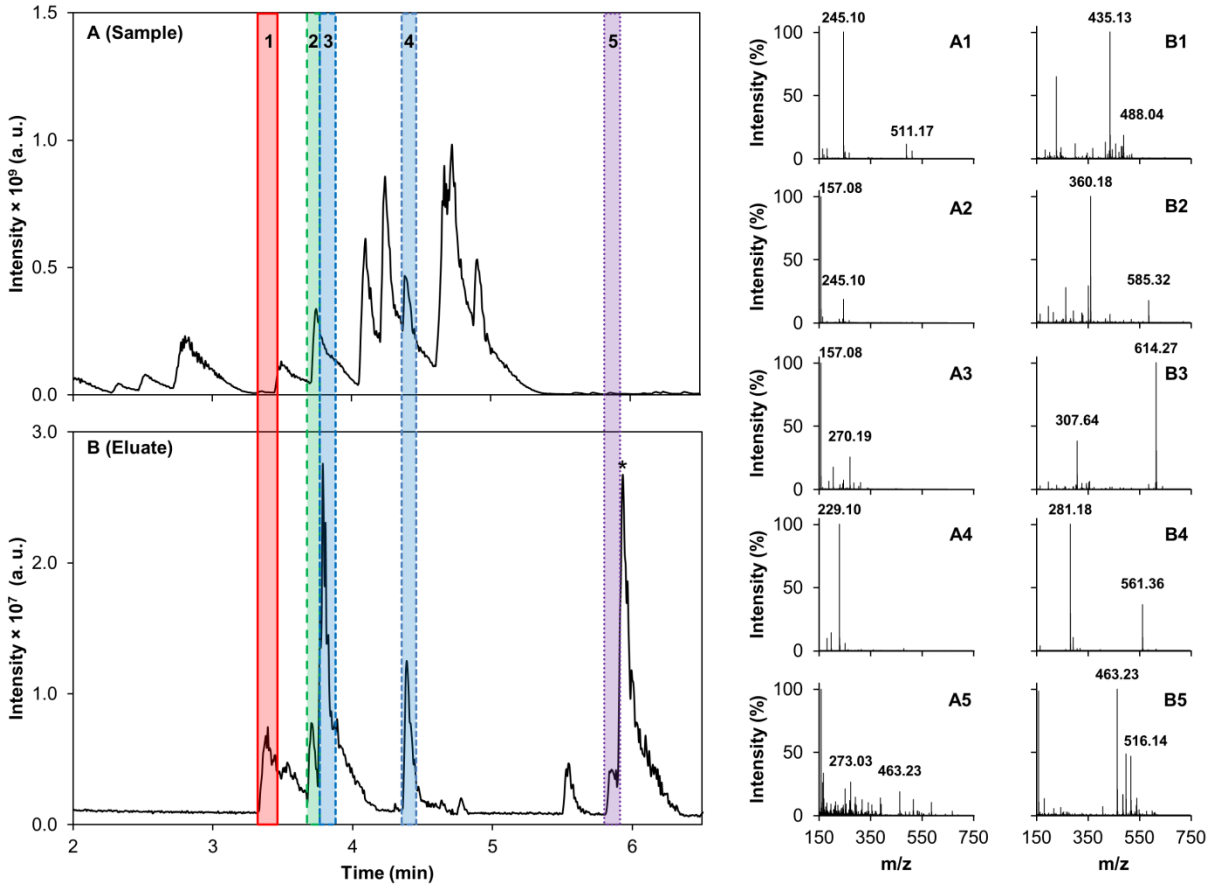

Figure 12. Background-subtracted base peak chromatograms (LC-ESI(+)-HRMS) of (A) 50 mL CAS negative crude bacterial culture supernatant spiked with DFOB, VF, PB and WBA (final concentration of 3.75, 75, 75 and 75 µM, respectively), adjusted to pH 4 and (B) TiO_2 cartridge eluate (0.5 M NaH_2PO_4, pH 2.4). The colored areas mark the time window used to extract mass spectra A1-B5.

Peak **2** was assigned to the doubly charged apo-PB ($[M+2H]^{2+}$ = $C_{34}H_{52}N_6O_{11}$, *m/z* 360.1842) (mass spectrum B2). DFOB ($[M+H]^+$= $C_{25}H_{49}N_6O_8$, *m/z* 561.3606) (Figure 12B4), was detected at 4.39 min (**4**) and the corresponding Fe(III)-complex FOB at 3.71 min (**3**) ($[M+H]^+$ = $C_{25}H_{46}N_6O_8Fe$, *m/z* 614.2721) (Figure 12B3). Peak **5** was assigned to apo-WBA ($[M+H]^+$ = $C_{20}H_{35}N_2O_{10}$, *m/z* 463.2286) (Figure 12B5). Notably, the total number of peaks in the base peak chromatogram as well as the number of coeluting ions were reduced by TDAC (Figure 12A vs. B). These data also showed the enrichment of siderophores in the base peak chromatogram (Figure 12D), resulting in less complex mass spectra. However, the second most intense peak in the base peak chromatogram of the eluate did not correlate to any of the *m/z* values used for quantification. Raising the question which compound was also enriched using the TDAC method. The marked base peak at 5.92 min is attributed to an $[M+H]^+$ ion with an *m/z* value of 445.2179. MS^2 experiments revealed that *m/z* 445.2179 showed a similar fragmentation pattern than WBA, forming the same daughter ions, but in a different ratio (Figure 13).

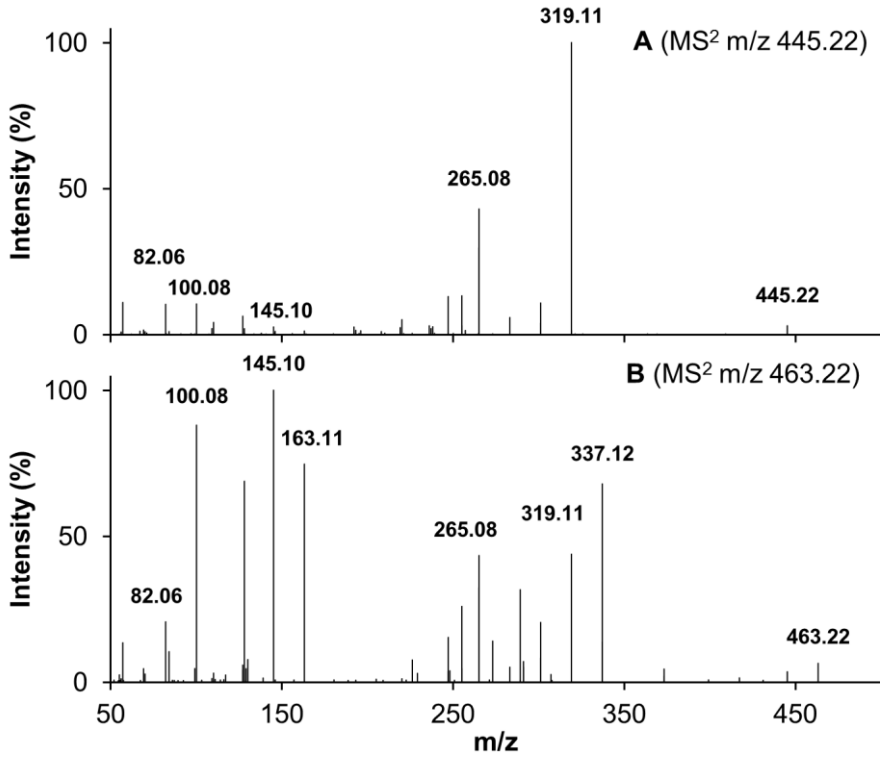

Figure 13. (A) MS^2 spectra of [M+H]$^+$ = *m/z* 445.22 corresponding to the marked peak (*) at 5.92 min in Figure 12C. (B) MS^2 spectra of [M+H]$^+$ = *m/z* 463.22 corresponding to WBA (Peak 5) at 5.87 min.

In combination with the mass difference of 18 u between *m/z* 445.2179 and WBA ([M+H]$^+$ = $C_{20}H_{35}N_2O_{10}$, *m/z* 463.2286) it was concluded that the observed base peak corresponds to WBA-H_2O ([M+H]$^+$ = $C_{20}H_{33}N_2O_9$, m/z_{cal} 445.2181, *Δppm* -0.35). However, no corresponding Fe(III) complex was detected. This *m/z* value was also detected in the original WBA standard but not in the permeate of this spiked bacterial culture supernatant sample. This observation suggested that the water loss from WBA was not a result of extraction with TiO_2 or elution with acidic phosphate elution solution.

3.3.4 Untargeted siderophore screening

Currently, the untargeted screening for siderophores or in general metallophores is based on the formation of metal complexes so that the characteristic isotopic patterns of the complexed metals or the metals themselves are detectable, facilitating the identification of siderophores in highly complex samples (Boiteau et al. 2016; Aron et al. 2022). However, this approach is limited to siderophores whose metal complexes do not decay during chromatographic separation or ionization in the mass spectrometer. To overcome this limitation, we investigated whether TDAC in combination with statistical analysis of LC-HRMS data via XCMS Online is able to identify siderophores, independent of metal isotopic patterns, but only based on the TDAC extraction behavior.

Two CAS active bacterial cultures supernatants, *Pseudoalteromonas sp.* LOF198-2 and *Marinomonas sp.* LOF59-2, were extracted with TDAC and compared to growth medium TDAC eluates via XCMS Online pairwise analysis. In case of *Pseudoalteromonas sp.* LOF198-2 the two features with the highest observed intensities corresponded to *m/z* 619.36795 (p = 0.004314) and *m/z* 672.27737 (p = 0.007078). These two *m/z* values were assigned as DFOG1 ($[M+H]^+$ = m/z_{cal} 619.36612, $C_{27}H_{51}N_6O_{10}$, *Δppm* 2.96) and FOG1 ($[M-3H+^{56}Fe+H]^+$ = m/z_{cal} 672.27759, $C_{27}H_{48}N_6O_{10}{}^{56}Fe$, *Δppm* -0.32), respectively. The annotation was based on the fragmentation pattern of *m/z* 619.37 (Figure 14F), which was consistent with the known MS^2 spectra of DFOG1 (Feistner et al. 1993; Feistner and Hsieh 1995).

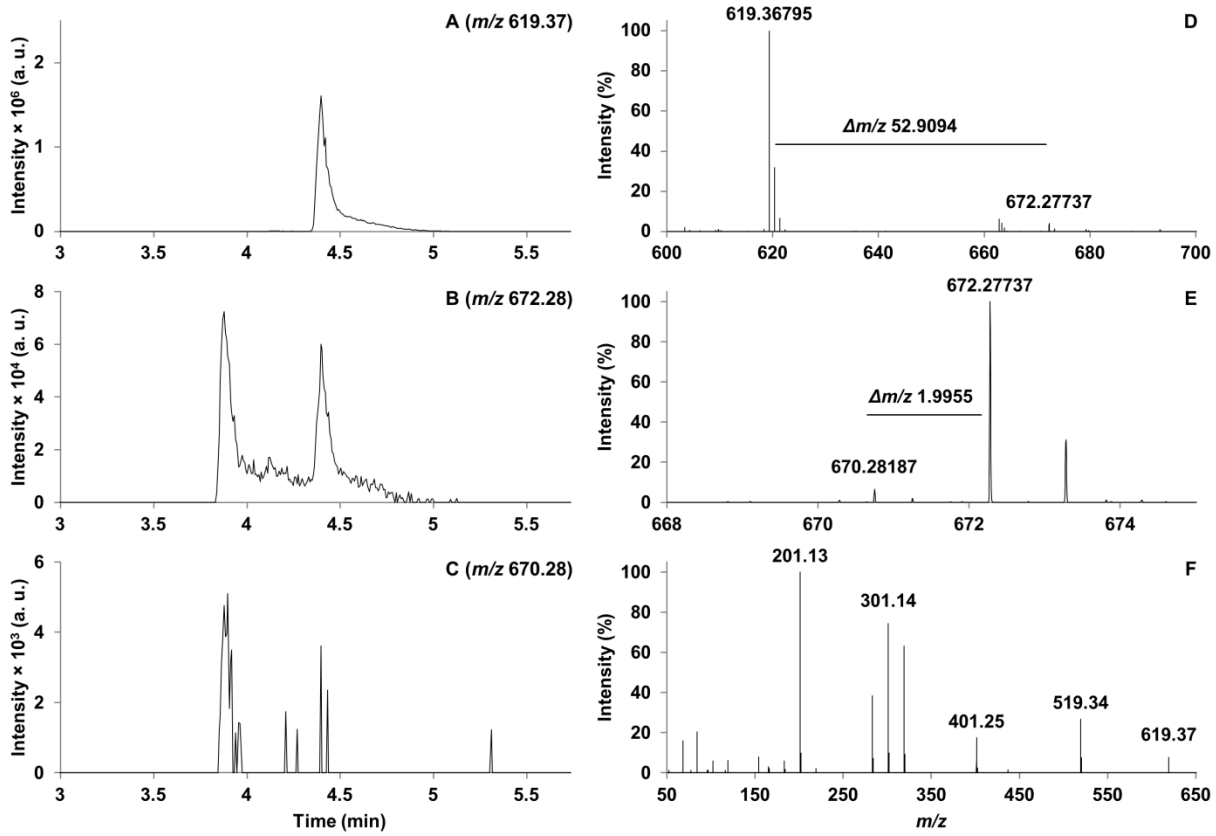

Figure 14. Comparison of EICs of (A) *m/z* 619.37, (B) *m/z* 672.28 and (C) *m/z* 670.28 with (D) corresponding mass spectra at 4.39 min and (E) 3.87 min. MS^2 spectrum of $[M+H]^+$ = *m/z* 619.37 is shown in (F). LC-HRMS and MS^2 data originated from *Pseudoalteromonas sp.* LOF198-2 TDAC eluate.

In addition, the observed *Δm/z* of 52.9094 and of 1.9955 with an intensity ratio of 6.35/100 (Figure 14D, E) indicated the iron isotopic pattern (Baars et al. 2014; Baumeister et al. 2018; Aron et al. 2022), which was confirmed by the chromatographic coherence of *m/z* 619.37 (DFOG1), *m/z* 672.28 (^{56}Fe-FOG1) and *m/z* 670.28 (^{54}Fe-FOG1) (Figure 14A-C). These observations fitted well to our expectations since this strain is known to produce DFOG1 (Egbers et al. 2020). However, no additional putative siderophores were identified via XCMS Online analysis of the obtained LC-HRMS data set of the *Pseudoalteromonas sp.* LOF198-2 TDAC eluates.

The XCMS Online pairwise analysis of *Marinomonas sp.* LOF59-2 TDAC eluates with growth medium TDAC eluates resulted in the detection of numerous features. In addition to the feature corresponding to WBA (*m/z* 463.22870, *Δppm* 0.17) (p = 0.005) more features were determined whose linked *m/z* values suggested a woodybactin like sum formula (Table 3).

Table 3. Significant *m/z* values detected in the TDAC eluate of *Marinomonas sp.* LOF59-2 assigned to woodybactin derivates.

Name	*p*-value	Measured *m/z* $[M+H]^+$	Theoretical *m/z* $[M+H]^+$	*Δppm*	Sum formula $[M+H]^+$
unknown WB (**1**)	0.00014	515.26070	515.25992	1.51	$C_{24}H_{39}O_{10}N_2$
^{56}Fe-WBB/ ^{56}Fe-WBC[a]	0.00038	530.15622	530.15574	0.91	$C_{21}H_{34}O_{10}N_2{}^{56}Fe$
^{56}Fe-WBD[a]	0.00247	544.17192	544.17139	0.98	$C_{22}H_{36}O_{10}N_2{}^{56}Fe$
unknown WB (**4**)	0.00262	588.19818	588.19760	0.98	$C_{24}H_{40}O_{11}N_2{}^{56}Fe$
WBA[a]	0.005	463.22870	463.22862	0.17	$C_{20}H_{35}O_{10}N_2$
unknown WB (**2**)	0.0038	507.25572	507.25484	1.74	$C_{22}H_{39}O_{11}N_2$
unknown ^{56}Fe-WB (**2**)	0.00545	560.16693	560.16630	1.12	$C_{22}H_{36}O_{11}N_2{}^{56}Fe$
unknown WB (**3**)	0.0079	449.21355	449.21297	1.29	$C_{19}H_{33}O_{10}N_2$
WBB/ WBC[a]	0.00926	477.24468	477.24427	0.86	$C_{21}H_{37}O_{10}N_2$
WBD[a]	0.02262	491.26043	491.25992	1.04	$C_{22}H_{39}O_{10}N_2$
unknown ^{56}Fe-WB (**3**)	0.03349	502.12510	502.12444	1.32	$C_{19}H_{30}O_{10}N_2{}^{56}Fe$
unknown WB (**4**)	0.03705	535.28652	535.28614	0.72	$C_{24}H_{43}O_{11}N_2$

[a] (Carmichael et al. 2019)

To verify the presence of such putative woodybactin derivates additional MS^2 experiments of the corresponding apo-siderophores were carried out. All MS^2 experiments resulted in similar fragmentation patterns (Figure 15), including the characteristic fragments *m/z* 100.08, 128.07, 145.10, 163.11 and 337.12 indicating for N^6-hydroxy-L-lysine (Martin et al. 2006; Gauglitz et al. 2012; Carmichael et al. 2019). These fragments are not only common to all known woodybactins (Carmichael et al. 2019) but also to ochrobactins (Martin et al. 2006).

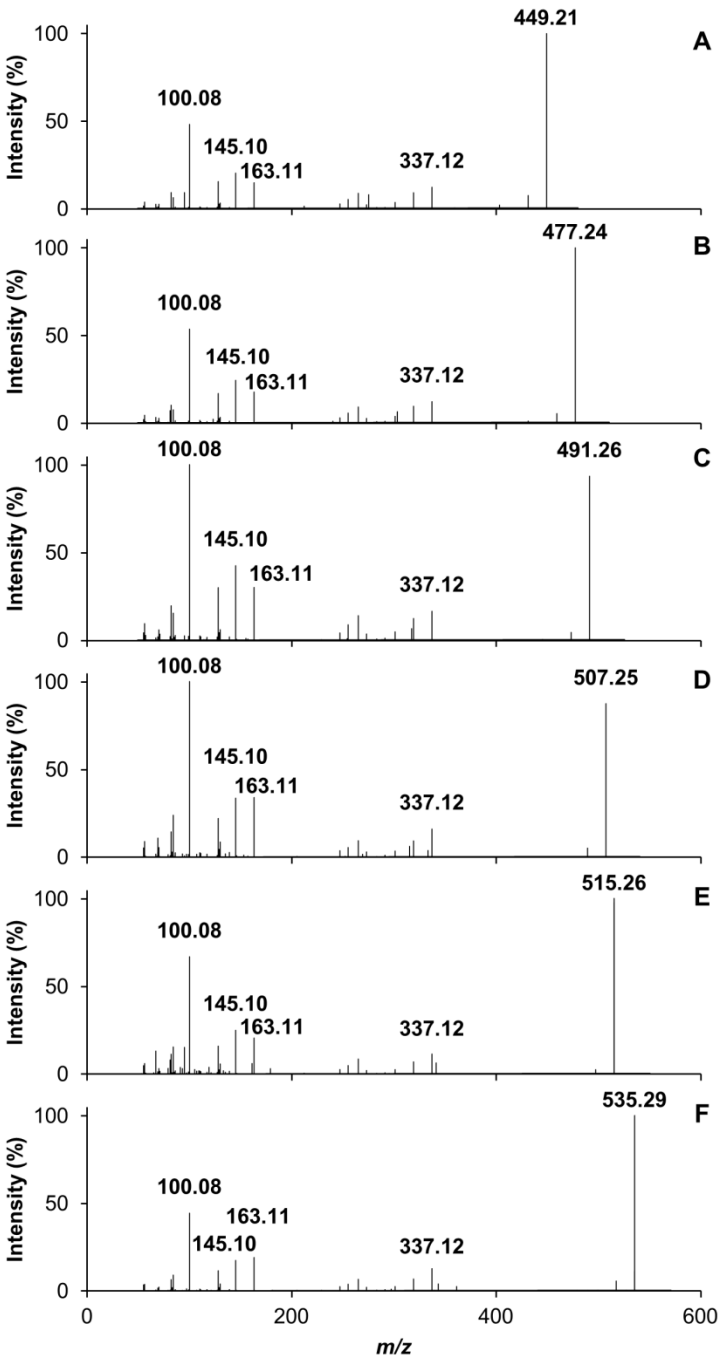

Figure 15. MS^2 spectra of significant *m/z* values detected in LOF59-2 TDAC eluate corresponding to apo-woodybactin derivates: (A) MS^2 *m/z* 449.21 (unknown WB (3)), (B) MS^2 *m/z* 477.24 (WBB or C), (C) MS^2 *m/z* 491.26 (WBD), (D) MS^2 *m/z* 507.25 (unknown WBD (2)), (E) MS^2 *m/z* 515.26 (unknown WB (1)) and (F) MS^2 *m/z* 535.29 (unknown WB (4)).

Besides the already known woodybactins WBA, WBB, WBC and WBD (Figure 16) the pairwise XCMS analysis shed light on four unknown woodybactin derivates (**1**-**4**) ([M+H]$^+$ = *m/z* 449, 507, 515 and 535) that were extracted via TDAC. Typical for the known woodybactins is a mass difference of 14 u, which corresponds to a single CH_2 unit change in the fatty acid appendage (Figure 16). However, only WB (**3**) fitted this pattern and indicated for a C_7 fatty acid appendage.

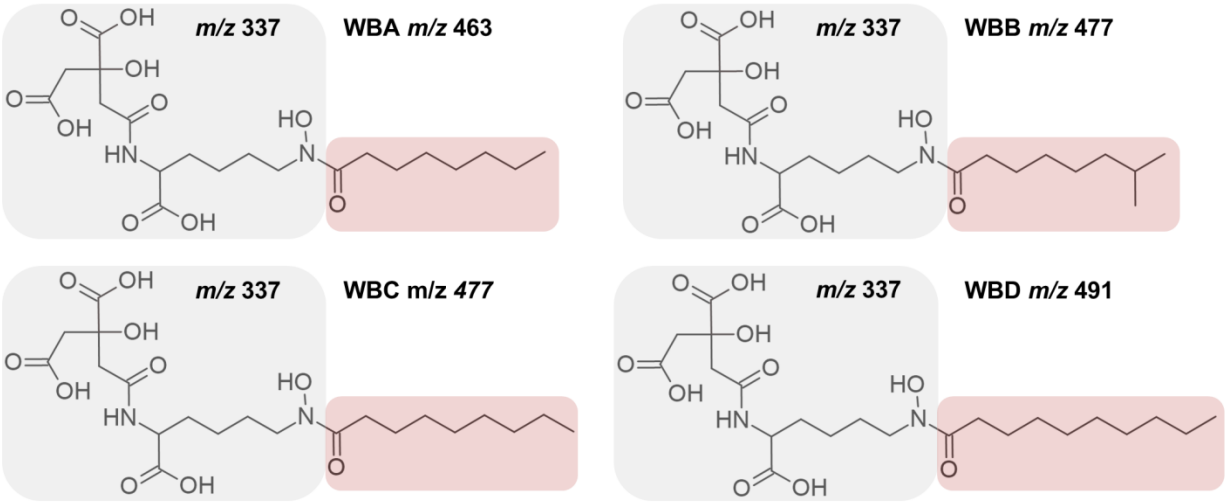

Figure 16. Molecular structures of woodybactins A-D with biggest similar fragment highlighted in grey and fatty acid appendage in red. Figure was adapted from (Carmichael et al. 2019).

Since the remaining woodybactin derivates (**1**, **2** and **4**) deviated from this trend but showed the characteristic fragments including *m/z* 337 (Figure 15), it was assumed that the structural differences had to be located in their fatty acid appendages. In case of WB (**1**), the detected *m/z* of 515.26070 in combination with the observed MS^2 spectra suggested the molecular formula of [M+H]+ = $C_{24}H_{39}O_{10}N_2$ (*Δppm* 1.51) indicating a doubly unsaturated C_{12} fatty acid appendage. This is the first time a woodybactin derivate with an unsaturated fatty acid moiety was identified. Although no woodybactins with unsaturated fatty acid residues were identified so far, unsaturated fatty acid appendages are common to a number of siderophores such as ochrobactins, marinobactins, aquachelins, amphibactins, acinetoferrin and rhizoferrin 1021 (Persmark et al. 1993; Okujo et al. 1994; Martinez et al. 2000, 2003; Martin et al. 2006). In contrast to WB (**1**), the MS data of WB (**2**) ($[M+H]^+$ = *m/z* 507.25572, $C_{22}H_{39}O_{11}N_2$, *Δppm* 1.74) and WB (**4**) ($[M+H]^+$ = *m/z* 535.28652, $C_{24}H_{43}O_{11}N_2$, *Δppm* 0.72) did not indicate an unsaturated fatty acid residue, but rather the presence of singly hydroxylated C_{10} or C_{12} fatty acid appendages, respectively. Hydroxy-fatty acid moieties are much less prominent in amphiphilic siderophores, but exceptions to this trend include certain amphibactins and potashchelins (Martinez et al. 2003; Li et al. 2020). However, distinct structural suggestions for the fatty acid residues of WB (**1**-**4**) cannot be made on the basis of the present MS and MS^2 data alone. For the structural characterization of the fatty acid groups, further investigations are necessary. Techniques like NMR, especially the correlation between ^1H-^{13}C HSQC and ^{13}C NMR spectra (Gauglitz et al. 2012), or GC-MS in combination with prior hydrolysis of the siderophores and subsequent esterification of the fatty acids (Martinez et al. 2003) would deliver the missing structural information.

In addition to the pairwise analysis between the TDAC eluates of CAS active bacterial cultures and TDAC eluates of growth medium blanks, a second pairwise analysis was performed be-

tween the corresponding crude bacterial culture supernatants and growth medium blanks. In case of *Pseudoalteromonas sp.* LOF198-2 the pairwise analysis of TDAC eluates resulted in the detection of 3574 feature hits in the bacterial culture TDAC eluate. Whereas the pairwise analysis of crude bacterial culture supernatants and growth medium showed 15462 feature hits. Similar to these results, the pairwise analysis of *Marinomonas sp.* LOF59-2 samples resulted in the detection of 3250 feature hits for the TDAC eluate but 15314 feature hits for the crude bacterial supernatant. This comparison of observed feature hits clearly illustrates the ability of TDAC to reduce sample complexity and thus facilitate siderophore identification.

3.4 Conclusion

In this study, we developed a titanium dioxide affinity chromatography (TDAC) for the selective purification of all major siderophore classes, i.e. catecholates, α-hydroxycarboxylates, hydroxamates and mixed ligands. The method is scalable utilizing ~ 50 µm diameter TiO_2 particles packed in SPE cartridges, robust against inorganic as well as organic contaminants, and yielded high levels of purification and recoveries for all tested siderophores. Optimal elution for each functional group/ siderophore-type was achieved with the adjustment of elution solution pH, type of counter anion or anion concentration. The hydroxamate siderophore DFOB, for example, showed the best elution with alkaline elution solutions containing phosphate, sulphate or chloride (DFOB desorption efficiencies of up to 82%), whereas the quantitative elution of the catecholate siderophore PB was possible with acidic phosphate or an alkaline ammonia elution solution (both cases approximately 70% desorption efficiency). The desorption efficiency for the α-hydroxycarboxylate containing siderophores VF und WBA differed clearly. VF showed best desorption efficiency with acidic phosphate elution solution (up to 58%) while WBA with its one hydroxamate group was only eluted quantitatively with alkaline elution solutions containing phosphate or sulphate (up to 78%). The measured differences in desorption efficiency suggested the separation of siderophore classes by their specific functional groups using different elution solution compositions. But our results clearly showed that TDAC did not allow such an approach with the investigated elution solutions. Instead, a single-step elution with acidic phosphate buffer (> 0.1 M phosphate) is most suited for the untargeted concurrent screening of all siderophore classes. If, on the other hand, a specific siderophore class is targeted, the elution profiles obtained recommend tailoring the extraction protocol to the composition of the sample. This strategy is a useful methodological addition to existing polarity- or molecular weight-based separation techniques when different siderophore classes are present in the same complex sample. Thus, the TDAC SPE method simplifies the screening of siderophores in biological or environmental samples. TDAC selectively purified siderophores and almost completely removed organic ‘contaminants’ from a bacterial culture supernatant mix containing all four types of model siderophores with recoveries of up to 82% (PB). In comparison to the crude sample, all sider-

ophores could be identified in the LC-HRMS base peak chromatograms. LC-HRMS was used for all analyses, however, siderophore detection and quantification is likely also possible with lower resolution mass spectrometers after TDAC SPE clean-up as suggested by the rather large mass range used for generating the extracted ion chromatograms (± 5 ppm). Furthermore, our results of the untargeted siderophore screening approach using TDAC in combination with statistical analysis via XCMS Online highlighted not also the capabilities of TDAC to facilitate the identification of unknown siderophores (WB (**1**-**4**)) in complex samples, but also that the number of feature hits was dramatically reduced by the use of TDAC, underlining the potential of this method to decrease sample complexity.

This new instrument may facilitate the discovery and quantification of siderophores in a variety of natural samples such as seawater, soil, or blood and urine. Especially in these habitats or samples, the identification of unknown iron ligands is the key to understanding far-reaching mechanisms or the starting point for new therapeutic approaches. Siderophores, independent of their structural composition are concentrated from complex samples via TDAC if the target analyte is present in reasonable concentrations. While this is likely sufficient for many research applications, a major methodological challenge will be to achieve the same recovery and selectivity for pM concentrations of siderophores in some natural samples, especially seawater. For this application, co-adsorption, self-assembly, metal contamination and natural phosphate concentrations will all interfere with the efficiency of TDAC. Nonetheless, we suggest that this method - as presented here - is robust against many chromatographically challenging conditions and will facilitate the study of microbial iron cycling, pathogenicity and symbiosis.

3.5 Acknowledgements

This work was supported by the Deutsche Forschungsgemeinschaft (DFG) in the framework of the priority program "Antarctic Research with comparative investigations in Arctic ice areas" SPP 1158 by the grant TE 1205/3-1 and by the University of Bremen Exploration Project 06A. Furthermore we thank Jennifer Bergemann for support with the bacterial cultures. We thank Alexandra Dürwald and Thomas Schweder for the Paracoccus strain.

4. Extraction of siderophores from seawater by means of TDAC

In Chapter 4 I investigated if TDAC could facilitate the specific extraction of siderophores from artificial and natural seawater, since it is of high interest to overcome the occurring extraction biases using traditional sorbents and therefore to be able to mirror the natural siderophore chemistry as precise as possible. However, I report in this chapter that the used TiO_2 sorbent showed drawbacks in terms of large volume extraction, possible caused by its low specific surface area. I was responsible for conducting all extraction experiments as well as all LC-HRMS measurements. The interpretation of the gained data and writing of this chapter was also my solely done by me. The used siderophore standards are the sane than the ones used in the previous chapter which were quantified via NMR by Christian Zurhelle.

4.1 Introduction

In order to gain a more detailed understanding of the bioavailability of iron in the world's oceans and thus develop more accurate models of the global carbon cycle, deciphering the composition of the marine iron ligand pool is of central importance. In this chapter we therefore investigated whether the developed TDAC method provides an unbiased view of the siderophores present in seawater.

More than 99% of all iron dissolved in seawater is complexed by organic ligands like siderophores, which are known to comprise one fraction of this diverse ligand pool (Gledhill and Buck 2012). Over the course of the last 20 years, several studies have been conducted to directly detect siderophores in seawater. But only ferrioxamines, amphibactins, synechobactins and petrobactin were identified in this period (Mawji et al. 2008; Velasquez et al. 2011; Boiteau et al. 2016, 2019b; Bundy et al. 2018; Manck et al. 2021). All those studies used apolar sorbents like ENV+ for the extraction and concentration of siderophores from sample volumes of up to 600 L. Detection of the siderophores was carried out using different LC-MS techniques. The most advanced approach used a post-LC flow splitter that allowed simultaneous acquisition of elemental data using ICP-MS and structural information using ESI-MS (Boiteau et al. 2016, 2019b). All the mentioned studies underlined the particular high concentrations of siderophores in the HNLC regions, but it was also found that siderophores are present in iron-replete regions like the subtropical North Atlantic, the tropical eastern South Pacific Ocean and the Californian coast (Mawji et al. 2008; Boiteau et al. 2016, 2019b). These observations seemed to be counterintuitive since siderophore production is expected to be down regulated under iron-replete conditions. Nevertheless, the addition of bioavailable inorganic iron stimulated the growth of phytoplankton under dissolved iron-replete conditions (King and Barbeau 2007) underlining the need to gain more knowledge about the chemical speciation of dissolved iron and its bioavailability to phytoplankton. Those studies revealed a significant variability of detected siderophores over a relatively short spatial and temporal scale (Boiteau et al. 2019b). Correlating the observed concentration of dissolved iron with the detected siderophore classes at discrete sampling sides led to the observation that in general, hydrophobic siderophores like amphibactins are observed in waters with low dissolved iron concentrations, whereas hydrophilic and strong iron complex forming ligands like ferrioxamines are present at relatively high iron concentration sites (Boiteau et al. 2016, 2019b; Bundy et al. 2018). In addition, photosensitive siderophores such as petrobactin and synechobactins were detected exclusively below 60 m water depth where the intensity of solar radiation has already decreased drastically (Boiteau et al. 2019b; Manck et al. 2021).

However, these studies have also highlighted that the interpretation of the siderophore composition is not trivial since different limitations need to be taken in to account. One being that other

siderophores could be actively produced but may be present in lower abundances due to rapid cycling or photochemical degradation (Boiteau et al. 2016; Yarimizu et al. 2019). Another bias is caused by the necessary step of solid phase extraction. Commonly used sorbents like ENV+, retain siderophores via van-der Waals interactions, hydrogen bonding or π–π interactions between aromatic structures, resulting in a preferred retention of nonpolar compounds (Waska et al. 2015). This drawback has already been described in several papers (Velasquez et al. 2011; Boiteau et al. 2016, 2019b; Bundy et al. 2018). Especially Bundy et al. highlighted that the majority of iron ligands present in seawater was not captured by ENV+, as evidenced by electrochemical measurements.

The need to obtain a detailed overview of the different siderophore compositions in the oceans and to draw not only qualitative but also reliable quantitative conclusions about the marine ligand pool is of central importance, since model studies have concluded that the iron ligand pool has a larger influence on the iron availability and resultant global carbon cycling than even the direct input of iron (Tagliabue et al. 2014). Modeling the variability of the ligand pool with possible differences in iron dissolution or uptake rates is therefore one of the major hurdles for realistic global bio-geochemical simulations of marine iron cycling (Tagliabue et al. 2015).

To overcome the potential compositional bias caused by the nonspecific retention mechanism of hydrophobic sorbents, and thus to achieve qualitatively accurate data of the marine ligand pool, an efficient and unbiased extraction approach is needed. The TDAC method (Chapter 2 and 3) showed promising features for the extraction of siderophores from seawater and could help to decipher the marine ligand pool composition. Especially the different retention mechanism focusing on siderophore-typical functional groups, rather than unspecific characteristics like polarity could allow for a more accurate display of the natural siderophore composition. In addition, it was found that the total concentration of strong iron ligands is generally above the concentration of total dissolved iron (Gledhill and Buck 2012; Bundy et al. 2018), implying the presence of strong iron-ligands such as siderophores in their apo-form (Boiteau et al. 2016). The presence of apo-siderophores is required to allow the extraction via the proposed affinity chromatography approach since it is based on the interaction between the free chelating groups and the TiO_2 surface.

Given that TDAC showed beneficial characteristics, such as good retention of all siderophore types from saline matrices and high tolerance to complex sample properties, the aim of this chapter was to investigate if this method is applicable for the large volume extraction of siderophores from seawater.

4.2 Experimental approach to investigate the applicability of TDAC for the targeted extraction of siderophores from seawater

To evaluate the suitability of TDAC for the efficient extraction of siderophores from large volumes of seawater, various technical parameters such as volume and flow rate had to be investigated, since detection of siderophores in seawater requires concentration from 20 or more liters. It was also investigated at which phosphate concentrations interferences with the siderophore adsorption occur, since such oxo-anions exhibit also a high affinity for TiO_2 surfaces and are more abundant in seawater than siderophores. To validate this approach, large volume of North Sea water was used as an authentic natural sample.

4.2.1 Investigation of extraction parameters on siderophore recovery from artificial seawater and North Sea water

Desferrioxamine B (DFOB) was used as a model siderophore for all extraction experiments because it is commercially available and because it has one of the best adsorptions on TiO_2 compared to the other siderophores studied, such as vibrioferrin. This means that if the adsorption of DFOB deteriorates, a much stronger deterioration of the adsorption of the other siderophores is expected. DFOB was obtained as desferrioxamine mesylate (Sigma-Aldrich) and a stock solution (5 mM) was prepared with ultrapure water. For the different extraction experiments, 3 mL and 6 mL polypropylene solid phase extraction (SPE) cartridges with fitting polyethylene filter elements were used (Chromabond, Macherey-Nagel). In addition, 8 mL flash cartridges with the corresponding polyethylene filter elements were employed for experiments at higher flow rates. The TiO_2 particles used as sorbent for these experiments were taken from the same batch as the material used in all experiments described in Chapter 3. This batch of grinded and wet-sieved TiO_2 oven clinker (Kronos Worldwide Inc., Nordenham Germany) had a surface area of 5.0 m²/g (BET) and a D_{50} mass-median-diameter of 54.092 µm. 3 mL SPE cartridges were packed with 0.2 g (± 5 mg) of TiO_2 whereas the 6 mL SPE and 8 mL flash cartridges were filled with either 1 or 5 g (± 5 mg) of TiO_2. All cartridges were compressed manually to ensure reproducible extraction performance. The SPE cartridges were run gravimetrically with a flow rate of 0.5 mL/min using the port valves. Acid washed 50 mL SPE cartridge reservoirs (Macherey-Nagel) were used for used for larger sample volumes. Flash cartridges were operated at a flow rate of 33.3 mL/min using a peristaltic pump and polytetrafluoroethylene (PTFE) tubing (Macherey-Nagel). Similar to the optimization experiments in Chapter 3, sample solutions were prepared by diluting DFOB stock solution with a sodium chloride solution (0.5 M, pH 4) (VWR international, Radnor PA USA). All sample solutions were prepared freshly prior to extraction in acid washed vessels to suppress any interfering complex formation. Four different sample volumes (2, 10, 50 and 500 mL) were prepared containing the same amount of DFOB resulting in concentrations of 10, 2, 0.4 and 0.04 µM, respectively. The effect of phosphate on the adsorption of DFOB under these conditions onto TiO_2 was also investigated by adding different amounts of

phosphate ($NaH_2PO_4 \times H_2O \geq 98\%$, Carl Roth, Germany) to sample solutions leading to concentrations from 0.1 to 1000 µM. 200 mg SPE cartridges were conditioned prior to use with 0.25 M NaH_2PO_4 at pH 2.4, followed by ultrapure water, 20 mM NaOH (Carl Roth, Germany) and 18 mL of ultrapure water. The remaining cartridges were conditioned in the same manner but with adjusted volumes. After cartridge conditioning, sample solutions were applied and all permeates were collected to calculate the relative adsorption efficiencies. Afterwards columns were washed with ultrapure water and eluted with alkaline phosphate buffer (100 mM NaH_2PO_4, pH 12.6), which has particularly high desorption efficiencies for hydroxamate siderophores, especially DFOB (see Chapter 2 and 3). 200 mg, 1 g and 5 g cartridges were eluted with 2, 6 or 12 mL of elution solutions, respectively. Eluates were neutralized with concentrated HCl (37%, VWR international) directly after collection and aliquots were measured via LC-HRMS without further processing. To investigate if the observed adsorption efficiencies and recoveries for DFOB were also observed for natural seawater, 500 mL of pH adjusted (pH 4) North Sea water was spiked with DFOB (final concentration of 0.04 µM) and processed with 5 g SPE cartridges as described in the previous paragraph. The North Sea water originated from the passage between Helgoland and the smaller neighboring island Düne and was sampled in summer of 2021. The following nutrient concentrations and salinity were determined: Nitrate 5.58 µM, nitrite 0.01 µM, phosphate 0.178 µM, ammonia 4.64 µM and salinity 33.2 psu. All experiments were performed in triplicates. Adsorption efficiencies were calculated relative to the original siderophore concentrations and the concentrations observed in the permeates.

4.2.2 Large volume natural seawater extraction with TDAC

2 × 20 L of North Sea water (same batch as in previous chapter) were filtered via glass microfiber filters (3 µm pore size, Whatman) and collected in two acid washed 20 L polycarbonate carboys (Nalgene). One 20 L carboy was acidified with concentrated HCl (37%, VWR international) to pH 2, whereas the pH in the other tank remained unchanged. DFOB, VF, PB and WBA were spiked to both tanks resulting at a final concentration of 0.1 nM for each siderophore. DFOB was the only purchased siderophore standard, whereas the other siderophores were isolated and purified in our lab (see Chapter 3). Both carboys were extracted with the following cartridge setup: (1) 8 mL flash cartridge packed with 20 g TiO_2 (mean particle size 54.092 µm), (2) 8 mL flash cartridge packed with 5 g ENV+ (Varian Bond Elut), (3) 8 mL flash cartridge packed with 20 g TiO_2 and (4) 5 g/60 mL prepacked PPL SPE cartridge (Varian Bond Elut). The modified styrene divinyl benzene polymer type sorbents (ENV+ and PPL) were conditioned with 10 mL methanol (LC-MS grade ≥ 99.95%, Carl Roth, Germany), followed by 20 mL of either acidified or neutral ultrapure water. Acidified ultrapure water for cartridge conditioning and washing after extraction was prepared with concentrated HCl. TiO_2 cartridges were conditioned as described in Chapter 4.2.1 with enlarged volumes. Extraction was performed at a flow rate of 33.3 mL/min using a PTFE diaphragm pump and PTFE tubing. After extraction and discarding of permeates,

all columns were washed with 200 mL of acidified or neutral ultrapure water. Apolar sorbent cartridges (ENV+, PPL) were eluted with 20 mL of acidified methanol containing 0.1% formic acid (LC-MS grade > 99%, Supelco) and TiO_2 cartridges were eluted with 25 mL of 0.5 M NaH_2PO_4, pH 2.4. Methanolic ENV+ and PPL eluates were dried using a rotary evaporator and taken up in 0.5 mL of neutral methanol. TiO_2 eluates were concentrated by extraction with 500 mg/6 mL PPL cartridges that were conditioned with acidified ultrapure water after activation with methanol. Elution was again performed with acidified methanol (2 mL) after cartridges were dried with N_2. Eluates were evaporated under N_2 to achieve a final volume of ~ 0.5 mL similar to the volume of ENV+ and PPL eluates. To calculate recoveries, 100 mL aliquots of the spiked and seawater samples were extracted with 200 mg/3 mL PPL SPE cartridges (Variant Bond Elut). After the columns were activated with 3 ml methanol they were washed with 6 mL of acidic or neutral ultrapure water, respectively. The columns were also washed with pH-adjusted ultrapure water (6 mL) before drying under N_2 and eluting with 1 mL methanol containing 0.1% formic acid.

4.2.3 LC-HRMS

LC-HRMS analysis was performed with a Vanquish UPLC system coupled to a Q-Exactive Plus mass spectrometer, using a heated electrospray ionization source (both Thermo). Separation was performed on a C18 column (C18 BEH, 100 × 2 mm, 1.7 µm particle size, ACQUITY Waters, equipped with guard-column). Positive and negative Ion Calibration Solution (Pierce, Thermo Fisher Scientific) was used for the calibration of the instrument. 1.5 mL short thread brown glass vials (Thermo Fisher Scientific) were used for all LC-HRMS measurements. The following solvent compositions and gradient settings were used for the measurement of siderophores: Solvent A = 0.1% formic acid in ultrapure water, solvent B = 0.1% formic acid in methanol; T_{0min}: B= 1%, $T_{0.2\ min}$ B = 1%, T_{4min}: B = 100%, $T_{4.9\ min}$: B = 100%; T_{5min}: B = 1% with a flow rate of 0.4 mL min^{-1}. The first 1.4 min of the LC method were kept at isocratic conditions and the flow diverted to avoid spraying nonvolatile salts into the mass spectrometer. MS measurements were performed using electrospray ionization in positive mode. Scans were obtained in data independent mode with a resolution of 70,000 (*m/z* 200) followed by MS^2 experiments (normalized collision energy of 30 eV, automatic gain control target of 3×10^6 and 50 ms maximum injection time) was used for the identification and quantification. DFOB was quantified using the species: DFOB ($[M+H]^+$= $C_{25}H_{49}N_6O_8$, *m/z* 561.3606), FOB ($[M+H]^+$ = $C_{25}H_{46}N_6O_8Fe$, *m/z* 614.2721), AlOB ($[M+H]^+$ = $C_{25}H_{46}N_6O_8Al$, *m/z* 585.3287) as well as the *m/z* 201.12 daughter ion of *m/z* 561.3606. For the quantification of VF, apo-VF ($[M+H]^+$ = $C_{16}H_{23}N_2O_{12}$, *m/z* 435.1246), Fe-VF ($[M+H]^+$ = $C_{16}H_{20}N_2O_{12}Fe$, *m/z* 488.0360) and the daughter ion *m/z* 181.10 of *m/z* 435.1246 were used. Similar to VF, WBA was also quantified by using the single charged apo- ($[M+H]^+$ = $C_{20}H_{35}N_2O_{10}$, *m/z* 463.2286), Fe(III)-containing species ($[M+H]^+$ = $C_{20}H_{32}N_2O_{10}Fe$, *m/z* 516.1401) as well as the daughter ion *m/z* 145.10 of the free ligand precur-

sor ion. Whereas PB was detected as the single ($[M+H]^+$ = $C_{34}H_{51}N_6O_{11}$, *m/z* 719.3610) or double protonated apo-PB ($[M+2H]^{2+}$ = $C_{34}H_{52}N_6O_{11}$, *m/z* 360.1842) with the corresponding daughter ion *m/z* 194.08.

4.3 Results and discussion

4.3.1 Investigation of extraction parameters on siderophore recovery from artificial seawater

To check the suitability of the TDAC method for large volume extraction of siderophores from seawater, different parameters like sample volume, flow rate, sorbent amount, phosphate and analyte concentration were investigated. Table 4 summarizes that in general the best adsorption efficiencies were observed for the most concentrated and smallest sample volumes. By increasing the volume from 2 mL to 500 mL but not the total amount of DFOB, the adsorption efficiency decreased from 95.3 ± 2.8% to 12.1 ± 8.4% in case of the 0.2 g cartridges. This decrease in adsorption efficiency with increasing volume was smaller the more sorbent was used. Thus, an adsorption efficiency of 89.5 ± 3.8% was observed for the 5 g cartridge at a sample volume of 500 mL. These observation matched the expected volume dependent adsorption efficiency of classic solid-phase extraction (Subra et al. 1988; Liska 1993; Hennion and Pichon 1994; Hennion 1999). In general, reduced adsorption efficiency indicates that breakthrough of the analyte took place during the extraction. Breakthrough of analytes occurred either if the analyte is no longer retained by the sorbent or when the capacity of the sorbent is exceeded (Hennion and Pichon 1994). Since the capacity of the 0.2 g cartridge is high enough to retain 95% of spiked DFOB from 2 mL, the limited adsorption efficiencies observed for the increasing volumes is presumably caused by poor retention of the analyte, as it is generally observed for the extraction of very polar substances from aqueous matrices using apolar sorbents (Buszewski and Szultka 2012). Besides the negative effect of increased sample volume on the extraction efficiency, it was also shown that increased flow rate resulted in lower adsorption efficiencies. In case of 1 g cartridges, the adsorption efficiency dropped from 62.1 ± 3.4% to less than 15% by increasing the flow rate from 3 mL/min to 33.3 mL/min when extracting 500 mL sample volume. Increasing the sorbent volume also resulted in smaller differences in adsorption efficiency at faster flow rates. Parameterization of both, sample volume and flow rate, indicated that DFOB showed poor retention on the TDAC cartridge with this experimental setup. This result was counterintuitive as it was expected that hydroxamate-containing analytes like DFOB would be retained more efficiently according to the results of Chapter 2 and 3. However, since the strong interaction between hydroxamates and TiO_2 surfaces are well documented (Yang et al. 2006; McNamara et al. 2009, 2010), I hypothesized that the retention of the model siderophore DFOB was rather rendered by the sorbent properties than the affinity of the siderophore

towards the TiO_2 surface. Sorbent properties that influence the analyte retention are surface area and activity as well as the packing density (Poole 2003).

Table 4. Influence of TiO_2 bed mass, DFOB concentration, sample volume, flow rate and sample matrix[a] on adsorption efficiency of DFOB.

TiO_2 (g)	DFOB (µM)	Volume (mL)	Flow rate (mL/min)	Phosphate (µM)	Adsorption efficiency (%)
0.2	0.04	500	0.5	/	12.1 ± 8.4
0.2	0.4	50	0.5	/	33.5 ± 7.3
0.2	2	10	0.5	/	71.4 ± 5.4
0.2	10	2	0.5	/	95.3 ± 2.8
1	0.04	500	0.5	/	62.1 ± 3.4
1	0.04	500	33.3	/	23.0 ± 8.7
1	0.4	50	0.5	/	80.7 ± 6.2
1	2	10	0.5	/	92.3 ± 3.7
5	0.04	500	0.5	/	89.5 ± 3.8
5	0.04	500	33.3	/	80.5 ± 5.3
5	0.04	500	33.3	0.1	75.2 ± 7.3
5	0.04	500	33.3	1	42.6 ± 6.4
5	0.04	500	33.3	10	18.7 ± 5.7
5	0.04	500	33.3	100	2.8 ± 3.7
5	0.04	500	33.3	1000	0.8 ± 0.7
5	0.4	50	0.5	/	85.2 ± 4.5
5	2	10	0.5	/	99.8 ± 0.8
1	0.04	500	33.3	0.178	4.3 ± 0.9
5	0.04	500	33.3	0.178	25.3 ± 2.8

[a] Adsorption experiments parameters and results conducted with NaCl 0.5 M, pH 4 as sample matrix are shown in top row (white background). Adsorption experiments conducted with filtered and pH adjusted North Sea water is highlighted in red.

The TiO_2 particles (diameter: 54.092 µm with 5.0 m²/g) were not porous and thus did not provide a large specific surface area as commonly used particles for solid-phase extraction. For example, the Chromabond C18 SPE cartridges by Macherey Nagel are filled with 45 µm particles owning a specific surface area of 500 m²/g. As the specific surface area of the sorbent increases, the equilibrium between the liquid and solid phases is more likely to be reached, which generally results in better retention of the analyte. To overcome poor retention, the sorbent bed volume could be increased, resulting in less channeling and longer equilibration time. Channeling is caused by voids that regularly occur when cartridges are packed manually. Those voids cause the moving mobile phase to move faster than the average flow rate, resulting in reduced retention or peak broadening. However, increased bed mass will also lead to increased non-

specific matrix adsorption (Poole 2003) and therefore ultimately render the efficiency and specificity for siderophores. Phosphate concentrations in seawater reach up to micromolar concentrations (Bruland 1980; Martin et al. 1989), and due to the known affinity of such oxoanions towards TiO_2, the impact of different phosphate concentrations (0.1, 1, 10, 100 and 1000 µM) on the adsorption efficiency of DFOB onto TiO_2 was investigated. Table 4 shows that the adsorption efficiency of TDAC for DFOB was reduced in presence of phosphate, even under standardized conditions (NaCl 0.5 M, pH 4). The lowest investigated phosphate concentration of 0.1 µM already led to a decreased adsorption efficiency of 75.2 ± 7.3% under otherwise identical extraction conditions. With increasing phosphate concentration, the adsorption efficiency decreased further until almost no adsorption of DFOB was observed at phosphate concentrations above 100 µM. It was expected that phosphate concentrations above 100 µM would decrease the adsorption of siderophores, since it was shown in Chapter 3 that such phosphate concentrations lead to partial elution of siderophores from TiO_2 under acidic conditions. However, it is surprising that siderophore adsorption to TiO_2 was already hindered at expected seawater concentrations of phosphate. The extraction under alkaline conditions could prevent adsorption of phosphate due to electrostatic interactions (Connor and McQuillan 1999) and further ensure surface complexation of DFOB. However, it was observed that the affinity of pure alpha-hydroxycarboxylate siderophores such as VF to TiO_2 decreased at pH > 8.

In order to check to what extent these observations under standardized conditions were applicable to a seawater sample matrix, two additional experiments were carried out with filtered and acidified North Sea water using 1 g and 5 g cartridges. Using the same flow rate of 33.3 mL/min and the same pH conditions (pH 4) in combination with the natural phosphate concentration of 0.178 µM, an adsorption efficiency of only 4.3 ± 0.9% was determined for the smaller cartridge. This corresponds to only one fifth of the adsorption efficiency under idealized conditions. Similar results were observed for the adsorption efficiency of the 5 g cartridge. Despite a phosphate concentration of the same order of magnitude and otherwise identical extraction conditions, the adsorption efficiency of the 5 g cartridge is three times lower (25.3 ± 2.8%) for the natural seawater than for the NaCl solution containing 0.1 µM phosphate. These observations indicate that, in addition to phosphate, other substances that suppress the adsorption of siderophores are present in seawater. Possible substance classes include other oxoanions, such as sulphate, which interact with titanium dioxide surfaces in a similar but weaker way than phosphate groups. Although sulphate forms only weaker surface complexes on metal oxides, the marine sulphate concentration of about 30 mM (Canfield and Farquhar 2009) (three orders of magnitude higher than marine phosphate concentration), nevertheless indicates a negative effect on the adsorption of siderophores. Other possible substance classes in seawater that could hinder the interaction of siderophores with TiO_2 are carboxylic or phenolic compounds (Aluwihare et al. 2002; Hertkorn et al. 2006; Yang and Van Den Berg 2009; Lechtenfeld et al. 2015). It is ex-

pected that those molecules exhibit strong and multiple ligand character (Hertkorn et al. 2006), suggesting that such components could also interact with TiO_2 and thus prevent the adsorption of siderophores. Typical representatives of carboxylic/phenolic rich compounds are humic substances, which can be divided into humic and fulvic acids and are also found in seawater (Aluwihare et al. 2002; Singh 2015). The interaction of humic substances with TiO_2 has already been intensively studied under the aspects of water purification as well as bioaccumulation and toxicity of nanoparticles (Chowdhury et al. 2012; Loosli et al. 2013; Erhayem and Sohn 2014; Liu et al. 2014; Wang et al. 2014a). All these studies showed a strong interaction of humic substances with TiO_2 at seawater pH, highlighting the possible interference of such oxygen-rich compounds with siderophores during extraction from marine waters using TDAC. In addition to these anionic substance classes, it is also worth mentioning that the presences of cations could have caused decreased adsorption, by forming complexes with the spiked siderophore prior to extraction. The concentration of dissolved iron in the North Sea ranges from 0.4 to 28 nM (Gledhill et al. 1998), which would allow complexation of nanomolar amounts of spiked DFOB. However, it was also shown that almost all dissolved iron is already complexed and thus complexation with free DFOB probably did not occur to any significant extent since the prepared sample solutions were also processed immediately after spiking.

4.3.2 Large volume natural seawater extraction with TDAC

Since the natural concentration of siderophores in seawater ranges from 0.1 to 20 pM (Mawji et al. 2008; Boiteau et al. 2016, 2019b; Bundy et al. 2018), and the detection limits of the most modern mass spectrometers are usually several orders of magnitude above those levels, siderophore concentration factors of at least 10,000 are necessary. Moreover, since the extraction efficiency of TDAC is assumed to be < 25%, it is inevitable to concentrate double or triple digits liters of seawater in order to be within the detection thresholds of such instruments. To investigate the suitability of TDAC for the extraction of siderophores from seawater under realistic conditions, 20 L of filtered North Sea water was spiked with four model siderophores (DFOB, VF, PB and WBA: final concentration 0.1 nM) and extracted at pH 2 or pH 8 via a column apparatus consisting of four columns linked in series. The first and third columns were both filled with TiO_2, the second and fourth with the polystyrene polymers ENV+ or PPL. The eluates of each column were further concentrated to achieve theoretical concentration factors of ~ 40,000.

The recoveries of the eight different eluates clearly showed that TDAC was not suitable for the extraction of siderophores from seawater under these experimental conditions (Table 5). No TiO_2 eluate contained siderophores at concentrations above the detection limit, while recoveries of up to 95% (DFOB) were observed in the eluate of the ENV+ cartridge processed at pH 2. The results for the 20 L TiO_2 extracts followed the same trend already observed in the experiments with smaller volumes (Table 4).

Table 5. Recoveries of desferrioxamine B (DFOB), vibrioferrin (VF), petrobactin (PB), woodybactin A (WBA) in eluates of the four sequentially processed cartridges of 20 L spiked seawater.

Cartridge	Siderophore recovery (%)							
	pH 2				pH 8			
	DFOB	VF	PB	WBA	DFOB	VF	PB	WBA
TiO_2	ND	ND	ND	ND	ND	ND	ND	ND
ENV+	95.8	35.2	46.3	85.3	50.8	12.3	26.7	45.6
TiO_2	ND	ND	ND	ND	ND	ND	ND	ND
PPL	ND	ND	8.6	5.3	ND	ND	ND	18.2

In connection with the recoveries for the apolar columns, the DFOB example also shows that the adsorption efficiency on the first TiO_2 column at pH 2 must have been below 5%, since otherwise a lower recovery would have been observed for the ENV+ eluate. For the extraction at pH 8, it is concluded that the adsorption efficiency must have been in the single digit range, as it has been demonstrated that the recovery of DFOB from seawater at pH ~ 8 with ENV+ ranges between 34% and 46% (Mawji et al. 2008), which matches the observed recovery of ~ 50%. The general observation that more siderophores were recovered under acidic conditions is consistent with the protocol developed for the most efficient DOM extraction from natural waters, including free ligand and acid-stable complexes (Monzyk and Crumbliss 1982; Dittmar et al. 2008; Waska et al. 2015). The comparison between the recoveries of each siderophore and the detection of PB and WBA in the eluates of the last cartridges filled with PPL further illustrate that the extraction efficiencies were different for each siderophore (McCormack et al. 2003). In general, the extraction efficiency of siderophores using apolar sorbents correlates with the retention times observed for those siderophores on a reversed phase LC system (Supporting information to Chapter 3). These results support the previous conclusion that the interpretation of seawater extracts in terms of their siderophore composition and abundance of specific siderophore classes has a strong bias towards siderophores that exhibit high extraction efficiencies for commonly used apolar sorbent (Velasquez et al. 2011; Boiteau et al. 2016, 2019b; Bundy et al. 2018). In interpreting their data, Velasquez et al. attributed this possible bias to cause the primary detection of ferrioxamine-like substances. Consistent with the results displayed in Table 5 and the suggested interpretation, ferrioxamines and amphiphilic siderophores like amphibactins are most regularly among the identified siderophores in such extracts (Mawji et al. 2008; Velasquez et al. 2011; Boiteau et al. 2016, 2019b; Bundy et al. 2018). Another example consistent with this experimental drawback is the lack of directly detected very polar and small siderophores such as VF, in natural seawater. None of the studies listed above identified VF and similar siderophores in any of the world's oceans, despite the widespread occurrence of VF-encoding gene

clusters (Gärdes et al. 2013; Yarimizu et al. 2019). The only exception to this trend is a recent study that described the presence of petrobactin in marine waters for the first time (Manck et al. 2021). Similar to the listed publications, these authors also collected up to 20 L of seawater and extracted the filtered water without acid addition using pre-packed ENV+ cartridges. Considering the low recovery of PB observed in this experiment (Table 5, pH 8: 26.7%), it can be hypothesized that the majority of petrobactin was presumably not extracted, thus resulting in a less accurate picture of the petrobactin distribution across the North Pacific.

4.4 Conclusion

Despite the known importance of organic ligands for iron supply of marine microorganisms, the likely dynamic composition of the ligand pool and associated bioavailability is still poorly understood. This study sought to shed light on the naturally occurring ligand pool using the new affinity extraction approach to overcome the bias of siderophore composition in natural seawater samples. However, it was shown that despite the chromatographic improvements and unique adsorption of siderophores on TiO_2, the extraction of the model siderophore DFOB from large volume of natural seawater (20 L), resulted in insufficient adsorption efficiencies under the observed experimental conditions. I assume that one of the reasons for the poor retention of DFOB was the relatively small specific surface area of the TiO_2 particles used in this study. This assumption is based on the fact that in the previous studies, presented in this thesis as well as in the literature, the strong interaction of hydroxamates with TiO_2 surfaces was well documented. Nonetheless, this study confirmed the affinity of DFOB for TiO_2 in small volumes of highly concentrated sample solutions. Further, it was also shown that the presence of phosphate in seawater decreased the adsorption efficiency, due to the competitive interaction between phosphate and siderophore for the TiO_2 binding sites. However, this negative effect of phosphate was only observed at concentrations above the expected phosphate concentrations in natural seawater. The comparison between artificial and natural seawater with an approximately equal phosphate concentration also highlighted that natural seawater contained other substances that also interacted competitively with siderophores and phosphate for the binding sites on the TiO_2 surface. In addition, these results offered additional proof for the compositional ligand pool bias with extraction sorbents like ENV+. The highest recoveries, independent of pH during extraction, were observed for the siderophores DFOB and WBA, whereas VF and PB showed only half the recovery compared to the more apolar ones. In summary, the TDAC method needs further adjustment to be used for the direct extraction of siderophores from seawater. Especially the sorbent material requires higher porosity to increase the surface area to allow the processing of large volumes of seawater. Therefore, a bias-free extraction approach for the identification and quantification of siderophores from seawater remains the “holy grail” to understand global marine iron cycling.

5. Siderophore identification in complex seawater extracts

Traditionally produced seawater extracts using apolar sorbents (Dittmar et al. 2008) present a particular analytical challenge, since the extracted DOM is no longer separable by 1D chromatography approaches alone, regardless of whether common purification techniques like normal or reversed-phase or ion exchange chromatography are applied (Sandron et al. 2015). Therefore, in Chapter 5 I investigated the applicability of TDAC for the targeted extraction of siderophores from natural DOM extracts. I reported that by means of TDAC and adjusted adsorption conditions siderophores were concentrated while DOM was depleted, simplifying the identification of siderophores in such highly complex samples. I also showed that the reprocessing of DOM extracts from the HE533 cruise with the adjusted TDAC method led to the identification of putative unknown siderophores. In this study I was responsible for the adjustment of the TDAC method and all following LC-HRMS measurements. Seawater extracts were prepared by Jan Tebben during cruise HE533.

5.1 Introduction

The established approaches to study the molecular composition of the marine ligand pool work with highly complex solid-phase extracts in which the detection of siderophores is very challenging despite high-resolution MS. In this chapter, it was investigated if the application of TDAC facilitates the identification of siderophores in such complex sample matrices, since the results in the previous chapters suggested a possible direct workup of conventional apolar SPE extracts. Dissolved organic matter (DOM) is the overarching term to describe the highly complex mixture of biologically derived organic molecules dissolved in fresh and seawater (Hawkes et al. 2018). Approximately 624 Gt of carbon is present as recalcitrant DOM (RDOM) which accounts to almost the same carbon reservoir capacity as atmospheric CO_2 (Jiao et al. 2010). RDOM is resistant to microbial utilization and persists in the oceans for thousands of years, accounting for more than 95% of the total DOM (Jiao et al. 2010). Therefore DOM plays not only a crucial role in the marine carbon cycle but also as one of the world's most important carbon sinks (Hertkorn et al. 2008; Lipczynska-Kochany 2018). Extensive cycling involving natural and anthropogenic processes leads to an immense structural diversity of DOM (Raeke et al. 2016; Lau et al. 2020; Wünsch and Hawkes 2020). State-of-the-art DOM analysis is performed by the hyphenation of LC techniques with ultra-high resolution Fourier-transform ion cyclotron resonance (FT-ICR) or Orbitrap mass spectrometry allowing accurate molecular characterization (Petras et al. 2017; Hawkes et al. 2018; Patriarca et al. 2018; Han et al. 2021). But due to the large number of possible isomers per molecular mass and their great diversity, overlapping retention times occur, which results in the "unresolved DOM hump" (Figure 17) consisting of individual extracted ion chromatograms (EICs) showing broad distributions rather than peaks (Sandron et al. 2015; Petras et al. 2017; Hawkes et al. 2018; Patriarca et al. 2018).

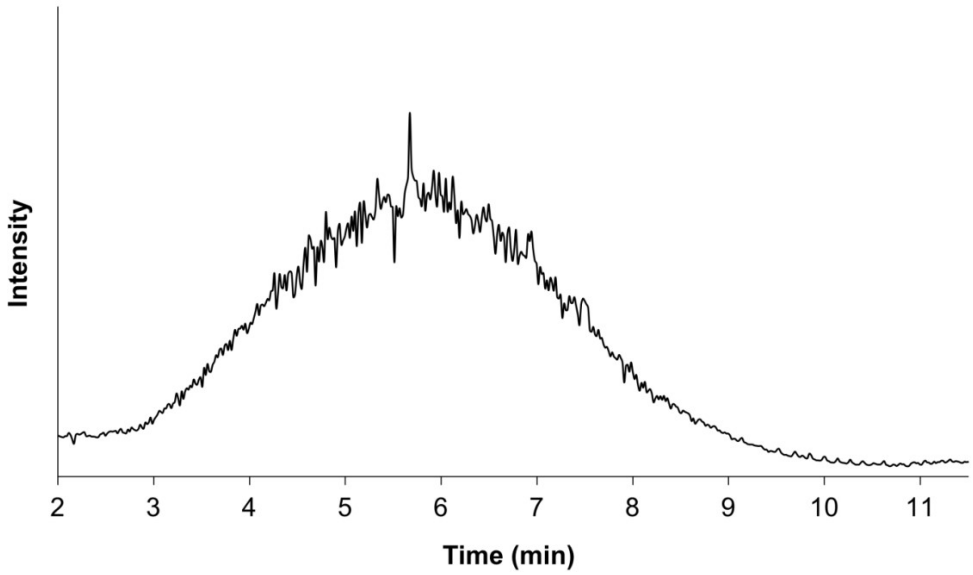

Figure 17. Total ion chromatogram (TIC) in negative ionization mode of PPL seawater extract (NSS pH 2) using LC-ESI-MS equipped with C18 column representing the characteristic DOM hump (own data).

However, adding model compounds as standards to DOM extracts does not affect their retention times in LC-MS measurements, confirming that the naturally present isomers in DOM are not influencing the chromatographic behavior of spiked model compounds (Han et al. 2021). Sandron et al. gave a detailed overview of the various LC techniques applied to fractionate generated DOM extracts via reversed phase SPE. No single separation approach focusing on polarity, molecular weight, charge or degree of unsaturation is capable of achieving the resolution required for molecular-level separation of DOM (Sandron et al. 2015). In general, 1D chromatography is limited to a resolution not sufficient enough to achieve total resolution of the tens of thousands of individual components compromising such complex mixtures. Therefore, the identification of distinct substances in DOM samples remains challenging to this date.

The detection of siderophores in DOM samples is traditionally facilitated using the complex-forming properties of siderophores. The first work that identified and quantified siderophores in natural water samples established an ICP-MS method with gallium labeling prior to analysis and retention time comparison using available standards (Mawji et al. 2008). The advantages of this approach are obvious, since monitoring the ^{69}Ga signal rather than iron isotope signals leads to far less interferences as a result of its low background presence. In general, elemental analyses focusing on the metal content of the sample help to overcome the tremendous complexity of the DOM matrix. However, elemental analysis alone makes it impossible to obtain structural information about possible unknown siderophores present in natural extracts. Therefore, it is inevitable to extend the siderophore analysis to include molecular detection methods. However, the low concentration of siderophores, but more importantly as highlighted in this chapter, the complexity and chromatographic behavior of DOM provide significant analytical difficulties for the molecular identification and characterization of siderophores in seawater extracts. Nonetheless, with the improvement of soft ionization mass spectrometry, it became possible to identify known ferrioxamines in seawater extracts via the characteristic iron isotopic pattern and MS/MS fragmentation using LC-ESI-MS (Velasquez et al. 2011). As already described in Chapter 1.3.3, both elemental and molecular approaches suffer from several drawbacks involving the detection of iron and its isotopic pattern: (i) instable complexes that dissociate during ionization or (ii) the hampered complex formation under commonly applied chromatographic conditions. Therefore the latest studies developed two different approaches to tackle this uncertainty: The split flow approach, combining element and molecule detecting techniques, and the so-called native metabolomics approach, consisting of pH adjustment followed by metal salt infusion after separation on the LC-system (Boiteau et al. 2016, 2019b; Aron et al. 2022). Although these new methods can largely solve the problems of untargeted iron-complex analysis, they require expensive and specially adapted equipment, intensive maintenance due to the high input of metal ions into the ionization source and extensive data analysis necessary because of the still high sample complexity of DOM extracts. Therefore, there is a continuing need to detect sidero-

phores in complex samples without extensive data mining, using less-specialized equipment and a low-maintenance and instrument protective protocol. Such a method must therefore minimize the overall complexity of the DOM extract prior to measurement, in order to avoid relying solely on the detection of the isotopic pattern and other specific *m/z* differences that would only become overwhelmingly apparent with the addition of metal ions in excess. However, such a new purification method would not overcome the bias caused by the choice of sorbent for the extraction of natural waters.

The TiO_2-based affinity chromatography (TDAC) presented in the previous chapters was hypothesized to tackle this issue, as this method was not only capable of efficiently extracting siderophores from small-volume and high-concentration samples, but also retained siderophores under apolar conditions, which allows the direct workup of conventional SPE extracts. Based on these promising properties of TDAC, in this chapter I have investigated the applicability of this new method as a purification step of marine DOM extracts. First, I investigated the conditions during the adsorption phase that allow specific retention of siderophores on TiO_2 and prevent non-specific interaction of North Sea DOM with TiO_2. The goal was to obtain TDAC eluates enriched in siderophores and depleted in DOM compared to the original SPE extracts. Subsequently, the developed protocol was applied to process seawater extracts from the research vessel Heincke cruise HE533 to the Arctic fjords of Norway in order to characterize the ligand pool in these waters.

5.2 Experimental procedures

5.2.1 Targeted siderophore extraction from DOM extracts

To evaluate the performance of TDAC for the purification of siderophores from complex methanolic DOM extracts, the four siderophores DFOB, VF, WBA and PB were used as standard compounds. DFOB was purchased as desferrioxamine mesylate from Sigma-Aldrich, the other siderophore standards were prepared in our lab (Chapter 3). North Sea water extracted at pH 2 was used as the DOM matrix. The North Sea water was collected in April 2016 during a transect from Helgoland to Bremerhaven. 250 L seawater was sampled into acid-cleaned containers. The sampled water was filtered through 0.2 µm PFTE membranes (Whatman) and stored at 5 °C until use. Seawater was first extracted at neutral pH using prepacked 5 g PPL cartridges (Varian, Agilent). Prior to extraction, cartridges were conditioned with one cartridge volume of methanol, followed by two cartridge volumes of ultrapure water. One aliquot of 50 L filtered seawater was processed with one cartridge at a flow rate not exceeding 20 mL/min. The permeates were collected, acidified to pH 2 and re-extracted at the same flow rate using fresh PPL cartridges conditioned with acidified ultrapure water after activation with methanol. After extraction, cartridges were washed with two cartridge volumes of ultrapure water at the appropriate

pH, dried and eluated with 50 mL methanol, resulting in ~200 mL neutral and acidic extract. In the following the acidic extract is called North Sea standard pH 2 (NSS pH 2). Sampling and processing of the North Sea water was conducted by the working group of Boris Koch (AWI). To investigate how the composition of solvent (polarity, type of anion and anion concentration) affects the adsorption of DOM and siderophores on TiO_2, siderophore standards were mixed with the NSS pH 2 DOM standard and diluted with 12 different organic solvent or 15 different aqueous buffers prior to TDAC (Table SI 3). Sample solutions were prepared by diluting 10 µL siderophore mix (0.1 µM DFOB, 10 µM WBA, 100 µM VF and PB) with 180 µL NSS pH 2 and 1.61 mL of the corresponding solvent or buffer. Polypropylene solid phase extraction (SPE) cartridges (3 mL) and matching polyethylene filter elements (Macherey-Nagel) were used throughout the experiment. Cartridges were packed with 200 mg (± 5 mg) of TiO_2 as described in Chapter 3 and 4. A volume of 1.5 mL sample solution was passed over one column and the permeate was collected. 200 µL of sample solution were kept to determine original concentrations before extraction. Columns were washed with 3 mL of the respective sample solution, solvent or buffer, followed by 6 mL of ultrapure water. All wash solutions were discarded and columns were eluated with 2 mL of 0.5 M NaH_2PO_4 at pH 2.4. Eluates were measured by LC-HRMS without further steps, while aliquots of the original samples in organic solvents as well as the corresponding permeates were dried under N_2 stream. The dried samples were taken up in methanol (LC-MS grade) and measured accordingly. Adsorption efficiencies were calculated as described in Chapter 4.2.1. Recoveries were calculated by determining the concentrations in the eluates by external calibration with siderophores and DOM prepared in the applied phosphate elution solution.

5.2.2 TDAC reprocessing of large volume seawater extracts from expedition HE533

During the HE533 cruise (Figure 18), different volumes of seawater (Table 6) were extracted with polystyrene-divinylbenzene (HP20, Diaion). Prior to extraction, seawater was sequentially filtered with 10 µm, 3 µm and 1 µm filter bags and acidified to pH 4 using 37% HCl. After extraction, HP20 was washed with ultrapure water and transferred into 100 mL brown glass centrifuge vessels and stored at -20 °C until further processing. The adsorbed components were eluted in the laboratory in Bremerhaven by washing the HP20 sorbent five times with ~ 50 mL LC-MS grade methanol. Eluates were combined, concentrated by rotary evaporation and completely dried by freeze drying. Afterwards, samples were resuspended in 2 mL methanol and 100 µL aliquots were taken and diluted with 1.7 mL of 0.5 M NaCl, pH 4. Then 300 µL aliquots of the diluted original samples were taken and 1.5 mL were extracted with 200 mg/3 mL TiO_2 cartridges. Column conditioning, extraction, washing and elution were performed as for the method development described in Chapter 5.2.1. Blank samples were prepared by replacing the NSS pH 2 DOM standard with methanol (LC-MS grade), but otherwise treated in the same manner.

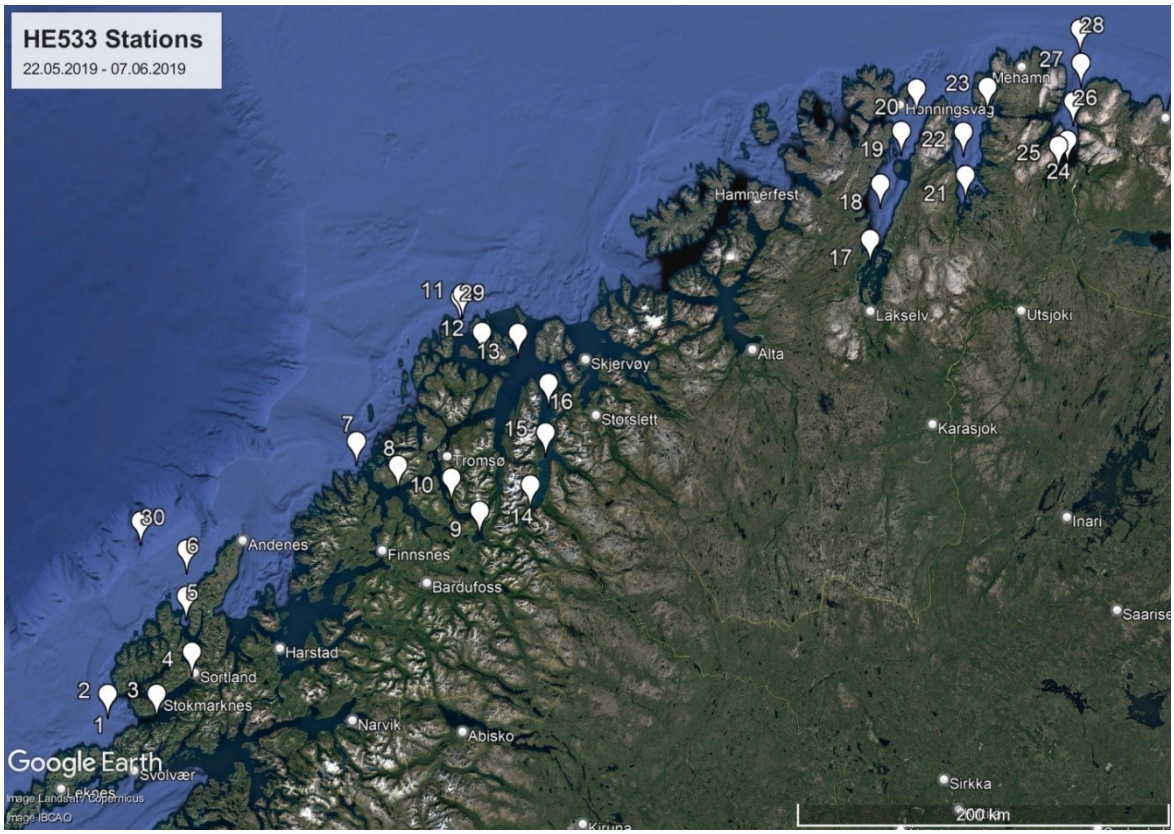

Figure 18. Geographic positions of the stations 1-30 of expedition HE533 in summer 2019 to the arctic fjords of Norway.

Table 6. Large volume extraction at different stations during expedition HE533.

Station No.	Volume (L)	Station No.	Volume (L)	Station No.	Volume (L)
2	450	10[c]	200	19	220
3	450	10[c, d]	300	20	130
4	370	11	250	21	230
5	370	12	50	22	150
6	550	13	50	23	130
7	100	14	350	25	150
8	650	15	380	26	200
9[a]	50	17	80	27	200
9[b]	150	18	200	28	600
10[c]	100	19	120		

[a] Water sampled from 3 m depth, corresponding to the chlorophyll maximum at this station
[b] Water sampled from 14 m depth
[c] Cell concentration >25 × 10^6 c/L of toxic *Chrysochromulina leadbeateri*
[d] Extraction without filtration

5.2.3 LC-HRMS

To characterize the eluates of the large volume extractions, samples were measured with the following settings optimized for siderophore (see Chapter 4.2.3) and dissolved organic matter (DOM): Solvent A = 0.1% formic acid in ultrapure water, solvent B = 0.1% formic acid in methanol; T_{0min} B= 1%, $T_{1.5\ min}$ B = 1%, $T_{10\ min}$ B = 50%, T_{12min} B = 99%, $_{T14\ min}$ B = 99%; $T_{15\ min}$ B = 1% with a flow rate of 0.4 mL min^{-1}. The first 2 min of the LC method were isocratic and the flow diverted to the waste channel. MS measurements were performed using electrospray ionization in negative mode at full scan resolution of 280,000 (*m/z* 200) and a scan range of 150-1500 *m/z*. To approximate the adsorption efficiency and recovery for DOM, the *m/z* values 367.10346, 409.11402, 421.11402, 439.12458 and 453.14023 used to determine the degradation index of DOM in negative ionization mode were taken into account (Flerus et al. 2012). The EICs corresponding to those *m/z* values showed the typical chromatographic behavior of DOM, resulting in broad peaks over several minutes of each run (Petras et al. 2017; Patriarca et al. 2018). Integration of those peaks was conducted manually using Thermo Fishers Xcalibur software since automated peak picking was impossible (Gavard et al. 2020). Data independent mode at full scan resolution of 70,000 (*m/z* 200) followed by MS^2 experiments (normalized collision energy of 30 eV, automatic gain control target of 3×10^6 and 50 ms maximum injection time) was used for further characterization of two putative siderophores ($[M-H]^-$ = *m/z* 819.36573 and *m/z* 1083.44946) and the corresponding adducts and iron complexes, which were detected at several stations in the Tromsø area.

5.3 Results and discussion

5.3.1 Targeted siderophore extraction from DOM extracts

Since TiO_2 is produced in large quantities and was already found in different environmental samples (Kaegi et al. 2008), several studies were conducted to assess its fate, transport and ecotoxicology (French et al. 2009; Yang et al. 2009, 2013; Zhang et al. 2009; Erhayem and Sohn 2014). All these studies underlined the occurring adsorption of DOM and its different components like humic acids, onto TiO_2 under different pH conditions, ionic strengths and in the presences of specific ions. Yang et al. emphasized in 2009 that the adsorption of humic acids onto TiO_2 was less affected by pH changes than for Al_2O_3 or ZnO. These results highlight the need to adjust the adsorption conditions for the targeted extraction of siderophores via TDAC from DOM extracts. To determine the conditions that lead to suppressed adsorption of DOM whilst still enabling efficient adsorption of siderophores on TiO_2 different parameters like solvent polarity, type of anion, anion concentration and pH were investigated.

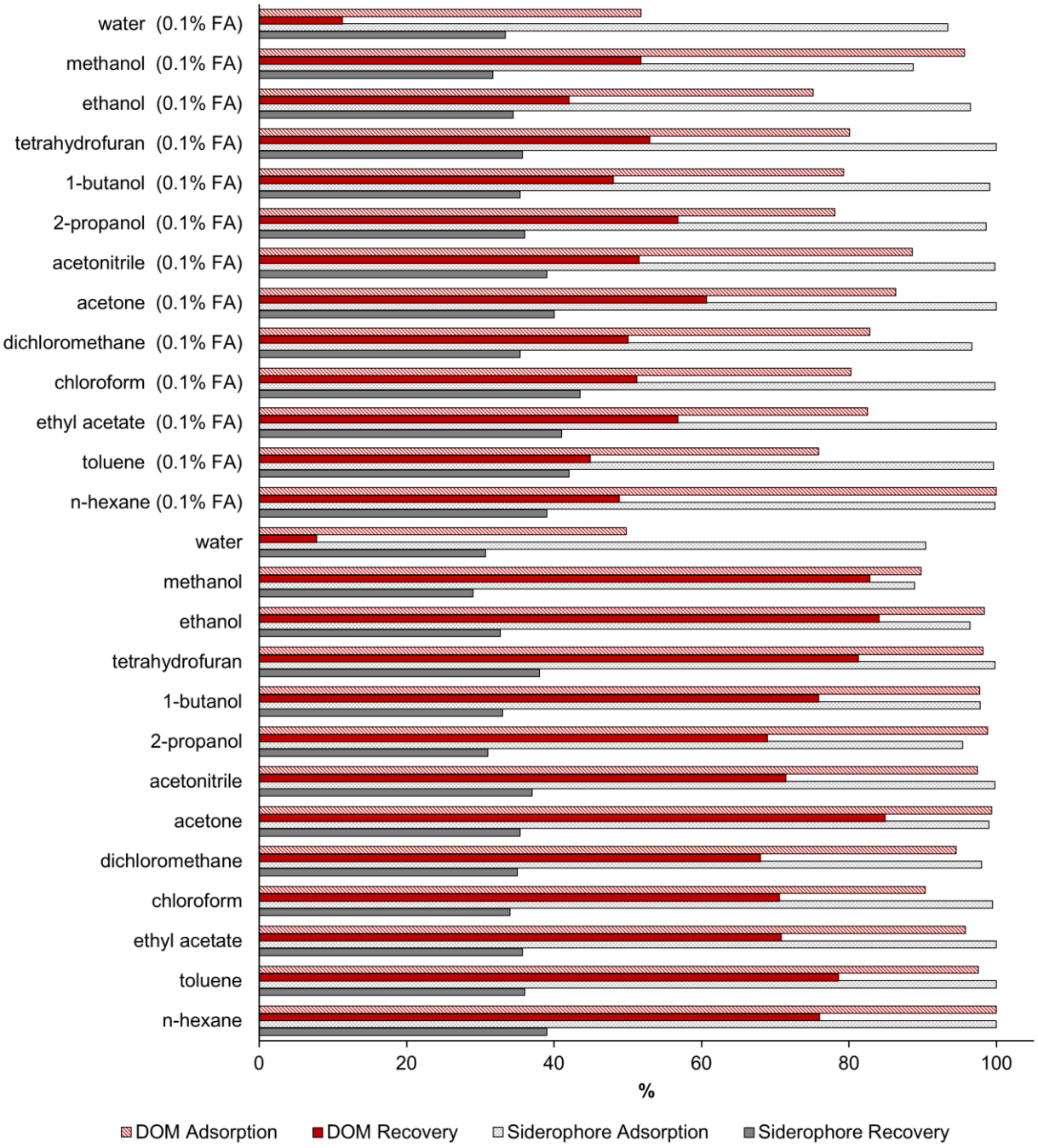

Figure 19. Comparison of DOM adsorption efficiency and recovery (DOM represented by negative correlating compounds according to Flerus et al. 2012) and averaged siderophore adsorption efficiency and recovery depending on organic solvent and pH. Vibrioferrin, desferrioxamine B, petrobactin and woodybactin A were used as model siderophores.

The results of these extraction experiments showed that the adsorption of DOM to TiO_2 is increased for all organic solvents (> 90% adsorption efficiency) in comparison to neutral ultrapure water (~ 50%) (Figure 19). However, when comparing only the organic solvents with each other, no clear trend was observed whether the adsorption efficiency of DOM increased with decreasing polarity of the solvent (solvents ordered by $E_T(30)$, water most polar, n-hexane most apolar (Reichardt 1994)). It was also observed that a decrease in pH (solvents with 0.1% formic acid) led to a decrease in adsorption efficiency of DOM for almost all investigated organic solvents.

The only exceptions to this observation were the determined adsorption efficiencies for acidified n-hexane (~ 100%) and methanol (~ 95%). Contrary to the observed adsorption behavior of DOM in different organic solvents, the pH of ultrapure water did not have a strong effect on the adsorption efficiency of DOM to TiO_2 (acidified ultrapure water ~ 50% adsorption efficiency). In contrast to these results, it was expected that DOM might exhibit better adsorption at slightly acidic conditions, since TiO_2 surfaces are positively charged at pH < 5 (Dobson et al. 1997; Suttiponparnit et al. 2011; Nduwa-Mushidi and Anderson 2017), and at this pH most of the acidic functionalities of DOM, such as carbocyclic acid groups, are deprotonated and thus negatively charged. Therefore increased adsorption of DOM due to attractive electrostatic interactions was expected. Recovery of DOM matched the trend of adsorption efficiency, meaning that the lowest recovery or the largest depletion of DOM in TDAC eluates was achieved when aqueous sample solutions were extracted. These findings underline that unspecific interactions are likely not causing the adsorption of DOM to TiO_2, since otherwise no or less adsorption would have been observed in organic solvents in comparison to ultrapure water. The results for the four model siderophores DFOB, VF, PB and WBA are displayed as averaged adsorption efficiency and averaged recovery. Independent of solvent and pH, averaged siderophore adsorption efficiency was > 89% for all extraction experiments. In comparison to the observed DOM adsorption efficiencies, it is particularly noticeable that the averaged adsorption efficiency of siderophores from ultrapure water is similar to that from the organic solvents. But similar to the observed DOM recoveries, the averaged siderophore recoveries (Ø 36%) were also proportional to the determined adsorption efficiencies. The comparison between the recoveries of DOM and siderophores illustrates that depletion of DOM relative to siderophores in the eluate occurred only under aqueous adsorption conditions. Therefore, to achieve an even greater depletion of DOM compared to siderophores in the TDAC eluate, additional aqueous adsorption conditions were investigated. The investigated adsorption buffers contained chloride, sulphate or phosphate at two concentrations (0.1 M or 0.5 M) and were adjusted to two pH values (2.4 or 4) or five different pH values (2.4, 4, 7, 9 and 10) in case of the phosphate containing buffers. In general, DOM adsorption efficiency decreased with increasing anion concentration (Figure 20). The specific effect of the anion present was particularly evident in the case of phosphate, which, under otherwise identical conditions (concentration and pH), led to poorer DOM adsorption efficiencies than sulphate and chloride. This ranking correlates with the observed anionic effect on the adsorption of natural organic matter onto TiO_2 nanoparticles (Erhayem and Sohn 2014). When comparing the different phosphate buffers with each other, it also became clear that at a constant phosphate concentration (0.1 M), the adsorption efficiency of DOM increased with increasing pH. These observations supported my expectations, as the affinity of phosphate towards TiO_2 and therefore the competition for binding sites decreases with increasing pH (Connor and McQuillan 1999).

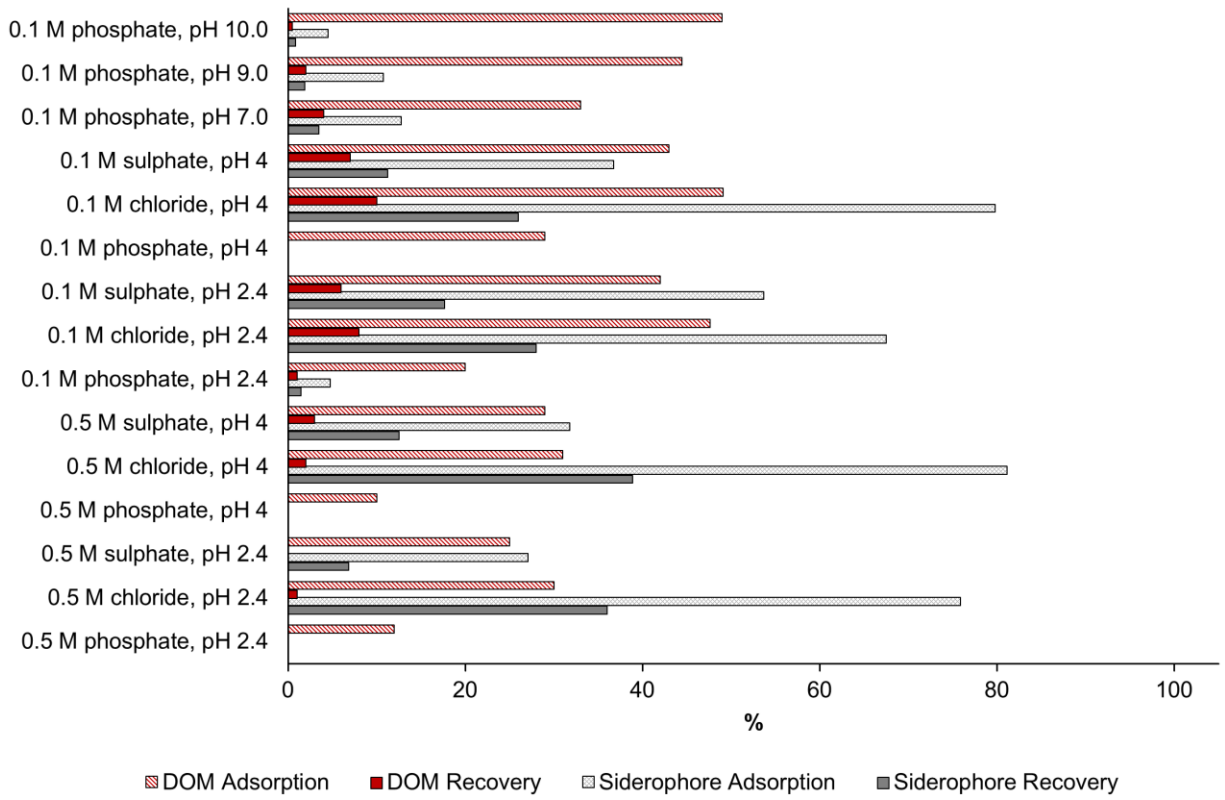

Figure 20. Comparison of DOM adsorption efficiency and recovery (DOM represented by negative correlating compounds according to Flerus et al. 2012) and averaged siderophore adsorption efficiency and recovery depending on buffer composition and pH. Vibrioferrin, desferrioxamine B, petrobactin and woodybactin A were used as model siderophores.

Similar to the observed DOM adsorption efficiencies, the averaged siderophore adsorption efficiencies were more reduced by the addition of phosphate under acidic conditions than by sulphate and chloride. All acidic phosphate buffers resulted in siderophore adsorption efficiencies of less than 5%. In contrast to those results, the siderophore adsorption efficiencies of the sulphate and chloride containing buffers were above 25% and 65%, respectively. These findings were in accordance with the observed influence of those anions on the elution of siderophores from TiO_2 described in Chapter 3. Comparison of extraction results shows that the buffer containing 0.5 M chloride at pH 4 achieved the greatest depletion of DOM (2% recovery) with the highest possible recovery of siderophores (38.9%).

5.3.2 TDAC reprocessing of large volume seawater extracts from expedition HE533

The working protocol to enrich siderophores and deplete DOM was applied to large volume extracts of Fjord DOM. The majority of TDAC eluates resulted in chromatograms similar to the base peak chromatograms (BPC) of the blank eluates, measured in negative as well as in positive ionization mode. One example is the BPC of the TDAC eluate of Station 7 given in Figure 21. These findings underline the absence of high siderophores concentrations in such extracts. This hypothesis is matching the observation, that no siderophores were identified in the crude

HP20 extracts with a data base comparison. The only TDAC eluate that showed distinct peaks in the LC-HRMS runs, positive as well as negative ionization mode (Figure 21), was the TDAC eluate of the 50 L HP20 extract from Station 9 that was sampled in 3 m water depth (Table 6). The two peaks observed in the BPC at negative ionization can be assigned to two distinct *m/z* values: 1083.44946 at 9.67 min and 819.36573 at 9.84 min (Figure 21).

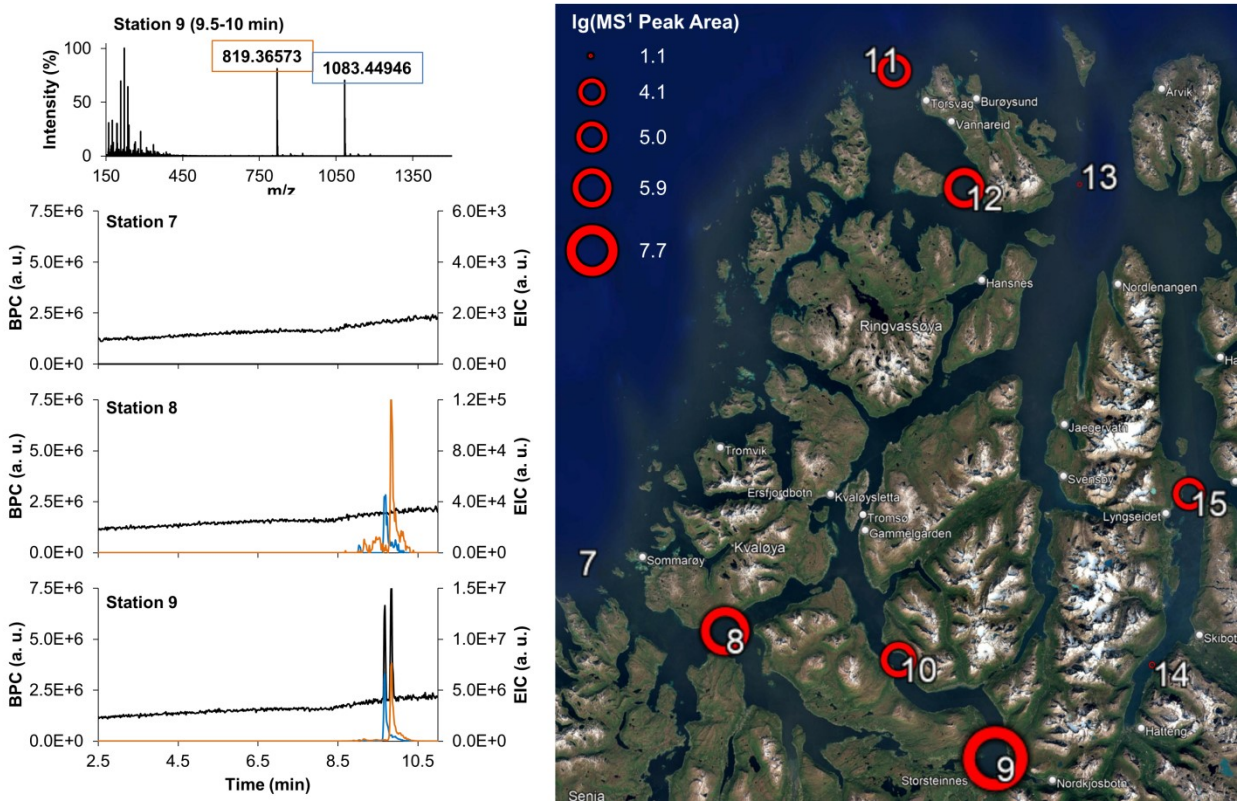

Figure 21. Negative base peak chromatograms (BPC, black) and extracted ion chromatograms (EIC) of *m/z* 819.36573 (orange) and *m/z* 1083.44946 (blue) responsible for observed base peaks in TDAC eluates. Chromatograms for Stations 7, 8, and 9 are given for comparison. The map shows the distribution and abundance of *m/z* 819.36573 corresponding to the determined peak areas in the TDAC eluates across the fjord systems around Tromsø (Stations 8, 9, 10, 11, 12, 14 and 15) in summer 2019.

In positive ionization mode the two peaks also occur in the TIC, but the corresponding mass spectrum is more complex (Figure SI 13) compared to the one obtained in negative mode, resulting in the absence of peaks in the positive BPC. The EICs of *m/z* 819.36573 and *m/z* 1083.44946 are also shown in the displayed chromatograms as well as the distribution of *m/z* 819.36573 across the fjords around Tromsø, underlining that especially this *m/z* value was not only observed in this extract of Station 9 but also in the those of Stations 8, 10, 11, 12, 14 and 15. Furthermore, these *m/z* values were also detected in the corresponding crude HP20 extracts of these stations prior to TDAC (Table SI 7). Those compounds were also observed in one additional HP20 extracts from the Tromsø area (Station 13) as well as from other regions like the Porsanerfjord (Station 17-19) and Laksefjord (Station 21) (Figure 18, Table SI 7). However, the abundance of those compounds in these samples was much lower than in the HP20

extracts from Stations 8, 9, 10 and 12. Additionally, none of these ions were observed in either the blank samples or the NSS pH 2 DOM standard. However, it was remarkable that these *m/z* values were predominantly observed in the samples from the fjord systems around Tromsø. The compound corresponding to *m/z* 1083.44946 was only detected in samples in which *m/z* 819.36573 was also measured. In all cases, the signal of *m/z* 819.36573 was more intense than that of *m/z* 1083.44946 (Table SI 7). The hotspot of the putative compounds seemed to be located at the end of the Balsfjord (Station 9). Zooming into the mass spectra shown in Figure 21, resulted in the observation that *m/z* 819.36573 and *m/z* 1083.44946 both exhibited characteristic *Δm/z* values (Figure 22). The *Δm/z* 52.9115 corresponds to the difference between the ^{12}C-isotope peak of the iron free compounds ($[M-H]^-$ = *m/z* 819.36573 and *m/z* 1083.44946) and the $^{56}Fe^{12}C$ isotope peak of the iron containing compound ($[M-4H+^{56}Fe]^-$ = *m/z* 872.27733 and *m/z* 1136.35986, respectively) (Baars et al. 2014). The difference of *Δm/z* 52.9115 indicates an Fe(III)-complex not only in positive but also in negative ionization mode, as shown for Fe(III)-EDTA (Chen et al. 2007; Zheng et al. 2008) or the siderophore coprogen (Simionato et al. 2006). Besides the *Δm/z* between free and iron-containing species, the more common *Δm/z* for the identification of iron containing ions is the characteristic *Δm/z* of 1.9954 (De Hoffmann and Stroobant 1991) for the isotope pair $^{54}Fe/^{56}Fe$ (*m/z* 872.27733/ *m/z* 870.28232 and *m/z* 1136.35986/ *m/z* 1134.36441). Together, the observed intensity ratio of 6.01/100 for *m/z* 870.28232/ *m/z* 872.27733 and 4.68/100 for *m/z* 1134.36441/ *m/z* 1136.35986, the chromatographic coherence (Figure 24) of the iron isotope and adduct patterns suggest that these parent compounds contain iron (Baars et al. 2014; Baumeister et al. 2018; Aron et al. 2022).

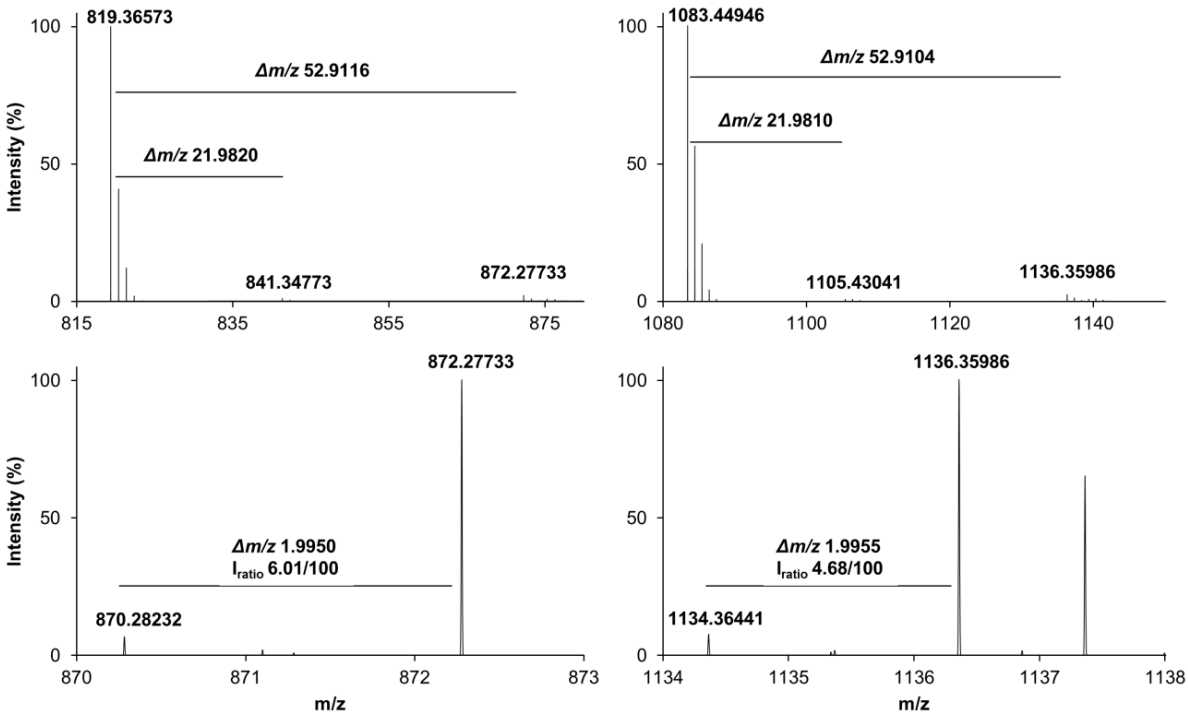

Figure 22. MS[1] spectra in negative ionization mode of *m/z* 819.36573 and *m/z* 1083.44946 extracted from the chromatogram of Station 9 TDAC eluate, which is shown in Figure 21.

In addition to the *Δm/z* values indicating the presence of an iron-species, the *Δm/z* of 21.9820 was observed for both, *m/z* 819.36573 and *m/z* 1083.44946, verifying the presence of a deprotonated ion ($[M-H]^-$) and its associated deprotonated sodium adduct ($[M-2H+Na]^-$ = *m/z* 841.34773 and *m/z* 1105.43041, respectively (Zhu et al. 2013). The corresponding iron species to the sodium adduct *m/z* 1105.43041 were also observed: $[M-5H+^{56}Fe+Na]^-$ = *m/z* 1158.34197 and $[M-5H+^{54}Fe+Na]^-$ = *m/z* 1156.34643 with *Δm/z* 1.9955 and an intensity ratio of 5.9/100 (Figure 23).

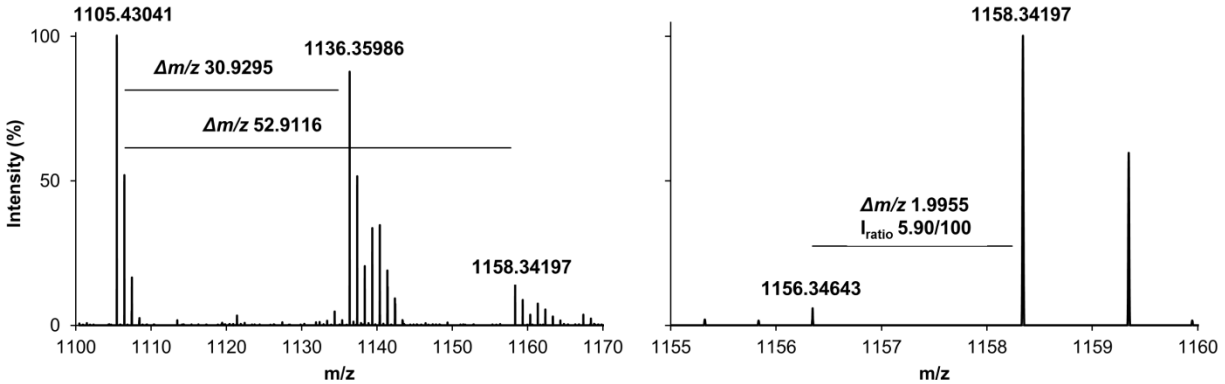

Figure 23. MS^1 spectra in negative ionization mode of *m/z* 1105.43041 extracted from the chromatogram of Station 9 TDAC eluate, which is shown in Figure 21.

In general, the presence of sodium adducts $[M-2H+Na]^-$ in negative ionization mode is a strong indication of acidic functionality (Nielsen et al. 2011) and could therefore also be considered indicative of siderophore-like substances. As mentioned above, the spectra obtained in positive mode were more complex and the corresponding $[M+H]^+$ ions to the deprotonated ions $[M-H]^-$ = *m/z* 819.36573 and $[M-H]^-$ = *m/z* 1083.44946 were not detected. Nevertheless, *m/z* values were observed consistent with the retention times of the ions detected in the negative mode (Figure 24), which also revealed the typical *Δm/z* values and intensity ratios described above. Corresponding to the sodium adducts in negative mode $[M-2H+Na]^-$, the sodium adducts in positive mode $[M+Na]^+$ = *m/z* 1107.44847 and $[M+Na]^+$ = *m/z* 843.36338 were detected at the same retention time. In addition, the iron-containing species of the sodium adducts were also observed: $[M-3H+^{56}Fe+Na]^+$ = *m/z* 1160.36021 or *m/z* 843.36338 and $[M-3H+^{54}Fe+Na]^+$ = *m/z* 1158.36729 or *m/z* 841.3678. Furthermore, doubly charged ions, showing the same chromatographic and isotopic coherence, were measured: $[M+H+Na]^{2+}$ = *m/z* 422.17924 or *m/z* 554.22236, $[M-3H+^{56}Fe+Na]^{2+}$ = *m/z* 448.64122 or *m/z* 580.68361 and $[M-2H+^{54}Fe+Na]^{2+}$ = *m/z* 447.64349 or *m/z* 579.68553. These interpretation can be made due to the observed *Δm/z* of 26.4609 and *Δm/z* of 0.9979 (*z* = 2) corresponding to the *Δm/z* 52.9115 and *Δm/z* 1.9954 (*z* = 1). MS^2 experiments of *m/z* 819.36573 and the corresponding iron species *m/z* 872.27733 and *m/z* 870.28232 revealed the characteristic $^{56}Fe/^{54}Fe$ *Δm/z* even after fragmentation (Figure 25, Table SI 4).

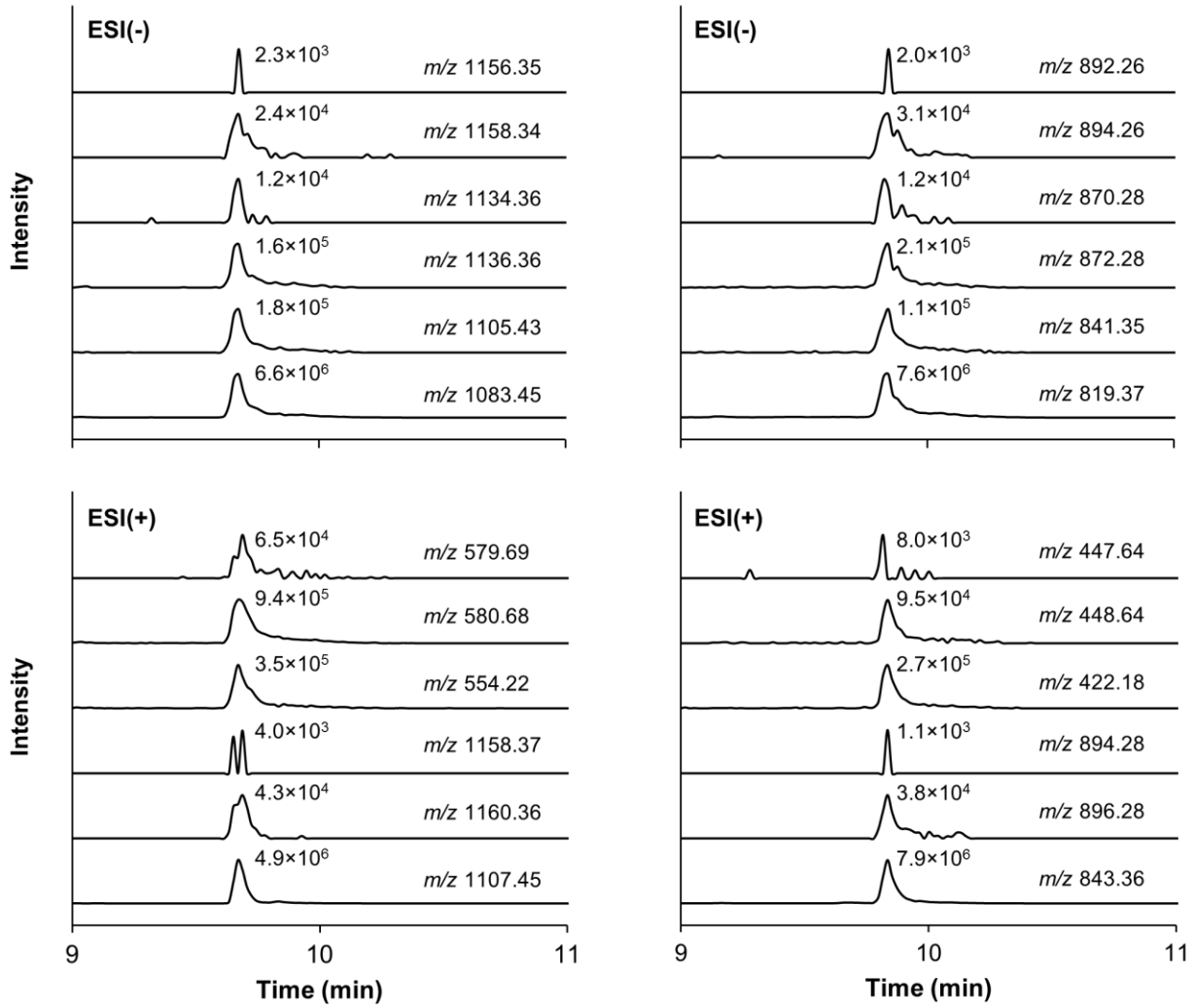

Figure 24. Comparison of extracted ion chromatograms corresponding to putative siderophore ions in negative and positive ionization mode.

A similar observation was made for the fragmentation of the iron species *m/z* 1136.35986 and *m/z* 1134.36441, but only one fragment could be compared due to the low intensities of the ^{54}Fe species (Figure 25, Table SI 5). The observable iron isotope pattern after fragmentation, further confirmed the presence of siderophore-like iron complexes rather than unspecific adducts formed in the ESI source, since the strong affinity of smaller fragments to bind iron is a characteristic of siderophore-type compounds (Velasquez et al. 2011). MS^2 experiments further underlined the structural similarity between these two parent compounds. Characteristic neutral losses of 114.07 Da and 204.10 Da were observed during the fragmentation of the iron free and iron-containing species of both components (Table 7). The neutral loss of 204 Da is regularly assigned to a loss of acetyl-hexose ($C_8H_{12}O_6$) (Ancillotti et al. 2017), but the poor accuracy of *Δppm* > 100 is denying this suggestion. Annotating the neutral loss to $C_9H_{16}O_5$ with an accuracy of *Δppm* -2.96 is more appropriate but gives no structural information about the parent ions, since no match was found in the literature.

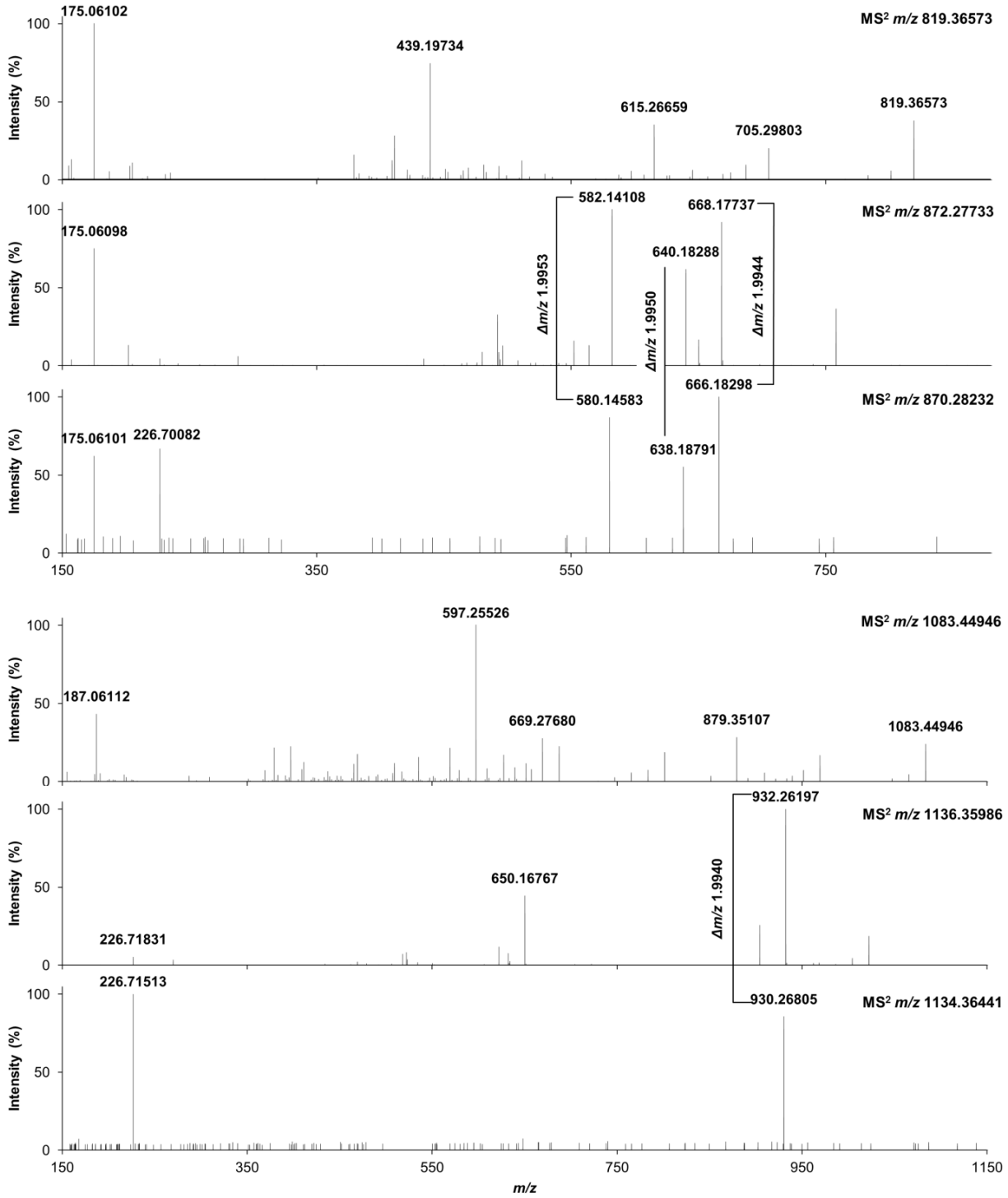

Figure 25. MS² spectra of *m/z* 819.36573, *m/z* 872.27733, *m/z* 870.28232, *m/z* 1083.44946, *m/z* 1136.35986 and *m/z* 1134.36441.

The neutral fragment 114.07 Da, corresponding to an elemental composition of $C_6H_{10}O_2$, is also not classified as a diagnostic device for one specific structural feature as an extensive literature research underlined. The neutral loss of 176.07 Da was observed to be a unique feature for the fragmentation of the parent ions 819.37, 870.27 and 872.27. Literature comparison suggested that this fragment corresponds to a glucuronide conjugate ($C_6H_8O_6$) (Ling et al. 2012), but similar to the neutral loss of 204 Da, the accuracy of *Δppm* > 100 led to exclusion of this sum formu-

la. Instead this neutral loss was annotated as $C_7H_{12}O_5$. MS^2 spectra in positive ionization mode of *m/z* 843.36338 and *m/z* 1107.44847 underline the structural similarities of these two molecules (Figure SI 13). The observed parent ions, corresponding fragments and neutral losses led to the conclusion that the detected putative unknown ligands contain no nitrogen. Especially the observation, that the fragments *m/z* 175.06 and *m/z* 187.06 showed subsequently neutral losses of 18 Da, implied the presents of oxygen in those small fragments. This requirement caused the exclusion of all sum formulas without oxygen, including possible parent ions containing nitrogen. Even considering sulfur and phosphorus, it was not possible to propose more suitable sum formulas compatible with all observed fragments and neutral losses. Therefore *m/z* 819.36573 and m/z 1083.44946 were assigned to $C_{38}H_{59}O_{19}$ and $C_{48}H_{75}O_{27}$, respectively (Table 8).

SIRIUS 4.9.15 (Dührkop et al. 2019) was used to verify the manually predicted molecular formulae of the putative siderophore-like compounds. The latest version of SIRIUS combines the formula annotation by MS^2 patterns with the structural characterization capabilities of CSI (Compound Structure Identification):FingerID (Dührkop et al. 2015) and the systematic classification approach of CANOPUS (Class assignment and ontology prediction using mass spectrometry) (Dührkop et al. 2021). In case of *m/z* 819.36573 and its corresponding ions, SIRIUS concluded the identical molecular formula of $C_{38}H_{59}O_{19}$ and CSI:FingerID calculation resulted in 24 structure suggestions, which all contained three glycosyl groups. The related structure with the highest structural similarity is shown in Figure 26.

Table 7. Characteristic neutral losses observed for putative unknown ligands and corresponding iron complexes in negative ionization mode.

Neutral loss / Da	Sum formula	Parent ion $[M-H]^-$
114.07	$C_6H_{10}O_2$	819.37; 1083.45
176.07	$C_7H_{12}O_5$	819.37
204.10	$C_9H_{16}O_5$	819.37; 1083.45
282.09	$C_{10}H_{18}O_9$	1083.45
Neutral loss / Da	**Sum formula**	**Parent ion $[M-4H+Fe]^-$**
114.07	$C_6H_{10}O_2$	872.27, 870.27; (1034.36), 1036.36
118.03	$C_4H_6O_4$	872.27, 870.27; (1034.36), 1036.36
176.07	$C_7H_{12}O_5$	872.27, 870.27
282.10	$C_{10}H_{18}O_9$	(1034.36), 1036.36

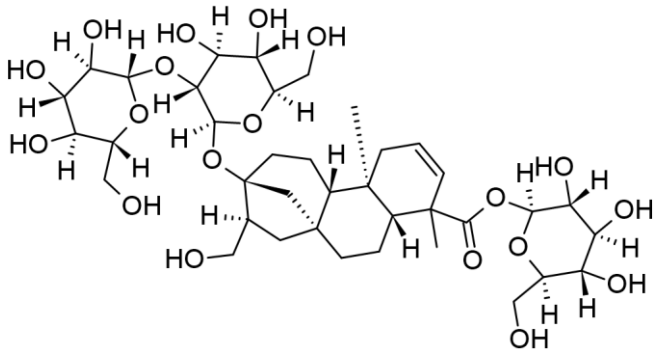

Figure 26. Structure of the most similar CSI:FingerID suggestion for [M-H]$^-$ = *m/z* 819.36573 with a similarity of 53%.

Table 8. Annotation of detected ions in negative and positive ionization mode.

Measured *m/z*	Theoretical *m/z*	*Δppm*	Charge *z*	Sum formula
819.36573	819.36560	0.16	-1	$C_{38}H_{59}O_{19}$
841.34773	841.34755	0.22	-1	$C_{38}H_{58}O_{19}Na$
870.28232	870.28285	0.67	-1	$C_{38}H_{56}O_{19}{}^{54}Fe$
872.27733	872.27707	0.30	-1	$C_{38}H_{56}O_{19}{}^{56}Fe$
892.26350	892.26369	-0.21	-1	$C_{38}H_{55}O_{19}{}^{54}FeNa$
894.25904	894.25901	0.03	-1	$C_{38}H_{55}O_{19}{}^{56}FeNa$
1083.44946	1083.45012	-0.69	-1	$C_{48}H_{75}O_{27}$
1105.43041	1105.43206	-1.49	-1	$C_{48}H_{74}O_{27}Na$
1134.36441	1134.36626	-1.63	-1	$C_{48}H_{72}O_{27}{}^{54}Fe$
1136.35986	1136.36159	-1.52	-1	$C_{48}H_{72}O_{27}{}^{56}Fe$
1156.34643	1156.34820	-1.54	-1	$C_{48}H_{71}O_{27}{}^{54}FeNa$
1158.34197	1158.34353	-1.35	-1	$C_{48}H_{71}O_{27}{}^{56}FeNa$
422.17924	422.18469	-12.91	+2	$C_{38}H_{61}O_{19}Na$
447.64349	447.64276	1.63	+2	$C_{38}H_{58}O_{19}{}^{54}FeNa$
448.64122	448.64042	1.78	+2	$C_{38}H_{58}O_{19}{}^{56}FeNa$
554.22236	554.22695	-8.28	+2	$C_{48}H_{77}O_{27}Na$
579.68553	579.68502	0.88	+2	$C_{48}H_{74}O_{27}{}^{54}FeNa$
580.68361	580.68268	1.59	+2	$C_{48}H_{74}O_{27}{}^{56}FeNa$
843.36338	843.3621	1.52	+1	$C_{38}H_{60}O_{19}Na$
894.27705	894.27824	-1.33	+1	$C_{38}H_{58}O_{19}{}^{54}FeNa$
896.27505	896.27357	1.66	+1	$C_{38}H_{58}O_{19}{}^{56}FeNa$
1107.44847	1107.44662	1.67	+1	$C_{48}H_{76}O_{27}Na$
1158.36729	1158.36276	3.41	+1	$C_{48}H_{74}O_{27}{}^{54}FeNa$
1160.36021	1160.35808	1.83	+1	$C_{48}H_{74}O_{27}{}^{56}FeNa$

In case of *m/z* 1083.44946 the sum formula of $C_{48}H_{75}O_{27}$ was within the top three SIRIUS suggestions. However, CSI:FingerID suggested no similar structures for this formula. The classification of both compounds with CANOPUS resulted in the level 6 annotation of *m/z* 819.36573 as an *o*-glycosyl compound and in the level 5 annotation of *m/z* 1083.44946 as an oligosaccharide. These classifications are based on the ClassyFire ChemOnt ontology (Feunang et al. 2016) and highlighted the saccharide-like character of these putative ligands.

Since almost all known siderophores contain nitrogen as part of the iron-binding hydroxamate group or in their peptide backbone structure (Hider and Kong 2010) and due to the lack of missing literature matches in terms of MS^2 patterns and exact masses as well as the classification via CANOPUS, it can be concluded that the observed ions do not belong to any described siderophore class. Nonetheless, the marine iron ligand pool contains other substance classes in addition to siderophores that are able to form complexes with Fe(III) and are not defined by a certain nitrogen content. The remaining ligands can generally be associated to either humic substances or to marine degradation and excretion products (Hassler et al. 2017). Humic substances, including humic and fulvic acids, are loosely-defined macromolecules which contain a mixture of carboxylated and fused alicyclic structures, known for metal binding capabilities (Hertkorn et al. 2006; Yang and Van Den Berg 2009; Gledhill and Buck 2012). Degradation and excretion products include a variety of different carbohydrates like polyphenolic compounds and saccharides showing also a distinct ligand character (Gyurcsik and Nagy 2000; Verdugo et al. 2004; Santana-Casiano et al. 2010, 2014; Rico et al. 2013). For example, monosaccharides like gluconic acid form iron complexes (log *K* 8.7) that are almost as stable as the Fe(III)-vibrioferrin complex (log *K* 10.9) (Croot and Johansson 2000; Amin et al. 2009a). In addition, saccharide concentrations are reported to be at least one order of a magnitude above siderophore concentrations highlighting their potential to outcompete strong ligands like siderophores (Panagiotopoulos and Sempéré 2005; Hassler et al. 2011b). However, most of the saccharides (3-50% of total dissolved and colloidal organic matter (Aluwihare et al. 1997; Verdugo et al. 2004; Hassler et al. 2011b)) are present as polysaccharides (Pakulski and Benner 1994). Such polysaccharides are synthesized by most marine organisms, which use those glycans either as internal energy storage or secrete them as extracellular polysaccharides (EPS) (Aluwihare et al. 1997; Nichols et al. 2005; Norman et al. 2015). The ability of EPS and corresponding degradation products to bind iron and to enhance its bioavailability to phytoplankton is well documented (Rue and Bruland 2001; Hassler et al. 2011b; a). All these findings correspond to the possible saccharide-like character of the observed putative siderophores.

In addition to the classification of these compounds, it was also suspected that the observed substances are related to the algal bloom of the toxic haptophyte *Chrysochromulina leadbeateri* in the Balsfjord. The toxins of this species are not known, but since *C. leadbeateri* belongs to

the genus *Prymnesium* the biosynthesis of similar toxins can be expected. For example, *P. parvum* produces a complex mix of toxins that includes lipopolysaccharides and galactolipids as well as ladder-frame polyether prymnsesins (Kozakai et al. 1982; Wagstaff et al. 2018). The majority of these toxins exhibits low or no nitrogen compositions as well as saccharide functionalities and thus meets the requirement of the observed substances. However, no matches with MS or MS^2 data of these toxins were obtained. A strong indication against linking the toxic algal bloom to the observed compounds is that the apparent hotspot for those compounds was not observed at Station 10, where the highest cell concentrations of *C. leadbeateri* were observed, but at the end of the fjord at Station 9. Since unfiltered water was also extracted at Station 10 and no increased abundances of those components were observed in these samples, it was also hypothesized that these substances are most likely not cell-associated with *C. leadbeateri* (Table SI 7). Rather, a link can be seen between the observed chlorophyll maximum, indicating the greatest concentration of phytoplankton, and the observed putative siderophore abundance at Station 9. This station was the only sample site where the chlorophyll maximum was detected at the surface of the water column (Figure 27). For all other stations on this cruise, the chlorophyll maximum was observed between 8-28 m water depths. In addition, Station 9 and Station 25 were the only locations where haloclines were observed, as indicated by the reduced salinity in the surface water (Figure 27 and Figure SI 14). However, none of the putative siderophores were detected in the extract of Station 25, emphasizing that the occurrence of these compounds may not be linked to the stratification of the water column or the influx of terrestrial material alone but to the primary production in the uppermost water layer. Nonetheless, the stratification of the water column in combination with the observed chlorophyll fluorescence suggested that all exudated metabolites are concentrated in the surface water since the formation of a halocline hampers the mixing of the water column.

At Station 9 two different large volume extractions were performed at 3 m (50 L) and at 14 m (150 L) water depth. As mentioned above, the highest abundance of putative siderophores was observed in the surface water extract, while in comparison only a tenth of *m/z* 819.36573 and a hundredth of *m/z* 1083.44946 was detected in the extract from 14 m water depth (Table SI 7). These findings matched the general expectations that excess ligand concentrations are highest in the upper water column (Rue and Bruland 1995; Boye et al. 2001; Thuroczy et al. 2010; Ibisanmi et al. 2011; Mohamed et al. 2011; Gledhill and Buck 2012). However, since the extraction efficiency of these substances was unknown and due to the extraction of different volumes, differences in signal intensities cannot be correlated with depth or chlorophyll fluorescence at this station. This limitation on data interpretation generally applied to all extracts, since different volumes of sea water were extracted, resulting presumably in different recoveries of these compounds at every sample site.

Therefore, the available data allowed only semi-quantitative statements about the occurrence of these substances. However, since both extracts from Station 9 exhibited the highest observed intensities of the putative siderophores it was concluded that these substances were most abundant at this location.

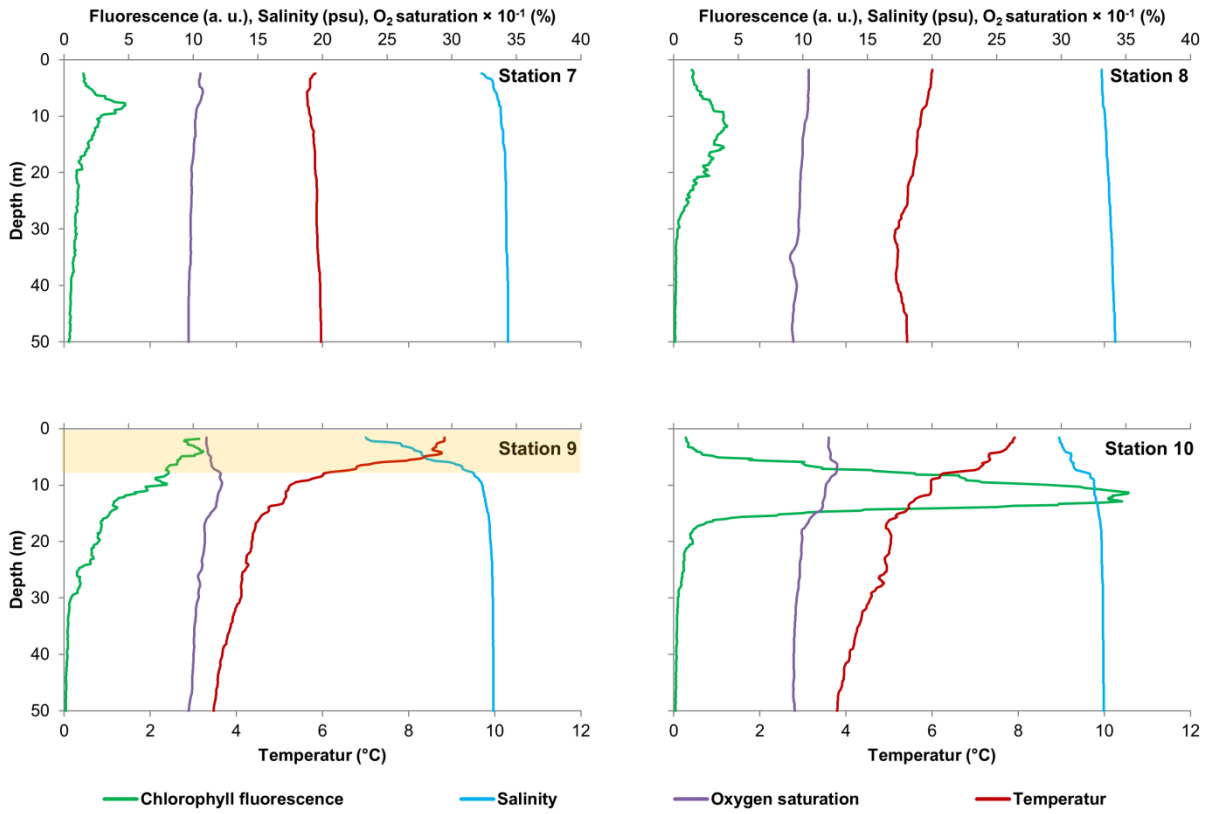

Figure 27. Depth profiles of chlorophyll fluorescence, salinity, O_2 saturation and temperature at Stations 7-10. The highest chlorophyll fluorescence, highest temperature and lowest salinity in surface water during the HE533 cruise was observed at Station 9 (highlighted in orange). Data was taken from the corresponding PANGEA entry (John and Wisotzki).

Linking chlorophyll concentrations and therefore primary production to iron ligand concentrations was undertaken in a variety of studies (Rue and Bruland 1995; van den Berg 1995; Witter and Luther III 1998; Boye et al. 2001, 2010; Croot et al. 2004; Gerringa et al. 2006; Gledhill and Buck 2012). Most of these studies underlined the correlation between the maxima of excess ligand concentration and chlorophyll fluorescence (Gledhill and Buck 2012). But only in a recent study it was shown that the presence of specific siderophores correlated with certain chlorophyll *a* concentrations and depth profiles (Boiteau et al. 2019b): Ferrioxamines were observed in surface waters of shallow continental shelf regions with high chlorophyll *a* concentrations (> 10 μgL^{-1}), while apolar siderophores like amphibactins were found in nepheloid layers or offshore waters with intermediate chlorophyll *a* concentrations (0.5–3 μgL^{-1}). Therefore these findings suggested a correlation between the polarities of the observed siderophores with the detected chlorophyll *a* concentrations at the specific sample sites. This correlation may also be

observed in this case since at Station 9 in 4 m water depth intermediate chlorophyll *a* concentrations were overserved (4.7 μgL^{-1}) (Voß et al.), and the retention behavior of the putative siderophores indicated a more apolar character than desferrioxamine B. With all these observations and links to the literature it remains to be clarified if the observed putative ligands are related to microbial saccharides or other ligand classes of the marine ligand pool. Further experiments are therefore necessary not only to achieve structural elucidation but also to verify the Fe(III)-chelating properties, since the iron species and corresponding free ligands were only detected at the same retention times. This observation indicates that either complex formation or dissociation appeared after separation on the LC and thus only one species was present in the TDAC eluates as well as in the HP20 extracts.

5.4 Conclusion

Although iron is limiting not only the primary production in most of the world's oceans, systematic approaches to characterize and to discover Fe(III)-binding ligands are limited. All commonly applied methods used for the identification of those ligands rely solely on the detection of the unique isotopic pattern of iron or on a targeted approach using established data bases. This TDAC method described here can help to identify iron-binding ligands in one of the most complex sample matrices like DOM, by reducing the sample complexity drastically. By using an adsorption buffer, containing 0.5 M chloride at pH 4, TDAC allowed the enrichment of siderophores with an averaged recovery of approximately 40%, while DOM recovery was below 2%.

This adapted TDAC protocol was then applied to the processing of large volume seawater extracts from the cruise HE533 of the research vessel Heincke. The analysis of the eluates showed that the adapted protocol is suitable for the efficient depletion of DOM, as most of the eluates showed blank-like base peak chromatograms. Only one Station sample (Station 9, surface water) showed two distinct peaks in the negative BPC. These peaks corresponded to two putative Fe(III)-ligands in their apo-form, since matching ions were detected showing the characteristic iron-isotope pattern as well as the associated sodium adducts. These results highlighted that the TDAC method allows the identification of chelating compounds not by intense data mining but due to the reduction of sample complexity prior to MS measurements. Using high-resolution MS and MS^2 experiments, it was possible to determine the molecular formulae of the two components, but due to missing matches with the literature, no detailed conclusions were made about their structure. However, CANOPUS classified both compounds as saccharide-like molecules based on their MS^2 pattern. The identified compounds were not only detected in samples from Station 9 but in general predominantly in the Tromsø area, with the presumably hotspot in the surface water at the end of the Balsfjord (Station 9). This sample site was characterized by clear stratification of the water column, including a surface layer of fresh water.

At this station not only the highest abundance of these compounds were detected but also the highest chlorophyll fluorescence in surface water. Raising the question how the observed compounds were linked to the primary production in such defined surface waters. These results highlighted the potential of TDAC as a powerful tool that contributes to solving the puzzle of iron cycling and ligand pool composition in the world's oceans.

6. Conclusion and perspective

This thesis provides a new affinity chromatography approach – TDAC – based on the inherent affinity of siderophores to TiO_2 allowing the specific separation of those iron ligands from complex sample matrices like bacterial cultures, saline matrices and marine DOM extracts. TDAC represents a novel type of affinity chromatography with unique adsorption and elution characteristics extending the tool box of siderophore analytics by simplifying the identification of putative siderophores in background depleted TDAC eluates. Especially the strong interaction of functional groups like hydroxamates, catecholates and α-hydroxycarboxylates with TiO_2 resulted in efficient adsorption and specific separation from the organic background. TDAC allowed the extraction of polar compounds from apolar solvents as well as from polar matrices even in the presence of high salinity or organic background. However, the detailed mechanisms of adsorption and desorption of the different functional groups need further investigation to fully understand why those iron chelating groups required different elution solution compositions. Extending the knowledge about the desorption mechanism will ultimately lead to refined elution conditions that could further enhance the separation performance of TDAC. Broader knowledge of the desorption process and the resulting improved separation performance would also likely suggest the potential of purifying other substance classes such as phosphocompounds, flavonoids, and cis-diols simultaneously with siderophores. Besides the excellent performance of TDAC in separating siderophores from small-volume and high-concentration samples, drawbacks were noted when TDAC was used for large-volume extraction of seawater. It was concluded that two different parameters limited the performance of TDAC under the investigated experimental setup. The first limitation was caused by the seawater matrix which contained inorganic components like phosphate ions and organic molecules like humic substances. Since both compound classes are more abundant in seawater than siderophores and are known to adsorb onto TiO_2 the specific adsorption of siderophores was presumably hampered by those matrix components. The second drawback resulted from the small surface area of the prepared TiO_2 sorbent, limiting the retention capabilities of TDAC if large sample volumes with small analyte concentrations were extracted at increased flow rates. Therefore the present TDAC material was not feasible for the targeted extraction of siderophores from seawater. It would be necessary to increase the surface area of the TiO_2 sorbent to overcome the limited retention under these needed extraction conditions. However, this adjustment alone would probably not result in satisfactory siderophore recoveries since the seawater matrix would still counteract the efficient adsorption of siderophores raising the question if or how the problem of competing ligands like phosphate or organic acids could be solved. Thus, it can be concluded that the TDAC adsorption step in particular needs to be further optimized to achieve a more efficient recovery of siderophores from seawater and thereby facilitate the characterization of the marine ligand pool.

Nevertheless, TDAC showed its potential in terms of deciphering the marine ligand pool and highlighting putative ligands in natural samples when this method was used to reprocess DOM extracts from cruise HE533. TDAC helped to identify two putative siderophores and to recognize a potential correlation between their abundance and the occurrence of particular high chlorophyll fluorescence in the surface water of the Balsfjord. These results demonstrated how valuable TDAC might become for the characterization of environmental extracts with respect to their iron ligand component. As a follow up experiment, it is planned to cultivate *Chrysochromulina leadbeateri* and use the established culture to investigate the possible linkage between the occurrence of the toxic algal bloom and the observed distribution of putative siderophores.

With the knowledge gained through the development of TDAC, studies of soil samples employing these adjustments could provide new insights into the terrestrial iron ligand pool. Previous studies have investigated the occurrence and composition of siderophores in soils, but were generally limited to dissolved ligands (Boiteau et al. 2018) or demonstrated that the soil type had a significant effect on the adsorption strength of siderophores on soil particles, hampering their desorption and detection (Rai et al. 2020). Since much effort was expended in this work to determine elution conditions that result in high siderophore desorption efficiencies from TiO_2, and similar metal oxide or related minerals are widely distributed in many soil types, washing such soil samples with the elution solutions studied here could lead to the detection of previously unknown siderophores that form more stable surface complexes on those minerals. In addition, such an adjusted washing protocol could determine the ratio of dissolved to adsorbed siderophores in the rhizosphere and thus provide new information on which type of siderophores participates mainly in mineral weathering. This information could also be used for new fertilization strategies, as most of the world's agricultural land exhibit low bioavailability of iron due to neutral or slightly alkaline conditions.

Since TiO_2 is a widely used material and was employed in the food industry for more than 50 years and is also still found in the pharmaceutical industry as a tablet ingredient, enormous amounts of TiO_2 are transported into nature and organisms. It is already the subject of current research to further describe its fate and toxicology of this material. However, it has not yet been considered whether this material poses negative effects on the iron uptake or metabolism of various organisms due to its strong interaction with iron ligands like siderophores as it was highlighted in this thesis.

References

Abrahamson, H. B., A. B. Rezvani, and J. G. Brushmiller. 1994. Photochemical and spectroscopic studies of complexes, of iron(III) with citric acid and other carboxylic acids. Inorganica Chim. Acta **226**: 117–127. doi:10.1016/0020-1693(94)04077-X

Akafia, M. M., J. M. Harrington, J. R. Bargar, and O. W. Duckworth. 2014. Metal oxyhydroxide dissolution as promoted by structurally diverse siderophores and oxalate. Geochim. Cosmochim. Acta **141**: 258–269. doi:10.1016/j.gca.2014.06.024

Aluwihare, L. I., D. J. Repeta, and R. F. Chen. 1997. A major biopolymeric component to dissolved organic carbon in surface sea water. Nature **387**: 166–169. doi:10.1038/387166a0

Aluwihare, L. I., D. J. Repeta, and R. F. Chen. 2002. Chemical composition and cycling of dissolved organic matter in the Mid-Atlantic Bight. Deep. Res. Part II Top. Stud. Oceanogr. **49**: 4421–4437. doi:10.1016/S0967-0645(02)00124-8

Amin, S. A., D. H. Green, M. C. Hart, and F. C. Ku. 2009a. Photolysis of iron - siderophore chelates promotes bacterial - algal mutualism. Pnas **106**: 17071–17076. doi:10.1073/pnas.0905512106

Amin, S. A., D. H. Green, F. C. Küpper, and C. J. Carrano. 2009b. Vibrioferrin, an unusual marine siderophore: Iron binding, photochemistry, and biological implications. Inorg. Chem. **48**: 11451–11458. doi:10.1021/ic9016883

Amin, S. A., M. S. Parker, and E. V. Armbrust. 2012. Interactions between Diatoms and Bacteria. **76**: 667–684. doi:10.1128/MMBR.00007-12

Ancillotti, C., L. Ciofi, D. Rossini, U. Chiuminatto, J. Stahl-Zeng, S. Orlandini, S. Furlanetto, and M. Del Bubba. 2017. Liquid chromatographic/electrospray ionization quadrupole/time of flight tandem mass spectrometric study of polyphenolic composition of different Vaccinium berry species and their comparative evaluation. Anal. Bioanal. Chem. **409**: 1347–1368. doi:10.1007/s00216-016-0067-y

Araujo, P. Z., P. J. Morando, and M. A. Blesa. 2005. Interaction of catechol and gallic acid with titanium dioxide in aqueous suspensions. 1. Equilibrium studies. Langmuir **21**: 3470–3474. doi:10.1021/la0476985

Arnow, L. E. 1937. Colorimetric determination of the components of 3,4-dihydroxyphenylalanine-tyrosine mixtures. J. Biol. Chem. **118**: 531–537. doi:10.1126/science.86.2225.176

Aron, A. T., D. Petras, R. Schmid, and others. 2022. Native mass spectrometry-based metabolomics identifies metal-binding compounds. Nat. Chem. **14**: 100–109. doi:10.1038/s41557-021-00803-1

Aschner, M., C. Palinski, M. Sperling, U. Karst, T. Schwerdtle, and J. Bornhorst. 2017. Imaging metals in: Caenorhabditis elegans. Metallomics **9**: 357–364. doi:10.1039/c6mt00265j

Atkin, C. L., J. B. Neilands, and H. J. Phaff. 1970. Rhodotorulic acid from species of Leucosporidium, Rhodosporidium, Rhodotorula, Sporidiobolus, and Sporobolomyces, and a new alanine-containing ferrichrome from Cryptococcusmelibiosum. J. Bacteriol. **103**: 722–733. doi:10.1128/jb.103.3.722-733.1970

Awatani, T., K. D. Dobson, A. J. McQuillan, B. Ohtani, and K. Uosaki. 1998. In Situ infrared spectroscopic studies of adsorption of lactic acid and related compounds on the TiO2 and

CdS semiconductor photocatalyst surfaces from aqueous solutions. Chem. Lett. 849–850. doi:10.1246/cl.1998.849

de Baar, H. J. W., U. Bathmannt, V. Smetacek, B. M. Löscher, and C. Veth. 1995. Importance of iron for plankton blooms and carbon dioxide drawdown in the Southern Ocean. Nature **373**: 412–415. doi:10.1038/373412a0

Baars, O., F. M. M. Morel, and D. H. Perlman. 2014. ChelomEx: Isotope-assisted discovery of metal chelates in complex media using high-resolution LC-MS. Anal. Chem. **86**: 11298–11305. doi:10.1021/ac503000e

Banerjee, S., D. D. Dionysiou, and S. C. Pillai. 2015. Self-cleaning applications of TiO2 by photo-induced hydrophilicity and photocatalysis. Appl. Catal. B Environ. **176–177**: 396–428. doi:10.1016/j.apcatb.2015.03.058

Barry, S. M., and G. L. Challis. 2009. Recent advances in siderophore biosynthesis. Curr. Opin. Chem. Biol. **13**: 205–215. doi:10.1016/j.cbpa.2009.03.008

Baumeister, T. U. H., N. Ueberschaar, W. Schmidt-Heck, J. F. Mohr, M. Deicke, T. Wichard, R. Guthke, and G. Pohnert. 2018. DeltaMS: a tool to track isotopologues in GC- and LC-MS data. Metabolomics **14**: 1–10. doi:10.1007/s11306-018-1336-x

Behrenfeld, M. J., A. J. Balet, Z. S. Kolber, J. Aikent, and P. G. Falkowski. 1996. Confirmation of iron limitation of phytoplankton photosynthesis in the equatorial Pacific Ocean. Nature **383**: 508–511. doi:10.1038/383508a0

van den Berg, C. M. G. 1995. Evidence for organic complexation of iron in seawater. Mar. Chem. **50**: 139–157. doi:10.1016/0304-4203(95)00032-M

Biener, J., J. Wang, and R. J. Madix. 1999. Direct observation of the growth of vanadium on TiO2(110)-(1 × 2). Surf. Sci. **442**: 47–54. doi:10.1016/S0039-6028(99)00835-3

Boiteau, R. M., S. J. Fansler, Y. Farris, J. B. Shaw, D. W. Koppenaal, L. Pasa-Tolic, and J. K. Jansson. 2019a. Siderophore profiling of co-habitating soil bacteria by ultra-high resolution mass spectrometry †. Metallomics **11**: 166–175. doi:10.1039/c8mt00252e

Boiteau, R. M., J. N. Fitzsimmons, D. J. Repeta, and E. A. Boyle. 2013. Detection of iron ligands in seawater and marine cyanobacteria cultures by high-performance liquid chromatography-inductively coupled plasma-mass spectrometry. Anal. Chem. **85**: 4357–4362. doi:10.1021/ac3034568

Boiteau, R. M., D. R. Mende, N. J. Hawco, and others. 2016. Siderophore-based microbial adaptations to iron scarcity across the eastern Pacific Ocean. Proc. Natl. Acad. Sci. **113**: 14237–14242. doi:10.1073/pnas.1608594113

Boiteau, R. M., and D. J. Repeta. 2022. Slow Kinetics of Iron Binding to Marine Ligands in Seawater Measured by Isotope Exchange Liquid Chromatography-Inductively Coupled Plasma Mass Spectrometry. Environ. Sci. Technol. **56**: 3770–3779. doi:10.1021/acs.est.1c06922

Boiteau, R. M., J. B. Shaw, L. Pasa-Tolic, D. W. Koppenaal, and J. K. Jansson. 2018. Micronutrient metal speciation is controlled by competitive organic chelation in grassland soils. Soil Biol. Biochem. **120**: 283–291. doi:10.1016/j.soilbio.2018.02.018

Boiteau, R. M., C. P. Till, T. H. Coale, J. N. Fitzsimmons, K. W. Bruland, and D. J. Repeta. 2019b. Patterns of iron and siderophore distributions across the California Current System. Limnol. Oceanogr. **64**: 376–389. doi:10.1002/lno.11046

Boukhalfa, H., and A. L. Crumbliss. 2002. Chemical aspects of siderophore mediated iron transport. BioMetals **15**: 325–339. doi:10.1023/A:1020218608266

Boyd, P. W., C. S. Law, C. S. Wong, Y. Nojiri, A. Tsuda, and M. Levasseur. 2004. The decline and fate of an iron-induced subarctic phytoplankton bloom. Nature **428**: 549–553. doi:10.1029/2001JB001129

Boyd, P. W., A. J. Watson, C. S. Law, and others. 2000. A mesosclae phytoplankton bloom in the polar Southern Ocean stimulated by iron fertilization. Nature **407**: 695–702. doi:10.1038/35037500

Boye, M., C. M. G. Van Den Berg, J. T. M. De Jong, H. Leach, P. Croot, and H. J. W. De Baar. 2001. Organic complexation of iron in the Southern Ocean. Deep. Res. Part I Oceanogr. Res. Pap. **48**: 1477–1497. doi:10.1016/S0967-0637(00)00099-6

Boye, M., J. Nishioka, P. Croot, P. Laan, K. R. Timmermans, V. H. Strass, S. Takeda, and H. J. W. de Baar. 2010. Significant portion of dissolved organic Fe complexes in fact is Fe colloids. Mar. Chem. **122**: 20–27. doi:10.1016/j.marchem.2010.09.001

Braich, N., and R. Codd. 2008. Immobilised metal affinity chromatography for the capture of hydroxamate-containing siderophores and other Fe(III)-binding metabolites directly from bacterial culture supernatants. Analyst **133**: 877–880. doi:10.1039/b802355g

Braud, A., V. Geoffroy, F. Hoegy, G. L. A. Mislin, and I. J. Schalk. 2010. Presence of the siderophores pyoverdine and pyochelin in the extracellular medium reduces toxic metal accumulation in Pseudomonas aeruginosa and increases bacterial metal toleranceemi. Environ. Microbiol. Rep. **2**: 419–425. doi:10.1111/j.1758-2229.2009.00126.x

Braun, V., A. Pramanik, T. Gwinner, M. Köberle, and E. Bohn. 2009. Sideromycins: Tools and antibiotics. BioMetals **22**: 3–13. doi:10.1007/s10534-008-9199-7

Brennan, B. J., M. J. Llansola Portolés, P. A. Liddell, T. A. Moore, A. L. Moore, and D. Gust. 2013. Comparison of silatrane, phosphonic acid, and carboxylic acid functional groups for attachment of porphyrin sensitizers to TiO2 in photoelectrochemical cells. Phys. Chem. Chem. Phys. **15**: 16605–16614. doi:10.1039/c3cp52156g

Broeckling, C. D., F. A. Afsar, S. Neumann, A. Ben-Hur, and J. E. Prenni. 2014. RAMClust: A novel feature clustering method enables spectral-matching-based annotation for metabolomics data. Anal. Chem. **86**: 6812–6817. doi:10.1021/ac501530d

Bruland, K. W. 1980. Oceanographic distributions of cadmium, zinc, nickel, and copper in the North Pacific. Earth Planet. Sci. Lett. **47**: 176–198. doi:10.1016/0012-821X(80)90035-7

Budzikiewicz, H. 2005. Siderophore-Antibiotic Conjugates Used as Trojan Horses Against Pseudomonas aeruginosa. Curr. Top. Med. Chem. **1**: 73–82. doi:10.2174/1568026013395524

Bundy, R. M., R. M. Boiteau, C. McLean, K. A. Turk-Kubo, M. R. McIlvin, M. A. Saito, B. A. S. Van Mooy, and D. J. Repeta. 2018. Distinct siderophores contribute to iron cycling in the mesopelagic at station ALOHA. Front. Mar. Sci. **5**: 1–15. doi:10.3389/fmars.2018.00061

Buszewski, B., and M. Szultka. 2012. Past, Present, and Future of Solid Phase Extraction: A Review. Crit. Rev. Anal. Chem. **42**: 198–213. doi:10.1080/07373937.2011.645413

Butler, A. 2005. Marine siderophores and microbial iron mobilization. BioMetals **18**: 369–374. doi:10.1007/s10534-005-3711-0

Butler, A., T. Harder, A. D. Ostrowski, and C. J. Carrano. 2021. Photoactive siderophores:

Structure, function and biology. J. Inorg. Biochem. **221**: 111457. doi:10.1016/j.jinorgbio.2021.111457

Butler, A., and R. M. Theisen. 2010. Iron(III)-siderophore coordination chemistry: Reactivity of marine siderophores. Coord. Chem. Rev. **254**: 288–296. doi:10.1016/j.ccr.2009.09.010

Cairo, G., F. Bernuzzi, and S. Recalcati. 2006. A precious metal: Iron, an essential nutrient for all cells. Genes Nutr. **1**: 25–39. doi:10.1007/bf02829934

Calvano, C. D., O. N. Jensen, and C. G. Zambonin. 2009. Selective extraction of phospholipids from dairy products by micro-solid phase extraction based on titanium dioxide microcolumns followed by MALDI-TOF-MS analysis. Anal. Bioanal. Chem. **394**: 1453–1461. doi:10.1007/s00216-009-2812-y

Canfield, D. E., and J. Farquhar. 2009. Animal evolution, bioturbation, and the sulfate concentration of the oceans. Proc. Natl. Acad. Sci. U. S. A. **106**: 8123–8127. doi:10.1073/pnas.0902037106

Carmichael, J. R., H. Zhou, and A. Butler. 2019. A suite of asymmetric citrate siderophores isolated from a marine Shewanella species. J. Inorg. Biochem. **198**: 110736. doi:10.1016/j.jinorgbio.2019.110736

Chen, X., and S. S. Mao. 2007. Titanium dioxide nanomaterials: Synthesis, properties, modifications and applications. Chem. Rev. **107**: 2891–2959. doi:10.1021/cr0500535

Chen, Z. L., M. Megharaj, and R. Naidu. 2007. Confirmation of iron complex formation using electrospray ionization mass spectrometry (ESI-MS) and sample stacking for analysis of iron polycarboxylate speciation by capillary electrophoresis. Microchem. J. **86**: 94–101. doi:10.1016/j.microc.2006.12.001

Choi, H., S. R. Al-Abed, D. D. Dionysiou, E. Stathatos, and P. Lianos. 2010. TiO2-Based Advanced Oxidation Nanotechnologies for Water Purification and Reuse, p. 229–254. *In* I.C. Escobar and A.I. Schäfer [eds.], Sustainability Science and Engineering. Elsevier.

Chowdhury, I., D. M. Cwiertny, and S. L. Walker. 2012. Combined factors influencing the aggregation and deposition of nano-TiO2 in the presence of humic acid and bacteria. Environ. Sci. Technol. **46**: 6968–6976. doi:10.1021/es2034747

Christ, B., W. Glaubitt, K. Berberich, T. Weigel, J. Probst, G. Sextl, and S. Dembski. 2022. Sol-Gel-Derived Fibers Based on Amorphous α-Hydroxy-Carboxylate-Modified Titanium (IV) Oxide as a 3-Dimensional Scaffold. Materials (Basel). **15**: 2752. doi:10.3390/ma15082752

Coale, K. H., K. S. Johnson, F. P. Chavez, and others. 2004. Southern Ocean Iron Enrichment Experiment : Carbon Cycling in High- and Low-Si Waters. Science (80-.). **304**: 408–414. doi:10.1126/science.1089778

Coale, K. H., K. S. Johnson, S. E. Fitzwater, and others. 1996. A massive phytoplankton bloom induced by an ecosystem-scale iron fertilization experiment in the equatorial Pacific Ocean. Nature **383**: 495. doi:10.1038/383495a0

Coale, T. H., M. Moosburner, A. Horák, M. Oborník, K. A. Barbeau, and A. E. Allen. 2019. Reduction-dependent siderophore assimilation in a model pennate diatom. Proc. Natl. Acad. Sci. U. S. A. **116**: 23609–23617. doi:10.1073/pnas.1907234116

Collins, K. D. 1997. Charge density-dependent strength of hydration and biological structure. Biophys. J. **72**: 65–76. doi:10.1016/S0006-3495(97)78647-8

Connor, P. A., K. D. Dobson, and A. J. Mcquillan. 1995. New Sol-Gel Attenuated Total

Reflection Infrared Spectroscopic Method for Analysis of Adsorption at Metal Oxide Surfaces in Aqueous Solutions. Chelation of TiO2, ZrO2, and Al2O3 Surfaces by Catechol, 8-Quinolinol, and Acetylacetone. Langmuir **11**: 4193–4195. doi:10.1021/la00011a003

Connor, P. A., and A. J. McQuillan. 1999. Phosphate adsorption onto TiO2 from aqueous solutions: an in situ internal reflection infrared spectroscopic study. Langmuir **15**: 2916–2921. doi:10.1021/la980894p

Correns, C. W. 1969. Handbook of Geochemistry, *In* K.H. Wedepohl [ed.], Handbook of Geochemistry. Springer.

Crichton, R. 2001. Inorganic Biochemistry of Iron Metabolism, 2nd ed. R. Crichton [ed.]. Wiley.

Croot, P. L., K. Andersson, O. Murat, and D. R. Turner. 2004. The distribution and speciation of iron along 6°E in the Southern Ocean. Deep. Res. I **51**: 2857–2879. doi:10.1016/j.dsr2.2003.10.012

Croot, P. L., and M. Johansson. 2000. Determination of iron speciation by cathodic stripping voltammetry in seawater using the competing ligand 2-(2-thiazolylazo)-p-cresol (TAC). Electroanalysis **12**: 565–576. doi:10.1002/(SICI)1521-4109(200005)12:8<565::AID-ELAN565>3.0.CO;2-L

Csaky, T. 1948. On the Estimation of Bound Hydroxylamine in Biological Materials. Acta Chem. Scand. **2**: 450–454. doi:10.3891/acta.chem.scand.02-0450

Curtin, J. P., M. Wang, T. Cheng, L. Jin, and H. Sun. 2018. The role of citrate, lactate and transferrin in determining titanium release from surgical devices into human serum. J. Biol. Inorg. Chem. **23**: 471–480. doi:10.1007/s00775-018-1557-5

Danner, E. W., Y. Kan, M. U. Hammer, J. N. Israelachvili, and J. H. Waite. 2012. Adhesion of mussel foot protein Mefp-5 to mica: An underwater superglue. Biochemistry **51**: 6511–6518. doi:10.1021/bi3002538

Diebold, U. 2003. The surface science of titanium dioxide. Surf. Sci. Rep. **48**: 53–229. doi:10.1016/S0167-5729(02)00100-0

Dittmar, T., B. Koch, N. Hertkorn, and G. Kattner. 2008. A simple and efficient method for the solid-phase extraction of dissolved organic matter (SPE-DOM) from seawater. Limnol. Oceanogr. Methods **6**: 230–235. doi:10.4319/lom.2008.6.230

Dobson, K. D., P. A. Connor, and A. J. McQuillan. 1997. Monitoring hydrous metal oxide surface charge and adsorption by STIRS. Langmuir **13**: 2614–2616. doi:10.1021/la961053q

Donat, J. R., P. J. Statham, and K. W. Bruland. 1986. An evaluation of a C-18 solid phase extraction technique for isolating metal-organic complexes from central North Pacific Ocean waters. Mar. Chem. **18**: 85–99. doi:10.1016/0304-4203(86)90078-2

Dührkop, K., M. Fleischauer, M. Ludwig, and others. 2019. SIRIUS 4: a rapid tool for turning tandem mass spectra into metabolite structure information. Nat. Methods **16**: 299–302. doi:10.1038/s41592-019-0344-8

Dührkop, K., L. F. Nothias, M. Fleischauer, and others. 2021. Systematic classification of unknown metabolites using high-resolution fragmentation mass spectra. Nat. Biotechnol. **39**: 462–471. doi:10.1038/s41587-020-0740-8

Dührkop, K., H. Shen, M. Meusel, J. Rousu, and S. Böcker. 2015. Searching molecular structure databases with tandem mass spectra using CSI:FingerID. Proc. Natl. Acad. Sci.

U. S. A. **112**: 12580–12585. doi:10.1073/pnas.1509788112

Dunford, R., A. Salinaro, L. Cai, N. Serpone, S. Horikoshi, H. Hidaka, and J. Knowland. 1997. Chemical oxidation and DNA damage catalysed by inorganic sunscreen ingredients. FEBS Lett. **418**: 87–90. doi:10.1016/S0014-5793(97)01356-2

Egbers, P. H., T. Harder, B. P. Koch, and J. Tebben. 2020. Siderophore purification with titanium dioxide nanoparticle solid phase extraction. Analyst **145**: 7303–7311. doi:10.1039/d0an00949k

Ejje, N., C. Z. Soe, J. Gu, and R. Codd. 2013. The variable hydroxamic acid siderophore metabolome of the marine actinomycete Salinispora tropica CNB-440. Metallomics **5**: 1519. doi:10.1039/c3mt00230f

Elbaz-Poulichet, F., G. Cauwet, D. M. Guan, D. Faguet, R. Barlow, and R. F. C. Mantoura. 1994. C18 Sep-Pak extractable trace metals in waters from the Gulf of Lions. Mar. Chem. **46**: 67–75. doi:10.1016/0304-4203(94)90046-9

Emsley, J. 1989. The Elements, Clarendon Press.

Erhayem, M., and M. Sohn. 2014. Stability studies for titanium dioxide nanoparticles upon adsorption of Suwannee River humic and fulvic acids and natural organic matter. Sci. Total Environ. **468**–**469**: 249–257. doi:10.1016/j.scitotenv.2013.08.038

Esch, T. R., I. Gadaczek, and T. Bredow. 2014. Surface structures and thermodynamics of low-index of rutile, brookite and anatase - A comparative DFT study. Appl. Surf. Sci. **288**: 275–287. doi:10.1016/j.apsusc.2013.10.021

Essén, S. A., D. Bylund, S. J. M. Holmström, M. Moberg, and U. S. Lundström. 2006. Quantification of hydroxamate siderophores in soil solutions of podzolic soil profiles in Sweden. BioMetals **19**: 269–282. doi:10.1007/s10534-005-8418-8

Feistner, G. J., and L. L. Hsieh. 1995. On the collision-activated fragmentation of proferrioxamines: Evidence for a succinimide-mediated mechanism. J. Am. Soc. Mass Spectrom. **6**: 836–846. doi:10.1016/1044-0305(95)00324-7

Feistner, G. J., D. C. Stahl, and A. H. Gabrik. 1993. Proferrioxamine siderophores of Erwinia amylovora. A capillary liquid chromatographic/electrospray tandem mass spectrometric study. Org. Mass Spectrom. **28**: 163–175. doi:10.1002/oms.1210280307

Ferrer, I., and D. Barceloè. 1999. Validation of new solid-phase extraction materials for the selective enrichment of organic contaminants from environmental samples. TrAC Trends Anal. Chem. **18**: 180–192. doi:10.1016/S0165-9936(98)00108-3

Ferret, C., T. Sterckeman, J. Y. Cornu, S. Gangloff, I. J. Schalk, and V. A. Geoffroy. 2014. Siderophore-promoted dissolution of smectite by fluorescent Pseudomonas. Environ. Microbiol. Rep. **6**: 459–467. doi:10.1111/1758-2229.12146

Feunang, Y. D., R. Eisner, C. Knox, and others. 2016. ClassyFire : automated chemical classification with a comprehensive , computable taxonomy. J. Cheminform. 1–20. doi:10.1186/s13321-016-0174-y

Finkelstein-Shapiro, D., S. K. Davidowski, P. B. Lee, and others. 2016. Direct Evidence of Chelated Geometry of Catechol on TiO2 by a Combined Solid-State NMR and DFT Study. J. Phys. Chem. C **120**: 23625–23630. doi:10.1021/acs.jpcc.6b08041

Flerus, R., O. J. Lechtenfeld, B. P. Koch, S. L. McCallister, P. Schmitt-Kopplin, R. Benner, K. Kaiser, and G. Kattner. 2012. A molecular perspective on the ageing of marine dissolved

organic matter. Biogeosciences **9**: 1935–1955. doi:10.5194/bg-9-1935-2012

Flower, D. R., A. C. T. North, and C. E. Sansom. 2000. The lipocalin protein family: Structural and sequence overview. Biochim. Biophys. Acta - Protein Struct. Mol. Enzymol. **1482**: 9–24. doi:10.1016/S0167-4838(00)00148-5

Forsberg, E. M., T. Huan, D. Rinehart, H. P. Benton, B. Warth, B. Hilmers, and G. Siuzdak. 2018. Data processing, multi-omic pathway mapping, and metabolite activity analysis using XCMS Online. Nat. Protoc. **13**: 633–651. doi:10.1038/nprot.2017.151

Francis, J., J. Madinaveita, H. M. Macturk, and G. A. Snow. 1949. Isolation from Acid-Fast Bacteria of a Growth-Factor for Mycobacterium johnei and of a Precursor of Phthiocol. Nature **163**: 365–366. doi:10.1038/163365b0

Franza, T., B. Mahé, and D. Expert. 2005. Erwinia chrysanthemi requires a second iron transport route dependent of the siderophore achromobactin for extracellular growth and plant infection. Mol. Microbiol. **55**: 261–275. doi:10.1111/j.1365-2958.2004.04383.x

French, R. A., A. R. Jacobson, B. Kim, S. L. Isley, L. Penn, and P. C. Baveye. 2009. Influence of ionic strength, pH, and cation valence on aggregation kinetics of titanium dioxide nanoparticles. Environ. Sci. Technol. **43**: 1354–1359. doi:10.1021/es802628n

Frueh, D. P., H. Arthanari, A. Koglin, D. A. Vosburg, A. E. Bennett, C. T. Walsh, and G. Wagner. 2008. Dynamic thiolation-thioesterase structure of a non-ribosomal peptide synthetase. Nature **454**: 903–906. doi:10.1038/nature07162

Fujishima, A., and K. Honda. 1972. Electrochemical Photolysis of Water at a Semiconductor Electrode. Nature **238**: 37–38. doi:10.1038/238038a0

Gärdes, A., C. Triana, S. A. Amin, D. H. Green, A. Romano, L. Trimble, and C. J. Carrano. 2013. Detection of photoactive siderophore biosynthetic genes in the marine environment. BioMetals **26**: 507–516. doi:10.1007/s10534-013-9635-1

Gauglitz, J. M., H. Zhou, and A. Butler. 2012. A suite of citrate-derived siderophores from a marine Vibrio species isolated following the Deepwater Horizon oil spill. J. Inorg. Biochem. **107**: 90–95. doi:10.1016/j.jinorgbio.2011.10.013

Gavard, R., H. E. Jones, D. C. Palacio Lozano, M. J. Thomas, D. Rossell, S. E. F. Spencer, and M. P. Barrow. 2020. KairosMS: A New Solution for the Processing of Hyphenated Ultrahigh Resolution Mass Spectrometry Data. Anal. Chem. **92**: 3775–3786. doi:10.1021/acs.analchem.9b05113

Gerringa, L. J. A., M. J. W. Veldhuis, K. R. Timmermans, G. Sarthou, and H. J. W. de Baar. 2006. Co-variance of dissolved Fe-binding ligands with phytoplankton characteristics in the Canary Basin. Mar. Chem. **102**: 276–290. doi:10.1016/j.marchem.2006.05.004

Gervais, F., and U. Riebesell. 2002. Changes in Primary Productivity and Chlorophyll a in Response to Iron Fertilization in the Southern Polar Frontal Zone. Limnol. Oceanogr. **47**: 1324–1335. doi:10.4319/lo.2002.47.5.1324

Giehl, R. F., A. R. Meda, and N. von Wirén. 2009. Moving up, down, and everywhere: signaling of micronutrients in plants. Curr. Opin. Plant Biol. **12**: 320–327. doi:10.1016/j.pbi.2009.04.006

Gillich, T., E. M. Benetti, E. Rakhmatullina, R. Konradi, W. Li, A. Zhang, A. D. Schlüter, and M. Textor. 2011. Self-assembly of focal point oligo-catechol ethylene glycol dendrons on titanium oxide surfaces: Adsorption kinetics, surface characterization, and nonfouling properties. J. Am. Chem. Soc. **133**: 10940–10950. doi:10.1021/ja202760x

Glebov, E. M., I. P. Pozdnyakov, V. P. Grivin, V. F. Plyusnin, X. Zhang, F. Wu, and N. Deng. 2011. Intermediates in photochemistry of Fe(III) complexes with carboxylic acids in aqueous solutions†. Photochem. Photobiol. Sci. **10**: 425–430. doi:10.1039/c0pp00158a

Gledhill, M. 2001. Electrospray ionisation-mass spectrometry of hydroxamate siderophores. Analyst **126**: 1359–1362. doi:10.1039/b101268l

Gledhill, M., and C. M. G. van den Berg. 1994. Determination of complexation of iron(III) with natural organic complexing ligands in seawater using cathodic stripping voltammetry. Mar. Chem. **47**: 41–54. doi:10.1016/0304-4203(94)90012-4

Gledhill, M., C. M. G. Van Den Berg, R. F. Nolting, and K. R. Timmermans. 1998. Variability in the speciation of iron in the northern North Sea. Mar. Chem. **59**: 283–300. doi:10.1016/S0304-4203(97)00097-2

Gledhill, M., and K. N. Buck. 2012. The organic complexation of iron in the marine environment: A review. Front. Microbiol. **3**: 1–17. doi:10.3389/fmicb.2012.00069

Glllam, A. H., A. G. Lewis, and R. J. Andersen. 1981. Quantitative Determination of Hydroxamic Acids. Anal. Chem. **53**: 841–844. doi:10.1021/ac00229a023

Glover, H. 1977. Effects of Iron Deficiency on Isochrysis Galbana (Chrysophyceae) and Phaeodactylum Tricornutum (Bacillariophyceae). J. Phycol. **13**: 208–212. doi:10.1111/j.1529-8817.1977.tb02917.x

Gokarn, K., and R. B. Pal. 2017. Preliminary evaluation of anti-tuberculosis potential of siderophores against drug-resistant Mycobacterium tuberculosis by mycobacteria growth indicator tube-drug sensitivity test. BMC Complement. Altern. Med. **17**: 1–8. doi:10.1186/s12906-017-1665-8

Grandcham, G. M., L. Caro, and E. A. Shank. 2017. Pirated Siderophores Promote Sporulation in Bacillus subtilis. Appl. Environ. Microbiol. **83**: 1–17. doi:10.1128/AEM.03293-16

Grätzel, M. 2001. Ultrafast colour displays. Nature **409**: 575–576. doi:10.1038/35054655

Gu, J., and R. Codd. 2012. Copper(II)-based metal affinity chromatography for the isolation of the anticancer agent bleomycin from Streptomyces verticillus culture. J. Inorg. Biochem. **115**: 198–203. doi:10.1016/j.jinorgbio.2012.01.015

Gu, J., and R. Codd. 2015. The resolution of two clinical agents, bleomycin and desferrioxamine B, from a Streptomyces verticillus fermentation mixture using multi-dimensional immobilised metal ion affinity chromatography. RSC Adv. **5**: 3443–3453. doi:10.1039/c4ra09315a

Guan, L. L., K. Kanoh, and K. Kamino. 2001. Effect of Exogenous Siderophores on Iron Uptake Activity of Marine Bacteria under Iron-Limited Conditions. Appl. Environ. Microbiol. **67**: 1710–1717. doi:10.1128/AEM.67.4.1710-1717.2001

Guerinot, M. Lou. 1994. Microbial iron transport. Annu. Rev. Microbiol. **48**: 743–773. doi:10.1146/annurev.mi.48.100194.003523

Guerinot, M. Lou, and Y. Yi. 1994. Iron: Nutritious, noxious, and not readily available. Plant Physiol. **104**: 815–820. doi:10.1104/pp.104.3.815

Gulley-Stahl, H., P. A. Hogan, W. L. Schmidt, S. J. Wall, A. Buhrlage, and H. A. Bullen. 2010. Surface complexation of catechol to metal oxides: An ATR-FTIR, adsorption, and dissolution study. Environ. Sci. Technol. **44**: 4116–4121. doi:10.1021/es902040u

Guo, Q., S. Lee, and D. W. Goodman. 1999. Vanadium oxides thin films grown on rutile TiO2(110)-(1 × 1) and (1 × 2) surfaces. Surf. Sci. **437**: 38–48. doi:10.1016/S0039-6028(99)00674-3

Gyurcsik, B., and L. Nagy. 2000. Carbohydrates as ligands: Coordination equilibria and structure of the metal complexes. Coord. Chem. Rev. **203**: 81–149. doi:10.1016/S0010-8545(99)00183-6

Hagfeldt, A., and M. Grätzel. 1995. Light-Induced Redox Reactions in Nanocrystalline Systems. Chem. Rev. **95**: 49–68. doi:10.1021/cr00033a003

Halcrow, M. A. 2008. Trapping and manipulating excited spin states of transition metal compounds. Chem. Soc. Rev. **37**: 278–289. doi:10.1039/b701085k

Han, L., J. Kaesler, C. Peng, T. Reemtsma, and O. J. Lechtenfeld. 2021. Online counter gradient LC-FT-ICR-MS enables detection of highly polar natural organic matter fractions. Anal. Chem. **93**: 1740–1748. doi:10.1021/acs.analchem.0c04426

Hassler, C. S., E. Alasonati, C. A. Mancuso Nichols, and V. I. Slaveykova. 2011a. Exopolysaccharides produced by bacteria isolated from the pelagic Southern Ocean - Role in Fe binding, chemical reactivity, and bioavailability. Mar. Chem. **123**: 88–98. doi:10.1016/j.marchem.2010.10.003

Hassler, C. S., C. M. G. van den Berg, and P. W. Boyd. 2017. Toward a Regional Classification to Provide a More Inclusive Examination of the Ocean Biogeochemistry of Iron-Binding Ligands. Front. Mar. Sci. **4**. doi:10.3389/fmars.2017.00019

Hassler, C. S., V. Schoemann, C. M. Nichols, E. C. V. Butler, and P. W. Boyd. 2011b. Saccharides enhance iron bioavailability to Southern Ocean phytoplankton. Proc. Natl. Acad. Sci. **108**: 1076–1081. doi:10.1073/pnas.1010963108

Hawkes, J. A., C. Patriarca, P. J. R. Sjöberg, L. J. Tranvik, and J. Bergquist. 2018. Extreme isomeric complexity of dissolved organic matter found across aquatic environments. Limnol. Oceanogr. Lett. **3**: 21–30. doi:10.1002/lol2.10064

Heine, T., M. Mehnert, R. Schwabe, and D. Tischler. 2017. Siderophore Purification via Immobilized Metal Affinity Chromatography. Solid State Phenom. **262**: 505–508. doi:10.4028/www.scientific.net/ssp.262.505

Hennion, M.-C. 1999. Solid-phase extraction: method development, sorbents, and coupling with liquid chromatography. J. Chromatogr. A **856**: 3–54. doi:10.1016/S0021-9673(99)00832-8

Hennion, M.-C., and V. Pichon. 1994. Solid-phase extraction of polar organic pollutants from water. Environ. Sci. Technol. **28**: 576–583. doi:10.1021/es00062a717

Hentze, M. W., M. U. Muckenthaler, and N. C. Andrews. 2004. Balancing Acts: Molecular Control of Mammalian Iron Metabolism. Cell **117**: 285–297. doi:10.1016/s0968-0004(05)00043-5

Herlinger, E., R. F. Jamesonb, and W. Linerta. 1995. Spontaneous Autoxidation of Dopamine. J. Chem. Soc. Perkin Trans. 2 **2**: 259–263. doi:10.1039/P29950000259

Hermenau, R., K. Ishida, S. Gama, B. Hoffmann, M. Pfeifer-Leeg, W. Plass, J. F. Mohr, T. Wichard, H.-P. Saluz, and C. Hertweck. 2018. Gramibactin is a bacterial siderophore with a diazeniumdiolate ligand system. Nat. Chem. Biol. **14**: 841–843. doi:10.1038/s41589-018-0101-9

Hermenau, J. L. Mehl, K. Ishida, B. Dose, S. J. Pidot, T. P. Stinear, C. Hertweck. 2019.

Genomics-Driven Discovery of NO-Donating Diazeniumdiolate Siderophores in Diverse Plant-Associated Bacteria. Angew. Chem. Int. Ed. **58**: 13024–13029. doi:10.1002/anie.201906326

Hertkorn, N., R. Benner, M. Frommberger, P. Schmitt-Kopplin, M. Witt, K. Kaiser, A. Kettrup, and J. I. Hedges. 2006. Characterization of a major refractory component of marine dissolved organic matter. Geochim. Cosmochim. Acta **70**: 2990–3010. doi:10.1016/j.gca.2006.03.021

Hertkorn, N., M. Frommberger, M. Witt, B. P. Koch, P. Schmitt-Kopplin, and E. M. Perdue. 2008. Natural organic matter and the event horizon of mass spectrometry. Anal. Chem. **80**: 8908–8919. doi:10.1021/ac800464g

Hickford, S. J. H., F. C. Küpper, G. Zhang, C. J. Carrano, J. W. Blunt, and A. Butler. 2004. Petrobactin sulfonate, a new siderophore produced by the marine bacterium Marinobacter hydrocarbonoclasticus. J. Nat. Prod. **67**: 1897–1899. doi:10.1021/np049823i

Hider, R. C., and X. Kong. 2010. Chemistry and biology of siderophores. Nat. Prod. Rep. **27**: 637. doi:10.1039/b906679a

De Hoffmann, E., and V. Stroobant. 1991. Fast atom bombardment tandem mass spectrometric analysis of hydroxamate siderophores. Biol. Mass Spectrom. **20**: 142–152. doi:10.1002/bms.1200200308

Hoffmann, L. J., I. Peeken, K. Lochte, P. Assmy, and M. Veldhuis. 2006. Different reacctions of Southern Ocean phytoplankton size classes to iron fertilization. Limnol. Ocean. **51**: 1217–1229. doi:10.4319/lo.2006.51.3.1217

Hoffmann, P. 2005. Speciation of Iron, p. 1–768. *In* R. Cornelis, J. Caruso, H. Crews, and K. Heumann [eds.], Handbook of Elemental Speciation, Handbook of Elemental Speciation II: Species in the Environment, Food, Medicine and Occupational Health. John Wiley & Sons.

Hogle, S. L., R. M. Bundy, J. M. Blanton, E. E. Allen, and K. A. Barbeau. 2016. Copiotrophic marine bacteria are associated with strong iron-binding ligand production during phytoplankton blooms. Limnol. Oceanogr. Lett. **1**: 36–43. doi:10.1002/lol2.10026

Holmén, B. A., and W. H. Casey. 1996. Hydroxamate ligands, surface chemistry, and the mechanism of ligand-promoted dissolution of goethite [α-FeOOH(s)]. Geochim. Cosmochim. Acta **60**: 4403–4416. doi:10.1016/S0016-7037(96)00278-5

Horányi, G. 2003. Investigation of the specific adsorption of sulfate ions on powdered TiO2. J. Colloid Interface Sci. **261**: 580–583. doi:10.1016/S0021-9797(03)00084-5

Ibisanmi, E., S. G. Sander, P. W. Boyd, A. R. Bowie, and K. A. Hunter. 2011. Deep-Sea Research II Vertical distributions of iron-(III) complexing ligands in the Southern Ocean. Deep. Res. Part II **58**: 2113–2125. doi:10.1016/j.dsr2.2011.05.028

Ikeguchi, Y., and H. Nakamura. 1997. Determination of Organic Phosphates by Column-Switching High Performance Anion-Exchange Chromatography Using On-Line Preconcentration on Titania. Anal. Sci. **13**: 479–483. doi:10.2116/analsci.13.479

Ikeguchi, Y., and H. Nakamura. 2000. Selective enrichment of phospholipids by titania. Anal. Sci. **16**: 541–543. doi:10.2116/analsci.16.541

Jain, R., F. Cirina, P. Kaden, and K. Pollmann. 2017. Investigation of the Ga complexation behaviour of the siderophore desferrioxamine B. Solid State Phenom. **262 SSP**: 643–646. doi:10.4028/www.scientific.net/SSP.262.643

Jiao, N., G. J. Herndl, D. A. Hansell, and others. 2010. Microbial production of recalcitrant dissolved organic matter: Long-term carbon storage in the global ocean. Nat. Rev. Microbiol. **8**: 593–599. doi:10.1038/nrmicro2386

John, U., and A. Wisotzki. Physical oceanography during HEINCKE cruise HE533 (2019). Alfred Wegener Institute, Helmholtz Centre for Polar and Marine Research, Bremerhaven, PANGAEA,.

Johnson, L. 2008. Iron and siderophores in fungal-host interactions. Mycol. Res. **112**: 170–183. doi:10.1016/j.mycres.2007.11.012

Jones, F. H. 2001. Teeth and bones: Applications of surface science to dental materials and related biomaterials. Surf. Sci. Rep. **42**: 75–205. doi:10.1016/S0167-5729(00)00011-X

Jones, K. E. 2017. Interactions of microbial siderophores with titanium ions and titanium bearing minerals.

Jones, K. E., K. L. Batchler, C. Zalouk, and A. M. Valentine. 2017. Ti(IV) and the Siderophore Desferrioxamine B: A Tight Complex Has Biological and Environmental Implications. Inorg. Chem. **56**: 1264–1272. doi:10.1021/acs.inorgchem.6b02399

Kabata-Pendias, A., and A. B. Mukherjee. 2007. Trace Elements from Soil to Human, Springer.

Kaegi, R., A. Ulrich, B. Sinnet, and others. 2008. Synthetic TiO2 nanoparticle emission from exterior facades into the aquatic environment. Environ. Pollut. **156**: 233–239. doi:10.1016/j.envpol.2008.08.004

Kalyanasundaram, K., and M. Grätzel. 1998. Applications of functionalized transition metal complexes in photonic and optoelectronic devices. Commun. Comput. Inf. Sci. **77**: 347–414. doi:10.1007/978-3-642-00205-2_12

Kang, X., S. Liu, Z. Dai, Y. He, X. Song, and Z. Tan. 2019. Titanium dioxide: From engineering to applications. Catalysts **9**: 191. doi:10.3390/catal9020191

Kawahara, M., H. Nakamura, and T. Nakajima. 1989. Group Separation of Ribonucleosides and Deoxyribonucleosides on a New Ceramic Titania Column. Anal. Sci. **5**: 763–764. doi:10.2116/analsci.5.763

Kazamia, E., R. Sutak, J. Paz-Yepes, and others. 2018. Endocytosis-mediated siderophore uptake as a strategy for Fe acquisition in diatoms. Sci. Adv. **4**. doi:10.1126/sciadv.aar4536

Kazarinov, V. E., V. N. Andreev, and A. P. Mayorov. 1981. Investigation of the adsorption properties of the TiO2 electrode by the radioactive tracer method. J. Electroanal. Chem. **130**: 277–285. doi:10.1016/S0022-0728(81)80395-6

Keith-Roach, M. J., M. V. Buratti, and P. J. Worsfold. 2005. Thorium complexation by hydroxamate siderophores in perturbed multicomponent systems using flow injection electrospray ionization mass spectrometry. Anal. Chem. **77**: 7335–7341. doi:10.1021/ac051069y

Khan, M. A., W. T. Wallace, S. Z. Islam, S. Nagpure, J. Strzalka, J. M. Littleton, S. E. Rankin, and B. L. Knutson. 2017. Adsorption and Recovery of Polyphenolic Flavonoids Using TiO2-Functionalized Mesoporous Silica Nanoparticles. ACS Appl. Mater. Interfaces **9**: 32114–32125. doi:10.1021/acsami.7b09510

Kim, T. Y., K. Alhooshani, A. Kabir, D. P. Fries, and A. Malik. 2004. High pH-resistant, surface-bonded sol-gel titania hybrid organic-inorganic coating for effective on-line hyphenation of capillary microextraction (in-tube solid-phase microextraction) with high-performance liquid

chromatography. J. Chromatogr. A **1047**: 165–174. doi:10.1016/j.chroma.2004.06.079

King, A. L., and K. A. Barbeau. 2007. Evidence for phytoplankton iron limitation in the southern California Current System. Mar. Ecol. Prog. Ser. **342**: 91–103. doi:10.3354/MEPS342091

Koenigsmann, C., T. S. Ripolles, B. J. Brennan, and others. 2014. Substitution of a hydroxamic acid anchor into the MK-2 dye for enhanced photovoltaic performance and water stability in a DSSC †. Phys. Chem. Chem. Phys **16**: 16629. doi:10.1039/c4cp02405b

Kozakai, H., Y. Oshima, and T. Yasumoto. 1982. Isolation and Structural Elucidation of Hemolysin from the Phytoflagellate Prymnesium parvum. Agric. Biol. Chem. **46**: 233–236. doi:10.1271/bbb1961.46.233

Kraemer, S. M. 2004. Iron oxide dissolution and solubility in the presence of siderophores. Aquat. Sci. **66**: 3–18. doi:10.1007/s00027-003-0690-5

Kramer, J., Ö. Özkaya, and R. Kümmerli. 2020. Bacterial siderophores in community and host interactions. Nat. Rev. Microbiol. **18**: 152–163. doi:10.1038/s41579-019-0284-4

Kuhl, C., R. Tautenhahn, C. Böttcher, T. R. Larson, and S. Neumann. 2012. CAMERA: An integrated strategy for compound spectra extraction and annotation of liquid chromatography/mass spectrometry data sets. Anal. Chem. **84**: 283–289. doi:10.1021/ac202450g

Kurepa, J., R. Nakabayashi, T. Paunesku, M. Suzuki, K. Saito, G. E. Woloschak, and J. A. Smalle. 2014. Direct isolation of flavonoids from plants using ultra-small anatase TiO2 nanoparticles. Plant J. **77**: 443–453. doi:10.1111/tpj.12361

Kustka, A. B., A. E. Allen, and F. M. M. Morel. 2007. Sequence analysis and transcriptional regulation of iron acquisition genes in two marine diatoms. J. Phycol. **43**: 715–729. doi:10.1111/j.1529-8817.2007.00359.x

Lamont, I. L., P. A. Beare, U. Ochsner, A. I. Vasil, and M. L. Vasil. 2002. Siderophore-mediated signaling regulates virulence factor production in Pseudomonas aeruginosa. Proc. Natl. Acad. Sci. U. S. A. **99**: 7072–7077. doi:10.1073/pnas.092016999

Larsen, M. R., T. E. Thingholm, O. N. Jensen, P. Roepstorff, and T. J. D. Jørgensen. 2005. Highly Selective Enrichment of Phosphorylated Peptides from Peptide Mixtures Using Titanium Dioxide Microcolumns. Mol. Cell. Proteomics **4**: 873–886. doi:10.1074/mcp.T500007-MCP200

Lau, S. S., X. Wei, K. Bokenkamp, E. D. Wagner, M. J. Plewa, and W. A. Mitch. 2020. Assessing Additivity of Cytotoxicity Associated with Disinfection Byproducts in Potable Reuse and Conventional Drinking Waters. Environ. Sci. Technol. **54**: 5729–5736. doi:10.1021/acs.est.0c00958

Laxma Reddy, P. V., B. Kavitha, P. A. Kumar Reddy, and K. H. Kim. 2017. TiO2-based photocatalytic disinfection of microbes in aqueous media: A review. Environ. Res. **154**: 296–303. doi:10.1016/j.envres.2017.01.018

Lechtenfeld, O. J., N. Hertkorn, Y. Shen, M. Witt, and R. Benner. 2015. Marine sequestration of carbon in bacterial metabolites. Nat. Commun. **6**: 1–8. doi:10.1038/ncomms7711

Lehner, S. M., L. Atanasova, N. K. N. Neumann, R. Krska, M. Lemmens, I. S. Druzhinina, and R. Schuhmacher. 2013. Isotope-assisted screening for iron-containing metabolites reveals a high degree of diversity among known and unknown siderophores produced by Trichoderma spp. Appl. Environ. Microbiol. **79**: 18–31. doi:10.1128/AEM.02339-12

Li, Y., W. Jiang, R. Gao, Y. Cai, Z. Guan, and X. Liao. 2018. Fe(III)-based immobilized metal–affinity chromatography (IMAC) method for the separation of the catechol siderophore from Bacillus tequilensis CD36. 3 Biotech **8**: 1–6. doi:10.1007/s13205-018-1396-7

Li, Y., L. Liu, G. Zhang, N. He, W. Guo, B. Hong, and Y. Xie. 2020. Potashchelins, a Suite of Lipid Siderophores Bearing Both L-threo and L-erythro Beta-Hydroxyaspartic Acids, Acquired From the Potash-Salt-Ore-Derived Extremophile Halomonas sp. MG34. Front. Chem. **8**. doi:10.3389/fchem.2020.00197

Liang, P., Q. Ding, and Y. Liu. 2006. Speciation of chromium by selective separation and preconcentration of Cr(III) on an immobilized nanometer titanium dioxide microcolumn. J. Sep. Sci. **29**: 242–247. doi:10.1002/jssc.200500301

Liang, P., and R. Liu. 2007. Speciation analysis of inorganic arsenic in water samples by immobilized nanometer titanium dioxide separation and graphite furnace atomic absorption spectrometric determination. Anal. Chim. Acta **602**: 32–36. doi:10.1016/j.aca.2007.09.012

Liang, W., Y. Chen, F. Zheng, and S.-X. Li. 2014. Titanium dioxide nanoparticle based solid phase extraction of trace Alizarin Violet, followed by its specrophotometric determination. Microchim. Acta **181**: 1513–1519. doi:10.1007/s00604-014-1194-9

Ling, Y., J. Zhu, M. Fan, B. Wu, L. Qin, and C. Huang. 2012. Metabolism studies of casticin in rats using HPLC-ESI-MSn. Biomed. Chromatogr. **26**: 1502–1508. doi:10.1002/bmc.2724

Linsebigler, A. L., L. Guangquan, and J. T. Yates Jr. 1995. Photocatalysis on Ti02 Surfaces: Principles, Mechanisms, and Selected Results. Chem. Rev. **95**: 735–758. doi:10.1021/cr00035a013

Lipczynska-Kochany, E. 2018. Effect of climate change on humic substances and associated impacts on the quality of surface water and groundwater: A review. Sci. Total Environ. **640**–**641**: 1548–1565. doi:10.1016/j.scitotenv.2018.05.376

Liska, I. 1993. On-line versus off-line solid-phase extraction in the determination of organic contaminants in water. Advantages and limitations. J. Chromatogr. A **655**: 163–176. doi:10.1016/0021-9673(93)83220-M

Liu, S., M. Lim, and R. Amal. 2014. TiO2-coated natural zeolite: Rapid humic acid adsorption and effective photocatalytic regeneration. Chem. Eng. Sci. **105**: 46–52. doi:10.1016/j.ces.2013.10.041

Liu, X., and F. J. Millero. 1999. The solubility of iron hydroxide in sodium chloride solutions. Geochim. Cosmochim. Acta **63**: 3487–3497. doi:10.1016/S0016-7037(99)00270-7

Liu, Z. D., and R. C. Hider. 2002. Design of clinically useful iron(III)-selective chelators. Med. Res. Rev. **22**: 26–64. doi:10.1002/med.1027

Liu, Z., T. M. Lin, M. Purro, and M. P. Xiong. 2016. Enzymatically Biodegradable Polyrotaxane-Deferoxamine Conjugates for Iron Chelation. ACS Appl. Mater. Interfaces **8**: 25788–25797. doi:10.1021/acsami.6b09077

Loomis, L. D., and K. N. Raymond. 1991. Solution Equilibria of Enterobactin and Metal-Enterobactin Complexes1. Inorg. Chem. **30**: 906–911. doi:10.1021/ic00005a008

Loosli, F., P. Le Coustumer, and S. Stoll. 2013. TiO2 nanoparticles aggregation and disaggregation in presence of alginate and Suwannee River humic acids. pH and concentration effects on nanoparticle stability. Water Res. **47**: 6052–6063. doi:10.1016/j.watres.2013.07.021

Loper, J. E., and J. S. Buyer. 1991. Siderophores in microbial interactions on plant surfaces. Mol. plant-microbe Interact. **4**: 5–13.

Ma, W. F., Y. Zhang, L. L. Li, and others. 2012. Tailor-made magnetic Fe 3O 4@mTiO 2 microspheres with a tunable mesoporous anatase shell for highly selective and effective enrichment of phosphopeptides. ACS Nano **6**: 3179–3188. doi:10.1021/nn3009646

Macrellis, H. M., C. G. Trick, E. L. Rue, G. Smith, and K. W. Bruland. 2001. Collection and detection of natural iron-binding ligands from seawater. Mar. Chem. **76**: 175–187. doi:10.1016/S0304-4203(01)00061-5

Maier, G. P., and A. Butler. 2017. Siderophores and mussel foot proteins: the role of catechol, cations, and metal coordination in surface adhesion. J. Biol. Inorg. Chem. **22**: 739–749. doi:10.1007/s00775-017-1451-6

Maldonado, M. T., and N. M. Price. 2001. Reduction and transport of organically bound iron by Thalassiosira oceanica (Bacillariophyceae). J. Phycol. **37**: 298–310. doi:10.1046/j.1529-8817.2001.037002298.x

Mancera-Arteu, M., N. Lleshi, V. Sanz-Nebot, E. Giménez, and F. Benavente. 2020. Analysis of glycopeptide biomarkers by on-line TiO2 solid-phase extraction capillary electrophoresis-mass spectrometry. Talanta **209**: 120563. doi:10.1016/j.talanta.2019.120563

Manck, L. E., J. Park, B. J. Tully, A. M. Poire, R. M. Bundy, C. L. Dupont, and K. A. Barbeau. 2021. Petrobactin, a siderophore produced by Alteromonas, mediates community iron acquisition in the global ocean. ISME J. 1–12. doi:10.1038/s41396-021-01065-y

Martin, J. D., Y. Ito, V. V. Homann, M. G. Haygood, and A. Butler. 2006. Structure and membrane affinity of new amphiphilic siderophores produced by Ochrobactrum sp. SP18. J. Biol. Inorg. Chem. **11**: 633–641. doi:10.1007/s00775-006-0112-y

Martin, J. H., K. H. Coale, K. S. Johnson, and others. 1994. Testing the iron hypothesis in ecosystems of the equatorial Pacific Ocean. Nature **371**: 123–129. doi:10.1038/371123a0

Martin, J. H., and S. E. Fitzwater. 1988. Iron deficiency limits phytoplankton growth in the north-east pacific subarctic. Nature **331**: 341–343. doi:10.1038/331341a0

Martin, J. H., R. M. Gordon, S. Fitzwater, and W. W. Broenkow. 1989. Vertex: phytoplankton/iron studies in the Gulf of Alaska. Deep Sea Res. Part A, Oceanogr. Res. Pap. **36**: 649–680. doi:10.1016/0198-0149(89)90144-1

Martinez, J. S., J. N. Carter-Franklin, E. L. Mann, J. D. Martin, M. G. Haygood, and A. Butler. 2003. Structure and membrane affinity of a suite of amphiphilic siderophores produced by a marine bacterium. Proc. Natl. Acad. Sci. **100**: 3754–3759. doi:10.1073/pnas.0637444100

Martinez, J. Z., G. P. Zhang, P. D. Holt, H. T. Jung, C. J. Carrano, M. G. Haygood, and A. Butler. 2000. Self-assembling amphilic siderophores from marine bacteria. Science (80-.). **287**: 1245–1247. doi:10.1126/science.287.5456.1245

Martini, L. A., G. F. Moore, R. L. Milot, L. Z. Cai, S. W. Sheehan, C. A. Schmuttenmaer, G. W. Brudvig, and R. H. Crabtree. 2013. Modular assembly of high-potential zinc porphyrin photosensitizers attached to TiO2 with a series of anchoring groups. J. Phys. Chem. C **117**: 14526–14533. doi:10.1021/jp4053456

Materna, K. L., B. J. Brennan, and G. W. Brudvig. 2015. Silatranes for binding inorganic complexes to metal oxide surfaces. Dalt. Trans. **44**: 20312–20315. doi:10.1039/c5dt03463a

Materna, K. L., R. H. Crabtree, and G. W. Brudvig. 2017. Anchoring groups for photocatalytic water oxidation on metal oxide surfaces. Chem. Soc. Rev. **46**: 6099–6110. doi:10.1039/c7cs00314e

Matsuda, H., H. Nakamura, and T. Nakajima. 1990. New Ceramic Titania: Selective Adsorbent for Organic Phosphates. Anal. Sci. **6**: 911–912. doi:10.2116/analsci.6.911

Mawji, E., M. Gledhill, J. A. Milton, and others. 2008. Hydroxamate siderophores: Occurrence and importance in the Atlantic Ocean. Environ. Sci. Technol. **42**: 8675–8680. doi:10.1021/es801884r

Mawji, E., M. Gledhill, J. A. Milton, M. V. Zubkov, A. Thompson, G. A. Wolff, and E. P. Achterberg. 2011. Production of siderophore type chelates in Atlantic Ocean waters enriched with different carbon and nitrogen sources. Mar. Chem. **124**: 90–99. doi:10.1016/j.marchem.2010.12.005

McCormack, P., P. J. Worsfold, and M. Gledhill. 2003. Separation and detection of siderophores produced by marine bacterioplankton using high-performance liquid chromatography with electrospray ionization mass spectrometry. Anal. Chem. **75**: 2647–2652. doi:10.1021/ac0340105

McNamara, W. R., R. L. Milot, H. E. Song, R. C. Snoeberger, V. S. Batista, C. A. Schmuttenmaer, G. W. Brudvig, and R. H. Crabtree. 2010. Water-stable, hydroxamate anchors for functionalization of TiO2 surfaces with ultrafast interfacial electron transfer. Energy Environ. Sci. **3**: 917–923. doi:10.1039/c001065k

McNamara, W. R., R. C. Snoeberger, G. Li, and others. 2009. Hydroxamate anchors for water-stable attachment to TiO2 nanoparticles. Energy Environ. Sci. **2**: 1173–1175. doi:10.1039/b910241h

McWhirter, M. J., P. J. Bremer, I. L. Lamont, and A. J. McQuillan. 2003. Siderophore-mediated covalent bonding to metal (oxide) surfaces during biofilm initiation by pseudomonas aeruginosa bacteria. Langmuir **19**: 3575–3577. doi:10.1021/la020918z

Millero, F. 2001. Speciation of metals in natural waters. Geochem. Trans. **2**: 56–64. doi:10.1039/b104809k

Mills, A., R. H. Davies, and D. Worsley. 1993. Water purification by semiconductor photocatalysis. Chem. Soc. Rev. **22**: 417–425. doi:10.1039/CS9932200417

Mills, G. L., A. K. Hanson, J. G. Quinn, W. R. Lammela, and N. D. Chasteen. 1982. Chemical studies of copper-organic complexes isolated from estuarine waters using C18 reverse-phase liquid chromatography. Mar. Chem. **11**: 355–377. doi:10.1016/0304-4203(82)90031-7

Mohamed, K. N., S. Steigenberger, M. C. Nielsdottir, M. Gledhill, and E. P. Achterberg. 2011. Dissolved iron(III) speciation in the high latitude North Atlantic Ocean. Deep. Res. I **58**: 1049–1059. doi:10.1016/j.dsr.2011.08.011

Monzyk, B., and A. L. Crumbliss. 1982. Kinetics and Mechanism of the Stepwise Dissociation of Iron(III) from Ferrioxamine B in Aqueous Acid. J. Am. Chem. Soc. **104**: 4921–4929. doi:10.1021/ja00382a031

Morel, F. M. M., and N. M. Price. 2003. The biogeochemical cycles of trace metals in the oceans. Science (80-.). **300**: 944–947. doi:10.1126/science.1083545

Nawrocki, J., C. Dunlap, A. McCormick, and P. W. Carr. 2004. Part I. Chromatography using ultra-stable metal oxide-based stationary phases for HPLC. J. Chromatogr. A **1028**: 1–30.

doi:10.1016/j.chroma.2003.11.050

Nduwa-Mushidi, J., and C. G. Anderson. 2017. Surface Chemistry and Flotation Behaviors of Monazite–Apatite–Ilmenite–Quartz–Rutile–Zircon with Octanohydroxamic Acid. J. Sustain. Metall. **3**: 62–72. doi:10.1007/s40831-016-0114-0

Neilands, J. B. 1995. Siderophores: Structure and function of microbial iron transport compounds. J. Biol. Chem. **270**: 26723–26726. doi:10.1074/jbc.270.45.26723

Nichols, C. M., S. G. Lardière, J. P. Bowman, P. D. Nichols, J. A. E. Gibson, and J. Guézennec. 2005. Chemical characterization of exopolysaccharides from Antarctic marine bacteria. Microb. Ecol. **49**: 578–589. doi:10.1007/s00248-004-0093-8

Nielsen, K. F., M. Månsson, C. Rank, J. C. Frisvad, and T. O. Larsen. 2011. Dereplication of microbial natural products by LC-DAD-TOFMS. J. Nat. Prod. **74**: 2338–2348. doi:10.1021/np200254t

Nixon, R. L., and A. R. S. Ross. 2016. Evaluation of Immobilized Metal-Ion Affinity Chromatography and Electrospray Ionization Tandem Mass Spectrometry for Recovery and Identification of Copper(II)-Binding Ligands in Seawater Using the Model Ligand 8-Hydroxyquinoline. Front. Mar. Sci. **3**: 1–10. doi:10.3389/fmars.2016.00246

Norman, L., I. A. M. Worms, E. Angles, and others. 2015. The role of bacterial and algal exopolymeric substances in iron chemistry. Mar. Chem. **173**: 148–161. doi:10.1016/j.marchem.2015.03.015

O'Brien, S., D. J. Hodgson, and A. Buckling. 2014. Social evolution of toxic metal bioremediation in Pseudomonas aeruginosa. Proc. R. Soc. B Biol. Sci. **281**. doi:10.1098/rspb.2014.0858

O'Regan, B., and M. Grätzel. 1991. A low-cost, high-efficiency solar cell based on dye-sensitized colloidal Ti02 films. Nature **353**: 737–740. doi:10.1016/0146-5724(84)90144-4

Okujo, N., Y. Sakakibara, T. Yoshida, and S. Yamamoto. 1994. Structure of acinetoferrin, a new citrate-based dihydroxamate siderophore from Acinetobacter haemolyticus. Biometals **7**: 170–176. doi:10.1007/BF00140488

Pakulski, J. D., and R. Benner. 1994. Abundance and distribution of carbohydrates in the ocean. Limnol. Oceanogr. **39**: 930–940. doi:10.4319/lo.1994.39.4.0930

Panagiotopoulos, C., and R. Sempéré. 2005. Analytical methods for the determination of sugars in marine samples: A historical perspective and future directions. Limnol. Oceanogr. Methods **3**: 419–454. doi:10.4319/lom.2005.3.419

Patriarca, C., J. Bergquist, P. J. R. Sjöberg, L. Tranvik, and J. A. Hawkes. 2018. Online HPLC-ESI-HRMS Method for the Analysis and Comparison of Different Dissolved Organic Matter Samples. Environ. Sci. Technol. **52**: 2091–2099. doi:10.1021/acs.est.7b04508

Persmark, M., P. Pittman, J. S. Buyer, B. Schwyn, P. R. Gill, and J. B. Neilands. 1993. Isolation and Structure of Rhizobactin 1021, a Siderophore from the Alfalfa Symbiont Rhizobium meliloti 1021. J. Am. Chem. Soc. **115**: 3950–3956. doi:10.1021/ja00063a014

Petras, D., I. Koester, R. Da Silva, and others. 2017. High-resolution liquid chromatography tandem mass spectrometry enables large scale molecular characterization of dissolved organic matter. Front. Mar. Sci. **4**. doi:10.3389/fmars.2017.00405

Petrone, L. 2013. Molecular surface chemistry in marine bioadhesion. Adv. Colloid Interface Sci. **195**–**196**: 1–18. doi:10.1016/j.cis.2013.03.006

Pfleger, B. F., J. Y. Lee, R. V. Somu, C. C. Aldrich, P. C. Hanna, and D. H. Sherman. 2007. Characterization and analysis of early enzymes for petrobactin biosynthesis in Bacillus anthracis. Biochemistry **46**: 4147–4157. doi:10.1021/bi6023995

Phillips, L. G., and D. M. Barbano. 1997. The Influence of Fat Substitutes Based on Protein and Titanium Dioxide on the Sensory Properties of Lowfat Milks. J. Dairy Sci. **80**: 2726–2731. doi:10.3168/jds.S0022-0302(97)76234-9

Pinkse, M. W. H., P. M. Uitto, M. J. Hilhorst, B. Ooms, and A. J. R. Heck. 2004. Selective isolation at the femtomole level of phosphopeptides from proteolytic digests using 2D-NanoLC-ESI-MS/MS and titanium oxide precolumns. Anal. Chem. **76**: 3935–3943. doi:10.1021/ac0498617

Poole, C. F. 2003. New trends in solid-phase extraction. TrAC - Trends Anal. Chem. **22**: 362–373. doi:10.1016/S0165-9936(03)00605-8

Porath, J., J. Carlsson, I. Olsson, and G. Belfrage. 1975. Metal chelate affinity chromatography, a new approach to protein fractionation. Nature **258**: 598–599. doi:10.1038/258598a0

Pozdnyakov, I. P., F. Wu, A. A. Melnikov, V. P. Grivin, N. M. Bazhin, S. V. Chekalin, and P. V. F. 2013. Photochemistry of iron(III)—lactic acid complex in aqueous solutions. Russ. Chem. Bull. Int. Ed. **62**: 1579–1585. doi:10.1007/s11172-013-0227-6

Qiao, L., N. Gan, J. Wang, H. Gao, F. Hu, H. Wang, and T. Li. 2015. Novel molecularly imprinted stir bar sorptive extraction based on an 8-electrode array for preconcentration of trace exogenous estrogens in meat. Anal. Chim. Acta **853**: 342–350. doi:10.1016/j.aca.2014.10.041

Raaijmakers, J. M., L. van der Sluis, M. Koster, P. A. H. M. Bakker, P. J. Weisbeek, and B. Schippers. 1995. Utilization of heterologous siderophores and rhizosphere competence of fluorescent Pseudomonas spp. Can. J. Microbiol. **41**: 126–135. doi:10.1139/m95-017

Raeke, J., O. J. Lechtenfeld, M. Wagner, P. Herzsprung, and T. Reemtsma. 2016. Selectivity of solid phase extraction of freshwater dissolved organic matter and its effect on ultrahigh resolution mass spectra. Environ. Sci. Process. Impacts **18**: 918–927. doi:10.1039/c6em00200e

Rai, V., N. Fisher, O. W. Duckworth, and O. Baars. 2020. Extraction and Detection of Structurally Diverse Siderophores in Soil. Front. Microbiol. **11**: 1–13. doi:10.3389/fmicb.2020.581508

Ratledge, C., and L. G. Dover. 2000. Iron Metabolism in Pathogenic Bacteria. Annu. Rev. Microbiol. **54**: 881–941. doi:10.1146/annurev.micro.54.1.881

Raymond, K. N., E. A. Dertz, and S. S. Kim. 2003. Enterobactin: An archetype for microbial iron transport. Proc. Natl. Acad. Sci. U. S. A. **100**: 3584–3588. doi:10.1073/pnas.0630018100

Reichardt, C. 1994. Solvatochromic dyes as solvent polarity indicators. Chem. Rev. **94**: 2319–2358. doi:10.1021/cr00032a005

Reid, R. T., D. H. Livet, D. J. Faulkner, and A. Butler. 1993. A siderophore from a marine bacterium with an exceptional ferric ion affinity constant. Nature **366**: 455–458. doi:10.1038/366455a0

Rico, M., A. López, J. M. Santana-Casiano, A. G. González, and M. González-Dávila. 2013. Variability of the phenolic profile in the diatom Phaeodactylum tricornutum growing under copper and iron stress. Limnol. Oceanogr. **58**: 144–152. doi:10.4319/lo.2013.58.1.0144

Rioux, C., D. C. Jordan, and J. B. M. Rattray. 1983. Colorimetric Determination of Catechol Siderophores in Microbial Cultures. Anal. Biochem. **133**: 163–169. doi:10.1016/0003-2697(83)90238-5

Römheld, V., and H. Marschner. 1986. Evidence for a Specific Uptake System for Iron Phytosiderophores in Roots of Grasses. Plant Physiol. **80**: 175–180. doi:10.1104/pp.80.1.175

Ross, A. R. ., M. G. Ikonomou, and K. J. Orians. 2003. Characterization of copper-complexing ligands in seawater using immobilized copper(II)-ion affinity chromatography and electrospray ionization mass spectrometry. Mar. Chem. **83**: 47–58. doi:10.1016/S0304-4203(03)00095-1

Rout, G. R., and S. Sahoo. 2015. Role of Iron in Plant Growth and Metabolism. Rev. Agric. Sci. **3**: 1–24. doi:10.7831/ras.3.1

Roy, E. G., M. L. Wells, and D. W. King. 2008. Persistence of iron(II) in surface waters of the western subarctic Pacific. Limnol. Oceanogr. **53**: 89–98. doi:10.4319/lo.2008.53.1.0089

Rue, E., and K. Bruland. 2001. Domoic acid binds iron and copper: A possible role for the toxin produced by the marine diatom Pseudo-nitzschia. Mar. Chem. **76**: 127–134. doi:10.1016/S0304-4203(01)00053-6

Rue, E. L., and K. W. Bruland. 1995. Complexation of iron(III) by natural organic ligands in the Central North Pacific as determined by a new competitive ligand equilibration/adsorptive cathodic stripping voltammetric method. Mar. Chem. **50**: 117–138. doi:10.1016/0304-4203(95)00031-L

Rue, E. L., and K. W. Bruland. 1997. The role of organic complexation on ambient iron chemistry in the equatorial Pacific Ocean and the response of a mesoscale iron addition experiment. Limnol. Oceanogr. **42**: 901–910. doi:10.4319/lo.1997.42.5.0901

Rueler, J. G., and D. R. Ades. 1987. The role of iron nutrition in photosynthesis and nitrogen assimilation in SCENEDESMUS QUADRICAUDA (Chlorophyceae). J. Phycol. **23**: 452–457. doi:10.1111/j.1529-8817.1987.tb02531.x

Sambi, M., G. Sangiovanni, G. Granozzi, and F. Parmigiani. 1996. Early stages of epitaxial growth of vanadium oxide at the(110) surface studied by photoelectron diffraction. Phys. Rev. B - Condens. Matter Mater. Phys. **54**: 13464–13467. doi:10.1103/PhysRevB.54.13464

Sambrano, J. R., J. Andrés, A. Beltran, F. R. Senseto, E. R. Leite, F. M. L. G. Stamato, and E. Longo. 1997. An Ab Initio Study of Oxygen Vacancies and Doping Process of Nb and Cr Atoms on TiO2 (110) Surface Models. Int. J. Quantum Chem. **65**: 625–631. doi:10.1088/0953-8984/25/39/395301

Samsonov, G. V. 1982. The Oxide Handbook, 1st ed. G.V. Samsonov [ed.]. Springer New York, NY.

Sandron, S., N. W. Davies, R. Wilson, A. R. Cardona, P. R. Haddad, P. N. Nesterenko, and B. Paull. 2018. Fractionation of Dissolved Organic Matter on Coupled Reversed-Phase Monolithic Columns and Characterisation Using Reversed-Phase Liquid Chromatography-High Resolution Mass Spectrometry. Chromatographia **81**: 203–213. doi:10.1007/s10337-017-3324-0

Sandron, S., A. Rojas, R. Wilson, and others. 2015. Chromatographic methods for the isolation, separation and characterisation of dissolved organic matter. Environ. Sci. Process. Impacts **17**: 1531–1567. doi:10.1039/c5em00223k

Sandy, M., and A. Butler. 2009. Microbial iron acquisition: Marine and terrestrial siderophores. Chem. Rev. **109**: 4580–4595. doi:10.1021/cr9002787

Santana-Casiano, J. M., M. González-Dávila, A. G. González, and F. J. Millero. 2010. Fe(III) reduction in the presence of Catechol in seawater. Aquat. Geochemistry **16**: 467–482. doi:10.1007/s10498-009-9088-x

Santana-Casiano, J. M., M. González-Dávila, A. G. González, M. Rico, A. López, and A. Martel. 2014. Characterization of phenolic exudates from Phaeodactylum tricornutum and their effects on the chemistry of Fe(II)-Fe(III). Mar. Chem. **158**: 10–16. doi:10.1016/j.marchem.2013.11.001

Sassone-Corsi, M., S. P. Nuccio, H. Liu, D. Hernandez, C. T. Vu, A. A. Takahashi, R. A. Edwards, and M. Raffatellu. 2016. Microcins mediate competition among Enterobacteriaceae in the inflamed gut. Nature **540**: 280–283. doi:10.1038/nature20557

Scazzocchio, C. 2000. The fungal GATA factors. Curr. Opin. Microbiol. **3**: 126–131. doi:10.1016/S1369-5274(00)00063-1

Schalk, I. J., M. Hannauer, and A. Braud. 2011. New roles for bacterial siderophores in metal transport and tolerance. Environ. Microbiol. **13**: 2844–2854. doi:10.1111/j.1462-2920.2011.02556.x

Schmelz, S., N. Kadi, S. A. McMahon, and others. 2009. AcsD catalyzes enantioselective citrate desymmetrization in siderophore biosynthesis. Nat. Chem. Biol. **5**: 174–182. doi:10.1038/nchembio.145

Schmid, R., D. Petras, L. F. Nothias, and others. 2021. Ion identity molecular networking for mass spectrometry-based metabolomics in the GNPS environment. Nat. Commun. **12**. doi:10.1038/s41467-021-23953-9

Schwyn, B., and J. B. Neilands. 1987. Universal chemical assay for the detection and determination of siderophore. Anal. Biochem. **160**: 47–56. doi:10.1016/0003-2697(87)90612-9

Seymour, J. R., S. A. Amin, J. B. Raina, and R. Stocker. 2017. Zooming in on the phycosphere: The ecological interface for phytoplankton-bacteria relationships. Nat. Microbiol. **2**. doi:10.1038/nmicrobiol.2017.65

Simionato, A. V. C., G. D. De Souza, E. Rodrigues-Filho, J. Glick, P. Vouros, and E. Carrilho. 2006. Tandem mass spectrometry of coprogen and deferoxamine hydroxamic siderophores. Commun. MASS Spectrom. Rapid Commun. Mass Spectrom **20**: 193–199. doi:10.1002/rcm.2295

Singh, R. 2015. Water and Membrane Treatment, p. 81–178. *In* Membrane Technology and Engineering for Water Purification. Butterworth-Heinemann.

Sittig, C., M. Textor, N. D. Spencer, M. Wieland, and P. H. Vallotton. 1999. Surface characterization of implant materials c.p. Ti, Ti-6Al-7Nb and Ti-6Al-4V with different pretreatments. J. Mater. Sci. Mater. Med. **10**: 35–46. doi:10.1023/A:1008840026907

Stephan, H., S. Freund, J.-M. Meyer, G. Winkelmann, and G. Jung. 1993. Structure Elucidation of the Gallium-Ornibactin Complex by 2D-NMR Spectroscopy. Liebigs Ann. der Chemie **1993**: 43–48. doi:10.1002/jlac.199319930108

Subra, P., M.-C. Hennion, and R. Rosset. 1988. Recovery of organic compounds from large-volume aqueous samples using on-line liquid chromatographic preconcentration techniques. J. Chromatograp **456**: 121–141. doi:doi.org/10.1016/0021-9673(86)80011-5

Sundgren, J. E., P. Bodö, and I. Lundström. 1986. Auger electron spectroscopic studies of the interface between human tissue and implants of titanium and stainless steel. J. Colloid Interface Sci. **110**: 9–20. doi:10.1016/0021-9797(86)90348-6

Suttiponparnit, K., J. Jiang, M. Sahu, S. Suvachittanont, T. Charinpanitkul, and P. Biswas. 2011. Role of Surface Area, Primary Particle Size, and Crystal Phase on Titanium Dioxide Nanoparticle Dispersion Properties. Nanoscale Res. Lett. **6**: 1–8. doi:10.1007/s11671-010-9772-1

Swayambhu, G., M. Bruno, A. M. Gulick, and B. A. Pfeifer. 2021. Siderophore natural products as pharmaceutical agents. Curr. Opin. Biotechnol. **69**: 242–251. doi:10.1016/j.copbio.2021.01.021

Tagliabue, A., O. Aumont, and L. Bopp. 2014. The impact of different external sources of iron on the global carbon cycle. Geophys. Res. Lett. **41**: 920–926. doi:10.1002/2013GL059059.Received

Tagliabue, A., O. Aumont, R. DeAth, and others. 2015. How well do global ocean biogeochemistry models simulate dissolved iron distributions? Global Biogeochem. Cycles **30**: 149–174. doi:10.1111/1462-2920.13280

Tani, K., and M. Ozawa. 1999. Investigation of chromatographic properties of titania. I. On retention behavior of hydroxyl and other substituent aliphatic carboxylic acids: Comparison with zirconia. J. Liq. Chromatogr. Relat. Technol. **22**: 843–856. doi:10.1081/JLC-100101702

Tautenhahn, R., G. J. Patti, D. Rinehart, and G. Siuzdak. 2012. XCMS online: A web-based platform to process untargeted metabolomic data. Anal. Chem. **84**: 5035–5039. doi:10.1021/ac300698c

Taylor, P. D. P., R. Maeck, and P. De Bièvre. 1992. Determination of the absolute isotopic composition and Atomic Weight of a reference sample of natural iron. Int. J. Mass Spectrom. Ion Process. **121**: 111–125. doi:10.1016/0168-1176(92)80075-C

Taylor, S. R. 1964. Abundance of chemical elements in the continental crust: a new table. Geochim. Cosmochim. Acta **28**: 1273–1285. doi:10.1016/0016-7037(64)90129-2

Telfer, T. J., J. R. Liddell, C. Duncan, A. R. White, and R. Codd. 2017. Adamantyl- and other polycyclic cage-based conjugates of desferrioxamine B (DFOB) for treating iron-mediated toxicity in cell models of Parkinson's disease. Bioorganic Med. Chem. Lett. **27**: 1698–1704. doi:10.1016/j.bmcl.2017.03.001

Thuroczy, C.-E., L. J. A. Gerringa, M. B. Klunder, R. Middag, P. Laan, K. R. Timmermans, and H. J. W. de Baar. 2010. Speciation of Fe in the Eastern North Atlantic Ocean. Deep. Res. I **57**: 1444–1453. doi:10.1016/j.dsr.2010.08.004

Trick, C. G. 1989. Hydroxamate-siderophore production and utilization by marine eubacteria. Curr. Microbiol. **18**: 375–378. doi:10.1016/j.chaos.2005.08.145

Troxell, B., and H. M. Hassan. 2013. Transcriptional regulation by Ferric Uptake Regulator (Fur) in pathogenic bacteria. Front. Cell. Infect. Microbiol. **4**: 1–13. doi:10.3389/fcimb.2013.00059

Tsuda, A., S. Takeda, H. Saito, J. Nishioka, Y. Nojiri, I. Kudo, and H. Kiyosawa. 2003. A Mesoscale Iron Enrichment in the Western Subarctic Pacific Induces a Large Centric Diatom Bloom. Science (80-.). **300**: 958–961. doi:10.1126/science.1082000

Tulevski, G. S., Q. Miao, M. Fukuto, and others. 2004. Attaching organic semiconductors to

gate oxides: In situ assembly of monolayer field effect transistors. J. Am. Chem. Soc. **126**: 15048–15050. doi:10.1021/ja044101z

U.S. Geological Survey. 2022. Mineral Commodity Summaries: Titanium and titanium dioxide.

Upritchard, H. G., J. Yang, P. J. Bremer, I. L. Lamont, and A. J. McQuillan. 2007. Adsorption to metal oxides of the Pseudomonas aeruginosa siderophore pyoverdine and implications for bacterial biofilm formation on metals. Langmuir **23**: 7189–7195. doi:10.1021/la7004024

Upritchard, H. G., J. Yang, P. J. Bremer, I. L. Lamont, and A. J. McQuillan. 2011. Adsorption of enterobactin to metal oxides and the role of siderophores in bacterial adhesion to metals. Langmuir **27**: 10587–10596. doi:10.1021/la202352j

Velasquez, I., B. L. Nunn, E. Ibisanmi, D. R. Goodlett, K. A. Hunter, and S. G. Sander. 2011. Detection of hydroxamate siderophores in coastal and Sub-Antarctic waters off the South Eastern Coast of New Zealand. Mar. Chem. **126**: 97–107. doi:10.1016/j.marchem.2011.04.003

Verdugo, P., A. L. Alldredge, F. Azam, D. L. Kirchman, U. Passow, and P. H. Santschi. 2004. The oceanic gel phase: A bridge in the DOM-POM continuum. Mar. Chem. **92**: 67–85. doi:10.1016/j.marchem.2004.06.017

Völker, C., and D. A. Wolf-Gladrow. 1999. Physical limits on iron uptake mediated by siderophores or surface reductases. Mar. Chem. **65**: 227–244. doi:10.1016/S0304-4203(99)00004-3

Voß, D., A. Müller, R. Henkel, U. John, and O. Zielinski. Chlorophyll a measurements from discrete water samples during RV HEINCKE cruise HE533 (2021).

Vraspir, J. M., and A. Butler. 2009. Chemistry of Marine Ligands and Siderophores. Ann. Rev. Mar. Sci. **1**: 43–63. doi:10.1146/annurev.marine.010908.163712

Wagstaff, B. A., E. S. Hems, M. Rejzek, and others. 2018. Insights into toxic prymnesium parvum blooms: The role of sugars and algal viruses. Biochem. Soc. Trans. **46**: 413–421. doi:10.1042/BST20170393

Wang, H., R. M. Burgess, M. G. Cantwell, L. M. Portis, M. M. Perron, F. Wu, and K. T. Ho. 2014a. Stability and aggregation of silver and titanium dioxide nanoparticles in seawater: Role of salinity and dissolved organic carbon. Environ. Toxicol. Chem. **33**: 1023–1029. doi:10.1002/etc.2529

Wang, S. T., W. Huang, Y. F. Deng, Q. Gao, B. F. Yuan, and Y. Q. Feng. 2014b. “Old” metal oxide affinity chromatography as “novel” strategy for specific capture of cis-diol-containing compounds. J. Chromatogr. A **1361**: 100–107. doi:10.1016/j.chroma.2014.07.091

Wang, S. T., W. Huang, W. Lu, B. F. Yuan, and Y. Q. Feng. 2013. TiO2-based solid phase extraction strategy for highly effective elimination of normal ribonucleosides before detection of 2′- deoxynucleosides/low-abundance 2′-O-modified ribonucleosides. Anal. Chem. **85**: 10512–10518. doi:10.1021/ac4025297

Waska, H., A. Koschinsky, and T. Dittmar. 2016. Fe- and Cu-Complex Formation with Artificial Ligands Investigated by Ultra-High Resolution Fourier-Transform ion Cyclotron Resonance Mass Spectrometry (FT-ICR-MS): Implications for Natural Metal-Organic Complex Studies. Front. Mar. Sci. **3**: 1–19. doi:10.3389/fmars.2016.00119

Waska, H., A. Koschinsky, M. J. Ruiz Chancho, and T. Dittmar. 2015. Investigating the potential of solid-phase extraction and Fourier-transform ion cyclotron resonance mass spectrometry (FT-ICR-MS) for the isolation and identification of dissolved metal-organic

complexes from natural waters. Mar. Chem. **173**: 78–92. doi:10.1016/j.marchem.2014.10.001

Wehrli, B., E. Wieland, and G. Furrer. 1990. Chemical mechanisms in the dissolution kinetics of minerals; the aspect of active sites - Dedicated to Werner Stumm for his 65th birthday. Aquat. Sci. **52**: 3–31. doi:10.1007/BF00878239

Winterbourn, C. C. 1995. Toxicity of iron and hydrogen peroxide: the Fenton reaction. Toxicol. Lett. **82**–**83**: 969–974. doi:10.1016/0378-4274(95)03532-X

Von Wirén, N., S. Klair, S. Bansal, J. F. Briat, H. Khodr, T. Shioiri, R. A. Leigh, and R. C. Hider. 1999. Nicotianamine chelates both Fe(III) and Fe(II) implications for metal transport in plants. Plant Physiol. **119**: 1107–1114. doi:10.1104/pp.119.3.1107

Witter, A. E., and G. W. L. Luther III. 1998. Variation in Fe-organic complexation with depth in the Northwestern Atlantic Ocean as determined using a kinetic approach. Mar. Chem. **62**: 241–258. doi:10.1016/S0304-4203(98)00044-9

Wünsch, U. J., and J. A. Hawkes. 2020. Mathematical chromatography deciphers the molecular fingerprints of dissolved organic matter. Analyst **145**: 1789–1800. doi:10.1039/c9an02176k

Xu, J., P. Wu, E. C. Ye, B. F. Yuan, and Y. Q. Feng. 2016. Metal oxides in sample pretreatment. TrAC - Trends Anal. Chem. **80**: 41–56. doi:10.1016/j.trac.2016.02.027

Yamamoto, S., Y. Fujita, N. Okujo, C. Minami, S. Matsuura, and S. Shinoda. 1992. Isolation and partial characterization of a compound with siderophore activity from Vibrio parahaemolyticus. FEMS Microbiol. Lett. **94**: 181–186. doi:10.1016/0378-1097(92)90605-N

Yamamoto, S., N. Okujo, T. Yoshida, S. Matsuura, and S. Shinoda. 1994. Structure and iron transport activity of vibrioferrin, a new siderophore of Vibrio parahaemolyticus. J. Biochem. **115**: 868–874. doi:10.1093/oxfordjournals.jbchem.a124432

Yan, J., X. Li, L. Yu, Y. Jin, X. Zhang, X. Xue, Y. Ke, and X. Liang. 2010. Selective enrichment of glycopeptides/phosphopeptides using porous titania microspheres. Chem. Commun. **46**: 5488–5490. doi:10.1039/c000094a

Yang, J., P. J. Bremer, I. L. Lamont, and A. J. McQuillan. 2006. Infrared spectroscopic studies of siderophore-related hydroxamic acid ligands adsorbed on titanium dioxide. Langmuir **22**: 10109–10117. doi:10.1021/la061365l

Yang, K., D. Lin, and B. Xing. 2009. Interactions of Humic Acid with Nanosized Inorganic Oxides. Langmuir **25**: 3571–3576. doi:10.1016/j.envpol.2008.11.007

Yang, R., and C. M. G. Van Den Berg. 2009. Metal complexation by humic substances in seawater. Environ. Sci. Technol. **43**: 7192–7197. doi:10.1021/es900173w

Yang, S. P., O. Bar-Ilan, R. E. Peterson, W. Heideman, R. J. Hamers, and J. A. Pedersen. 2013. Influence of humic acid on titanium dioxide nanoparticle toxicity to developing zebrafish. Environ. Sci. Technol. **47**: 4718–4725. doi:10.1021/es3047334

Yarimizu, K., R. Cruz-López, E. García-Mendoza, M. Edwards, M. L. Carter, and C. J. Carrano. 2019. Distribution of dissolved iron and bacteria producing the photoactive siderophore, vibrioferrin, in waters off Southern California and Northern Baja. BioMetals **32**: 139–154. doi:10.1007/s10534-018-00163-3

Younes, M., G. Aquilina, L. Castle, and others. 2021. Safety assessment of titanium dioxide (E171) as a food additive. EFSA J. **19**. doi:10.2903/j.efsa.2021.6585

Yu, J., W. Wei, M. S. Menyo, A. Masic, J. H. Waite, and J. N. Israelachvili. 2013. Adhesion of mussel foot protein-3 to TiO2 surfaces: The effect of pH. Biomacromolecules **14**: 1072–1077. doi:10.1021/bm301908y

Yuan, S., W. Chen, and S. Hu. 2005. Fabrication of TiO2 nanoparticles/surfactant polymer complex film on glassy carbon electrode and its application to sensing trace dopamine. Mater. Sci. Eng. C **25**: 479–485. doi:10.1016/j.msec.2004.12.004

Zajdowicz, S., J. C. Haller, A. E. Krafft, and others. 2012. Purification and structural characterization of siderophore (corynebactin) from corynebacterium diphtheriae. PLoS One **7**. doi:10.1371/journal.pone.0034591

Zhang, L., and J. M. Cole. 2015. Anchoring groups for dye-sensitized solar cells. ACS Appl. Mater. Interfaces **7**: 3427–3455. doi:10.1021/am507334m

Zhang, W., M. Lin, P. Tong, Q. Lu, and L. Zhang. 2016. Ferrite nanospheres-based magnetic solid-phase extraction for determination of domoic acid in seawater samples using high-performance liquid chromatography with tandem mass spectrometry. J. Chromatogr. A **1443**: 54–61. doi:10.1016/j.chroma.2016.03.055

Zhang, Y., Y. Chen, P. Westerhoff, and J. Crittenden. 2009. Impact of natural organic matter and divalent cations on the stability of aqueous nanoparticles. Water Res. **43**: 4249–4257. doi:10.1016/j.watres.2009.06.005

Zheng, L., D. G. Watson, J. N. A. Tettey, and C. A. Clements. 2008. The determination of iron as its EDTA complex in Helix aspera by hydrophilic interaction liquid chromatography coupled to Fourier transform electrospray ionisation mass spectrometry. Talanta **76**: 1165–1169. doi:10.1016/j.talanta.2008.05.018

Zhou, Q., and Z. Fang. 2015. Graphene-modified TiO2 nanotube arrays as an adsorbent in micro-solid phase extraction for determination of carbamate pesticides in water samples. Anal. Chim. Acta **869**: 43–49. doi:10.1016/j.aca.2015.02.019

Zhu, Z. J., A. W. Schultz, J. Wang, C. H. Johnson, S. M. Yannone, G. J. Patti, and G. Siuzdak. 2013. Liquid chromatography quadrupole time-of-flight mass spectrometry characterization of metabolites guided by the METLIN database. Nat. Protoc. **8**: 451–460. doi:10.1038/nprot.2013.004

Appendix

Supporting information: Siderophore purification with titanium dioxide nanoparticle solid phase extraction

Electronic Supplementary Material (ESI) for Analyst.
This journal is © The Royal Society of Chemistry 2020

Supporting Information

Siderophore purification with TiO_2 nanoparticle solid phase extraction

Philipp H. Egbers[⊥], Tilmann Harder[⊥,#], Boris P. Koch[#,+], Jan Tebben[#*]

[⊥] University of Bremen, Faculty of Biology and Chemistry, Leobener Straße 6, 28359 Bremen, Germany

[#] Department of Ecological Chemistry, Alfred Wegener Institute, Helmholtz Centre for Polar and Marine Research, Am Handelshafen 12, 27570 Bremerhaven, Germany

[+] University of Applied Sciences, An der Karlstadt 8, D-27568 Bremerhaven, Germany

The Supporting Information includes following items:

PROTOCOL FOR TiO_2 NP-BASED SPE FROM BACTERIAL CULTURE SUPERNATANTS

Materials
Reagents:
TiO_2 nanopowder 21 nm
NaH_2PO_4
Methanol and formic acid
NaOH
Ultrapure water (Sartorius)
HCl 35%
$HClO_4$
$Fe(ClO_4)_3$
Equipment:
2 mL screw cap micro tubes
Cryomill (or shaker)
Vortex mixer
Centrifuge
1.5 mL micro tubes
Setup:
Acid washing: Soak 2 mL screw cap micro tubes with 5 M HCl for 24 h and then rinse with ultrapure water 5 times. Store acid washed screw cap microtubes closed in clean bags until needed.
Hydroxamate assay solution (Atkin's assay): 5 mmol L^{-1} $Fe(ClO_4)_3$ in 0.1 M $HClO_4$. Mix 1 part of crude sample with 1 part of assay solution. If sample contains hydroxamates brownish/reddish colour appears immediately after mixing the two solutions. If possible, compare this result to a similarly prepared blank.
TiO_2: Prepare a suspension by mixing 10 g TiO_2 nanopowder with 100 mL ultrapure water. Vortex the suspension shortly before use.
Washing solution: Formic acid in methanol (0.02 vol%)
Eluent: NaH_2PO_4 100 mmol L^{-1} in ultrapure water and pH adjusted to 12.6 with NaOH.
Neutralization solution: 100 mmol L^{-1} $FeCl_3$ in aqueous formic acid (0.2 vol%).

Procedure

1. Transfer 0.1 mL TiO_2 suspension into acid washed screw cap micro tube
2. Apply 1 mL of Atkin's assay positive sample to the TiO_2 suspension and vortex occasionally for at least 20 min to achieve complete adsorption.
3. Centrifugation of the screw cap micro tube at 14000 rpm for 2 min.
4. Separate supernatant from the TiO_2 pellet by decanting. Collect the supernatant and check with Atkin's assay. If the supernatant is showing still a positive reddish colouration repeat step 1.-3. to extract the reaming hydroxamates.
5. Rinse TiO_2 with 1 mL ultrapure water and re-suspend the pellet by shaking the sample for 2 min at 30 Hz with a Cryomill. If a Cryomill is not available, it is also possible to achieve dissolution of the pellet manually. After re-suspending, the sample is occasionally vortexed for 5 min.
6. Centrifugation of the screw cap micro tube at 14000 rpm for 2 min and the ultrapure water supernatant is discarded. Perform ultrapure water rinsing steps 5. and 6. again
7. Repeat steps 5.-6. but instead of ultrapure water use washing solution. Supernatant are also discarded.
8. To achieve elution of hydroxamates add 1 mL of eluent and process the TiO_2 pellet as for the previous steps. Collect supernatant in 1.5 mL microtubes. This step is repeated three times to achieve complete elution of bound hydroxamates.
9. Add 0.2 mL of neutralization solution to each 1.5 mL microtube and centrifuge for 20 min at 14000 rpm.
10. Transfer an aliquot of each sample into untreated LC-Vials and let it stand for 48 h to achieve complete complexation of the eluted free hydroxamate ligands.
11. Measure samples via LC-MS to detected isotopic pattern of Fe and therefor confirm the presents of Fe-ligands in the eluate.

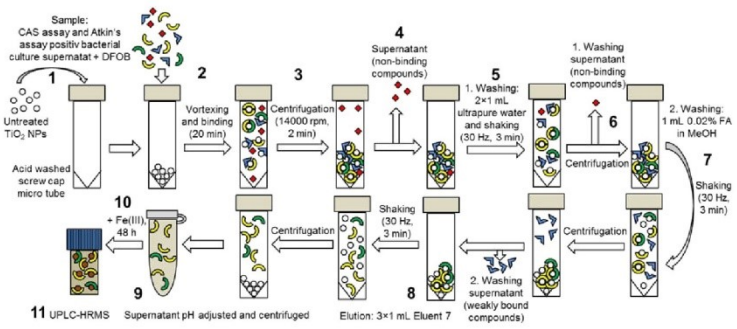

Figure S1. TiO_2 nanoparticle based SPE of hydroxamates from bacterial culture supernatants.

BACTERIAL GROWTH MEDIUM RECIPE

990 ml ultrapure water
Add:

Ingredients	Amount (g)
Casein hydrolysate	2
NH_4Cl	1
Glycerol	6
NaCl	23.926
Na_2SO_4	4.008
KCl	0.677
$NaHCO_3$	0.196
KBr	0.098
$StCl_2 \times 6H_2O$	0.024
H_3BO_3	0.026
NaF	0.003

Next: Chelex treatment
Add 25 g of Chelex to 1 L medium and stir for 1 h.
Separate Chelex from medium by using acid washed lass column.
Collect eluate in acid washed Ultra Yield bottles.

Add: 10.83 g $MCl_2 \times 6H_2O$ (iron free)
1.519 g $CaCl_2 \times 2H_2O$ (iron free)

Adjust pH to 7.6
Add 1 ml of supplement solution*
Fill up to 1 L
Autoclave sterilization

*Supplement solution

Ingredients	Amount/Volume
25% HCl	13.0 mL
Titriplex-(III) (Na_2EDTA)	5.2 g
$CoCl_2 \times 6H_2O$	190 mg
$ZnSO_4 \times 7H_2O$	144 mg
$MnCl_2 \times 4H_2O$	100 mg
$Na_2MoO_4 \times 2H_2O$	36 mg
H_3BO_3	30 mg
$NiCl_2 \times 6H_2O$	24 mg
$CuCl_2 \times 2H_2O$	2 mg
Ultrapure water	1000 mL

SALINE AQUEOUS MATRIX RECIPE

990 mL of ultrapure water
Add:

Ingredients	Amount/Volume
NaCl	20.8 g
$MCl_2 \times 6H_2O$	9.6 g
Na_2SO_4	3.5 g
$CaCl_2$ (1 M)	9 mL
KCl	0.6 g

Adjust pH to 8.0 – 8.2
Add 1 ml of supplement solution*
Fill up to 1 L

DATA & RESULTS

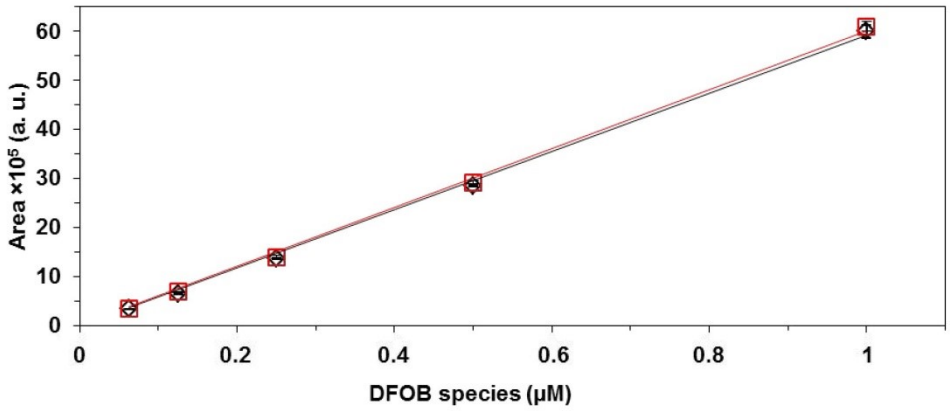

Fig. S2 Calibration of (black diamonds) FOB ($[M+H]^+$ = $[^{56}Fe(III)\ C_{25}H_{46}N_6O_8]^+$, m/z 614) and (red squares) AlOB ($[M+H]^+$ = $[^{27}Al(III)\ C_{25}H_{46}N_6O_8]^+$, m/z 585) in ultrapure water. FOB: LOD = 56.451 nmol L^{-1}; LOQ = 112.902 nmol L^{-1}; R^2 = 0.9997; N = 5. AlOB: LOD = 52.118 nmol L^{-1}; LOQ = 104.235 nmol L^{-1}; R^2 = 0.9997; N = 5. Limit of detection (LOD) and limit of quantification (LOQ) were calculated according to DIN standard 32645. Three different calibrations were prepared and average area value was used for calculations.

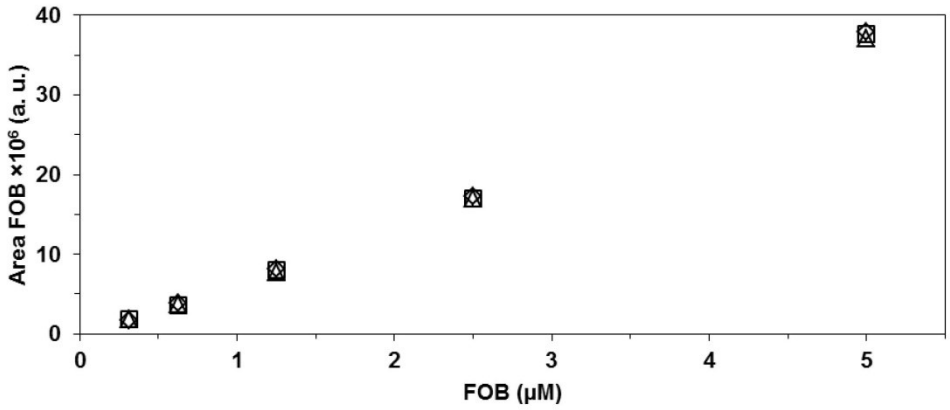

Fig. S3 Calibration of FOB ($[M+H]^+$ = $[^{56}Fe(III)\ C_{25}H_{46}N_6O_8]^+$, m/z 614) in saline aqueous matrix (diamonds), (squares) neutralized Eluent 7 (squares) and in ultrapure water (triangles).

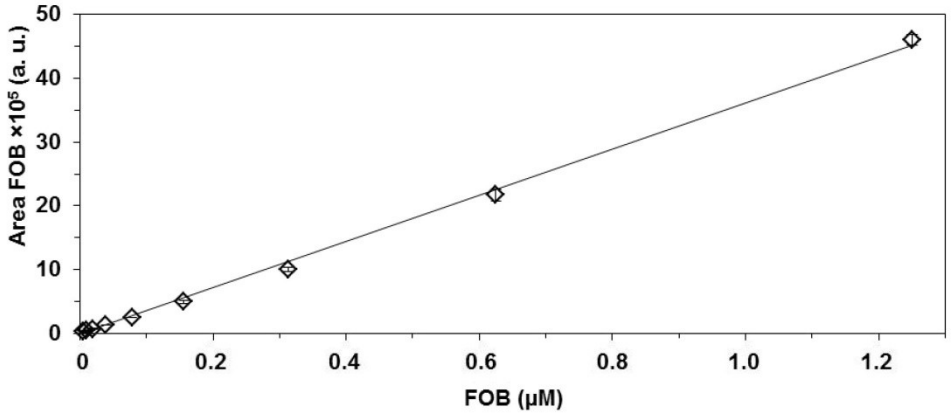

Fig. S4 Calibration of FOB ($[M+H]^+$ = $[^{56}Fe(III)\ C_{25}H_{46}N_6O_8]^+$, m/z 614) in ultrapure water used for quantification of method development and bacterial processing experiments. LOD = 56.572 nmol L^{-1}; LOQ = 113.144 nmol L^{-1}; R^2 = 0.9992; N = 9. Limit of detection (LOD) and limit of quantification (LOQ) were calculated according to DIN standard 32645. Three different calibrations were prepared and average area value was used for calculations.

Table S1 Adsorption efficiency of DFOB before eluent optimization experiments

Adsorption efficiency[a] (%)			Experiment
Triplicate 1	Triplicate 2	Triplicate 3	
99.7	99.6	99.8	Used for elution experiment with E1
99.4	99.8	99.6	Used for elution experiment with E2
99.4	96.4	99.3	Used for elution experiment with E3
99.3	99.4	99.5	Used for elution experiment with E4
99.8	99.1	99.6	Used for elution experiment with E5
99.8	99.6	99.6	Used for elution experiment with E6
99.8	99.4	99.9	Used for elution experiment with E7
-0.7 (FOB)	0.4 (FOB)	0.3 (FOB)	Used for elution experiment with E7

(a) Adsorption efficiency is defined as the ratio of AlOB and FOB concentration detected in the supernatant decreased to the AlOB and FOB concentration in the initial solution before extraction expressed in %. Supernatants and aliquots of initial solution were spiked with $FeCl_3$ before LC-HRMS measurement (Section: Standardized siderophore adsorption).

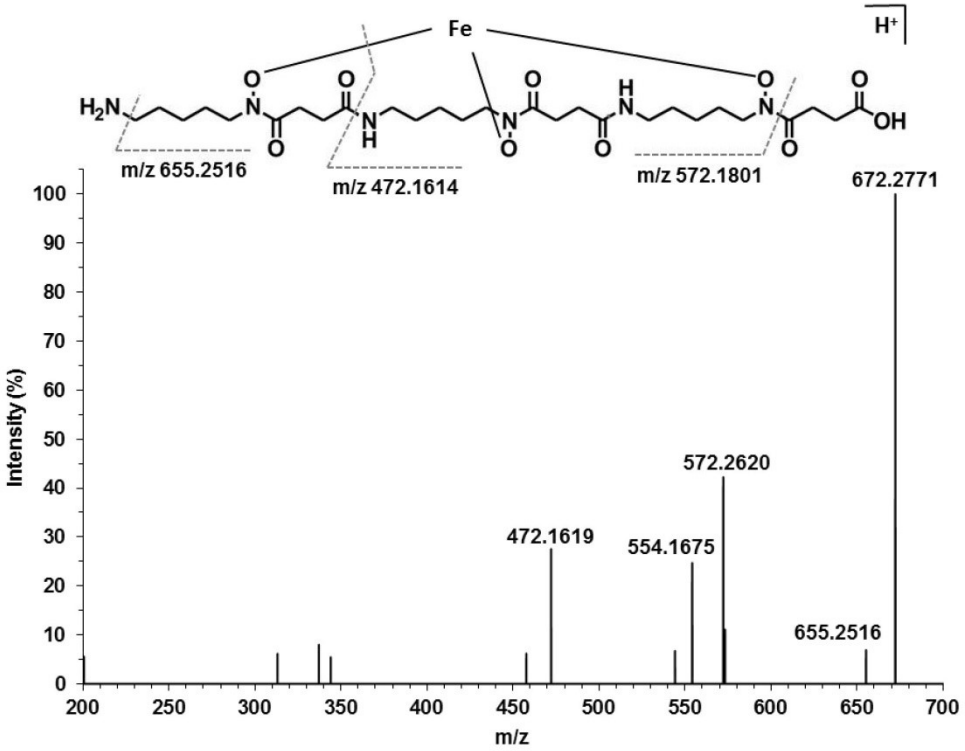

Fig. S5 MS^2 spectra and structure of FOG1 ($[M+H]^+ = [^{56}Fe(III)\ C_{27}H_{48}N_6O_{10}]^+$, m/z 672) showing the main cleavages accounting for product ions observed (grey dotted lines) (similar to results of Mawji et al.[1]). Desaturation/proton removal sites are general and will need further evaluation for exact determination of location (according to Sidebottom et al.[2]).

Table S2 Theoretical and measured m/z and corresponding sum formula of FOG1 (m/z 672, MS^2).

Measured m/z $[M+H]^+$	Theoretical m/z $[M+H]^+$	Δppm	Sum formula $[M+H]^+$
472.16193	472.16149	0.93	$C_{18}H_{32}O_7N_4Fe$
554.16748	554.16697	0.81	$C_{22}H_{34}O_9N_4Fe$
572.26202	572.26154	0.84	$C_{23}H_{44}O_7N_6Fe$
655.25159	655.25104	0.85	$C_{27}H_{45}O_{10}N_5Fe$
672.27710	672.27759	0.37	$C_{27}H_{48}O_{10}N_6Fe$

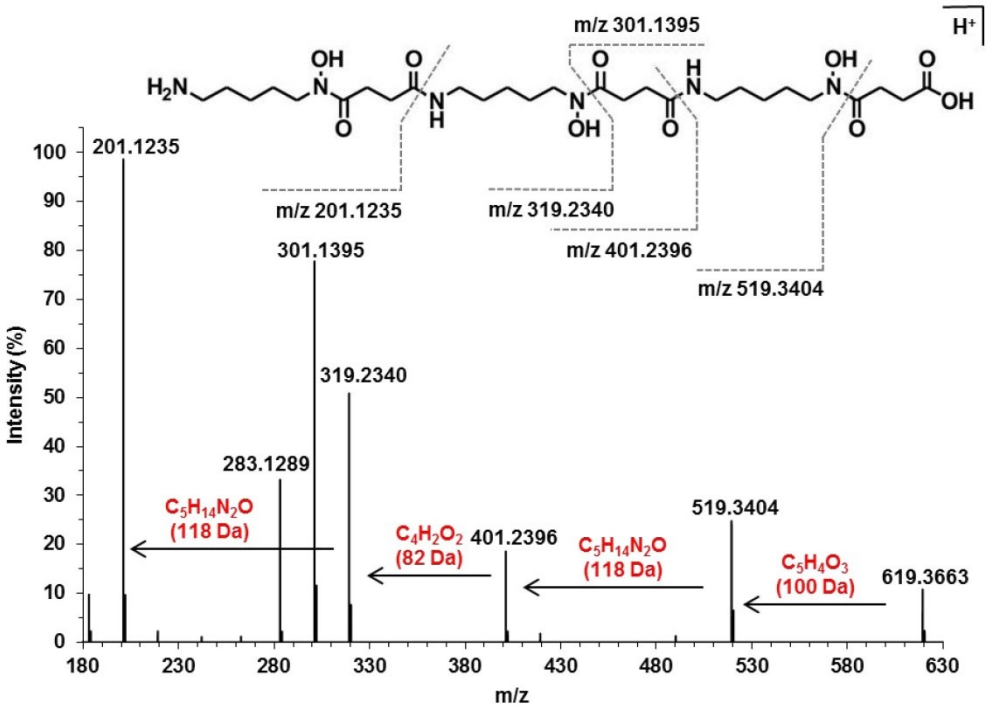

Fig. S6 MS^2 spectra and structure of DFOG1 ($[M+H]^+ = [C_{27}H_{51}O_{10}N_6]^+$, m/z 619), showing the main cleavages accounting for product ions observed (grey dotted lines) (compare to Feistner et al.[3,4]). Desaturation/proton removal sites are general and will need further evaluation for exact determination of location (according to Sidebottom et al.[2]).

Table S3 Theoretical and measured m/z and corresponding sum formula of DFOG1 (m/z 619, MS^2).

Measured m/z $[M+H]^+$	Theoretical m/z $[M+H]^+$	Δppm	Sum formula $[M+H]^+$
201.12346	201.12337	0.44	$C_9H_{17}O_3N_2$
283.12888	283.12885	0.09	$C_{13}H_{19}O_5N_2$
301.13947	301.13941	0.17	$C_{13}H_{21}O_6N_2$
319.23401	319.23398	0.08	$C_{14}H_{31}O_4N_4$
401.23962	401.23946	0.41	$C_{18}H_{33}O_6N_4$
519.34040	519.35007	0.63	$C_{23}H_{47}O_7N_6$
619.36633	619.36612	0.34	$C_{27}H_{51}O_{10}N_6$

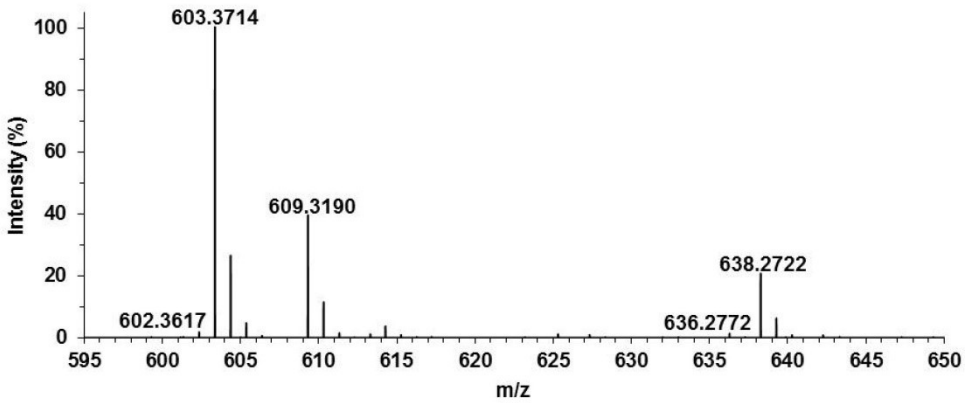

Fig. S7 MS spectra of TiO_2 E7 eluate at 2.82 min.

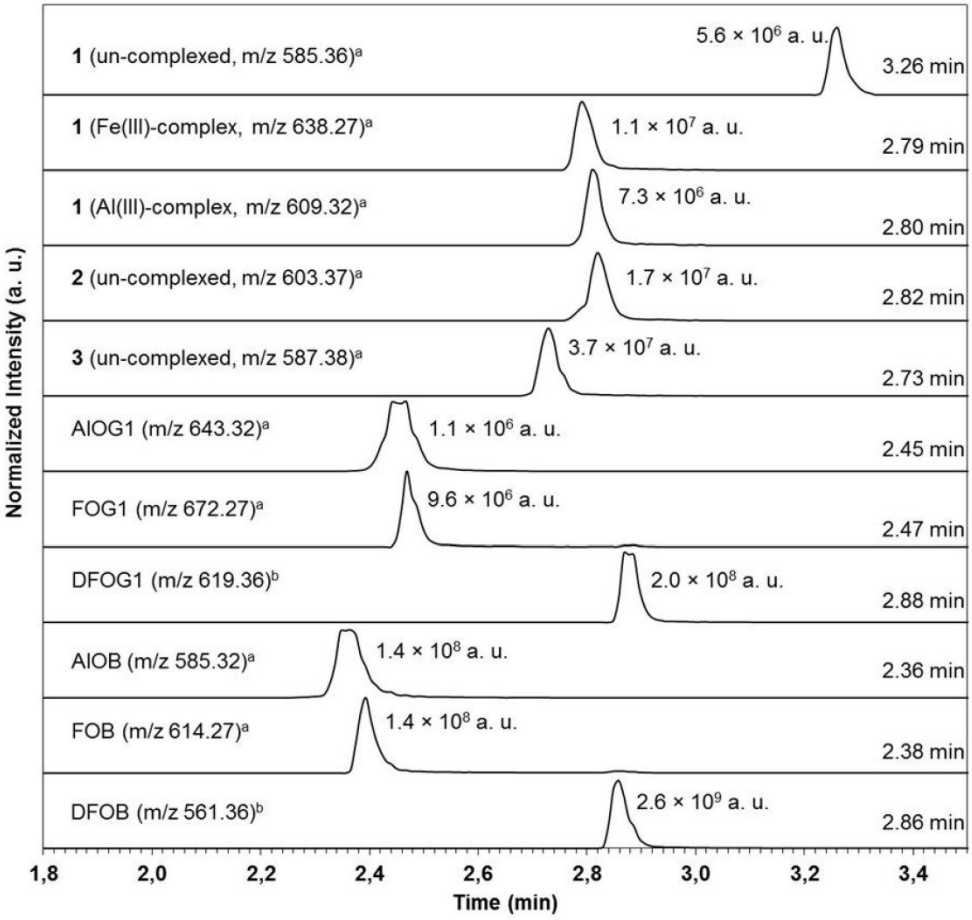

Fig. S8 Stacked normalized extracted ion chromatograms (nominal mass ± 0.01 Da) of peaks detected in (a) the $FeCl_3$ saturated TiO_2 E7 eluate (see also Figure 5D) and (b) the raw bacterial culture supernatant.

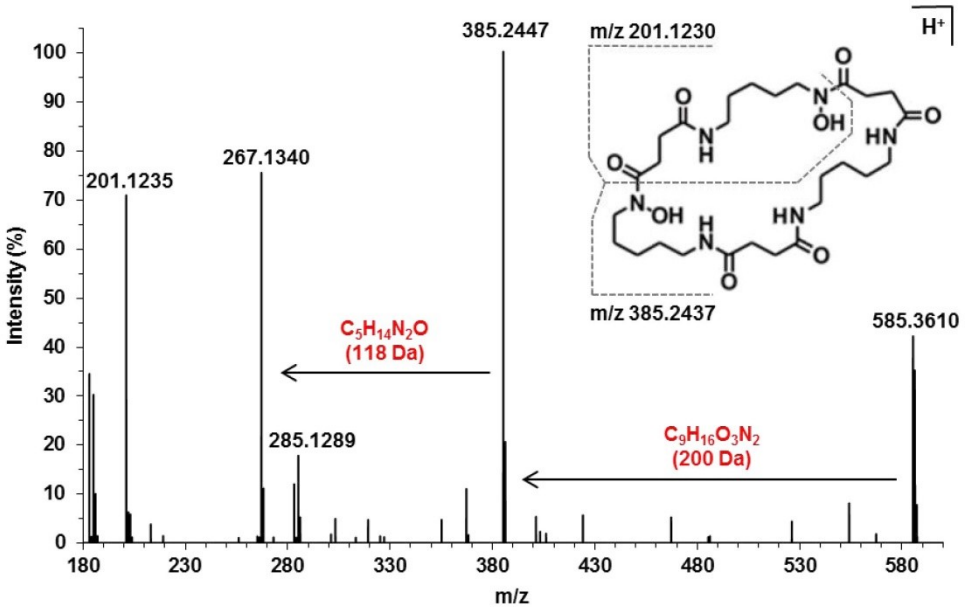

Fig. S9 MS^2 spectra and the proposed structure of **1** ($[M+H]^+$ = $[C_{27}H_{49}O_8N_6]^+$, m/z 585), showing the main cleavages accounting for product ions observed (grey dotted lines) Desaturation/proton removal sites are general and will need further evaluation for exact determination of location (according to Sidebottom et al.[2]).

Table S4 Theoretical and measured m/z and corresponding sum formula of 1 (m/z 585, MS^2).

Measured m/z $[M+H]^+$	Theoretical m/z $[M+H]^+$	Δppm	Sum formula $[M+H]^+$
201.12347	201.12337	0.52	$C_9H_{17}O_3N_2$
267.13400	267.13393	0.26	$C_{13}H_{19}O_4N_2$
283.12894	283.12885	0.31	$C_{13}H_{19}O_5N_2$
285.14456	285.14450	0.22	$C_{13}H_{21}O_5N_2$
385.24469	385.24455	0.37	$C_{18}H_{33}O_5N_4$
585.36096	585.36064	0.55	$C_{27}H_{49}O_8N_6$

Table S5 Theoretical m/z and corresponding sum formula of DFOE (m/z 601) and expected fragment ions.[3,4]

Theoretical m/z $[M+H]^+$	Sum formula $[M+H]^+$
201.12337	$C_9H_{17}O_3N_2$
283.12885	$C_{13}H_{19}O_5N_2$
301.13941	$C_{13}H_{19}O_6N_2$
401.23946	$C_{18}H_{33}O_6N_4$
601.35555	$C_{27}H_{49}O_9N_6$

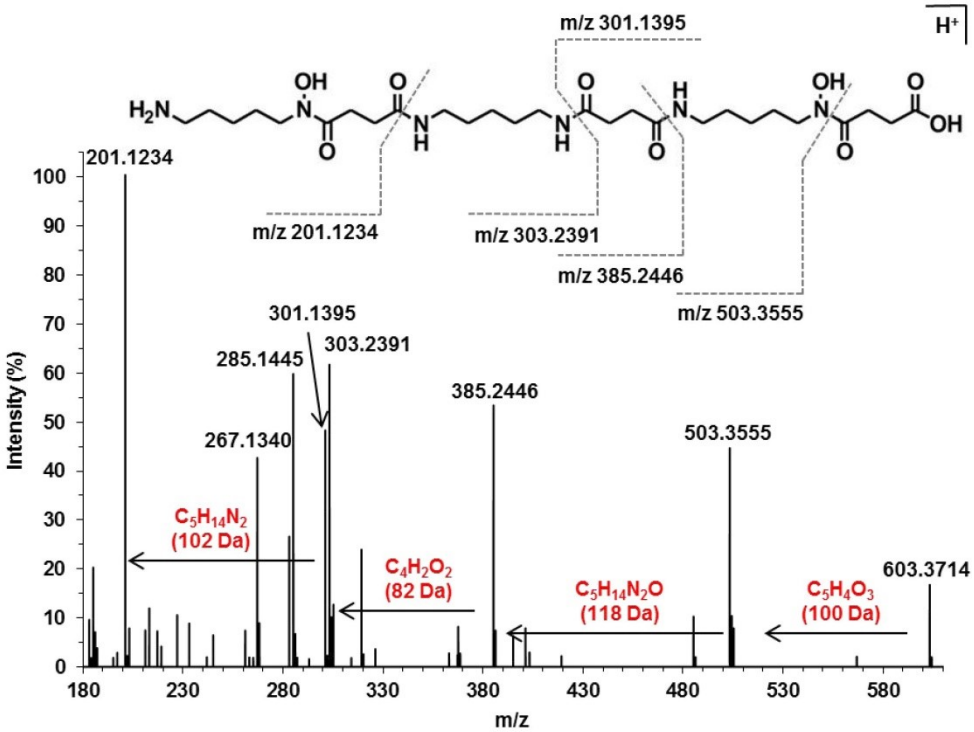

Fig S10 MS^2 spectra and proposed structure of **2** ($[M+H]^+ = [C_{27}H_{51}O_9N_6]^+$, m/z 603), showing the main cleavages accounting for product ions observed (grey dotted lines) Desaturation/proton removal sites are general and will need further evaluation for exact determination of location (according to Sidebottom et al.[2]).

Table S6 Theoretical and measured m/z and corresponding sum formula of 2 (m/z 603, MS^2).

Measured m/z $[M+H]^+$	Theoretical m/z $[M+H]^+$	Δppm	Sum formula $[M+H]^+$
201.12344	201.12337	0.38	$C_9H_{17}O_3N_2$
267.13396	267.13393	0.09	$C_{13}H_{19}O_4N_2$
285.14452	285.1445	0.09	$C_{13}H_{21}O_5N_2$
301.13951	301.13941	0.34	$C_{13}H_{21}O_6N_2$
303.23910	303.23907	0.12	$C_{14}H_{31}O_3N_4$
385.24464	385.24455	0.25	$C_{18}H_{33}O_5N_4$
503.35549	503.35516	0.66	$C_{23}H_{47}O_6N_6$
603.37141	603.37120	0.35	$C_{27}H_{51}O_9N_6$

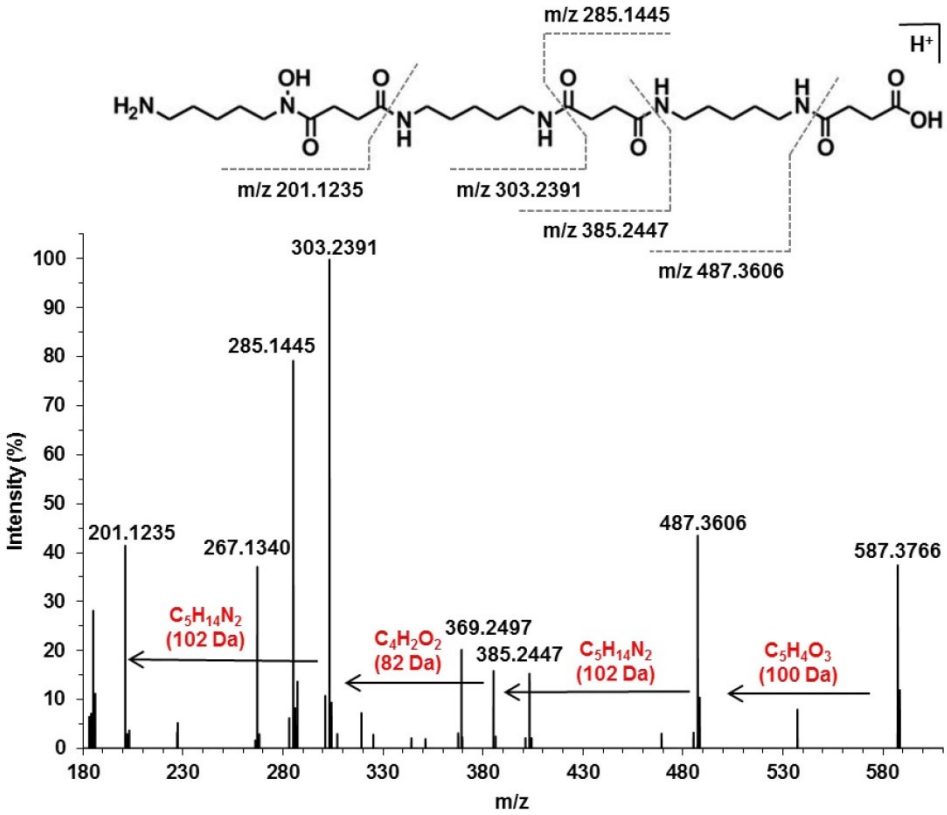

Fig. S11 MS² spectra and proposed structure of **3** ($[M+H]^+ = [C_{27}H_{51}O_8N_6]^+$, m/z 587), showing the main cleavages accounting for product ions observed (grey dotted lines) Desaturation/proton removal sites are general and will need further evaluation for exact determination of location (according to Sidebottom et al.[2]).

Table S7 Theoretical and measured m/z and corresponding sum formula of 3 (m/z 587, MS²).

Measured m/z $[M+H]^+$	Theoretical m/z $[M+H]^+$	Δppm	Sum formula $[M+H]^+$
201.12347	201.12337	0.52	$C_9H_{17}O_3N_2$
267.13397	267.13393	0.14	$C_{13}H_{19}O_4N_2$
285.14453	285.1445	0.11	$C_{13}H_{21}O_5N_2$
303.23911	303.23907	0.12	$C_{14}H_{31}O_3N_4$
369.24973	369.24963	0.25	$C_{18}H_{33}O_4N_4$
385.24469	385.24455	0.37	$C_{18}H_{33}O_5N_4$
487.36063	487.36025	0.64	$C_{23}H_{47}O_5N_6$
587.37659	587.37629	0.51	$C_{27}H_{51}O_8N_6$

Table S8 TiO_2 NPs and IMAC binding capacities for SPE from saline aqueous matrices.

Method	Analyte	Binding Capacity
TiO_2 NP	DFOB	15.7 ± 0.2 µmol/mg TiO_2[a]
TiO_2 NP	TMP	17.4 ± 0.9 nmol/mg TiO_2[5]
TiO_2 NP	TPP	27.5 ± 2.8 nmol/mg TiO_2[5]
TiO_2 NP	DFOB	8.8 ± 0.1 µmol/mg TiO_2[b]
Ni(II)-IDA	DFOB	3.5 µmol/mL resin[6,7]
Yb(III)-BEDTRA	DFOB	8.0 µmol/mL resin[6]

TMP = Thiamine monophosphate; TPP = Thiamine pyrophosphate; (a) calculated from Figure 3 according to Krenkova et al.[8]; (b) calculated from Figure 3 according to Gu et al.[6]

Table S9 Summary of neutral losses with corresponding sum formula, parent ions and parent ion structure feature.

Neutral loss / Da	Sum formula [M]	Parent ion $[M+H]^+$	Parent ion structure
82	$C_4H_2O_2$	DFOG1 (m/z 619); **2** (m/z 603); **3** (m/z 587)	Linear
100	$C_5H_4O_3$	DFOG1 (m/z 619); **2** (m/z 603); **3** (m/z 587)	Linear
102	$C_5H_{14}N_2$	**2** (m/z 603); **3** (m/z 587)	Linear
118	$C_5H_{14}N_2O$	DFOG1 (m/z 619); **2** (m/z 603); **3** (m/z 587)	Linear
200	$C_9H_{16}N_2O_3$	DFOE (m/z 601); **1** (m/z 585)	Cyclic

REFERENCE

1 E. Mawji, M. Gledhill, P. J. Worsfold, E. P. Achterberg *Rapid Commun. Mass Spectrom.,* 2008, **22**, 2195–2202.
2 A. M. Sidebottom, J. A. Karty, E. E. Carlson *J. Am. Soc. Mass Spectrom.*, 2015, **26**, 1899–1902.
3 G. J. Feistner, D. C. Stahl, A. H. Gabrik, *Org. Mass Spectrom.* 1993, **28**, 163–175.
4 G. J. Feistner, L. L. Hsieh, *J. Am. Soc. Mass Spectrom*., 1995. **6**. 836–846.
5 S. Dziomba, A. Pawelec, K. Ciura, M. Dolegowska, A. Klimowska, W. Rodzaj, M. Guerrouache, B. Carbonnier and B. Wielgomas, *Microchem. J.*, 2019, **145**, 784–790.
6 J. Gu and R. Codd, *RSC Adv.*, 2015, **5**, 3443–3453.
7 N. Braich and R. Codd, *Analyst*, 2008, **133**, 877–880.

Supporting information: Selective purification of catecholate, hydroxamate and α-hydroxycarboxylate siderophores with Titanium Dioxide Affinity Chromatography

BACTERIAL GROWTH MEDIUM RECIPE

990 ml ultrapure water

Add:

Ingredients	Amount (g)
Casein hydrolysate	2
NH_4Cl	1
Glycerol	6
NaCl	23.926
Na_2SO_4	4.008
KCl	0.677
$NaHCO_3$	0.196
KBr	ND98
$StCl_2 \times 6H_2O$	ND24
H_3BO_3	ND26
NaF	ND03

Next: Chelex treatment

Add 25 g of Chelex to 1 L medium and stir for 1 h.

Separate Chelex from medium by using acid washed lass column.

Collect eluate in acid washed Ultra Yield bottles.

Add: 10.83 g $MCl_2 \times 6H_2O$ (iron free)
1.519 g $CaCl_2 \times 2H_2O$ (iron free)

Adjust pH to 7.6

Add 1 ml of supplement solution*

Fill up to 1 L

Autoclave sterilization

*Supplement solution

Ingredients	Amount/Volume
25% HCl	13.0 mL
Titriplex-(III) (Na_2EDTA)	5.2 g
$CoCl_2 \times 6H_2O$	190 mg
$ZnSO_4 \times 7H_2O$	144 mg
$MnCl_2 \times 4H_2O$	100 mg
$Na_2MoO_4 \times 2H_2O$	36 mg
H_3BO_3	30 mg
$NiCl_2 \times 6H_2O$	24 mg
$CuCl_2 \times 2H_2O$	2 mg
Ultrapure water	1000 mL

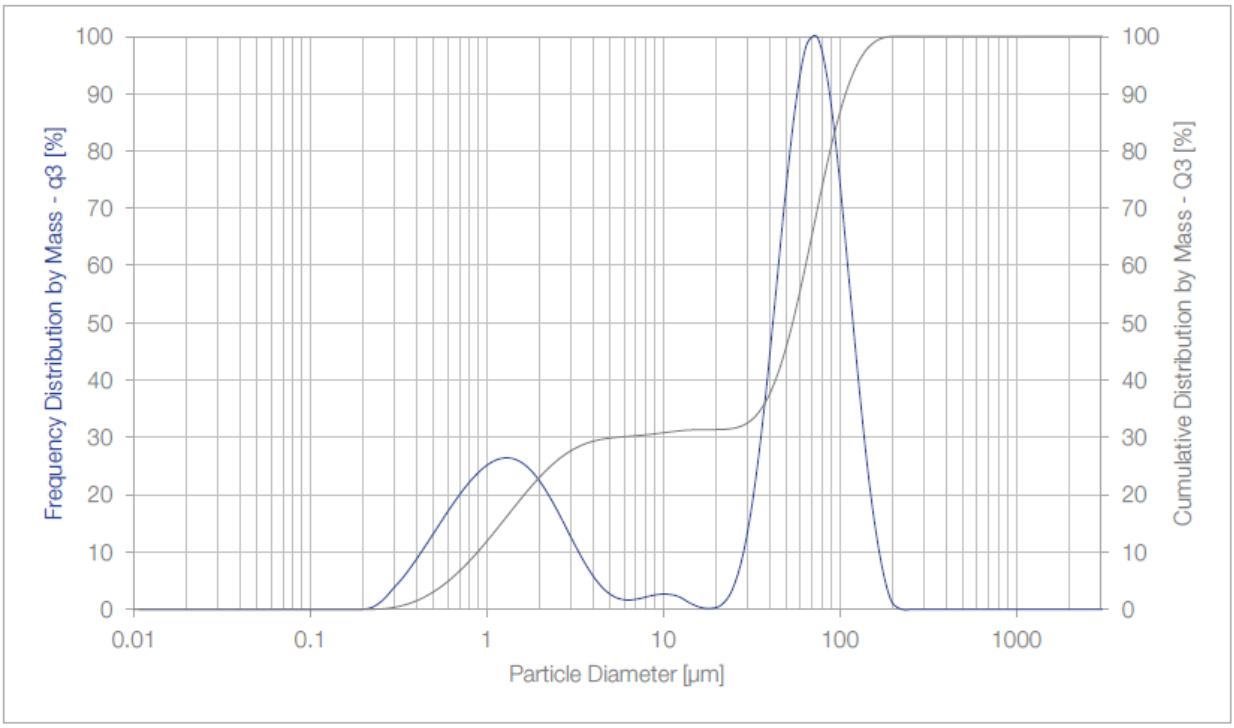

Parameter	Value	Unit
Distribution Type	mass-based	-
Median (d50)	54.092	µm
Mode	70.843	µm
Distribution Width (sLog)	0.93	-
< 0.2µm	0.00	%
> 0.6µm	95.17	%

Figure SI 1. Particle size distribution of grinded and sieved TiO_2 oven clinker according to BET (Measurements performed by KRONOS INTERNATIONAL, Inc.).

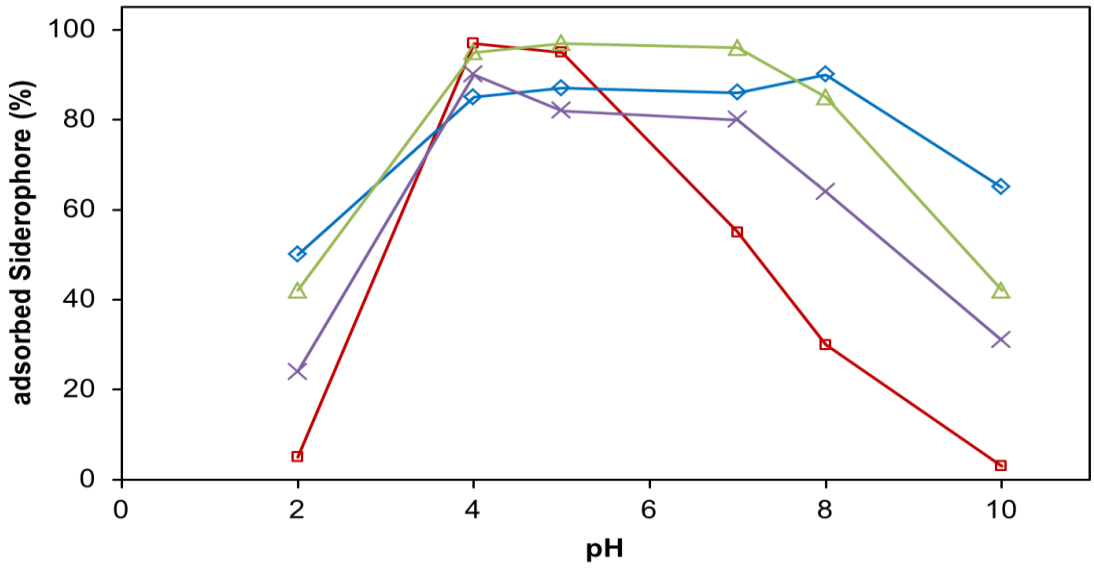

Figure SI 2. Disperse solid phase extraction of DFOB (blue diamonds), VF (red squares), PB (green triangles) and WBA (purple crosses) using 10 µM siderophore concentrations in 0.5 M NaCl at different pH values with 100 mg TiO_2.

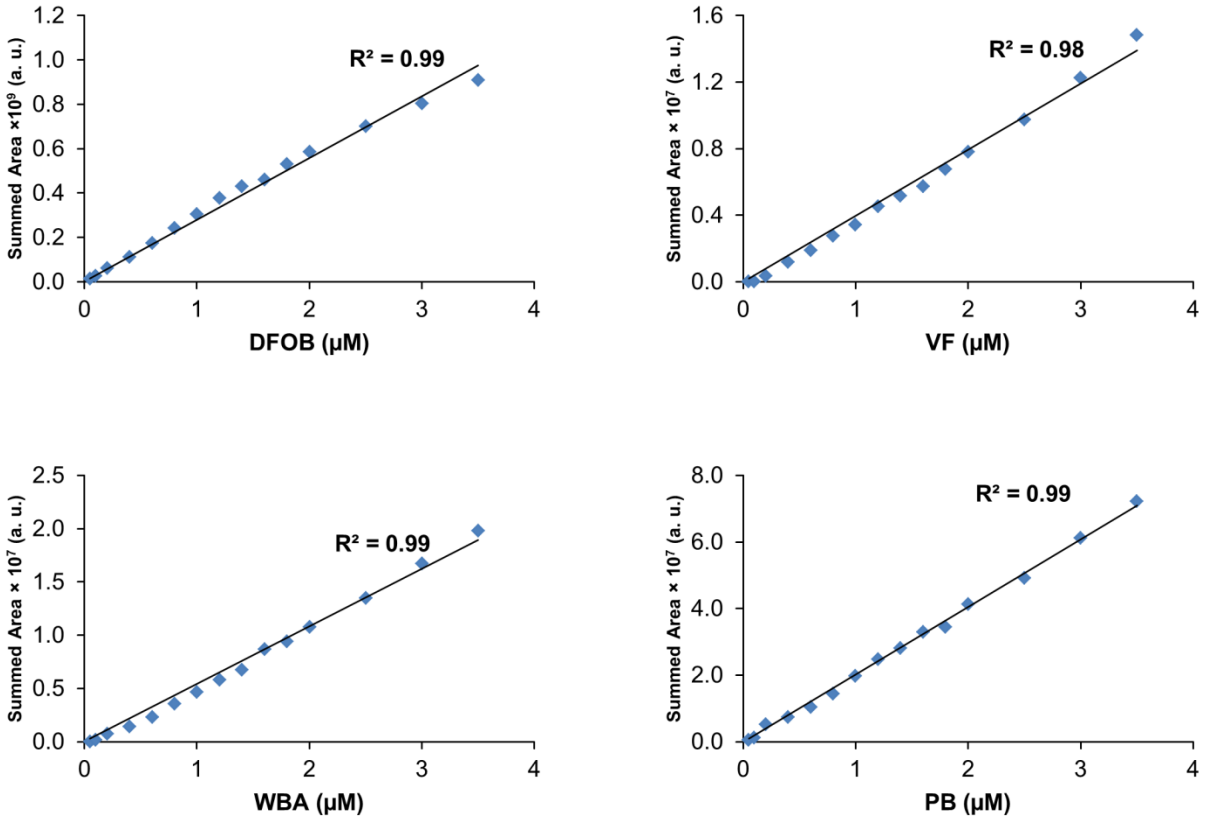

Figure SI 3. Calibration curves (Injection volume = 10 µL) of WBA using the summed area of apo-WBA ($[M+H]^+$ = $C_{20}H_{35}N_2O_{10}$, *m/z* 463.23) and Fe(III)-WBA , ($[M+H]^+$ = $C_{20}H_{32}N_2O_{10}Fe$, *m/z* 516.14), PB using the summed area of the singly ($[M+H]^+$ = $C_{34}H_{51}N_6O_{11}$, *m/z* 719.36) or doubly protonated apo-PB ($[M+2H]^{2+}$ = $C_{34}H_{52}N_6O_{11}$, *m/z* 360.18), VF using the summed area of apo-VF ($[M+H]^+$ = $C_{16}H_{23}N_2O_{12}$, *m/z* 435.13) and Fe(III)-VF ([M+H]+ = $C_{16}H_{20}N_2O_{12}Fe$, *m/z* 488.04), and DFOB using the summed area of the free ligand ($[M+H]^+$= $C_{25}H_{49}N_6O_8$, *m/z* 561.36) and of the complexes FOB ($[M+H]^+$ = $C_{25}H_{46}N_6O_8Fe$, *m/z* 614.27) and AlOB ($[M+H]^+$ = $C_{25}H_{46}N_6O_8Al$, *m/z* 585.32). Dilution were prepared in ES16 diluted 1:10 with counter solution 16, displaying the same composition than for the eluate samples. 10 µL were injected.

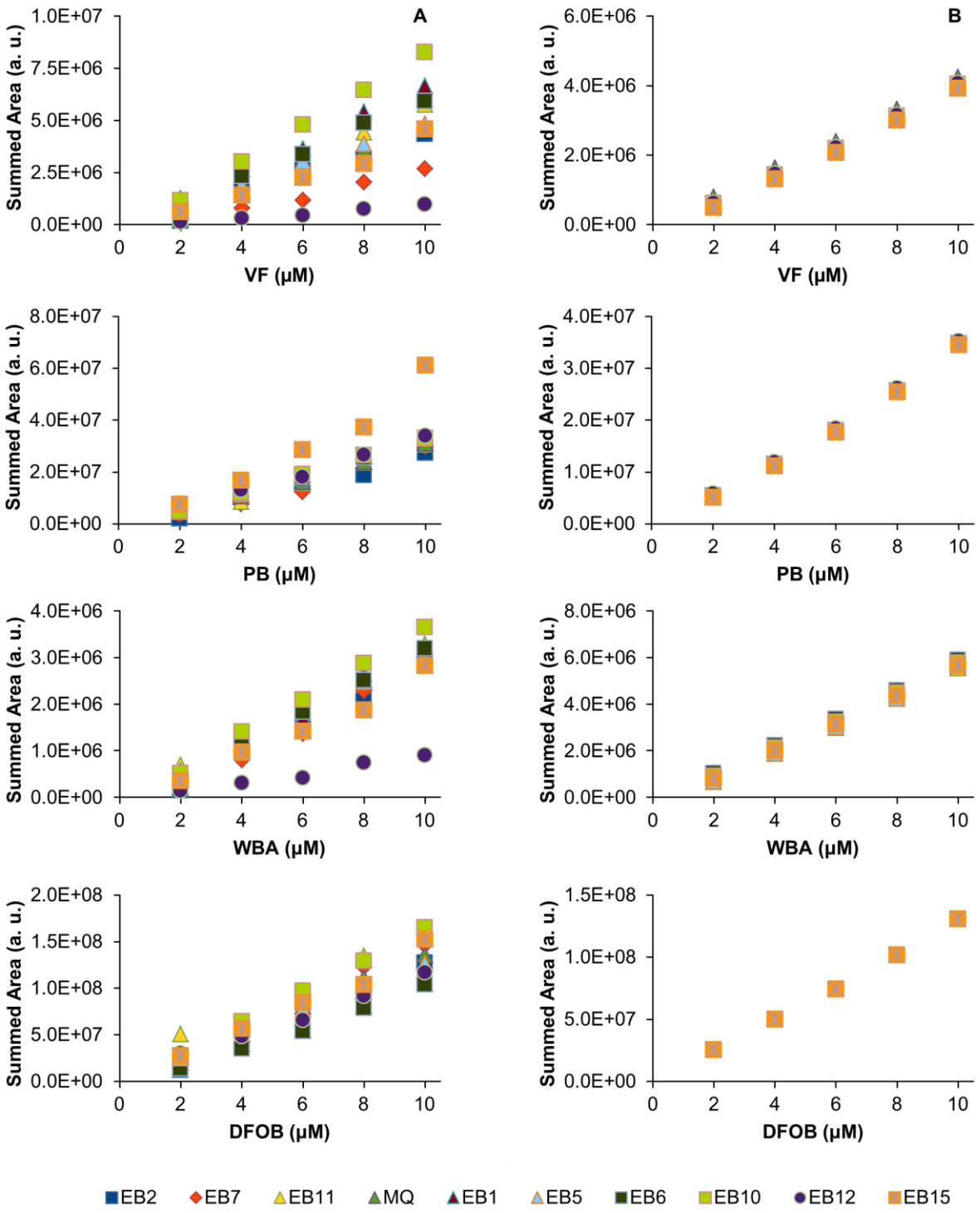

Figure SI 4. Calibration curves (Injection volume = 1 µL) of the four model siderophores in (A) pure elution solutions (Alkaline elution solutions were neutralized with conc. HCl prior to preparation of dilutions) and in (B) elution solutions diluted with corresponding counter solution (see Table SI 2). Summed areas were determined similar to the calibration shown in Figure SI 3.

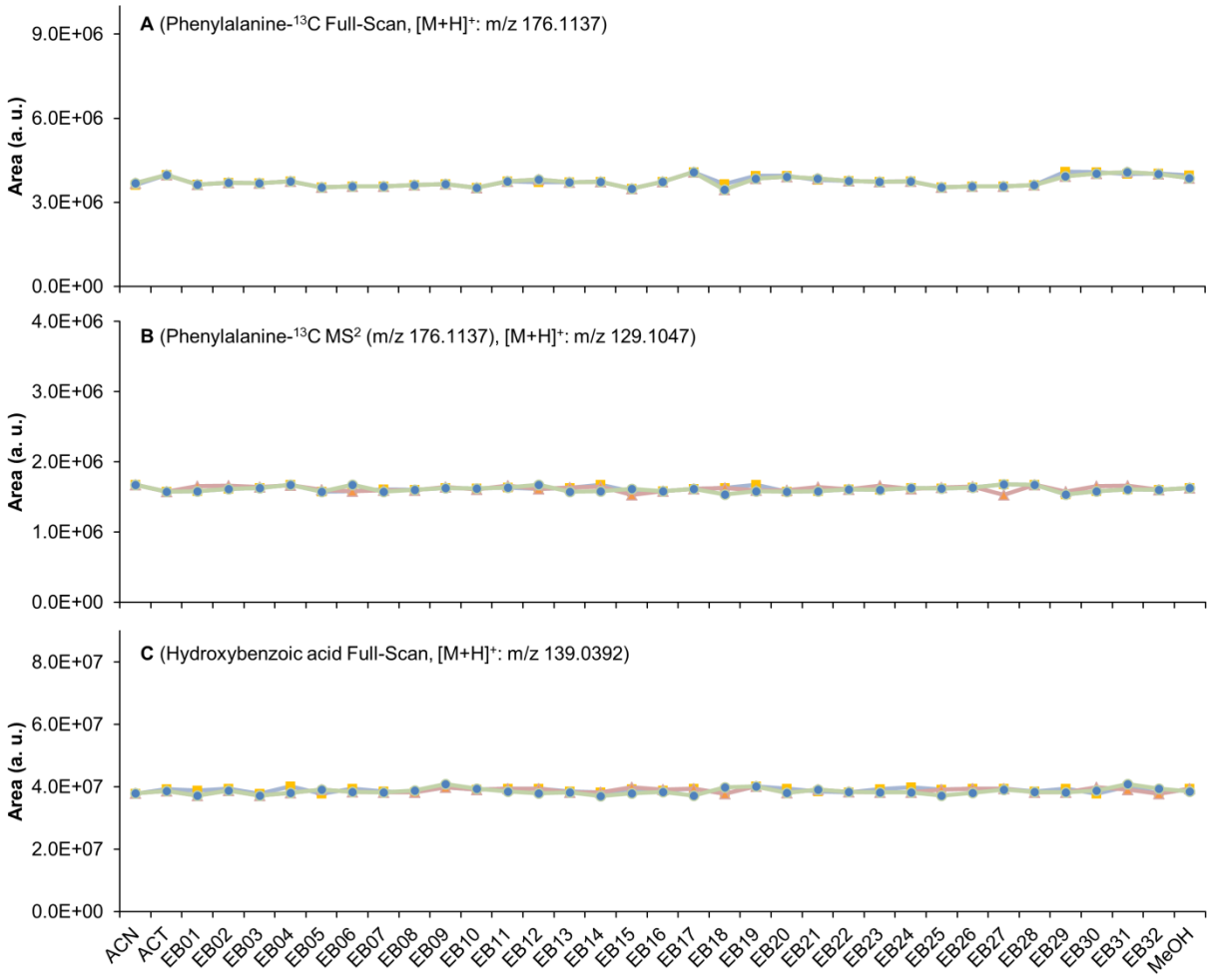

Figure SI 5. Comparison of the determined areas of the internal standards phenylalanine-^{13}C and hydroxybenzoic acid in measured elution solutions samples. Three different colors symbolize the triplicates.

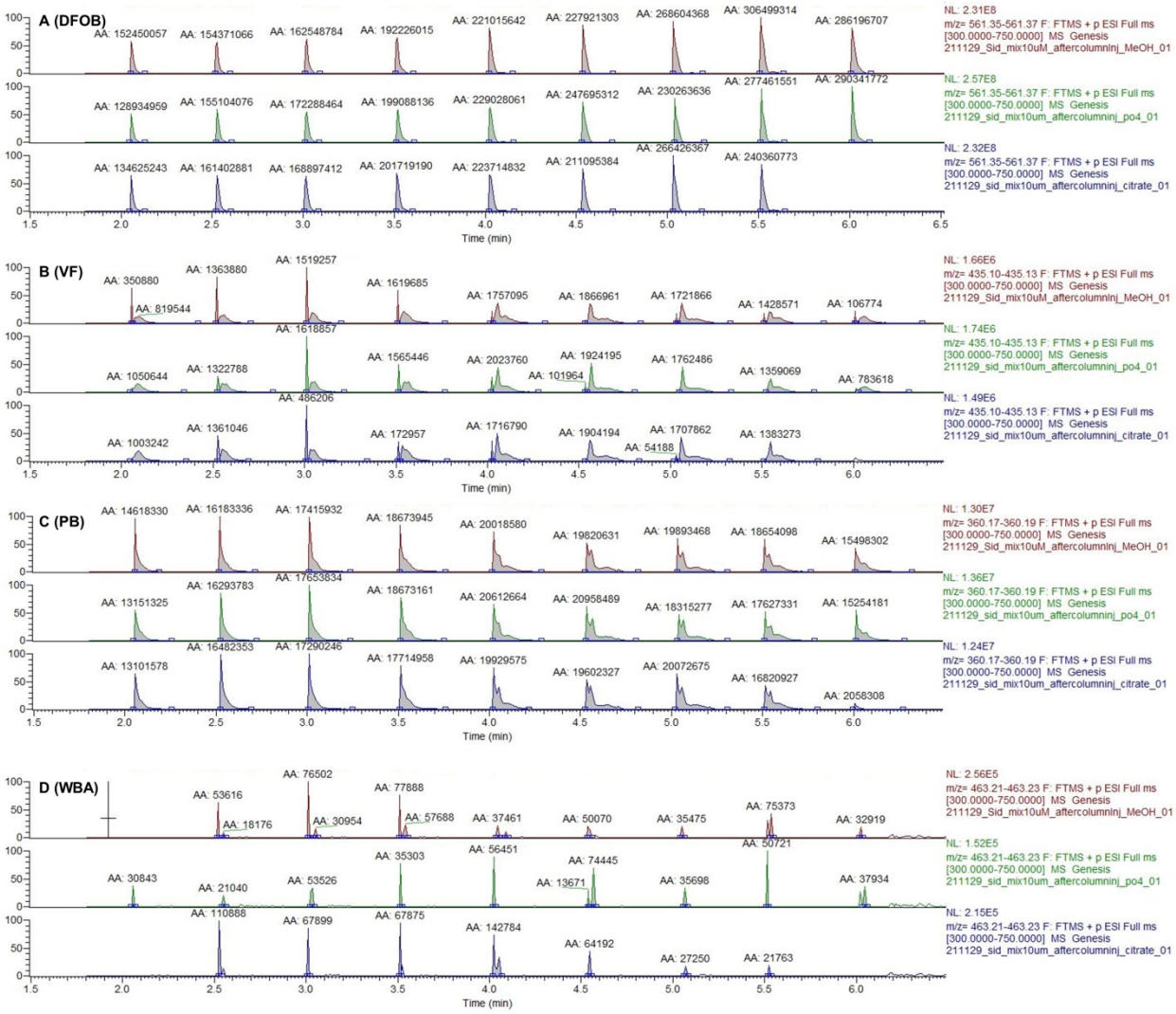

Figure SI 6. Investigation of possible matrix effect by phosphate and citrate. ES3 (0.5 M NaH_2PO4, pH 2.4, green), ES10 (20% citric acid, blue) and methanol (red) were injected as samples before the column, the four model siderophores DFOB, VF, PB and WBA (in ultrapure water) were injected repeatedly after column to monitor matrix effects of the buffer components. The gradient used for this measurement was the same as for all measurements (see Chapter 3.2.2).

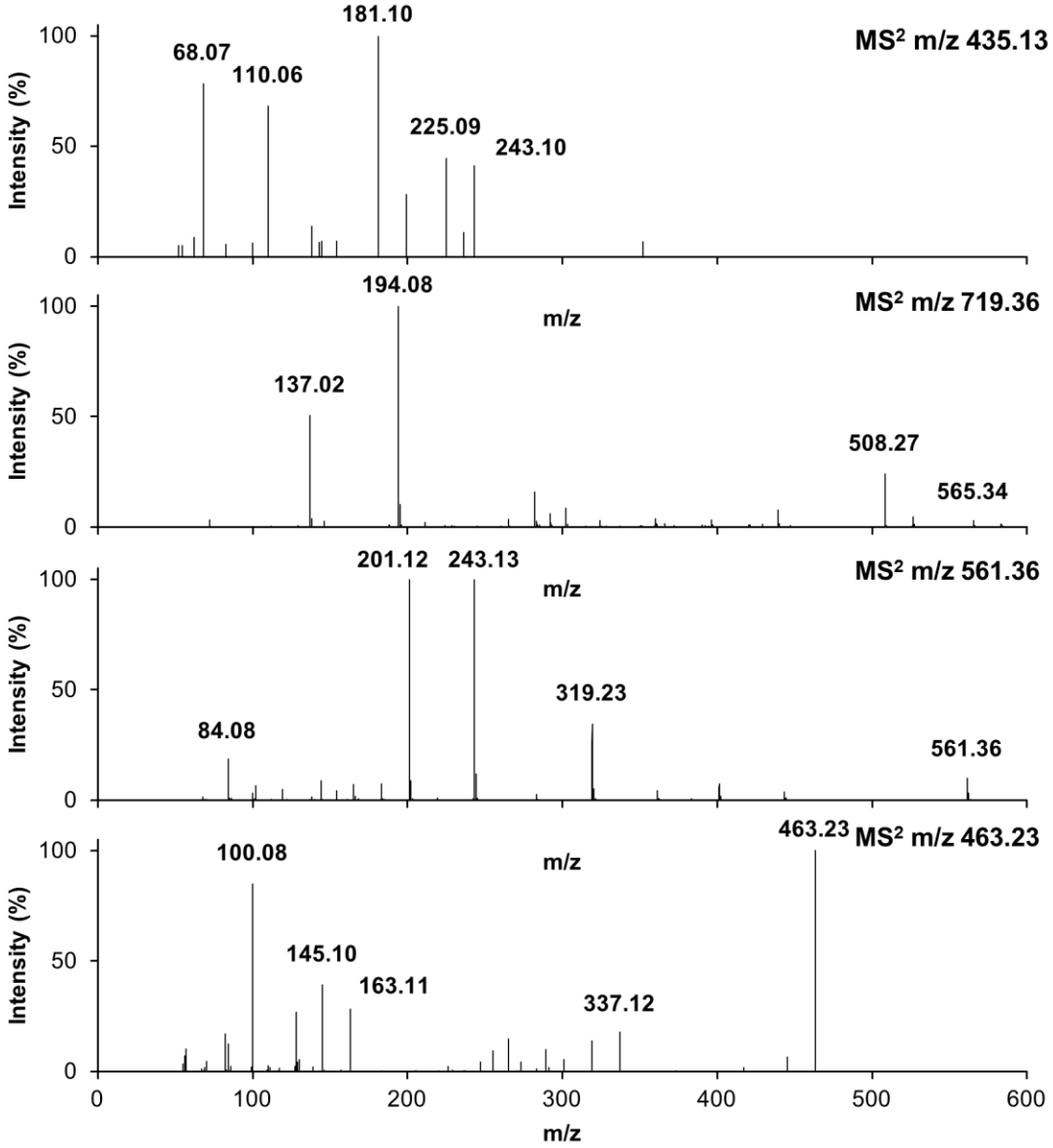

Figure SI 7. MS² spectra of apo-VF ([M+H]⁺ = $C_{16}H_{23}N_2O_{12}$, *m/z* 435.13), apo-PB ([M+H]⁺ = $C_{34}H_{51}N_6O_{11}$, *m/z* 719.36), DFOB ([M+H]⁺= $C_{25}H_{49}N_6O_8$, *m/z* 561.36) and apo-WBA ([M+H]⁺ = $C_{20}H_{35}N_2O_{10}$, *m/z* 463.23).

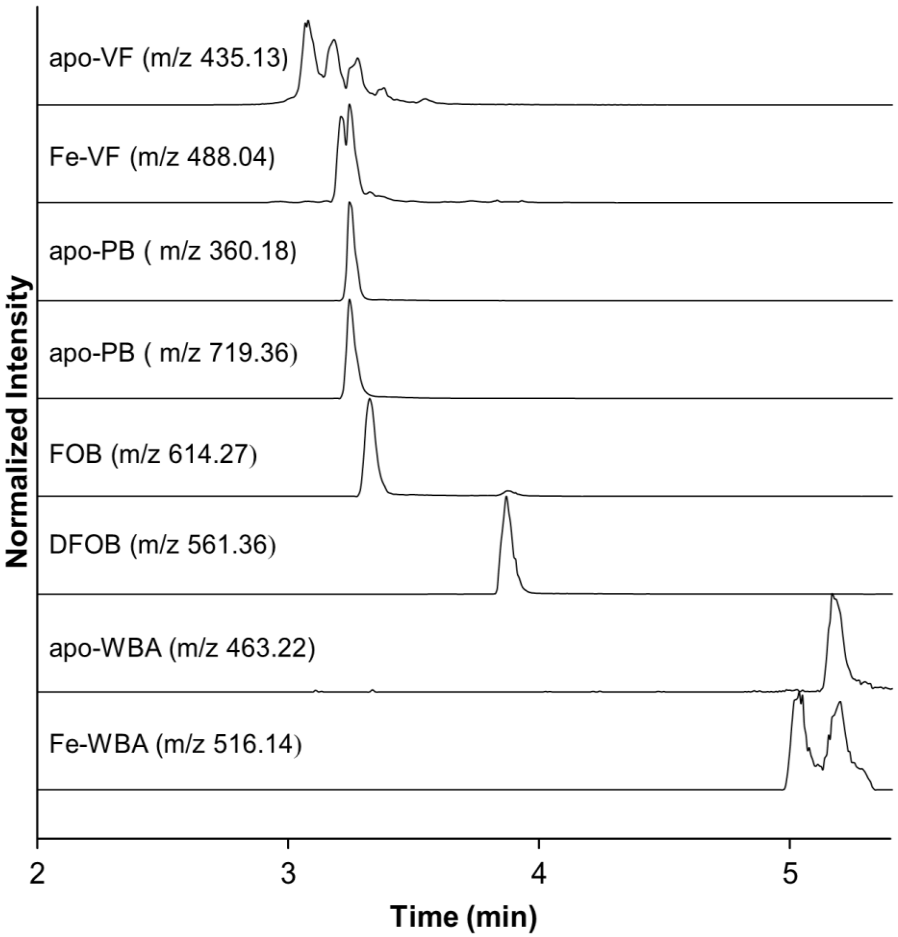

Figure SI 8. Stacked normalized extracted ion chromatograms (nominal mass ± 0.01 u) of siderophores and corresponding complexes used for method development.

Table SI 1. Summary of the siderophores and corresponding complexes used for method development.

Name	Charge / z	Measured m/z $[M+H]^+$	Theoretical m/z $[M+H]^+$	*Δppm*	Sum formula $[M+H]^+$
DFOB	1	561.36053	561.36064	-0.19	$C_{25}H_{49}N_6O_8$
FOB	1	614.27118	614.27211	-1.51	$C_{25}H_{46}N_6O_8Fe$
AlOB	1	585.31897	585.31870	0.46	$C_{25}H_{46}N_6O_8Al$
PB	1	719.36094	719.36103	-0.13	$C_{34}H_{51}N_6O_{11}$
PB	2	360.18398	360.18415	-0.47	$C_{34}H_{51}N_6O_{11}$
VF	1	435.12442	435.12455	-0.30	$C_{16}H_{23}N_2O_{12}$
Fe-VF	1	488.03580	488.03602	-0.54	$C_{16}H_{20}N_2O_{12}Fe$
WBA	1	463.22812	463.22862	-1.08	$C_{20}H_{35}N_2O_{10}$
Fe-WBA	1	516.13958	516.14009	-0.99	$C_{20}H_{32}N_2O_{10}Fe$

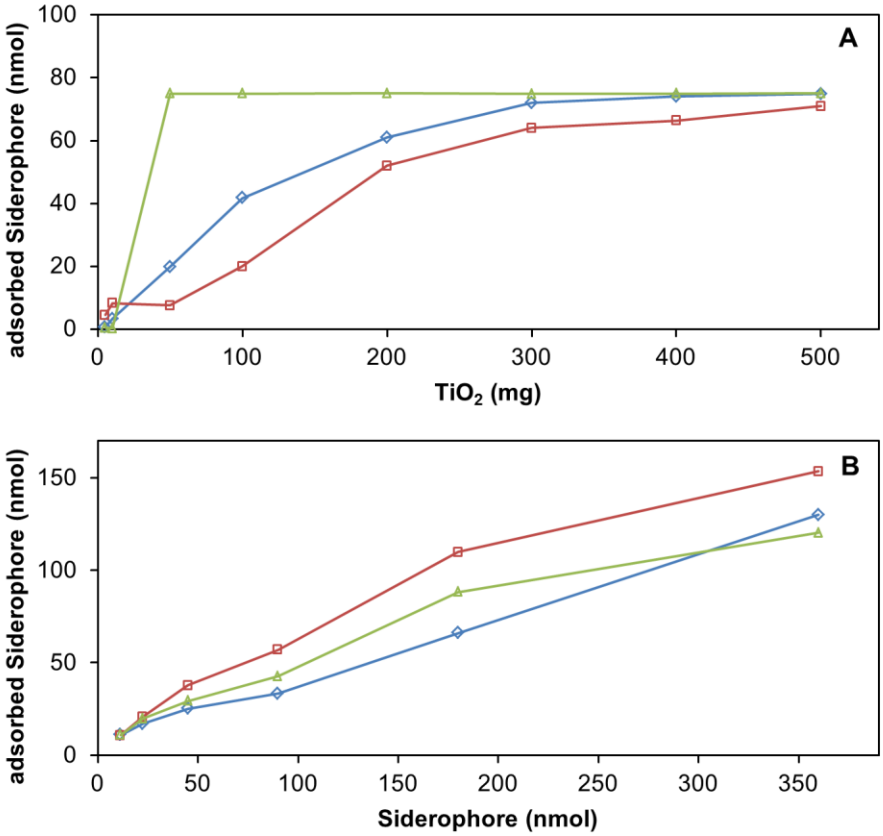

Figure SI 9. (A) Disperse solid phase extraction: Adsorption efficiency of either DFOB (blue diamond), VF (red squares) and PB (green triangles) from 1 mL (0.5 M NaCl, pH 4, siderophore concentration 75 µM) depending on TiO_2 sorbent amount. (B) 200 mg TiO_2-cartidges: Adsorption of DFOB, VF and PB from 1 mL (0.5 M NaCl, pH 4, with different amounts of siderophore standard) using 3 mL, 200 mg TiO_2 cartridges.

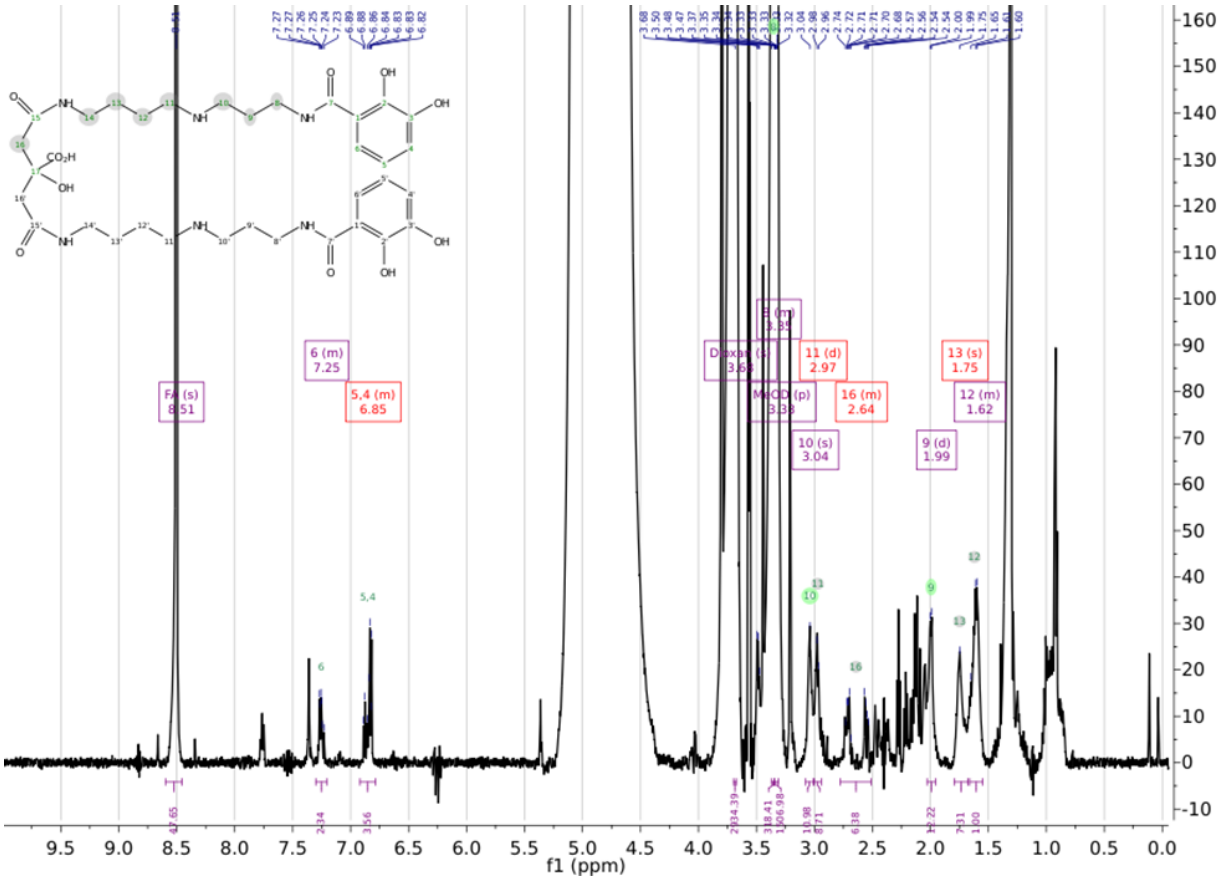

Figure SI 10. Proton spectra (600 MHz, 292 K) of Petrobactin (0.79 mM) in deuterated methanol containing dioxane as internal standard referenced to MeOD (3.33 ppm), signals used for quantification are marked with red multiplet-label.

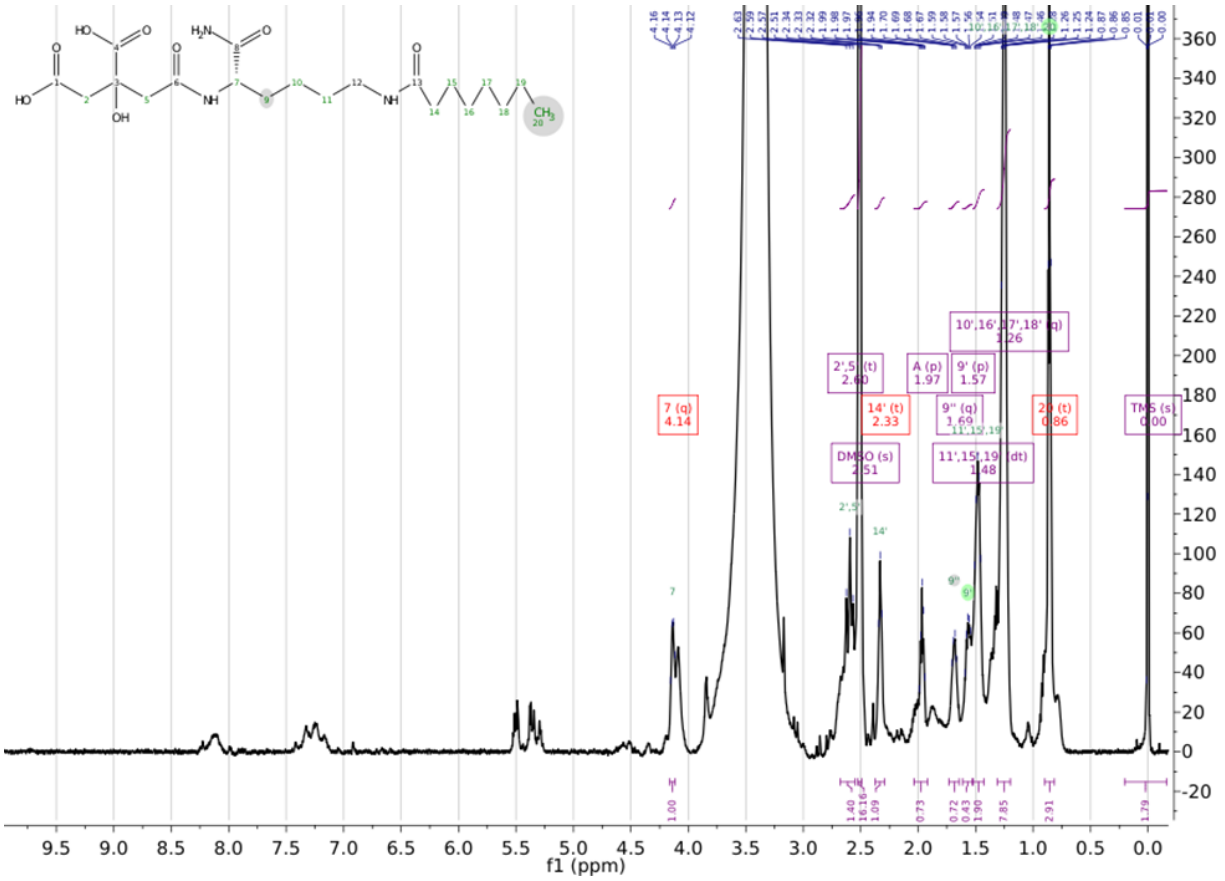

Figure SI 11. Proton spectra (600 MHz, 300 K) of Woodybactin A (0.5 M) in deuterated dimethyl sulfoxide containing tetramethylsilane as internal quantification and reference standard (ND0 ppm), signals used for quantification are marked with red multiplet-label.

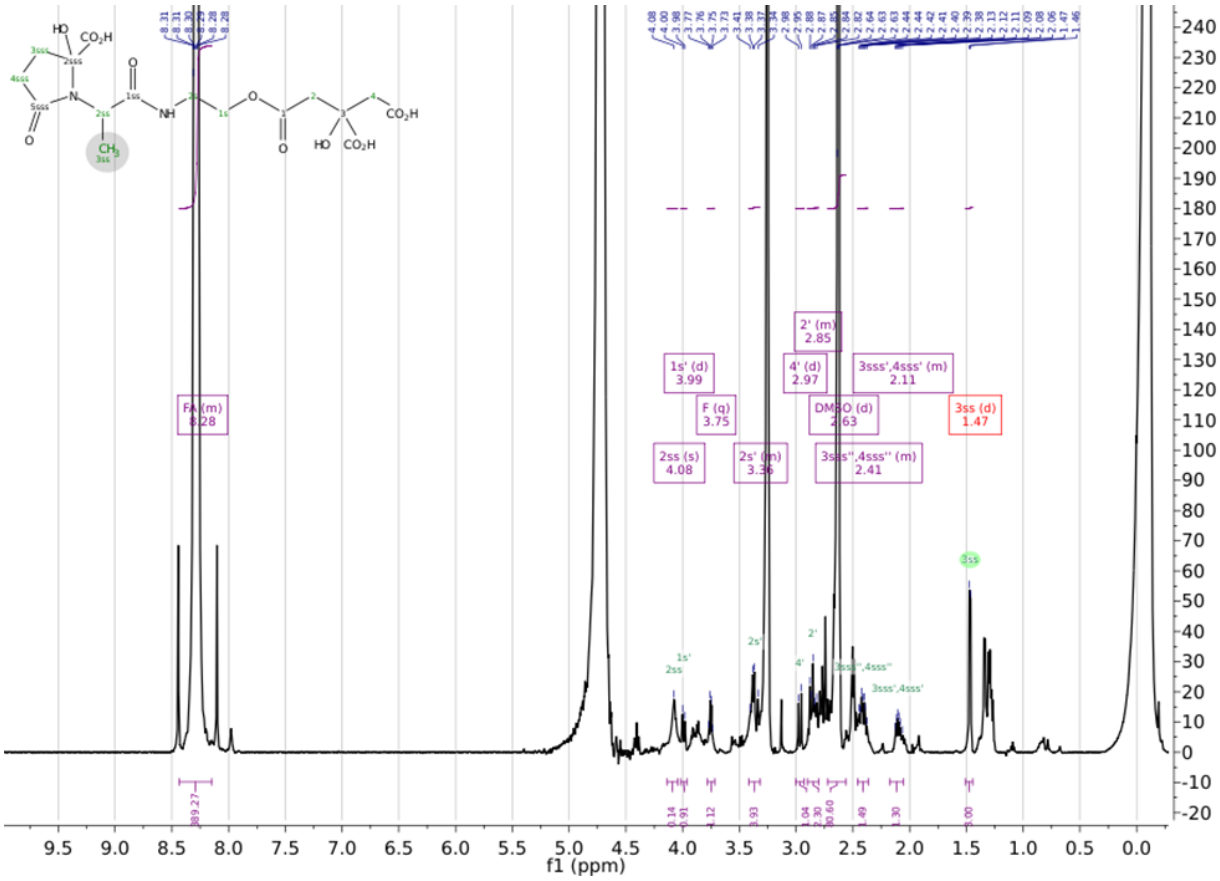

Figure SI 12. Proton spectra (600 MHz, 300 K) of Vibrioferrin (0.61 mM) in deuterated water containing dimethyl sulfoxide as internal standard referenced to TMS (ND0 ppm), signals used for quantification are marked with red multiplet-label.

Table SI 2. Counter solution assignment and composition.

Elution solution	Counter solution	NaH_2PO_4 [mM]	NaCl [mM]	Na_2SO4 [mM]	$CaCl_2$ [mM]	NH_3 [mM]	Citric acid [mM]
ES1	CS1	0.0	555.6	55.6	55.6	624.4	115.6
ES2	CS2	555.6	0.0	55.6	55.6	624.4	115.6
ES3	CS3	500.0	555.6	55.6	55.6	624.4	115.6
ES4	CS4	555.6	500.0	55.6	55.6	624.4	115.6
ES5	CS5	555.6	555.6	0.0	55.6	624.4	115.6
ES6	CS6	500.0	555.6	55.6	0.0	624.4	115.6
ES7	CS7	544.4	555.6	55.6	55.6	624.4	115.6
ES8	CS8	555.6	544.4	55.6	55.6	624.4	115.6
ES9	CS9	555.6	555.6	44.4	55.6	624.4	115.6
ES10	CS10	555.6	555.6	55.6	55.6	624.4	0.0
ES11	CS11	500.0	555.6	55.6	55.6	624.4	115.6
ES12	CS12	544.4	555.6	55.6	55.6	624.4	115.6
ES13	CS13	555.6	544.4	55.6	55.6	624.4	115.6
ES14	CS14	555.6	555.6	44.4	55.6	624.4	115.6
ES15	CS15	555.6	555.6	55.6	55.6	0.0	115.6
ES16	CS16	554.4	555.6	55.6	55.6	624.4	115.6
ES17	CS17	555.4	555.6	55.6	55.6	624.4	115.6
ES18	CS18	555.5	555.6	55.6	55.6	624.4	115.6
ES19	CS12						
ES20	CS12						
ES21	CS12						
ES22	CS12						
ES23	CS15						
ES24	CS15						
ES25	CS16						
ES26	CS16						
ES27	CS16						
ES28	CS16						
ES29	CS17						
ES30	CS17						
ES31	CS17						
ES32	CS17						

Supporting information: Siderophore identification in complex seawater extracts

Table SI 3. Organic solvents and buffers used for dilution of NSS pH2 and siderophore standards prior to TDAC

Organic solvents	Aqueous buffers
methanol	0.1 M phosphate, pH 10
ethanol	0.1 M phosphate, pH 9
tetrahydrofuran	0.1 M phosphate, pH 7
1-butanol	0.1 M phosphate, pH 4
2-propanol	0.1 M phosphate, pH 2.4
acetonitrile	0.5 M phosphate, pH 4
acetone	0.5 M phosphate, pH 2.4
dichloromethane	0.1 M sulphate, pH 4
chloroform	0.1 M sulphate, pH 2.4
ethyl acetate	0.5 M sulphate, pH 4
toluene	0.5 M sulphate, pH 2.4
n-hexane	0.1 M chloride, pH 4
	0.1 M chloride, pH 2.4
	0.5 M chloride, pH 4
	0.5 M chloride, pH 2.4

Table SI 4. Fragments and annotated sum formula of parent ions *m/z* 819.37, 870.28 and 872.28 in negative ionization mode

Measured *m/z*	Theoretical *m/z*	*Δppm*	Sum formula $[M-H]^-$
113.06069	113.06080	-1.00	$C_6H_9O_2$
125.06074	125.06080	-0.49	$C_7H_9O_2$
157.05046	157.05063	-1.09	$C_7H_9O_4$
175.06102	175.06120	-1.02	$C_7H_{11}O_5$
205.07157	205.07176	-0.94	$C_8H_{13}O_6$
379.17648	379.17623	0.72	$C_{20}H_{27}O_7$
411.20243	411.20244	-0.03	$C_{21}H_{31}O_8$
439.19734	439.19736	-0.03	$C_{22}H_{31}O_9$
511.21824	511.21849	-0.47	$C_{25}H_{35}O_{11}$
615.26659	615.26583	1.21	$C_{29}H_{43}O_{14}$
705.29803	705.29752	0.72	$C_{32}H_{49}O_{17}$
819.36573	819.36560	0.16	$C_{38}H_{59}O_{19}$
580.14583	580.14519	1.11	$C_{25}H_{34}O_{12}{}^{54}Fe$
638.18791	638.18705	1.34	$C_{28}H_{40}O_{13}{}^{54}Fe$
666.18298	666.18197	1.52	$C_{29}H_{40}O_{14}{}^{54}Fe$
582.14108	582.14052	0.97	$C_{25}H_{34}O_{12}{}^{56}Fe$
640.18288	640.18183	1.63	$C_{28}H_{40}O_{13}{}^{56}Fe$
668.17737	668.17675	0.93	$C_{29}H_{40}O_{14}{}^{56}Fe$

Table SI 5. Fragments and annotated sum formula of parent ion 1083.45 in negative ionization mode

Measured *m/z*	Theoretical *m/z*	*Δppm*	Sum formula $[M-H]^-$
155.07137	155.07082	0.01	$C_8H_{11}O_3$
187.06112	187.06120	-0.42	$C_8H_{11}O_5$
379.17623	379.17623	0.01	$C_{20}H_{27}O_7$
397.18680	397.18679	0.02	$C_{20}H_{29}O_8$
569.26203	569.26035	-0.17	$C_{28}H_{41}O_{12}$
597.25526	597.25526	-0.01	$C_{29}H_{41}O_{13}$
669.27680	669.27639	0.61	$C_{32}H_{45}O_{15}$
687.28803	687.28696	1.57	$C_{32}H_{47}O_{16}$
801.35549	801.35504	0.56	$C_{38}H_{57}O_{18}$
879.35107	879.35035	0.82	$C_{39}H_{59}O_{22}$
1083.45106	1083.45012	0.87	$C_{48}H_{75}O_{27}$
930.26805	930.26649	1.68	$C_{39}H_{56}O_{22}{}^{54}Fe$
650.16767	650.16673	1.44	$C_{29}H_{38}O_{13}{}^{56}Fe$
904.26752	904.26690	0.69	$C_{38}H_{56}O_{21}{}^{56}Fe$
932.26197	932.26181	0.16	$C_{39}H_{56}O_{22}{}^{56}Fe$

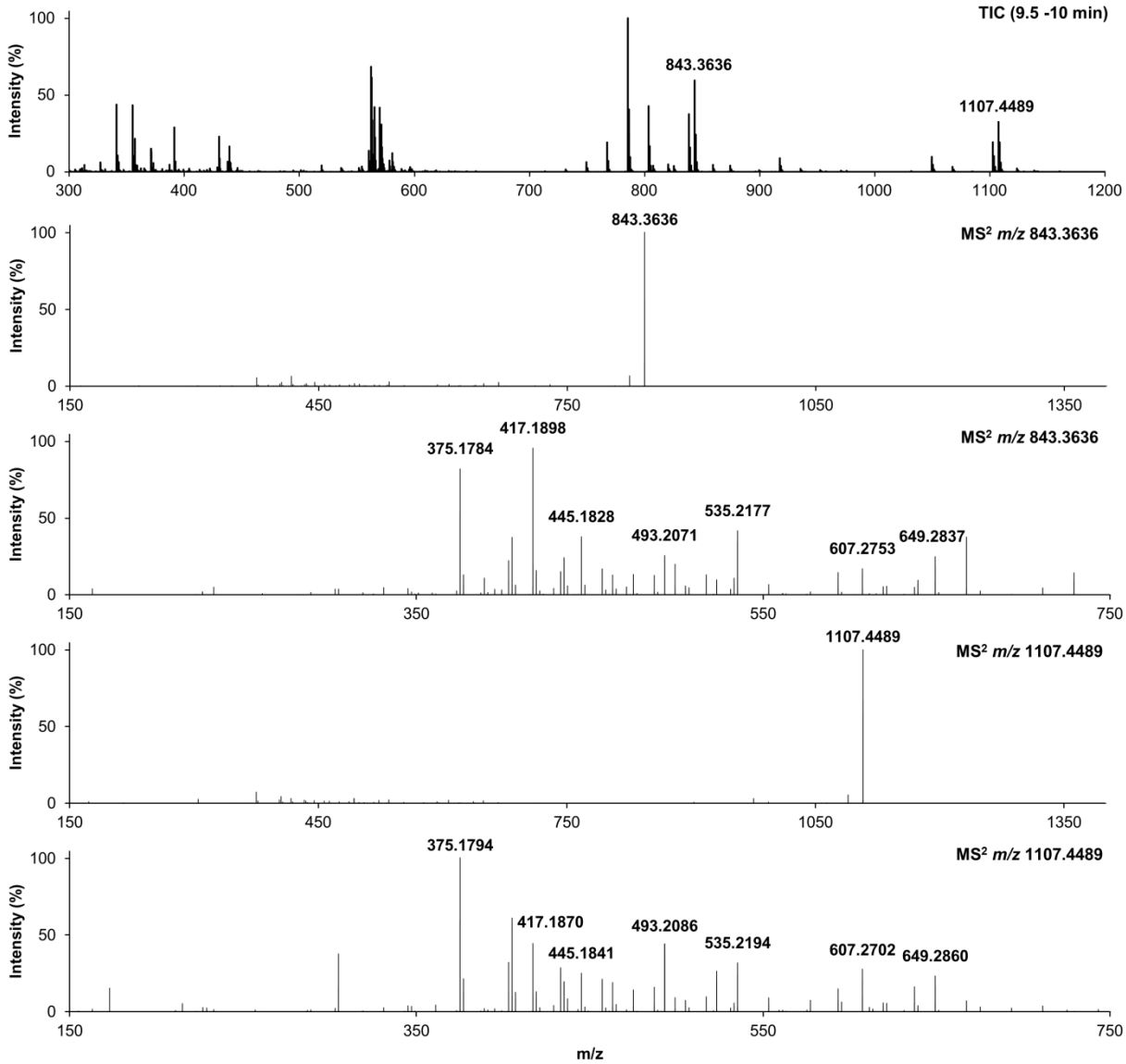

Figure SI 13. MS[1] and MS[2] of TDAC eluate of Station 9 in positive ionization mode.

Table SI 6. Fragments and annotated sum formula of parent ions *m/z* 843.36 and *m/z* 1107.45 in positive ionization mode

Measured *m/z*	Theoretical *m/z*	*Δppm*	Sum formula $[M+Na]^+$	Parent ion
305.08475	305.08485	-0.34	$C_{10}H_{18}O_9Na$	1107
375.17833; 375.17855	375.17836	-0.07; 0.51	$C_{19}H_{28}O_6Na$	843; 1107
403.18440	403.17327	1.14	$C_{20}H_{28}O_7Na$	1107
405.18902; 405.18932	405.18892	0.24; 0.98	$C_{20}H_{30}O_7Na$	843; 1107
417.18912; 417.18927	417.18892	0.48; 0.82	$C_{21}H_{30}O_7Na$	843; 1107
433.18440	433.18384	1.31	$C_{21}H_{30}O_8Na$	1107
435.19978	435.19949	0.68	$C_{21}H_{32}O_8Na$	843
445.18383	445.18384	-0.01	$C_{22}H_{30}O_8Na$	843
493.20549; 493.20563	493.20497	1.07; 1.35	$C_{23}H_{34}O_{10}Na$	843; 1107
535.21646; 535.21658	535.21553	1.74; 1.97	$C_{25}H_{36}O_{11}Na$	843; 1107
649.28399	649.28361	0.59	$C_{31}H_{46}O_{13}Na$	843
667.29502	667.29418	1.26	$C_{31}H_{48}O_{14}Na$	843
825.35352	825.35208	1.74	$C_{38}H_{58}O_{18}Na$	843
843.36356	843.36265	1.07	$C_{38}H_{60}O_{19}Na$	
975.40609	975.40609	1.22	$C_{43}H_{68}O_{23}Na$	1107
1089.43770	1089.43660	1.01	$C_{48}H_{74}O_{26}Na$	1107
1107.44884	1107.44717	1.51	$C_{48}H_{76}O_{27}Na$	

Table SI 7. MS[1] peak areas of *m/z* 819.36573 and *m/z* 1083.44946 observed in HP20 extracts of HE533 cruise in negative ionization mode.

Station No.	Extracted seawater volume (L)	Peak Area	
		m/z 819	*m/z* 1086
2	450	ND	ND
3	450	ND	ND
4	370	ND	ND
5	370	ND	ND
6	550	ND	ND
7	100	ND	ND
8	650	38038874	340989
9[a]	50	1290482741	37501524
9[b]	150	119485384	389630
10[c]	100	2894785	6091
10[c]	200	3214615	8954
10[c, d]	300	1333964	1784
11	250	628045	1838
12	50	5284851	35865
13	50	46733	ND
14	350	65183	ND
15	380	698226	6501
17	80	498768	ND
18	200	70240	ND
19	120	391092	ND
19	220	82329	ND
20	130	48498	ND
21	230	151619	ND
22	150	ND	ND
23	130	ND	ND
25	150	ND	ND
26	200	ND	ND
27	200	ND	ND
28	600	ND	ND

ND = not detected
[a] Water sampled from 3 m depth, corresponding to the chlorophyll maximum at this station
[b] Water sampled from 14 m depth
[c] Cell concentration >25 × 10^6 c/L of toxic *Chrysochromulina leadbeateri*
[d] Extraction without filtration

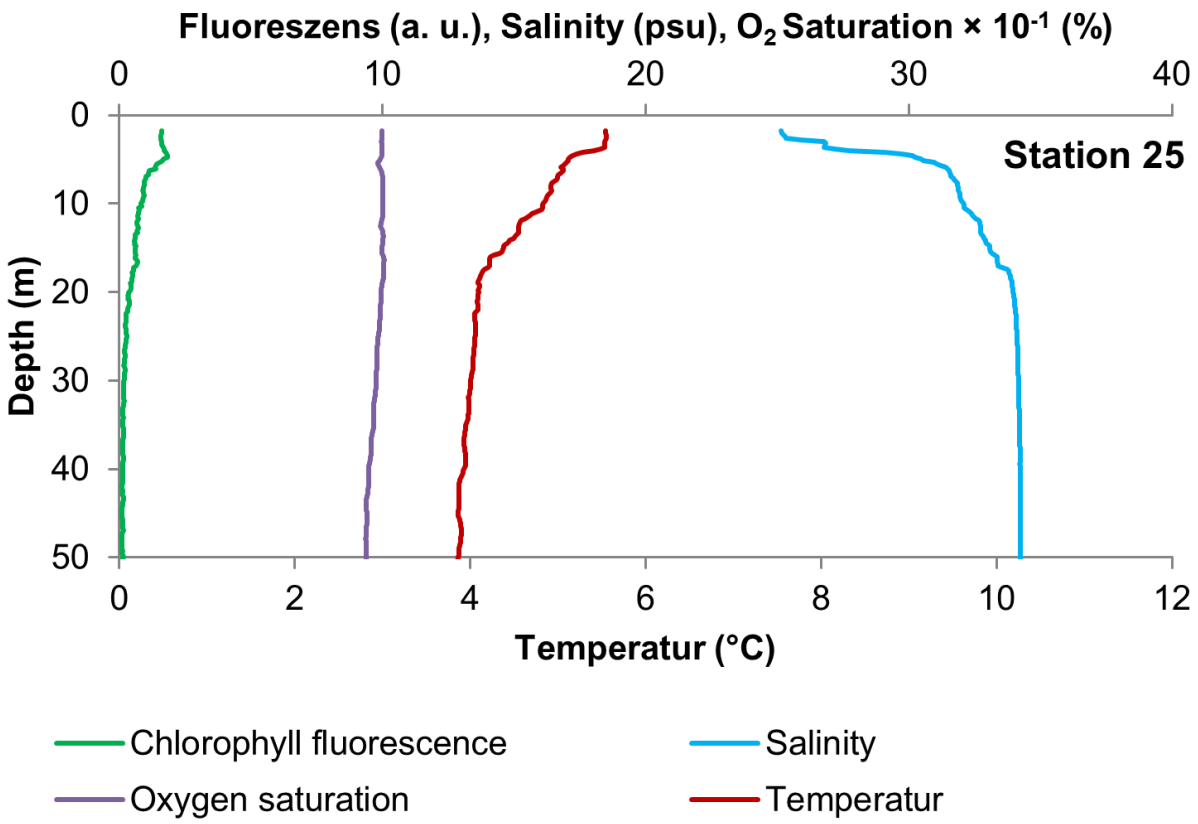

Figure SI 14. Depth profiles of chlorophyll fluorescence, salinity, O_2 saturation and temperature at Stations 25. Data is taken from the corresponding PANGEA entry (John and Wisotzki)